Behavior of reinforced concrete beams strengthened with anchored FRP sheets under cyclic load reversals

by

Salman Alshamrani

B.S., Al-Baha University, 2015
M.S., University of Dayton, 2020

AN ABSTRACT OF A DISSERTATION

submitted in partial fulfillment of the requirements for the degree

DOCTOR OF PHILOSOPHY

Department of Civil Engineering
Carl. R. Ice College of Engineering

KANSAS STATE UNIVERSITY
Manhattan, Kansas

2024

Abstract

The use of carbon fiber reinforced polymer (CFRP) composites is a widely accepted method for externally strengthening reinforced concrete members. However, there is a notable gap in the literature regarding the behavior of CFRP-strengthened beams fiber anchors under reversed cyclic loading. This study addresses this gap by examining the performance of normal and low-strength concrete, with a moderate steel ratio (0.005) and low steel ratio (0.0034), in constructing fourteen identical full-scale rectangular beams. These beams were strengthened with both unanchored and anchored CFRP sheets. Based on the concrete strength, steel ratio, and CFRP scheme, the beams were categorized into three groups. The first group comprised five beams with lightly reinforced steel and low-strength concrete. This group included a control specimen, as well as strengthened specimens with thin sheets with and without fiber anchors and strengthened specimens with thick sheets with and without fiber anchors. The second group replicated the first group in terms of CFRP scheme, but with a moderate steel ratio and higher-strength concrete. The third group consisted of four beams, two with the same lightly reinforced steel and low-strength concrete as those of group 1, and two with the same moderate steel ratio and higher-strength concrete as those of group 2. This third group consisted of two beams strengthened with double thick CFRP sheets top and bottom secured with fiber anchors. The other two were strengthened using a recent patent concept suggesting the use of a small steel plate as a ductility fuse by sandwiching it in between two layers of FRP at the critical plastic hinge region. All specimens underwent cyclic testing under displacement control, following the AC 125 loading protocol (Acceptance Criterion 125, ICC). The failure modes varied among all three groups, including excessive yielding, CFRP sheet debonding, CFRP sheet rupture, shear failure, and cover delamination. The hysteresis response loops of the different specimens were compared, including ultimate capacity, ductility, stiffness

degradation, and energy dissipation. Furthermore, this study involved the development of a phenomenological model to predict the response behavior of RC beams subjected to fully reversed loading cycles until failure. The comparative discussion and analysis of the results with the phenomenological model exhibited a promising correspondence. Finally, experimental observations were conducted to investigate the behavior of the structural systems with the indicated innovative materials under reverse cyclic loading, as well as the load-deflection, and the moment-curvature response. These observations aim to establish a basis for future analytical modeling of the hysteresis response of RC beams strengthened with CFRP sheets with and without fiber anchors.

Behavior of reinforced concrete beams strengthened with anchored FRP sheets under cyclic load reversals

by

Salman Alshamrani

B.S., Al-Baha University, 2015
M.S., University of Dayton, 2020

A DISSERTATION

submitted in partial fulfillment of the requirements for the degree

DOCTOR OF PHILOSOPHY

Department of Civil Engineering
Carl. R. Ice College of Engineering

KANSAS STATE UNIVERSITY
Manhattan, Kansas

2024

Approved by:

Major Professor
Hayder A. Rasheed

Copyright

Abstract

The use of carbon fiber reinforced polymer (CFRP) composites is a widely accepted method for externally strengthening reinforced concrete members. However, there is a notable gap in the literature regarding the behavior of CFRP-strengthened beams fiber anchors under reversed cyclic loading. This study addresses this gap by examining the performance of normal and low-strength concrete, with a moderate steel ratio (0.005) and low steel ratio (0.0034), in constructing fourteen identical full-scale rectangular beams. These beams were strengthened with both unanchored and anchored CFRP sheets. Based on the concrete strength, steel ratio, and CFRP scheme, the beams were categorized into three groups. The first group comprised five beams with lightly reinforced steel and low-strength concrete. This group included a control specimen, as well as strengthened specimens with thin sheets with and without fiber anchors and strengthened specimens with thick sheets with and without fiber anchors. The second group replicated the first group in terms of CFRP scheme, but with a moderate steel ratio and higher-strength concrete. The third group consisted of four beams, two with the same lightly reinforced steel and low-strength concrete as those of group 1, and two with the same moderate steel ratio and higher-strength concrete as those of group 2. This third group consisted of two beams strengthened with double thick CFRP sheets top and bottom secured with fiber anchors. The other two were strengthened using a recent patent concept suggesting the use of a small steel plate as a ductility fuse by sandwiching it in between two layers of FRP at the critical plastic hinge region. All specimens underwent cyclic testing under displacement control, following the AC 125 loading protocol (Acceptance Criterion 125, ICC). The failure modes varied among all three groups, including excessive yielding, CFRP sheet debonding, CFRP sheet rupture, shear failure, and cover delamination. The hysteresis response loops of the different specimens were compared, including ultimate capacity, ductility, stiffness

degradation, and energy dissipation. Furthermore, this study involved the development of a phenomenological model to predict the response behavior of RC beams subjected to fully reversed loading cycles until failure. The comparative discussion and analysis of the results with the phenomenological model exhibited a promising correspondence. Finally, experimental observations were conducted to investigate the behavior of the structural systems with the indicated innovative materials under reverse cyclic loading, as well as the load-deflection, and the moment-curvature response. These observations aim to establish a basis for future analytical modeling of the hysteresis response of RC beams strengthened with CFRP sheets with and without fiber anchors.

Table of Contents

List of Figures xii
List of Tables xviii
Nomenclature xix
Acknowledgements xxi
Dedication xxii
Chapter 1 - Introduction 1
1.1 Background 1
1.2 Objectives 2
1.3 Scope of Dissertation 3
Chapter 2 - Flexural Seismic Behavior of Low Concrete Strength-Steel Ratio RC Beams Strengthened by CFRP Sheets with and without Fiber Anchors 4
2.1. ABSTRACT 4
2.2. Introduction 5
2.3. Experimental Campaign 8
2.3.1. Specimen Matrix and Beam Parameters 8
2.3.2. Materials Characteristics 11
2.3.3. Specimen Fabrication 13
2.3.4. Specimen Strengthening 14
2.3.5. Loading Protocol and Measurement Instrumentation 14
2.3.6. Test Setup 15
2.4. Results and Discussions 16
2.4.1. Beam No.1 16
2.4.2. Beam No.2 18
2.4.3. Beam No.3 19
2.4.4. Beam No.4 21
2.4.5. Beam No.5 23
2.5. Comparison of Specimen Responses 25
2.5.1. Strength and Ductility 25
2.5.2. Stiffness Degradation 27
2.5.3. Experimental Envelope Curve 27
2.6. Analysis of the Envelope Curves 30

2.6.1. Cracking Point: 30
2.6.2. Yielding Point: 31
2.6.3. Ultimate Point: 31
2.7. Load-Strain and Moment-Curvature Response 36
2.8. Conclusions 39
Chapter 3 - Flexural Seismic Behavior of Moderate Concrete Strength-Steel Ratio RC Beams Strengthened by CFRP Sheets with and without Fiber Anchors 41
3.1. ABSTRACT 41
3.2. Introduction 41
3.3. Experimental Program 44
3.3.1. Specimen Design and geometric properties 44
3.3.2. Material Properties 48
3.3.3. Building and Casting of the Specimens 50
3.3.4. Preparing and Strengthening Techniques 50
3.3.5. Cyclic Loading and Instrumentation 51
3.3.6. Experimental Setup 52
3.4. Testing Outcomes 53
3.4.1. Beam No.10 53
3.4.2. Beam No.11 55
3.4.3. Beam No.12 57
3.4.4. Beam No.13 59
3.4.5. Beam No.14 61
3.5. Performance Comparison of Specimens 63
3.5.1. Strength and Ductility 63
3.5.2. Stiffness Degradation 65
3.6. Phenomenological Modeling of Hysteresis Loops 68
3.6.1. Assumptions 68
3.7. Conclusions 71
Chapter 4 - Analytical Modeling of the Envelope Curve and Phenomenological Depiction of Hysteretic Loops. 73
4.1. Introduction 73
4.2. Analysis of the Envelope Curves 75
4.2.1. Cracking Point: 75

4.2.2. Yielding Point: 76
4.2.3. Ultimate Point: 77
4.3. Hysteresis Loops Model 83
4.3.1. Analysis Steps 86
4.3.2. Model Calibration 87
4.3.3. Model Verification 89
4.4. Conclusions 91
Chapter 5 - Cyclic Response of RC Beams Strengthened and Anchored Using CFRP with and without Steel Fuse 92
5.1. ABSTRACT 92
5.2. Introduction 92
5.3. Testing Program 96
5.3.1. Design and Casting of Specimens 96
5.3.2. Material Properties 100
5.3.3. Strengthening Procedure 103
5.3.4. Test setup and Instrumentation. 106
5.4. Experimental Results 108
5.4.1. Load-Deflection Response 108
5.4.2. Failure Modes 124
5.4.3. Strength and Ductility 125
5.4.4. Energy Dissipation 129
5.4.5. Strains in CFRP Laminates and Steel Reinforcements 130
5.5. Conclusions 135
Chapter 6 - Experimental Observations for Future Analytical Modeling 137
6.1. Introduction 137
6.2. Load-Strain Curves 138
6.2.1. Steel Response 138
6.2.2. FRP Response 145
6.3. Moment-Curvature Curves 151
6.3.1. Steel Response 151
6.3.2. FRP Response 158
6.4. Load-Deflection Curves 166
6.4.1. Thin FRP Sheet (Beam No.3) 166

6.4.2. Thick FRP Sheet (Beam No.4) 168
6.4.3. Double-Thick FRP Sheet (Beam No.6) 170
6.4.4. Double-Thick FRP Sheet with Sandwiched Steel Plate (Beam No.7) Plus Shear Strengthening 170
6.5. Conclusions 172
Chapter 7 - Conclusions And Recommendations 174
7.1. Conclusions 174
7.2. Recommendations 177
References 178

List of Figures

Figure 2.1. Beam No.1 (Control beam) 9
Figure 2.2. Beam No.2 9
Figure 2.3. Beam No.3 10
Figure 2.4. Beam N.4 10
Figure 2.5. Beam No.5 11
Figure 2.6. Carbon fiber splay anchors. 11
Figure 2.7. (a-c) RC Beams during Surface Preparing and CFRP Installation. 14
Figure 2.8. Loading Protocol for Beam No.2. 15
Figure 2.9. Standard testing set-up of beam No.2. 16
Figure 2.10. Load-displacement response of beam No.10 (1 Kips=4.45 KN) 17
Figure 2.11. Specimen No.1. (a) before testing. (b) at failure 18
Figure 2.12. Load-displacement response of beam No.2 (1 Kips=4.45 KN) 19
Figure 2.13. Specimen No.2. (a) before testing. (b) at failure 19
Figure 2.14. Load-displacement response of beam No.3 (1 Kips=4.45 KN) 21
Figure 2.15. Specimen No.3. (a) before testing. (b) at failure 21
Figure 2.16. Load-displacement response of beam No.4 (1 Kips=4.45 KN) 22
Figure 2.17. Specimen No.4. (a) before testing. (b) at failure 23
Figure 2.18. Load-displacement response of beam No.5 (1 Kips=4.45 KN) 24
Figure 2.19. Specimen No.5. (a) before testing. (b) at failure 24
Figure 2.20. Envelope Carves Comparison of all Beams. 26
Figure 2.21. Energy dissipation of all beams 26
Figure 2.22. Peak ultimate load at failure for all beams 29
Figure 2.23. Peak displacement at failure for all beams 30
Figure 2.24. Analytical vs. Experimental Envelope Curve Comparison of beam No.1 33
Figure 2.25. Analytical vs. Experimental Envelope Curve Comparison of beam No.2 34
Figure 2.26. Analytical vs. Experimental Envelope Curve Comparison of beam No.3 34
Figure 2.27. Analytical vs. Experimental Envelope Curve Comparison of beam No.4 35
Figure 2.28. Analytical vs. Experimental Envelope Curve Comparison of beam No.5 35
Figure 2.29. Top FRP Load-Strain for Beam No.3 37

Figure 2.30. Bottom FRP Load-Strain for Beam No.3 37
Figure 2.31. Top Steel Rebar Load-Strain for Beam No.3 38
Figure 2.32. Bottom Steel Rebar Load-Strain for Beam No.3 38
Figure 2.33. Experimental and Modeled Moment-Curvature of Beam No.3 39
Figure 3.1. Beam No.10 (Control beam) 45
Figure 3.2. Beam No.11 46
Figure 3.3. Beam N.12 46
Figure 3.4. Beam N.13 47
Figure 3.5. Beam No.14 47
Figure 3.6. Carbon fiber splay anchors 48
Figure 3.7. (a-c) RC Beams during Surface Preparation and CFRP Installation and Anchoring. 51
Figure 3.8. Loading Protocol for Beam No.10. 52
Figure 3.9. Typical testing set-up (Beam No.13) 53
Figure 3.10. Load-displacement response of beam No.10 (1 Kips=4.45 KN) 54
Figure 3.11. Specimen No.10. (a) before testing. (b) at failure 55
Figure 3.12. Load-displacement response of beam No.11 (1 Kips=4.45 KN) 56
Figure 3.13. Specimen No.11. (a) before testing. (b) at failure 57
Figure 3.14. Load-displacement response of beam No.12 (1 Kips=4.45 KN) 58
Figure 3.15. Specimen No.12. (a) before testing. (b) at failure 59
Figure 3.16. Load-displacement response of beam No.13 (1 Kips=4.45 KN) 60
Figure 3.17. Specimen No.13. (a) before testing. (b) at failure 61
Figure 3.18. Load-displacement response of beam No.14 (1 Kips=4.45 KN) 62
Figure 3.19. Specimen No.14. (a) before testing. (b) at failure 62
Figure 3.20. Envelope Carves Comparison of all Beams (1 Kips=4.45 KN) 64
Figure 3.21. Energy dissipation of all beams 65
Figure 3.22. Peak displacement at failure for all beams 67
Figure 3.23. Peak ultimate load at failure for all beams 68
Figure 3.24. Three linear regions of the hysteresis loop model. 70
Figure 3.25. Regions a, b, c graphs to characterize the hysteresis loops beam No.11 70
Figure 3.26. Experimental vs. modeled hysteresis loops for beam No.11 (1 Kips=4.45 KN) 71
Figure 3.27. Experimental vs. modeled hysteresis loops for beam No.12 (1 Kips=4.45 KN) 71

Figure 4.1. Analytical vs. Experimental Envelope Curve Comparison of beam No.1 78
Figure 4.2. Analytical vs. Experimental Envelope Curve Comparison of beam No.2 79
Figure 4.3. Analytical vs. Experimental Envelope Curve Comparison of beam No.3 79
Figure 4.4. Analytical vs. Experimental Envelope Curve Comparison of beam No.4 80
Figure 4.5. Analytical vs. Experimental Envelope Curve Comparison of beam No.5 80
Figure 4.6. Analytical vs. Experimental Envelope Curve Comparison of beam No.10 81
Figure 4.7. Analytical vs. Experimental Envelope Curve Comparison of beam No.11 81
Figure 4.8. Analytical vs. Experimental Envelope Curve Comparison of beam No.12 82
Figure 4.9. Analytical vs. Experimental Envelope Curve Comparison of beam No.13 82
Figure 4.10. Analytical vs. Experimental Envelope Curve Comparison of beam No.14 83
Figure 4.11. Three Linear Regions of The Hysteresis Loop Model. 85
Figure 4.12. Hysteresis Regions Relative to The Backbone Curve. 85
Figure 4.13. Regions A, B, C Graphs to Characterize the Hysteresis Loops beam No.11. 86
Figure 4.14. Regions A, B, C Graphs to Characterize the Hysteresis Loops beam No.13. 86
Figure 4.15. Experimental vs. modeled hysteresis loops for beam No.11 (1 Kips=4.45 KN) 88
Figure 4.16. Experimental vs. modeled hysteresis loops for beam No.12 (1 Kips=4.45 KN) 88
Figure 4.17. Experimental vs. modeled hysteresis loops for beam No.11 (1 Kips=4.45 KN) 89
Figure 4.18. Experimental vs. modeled hysteresis loops for beam No.11 (1 Kips=4.45 KN) 90
Figure 4.19. Experimental vs. modeled energy dissipation for all beams. 90
Figure 5.1. Beam No.1 97
Figure 5.2. Beam No.10 98
Figure 5.3. Beam No.6 98
Figure 5.4. Beam No.15 99
Figure 5.5. Beam No.7 99
Figure 5.6. Beam No.16 100
Figure 5.7. Cross section of beam No.7, beam No.16, and the carbon fiber anchor. 100
Figure 5.8. Beams during surface preparation and CFRP installation phase............................. 105
Figure 5.9. Loading frame and testing setup.. 107
Figure 5.10. Loading points cross section 107
Figure 5.11. Loading Protocol for Beam No.6. 108
Figure 5.12 Specimen No.6. setup before testing. 110

Figure 5.13. Load-displacement response of beam No.10 (1 Kips=4.45 KN) 110
Figure 5.14. Specimen No.1 at failure. 111
Figure 5.15. Specimen No.6. setup before testing. 112
Figure 5.16. Load-displacement response of beam No.6 (1 Kips=4.45 KN) 113
Figure 5.17. Failure Mode of beam No.6 due to shear cracks. 113
Figure 5.18. Load-displacement response of beam No.7 (1 Kips=4.45 KN) 115
Figure 5.19. Test setup of beam No.7 before testing 115
Figure 5.20. Specimen No.7 after failure... 116
Figure 5.21. Test setup of beam No.10 before testing 117
Figure 5.22. Load-displacement response of beam No.10 (1 Kips=4.45 KN) 118
Figure 5.23. Specimen No.10 after failure... 118
Figure 5.24. Specimen No.15. before testing... 120
Figure 5.25. Load-displacement response of beam No.15 (1 Kips=4.45 KN) 120
Figure 5.26. Failure Mode of beam No.15.. 121
Figure 5.27. Formulation of concrete cover delamination and shear cracks of beam No.15 during testing 121
Figure 5.28. Specimen No.15. before testing... 123
Figure 5.29. Load-displacement response of beam No.16 (1 Kips=4.45 KN) 123
Figure 5.30. Failure mode of beam No.16. 124
Figure 5.31. Load-displacement envelope curves of all specimens... 127
Figure 5.32. Peak displacement at failure of all specimens 127
Figure 5.33. Peak load comparison of all specimens. 128
Figure 5.34. Hysteresis response of beams No.6 and No.7 128
Figure 5.35. Hysteresis response of beams No.15 and No.16 129
Figure 5.36. Energy dissipation comparison of all specimens... 130
Figure 5.37. Load-strain response of top steel rebars of beam No.6 132
Figure 5.38. Load-strain response of top steel rebars of beam No.7 132
Figure 5.39. Load-strain response of bottom steel rebars of beam No.6 133
Figure 5.40. Load-strain response of bottom steel rebars of beam No.7 133
Figure 5.41. Load-strain response of top FRP sheet of beam No.6 134
Figure 5.42. Load-strain response of top FRP sheet of beam No.7 134

Figure 5.43. Load-strain response of bottom FRP sheet of beam No.6 135
Figure 5.44. Load-strain response of bottom FRP sheet of beam No.7 135
Figure 6.1. Load-strain response of top steel rebars of beam No.3 139
Figure 6.2. Load-strain response of bottom steel rebars of beam No.3 140
Figure 6.3. Material response to cyclic loading: (a) purely elastic deformations, (b) elastic shakedown, (c) plastic shakedown and (d) ratchetting adapted from (Dollevoet, 2010). .. 140
Figure 6.4. Load-strain response of top steel rebars of beam No.4 141
Figure 6.5. Load-strain response of bottom steel rebars of beam No.4 142
Figure 6.6. Load-strain response of top steel rebars of beam No.6 143
Figure 6.7. Load-strain response of bottom steel rebars of beam No.6 143
Figure 6.8. Load-strain response of top steel rebars of beam No.7 144
Figure 6.9. Load-strain response of bottom steel rebars of beam No.7 145
Figure 6.10. Load-strain response of top FRP sheets of beam No.3 146
Figure 6.11. Load-strain response of bottom FRP sheets of beam No.3 146
Figure 6.12. Load-strain response of top FRP sheets of beam No.4 147
Figure 6.13. Load-strain response of bottom FRP sheets of beam No.4 148
Figure 6.14. Load-strain response of top FRP sheets of beam No.6 149
Figure 6.15. Load-strain response of bottom FRP sheets of beam No.6 149
Figure 6.16. Load-strain response of top FRP sheets of beam No.7 150
Figure 6.17. Load-strain response of bottom FRP sheets of beam No.7 150
Figure 6.18. Moment-Curvature prior to yielding from steel strain of beam No.3 152
Figure 6.19. Moment-Curvature after yielding from steel strain of beam No.3 152
Figure 6.20. Moment-Curvature prior to yielding from steel strain of beam No.4 153
Figure 6.21. Moment-Curvature after yielding from steel strain of beam No.4 154
Figure 6.22. Moment-Curvature prior to failure from steel strain of beam No.4 154
Figure 6.23. Moment-Curvature prior to yielding from steel strain of beam No.6 155
Figure 6.24. Moment-Curvature after yielding from steel strain of beam No.6 156
Figure 6.25. Moment-Curvature prior to yielding from steel strain of beam No.7 157
Figure 6.26. Moment-Curvature after yielding from steel strain of beam No.7 157
Figure 6.27. Moment-Curvature prior to failure from steel strain of beam No.7 158
Figure 6.28. Moment-Curvature prior to yielding from CFRP strain of beam No.3 159

Figure 6.29. Moment-Curvature after yielding from CFRP strain of beam No.3 160
Figure 6.30. Moment-Curvature prior to yielding from CFRP strain of beam No.4.................. 161
Figure 6.31. Moment-Curvature after yielding from CFRP strain of beam No.4 161
Figure 6.32. Moment-Curvature prior to failure from CFRP strain of beam No.4..................... 162
Figure 6.33. Moment-Curvature prior to yielding from CFRP strain of beam No.6.................. 163
Figure 6.34. Moment-Curvature after yielding from CFRP strain of beam No.6 163
Figure 6.35. Moment-Curvature prior to yielding from CFRP strain of beam No.7.................. 164
Figure 6.36. Moment-Curvature after yielding from CFRP strain of beam No.7 165
Figure 6.37. Moment-Curvature prior to failure from CFRP strain of beam No.7..................... 165
Figure 6.38. Load-Deflection response of beam No.3... 166
Figure 6.39. Energy dissipation comparison of all specimens investigated herein. 167
Figure 6.40. Peak displacement comparison of all specimens investigated herein. 167
Figure 6.41. Peak load comparison of all specimens investigated herein. 168
Figure 6.42. Load-Deflection response of beam No.4... 169
Figure 6.43. Load-Deflection response of beam No.3 vs beam No.4.. 169
Figure 6.44. Load-Deflection response of beam No.6... 170
Figure 6.45. Load-Deflection response of beam No.7... 171
Figure 6.46. Load-Deflection response of beam No.6 vs beam No.7.. 172

List of Tables

Table 2.1. Beams details summary. 8
Table 2.2.Concrete Compressive Strength Testing........ 12
Table 2.3. Mechanical properties of the tested steel bars. 13
Table 2.4. Mechanical Properties of CFRP per Manufacturer........ 13
Table 2.5. Forward loading against displacement (Push Side). 28
Table 2.6. Reversed loading against displacement (Pull Side). 28
Table 2.7. Forward loading against cycle size (Push Side). 28
Table 2.8. Reversed loading against cycle size (Pull Side). 29
Table 2.9. Comparison of average experimental results against analytical predictions. 33
Table 3.1. CFRP strengthening details of all specimens. 45
Table 3.2. Concrete Compressive Strength Testing........ 49
Table 3.3. Steel mechanical property testing results........ 49
Table 3.4. Mechanical Properties of CFRP per Manufacturer........ 50
Table 3.5. Forward loading against displacement (Push direction). 66
Table 3.6. Reversed loading against displacement (Pull direction). 66
Table 3.7. Forward loading against cycle displacement (Push direction). 66
Table 3.8. Reversed loading against cycle displacement (Pull direction). 67
Table 4.1. Comparison of average experimental results against analytical predictions. 78
Table 5.1 Concrete Compressive Strength Testing........ 101
Table 5.2 Steel mechanical property testing results........ 102
Table 5.3 Mechanical testing results for the short steel plates. 102
Table 5.4 Mechanical properties of CFRP sheet and anchor per Manufacturer specifications. . 103
Table 5.5 Beams flexural strengthening details. 104
Table 5.6 Beams shear strengthening categories. 105

Nomenclature

A_f	Area of FRP
As	Area of tension steel.
As’	Area of compression steel.
b	width of a cross-section.
Ci	location of the neutral axis at the inflection strains level.
Cy	location of the neutral axis at yielding.
d	location of the tension steel with respect to the extreme compression fiber.
d’	location of the compression steel with respect to the extreme compression fiber.
E_c	Initial concrete modulus (Young’s modulus).
Es	Steel modulus of elasticity.
Ef	FRP modulus of elasticity.
f'c	concrete compressive strength.
h	height of the cross-section.
I_g	gross moment of inertia of gross concrete section about centroidal axis.
M	moment due to applied load.
Mcr	minimum moment at which the cracking takes place at a cross-section.
My	minimum moment at which the yielding takes place at a cross-section.
M_n	moment corresponding to ultimate moment of section.
M_{res}	moment at the residual point in the moment-curvature response.
P	applied load at envelope.
$\bar{y}_c$	location of the neutral axis prior to cracking.
ϕ_{un}	curvature corresponding to the pre-cracking region.
ϕ_{cr}	curvature corresponding to cracking moment of section.

ϕ_y	curvature corresponding to yielding moment of section.
ϕ_n	curvature corresponding to ultimate moment of section.
Ec	modulus of elasticity of concrete.
I_{gt}	gross transformed section moment of inertia.
y_t	the centroid depth of the section to the extreme tension fiber.

Acknowledgements

I would like to express my gratitude and sincere appreciation to my sponsor, the University of Bisha in Saudi Arabia, for the scholarship provided to me to pursue my graduate study in the United States. To my advisor, Prof. Hayder Rasheed. Thank you for the encouragement, valuable guidance, helpful advice, and efforts during the preparation of this work. I would also like to extend my heartfelt thanks to the members of my dissertation committee, Dr. David Rosowsky, Dr. Krishna Ghimire, and Dr. Bill Zhang for giving me helpful instructions and suggestions for my research. Furthermore, I would like to express my gratitude to my parents, wife, and friends who have been a constant source of encouragement, love, and understanding. Finally, special thanks to my colleagues, and the research technologists at the structural laboratory at Kansas State University for their valuable support.

Dedication

I dedicate this work to…

To my parents, whose boundless love, sacrifices, and encouragement have shaped me into the person I am today.

To my dear wife, whose unwavering support, understanding, and encouragement have been my constant source of strength.

To my trusted friends, whose unwavering friendship, guidance, and support have been a constant source of inspiration.

SALMAN ALSHAMRANI

Chapter 1 - Introduction

1.1 Background

Most of the current standing buildings are vulnerable as a result of being exposed to harsh weather conditions, such as humidity, and environmental disasters, such as seismic activity. Therefore, the need for innovative and effective methods to retrofit these concrete structures becomes increasingly essential. One of the strengthening techniques available is the use of carbon fiber reinforced polymer (CFRP). CFRP strengthening has become an ideal technique for upgrading and retrofitting concrete elements due to its remarkable properties such as durability as well as high ultimate strength. In fact, CFRP is a corrosion resistant material and has a high strength-to-weight ratio (Lee et al. 2009, Singh et al. 2014, Wang et al. 2019, Siddika et al. 2018, Sbahieh et al. 2022-a, Sbahieh et al. 2022-b, and Vijayan et al. 2023). A large number of research studies have been done to investigate the use of CFRP as a strengthening material applied to reinforced concrete structures. However, the majority of these studies have focused on the behaviors of RC members strengthened with CFRP under monotonic loading (Dong et al. 2012, Dias et al. 2018, Alabdulhady et al. 2022, Barris et al. 2023, and Liu et al. 2023). Therefore, there is a need to better understand the seismic response of these strengthened RC members, since cyclic loading conditions, such as those induced by earthquakes, can significantly affect the structural performance and durability of RC elements.

Furthermore, there is a lack of studies investigating the effectiveness of using fiber anchors as an anchorage system that can mechanically transfer forces from the CFRP sheet to the concrete substrate. As a result, guidelines for installing fiber anchors are limited (Sbahieh et al. 2022-b). Factors such as anchor layout, hole inclination, depth and area of the anchor hole, anchor diameter, amount of CFRP materials, anchor fan length, fan angle, and anchor reinforcement influence the anchorage success (Garcia et al. 2014).

1.2 Objectives

The use of CFRP to strengthen the existing concrete members can be an alternative option due to their affordability, lightweight, as well as durability compared to demolishing the entire structure. Over the last two decades, the demand on retrofitting and enhancing the load-carrying capacity of existing structures has increased, leading to more research on using CFRP as a strengthening material. However, using CFRP sheets to strengthen RC beams subjected to cyclic loading has not been well covered yet in the literature. Therefore, this study aims to investigate the seismic behavior of full-scale RC simple beams that have been strengthened with CFRP sheets of varying thickness at the top and bottom surfaces of the member, with and without carbon fiber anchor arrangements, in comparison with a control specimen. The specified objectives of this research study are as follows:

- Investigate the seismic performance of RC beams strengthened with CFRP sheets.
- Develop an optimal strengthened technique using carbon fiber splay anchors.
- Study the effects of using various thickness of CFRP sheets with and without carbon fiber anchors.
- Examine the influences of using multiple layers of thick CFRP sheets simultaneously with or without steel plate acting as a ductility fuse.
- Develop a phenomenological model to simulate the hysteresis loops response of RC beams strengthened with CFRP sheets with or without anchors.
- Conduct an experimental investigation to establish a basis for future analytical modeling of the hysteresis response of RC beams strengthened with CFRP sheets.

1.3 Scope of Dissertation

This dissertation consists of seven chapters. The first chapter includes an overview of the topics, objectives of this research, and scope of this dissertation. Chapter two, Flexural Seismic Behavior of Low Concrete Strength-Steel Ratio RC Beams Strengthened by CFRP Sheets with and without Fiber Anchors, presents an experimental study of strengthened RC beams with low-strength concrete and lightly reinforced steel ratio to investigate their seismic performance. Chapter three, Flexural Seismic Behavior of Moderate Concrete Strength-Steel Ratio RC Beams Strengthened by CFRP Sheets with and without Fiber Anchors, includes further experimental investigation of the cyclic response of higher strength concrete and moderate steel ratio in RC beams strengthened with CFRP sheets with and without fiber anchors. Chapter four focuses on predicting the flexural response of the backbone curve using an available analytical model and developing a phenomenological modeling to simulate the hysteresis response of strengthened RC beams by various CFRP thickness secured with and without fiber anchors. Chapter five introduces an additional experimental program with a new test setup and a recent patent concept suggesting the use of a small steel plate as a ductility fuse by sandwiching it in between two layers of FRP at the critical plastic hinge region. In chapter six, experimental investigations and observations for future analytical modeling were highlighted to facilitate formulating and predicting the seismic performance of strengthened RC beams. In the last chapter, chapter seven, conclusions, and recommendations on the dissertation topics are presented.

Chapter 2 - Flexural Seismic Behavior of Low Concrete Strength-Steel Ratio RC Beams Strengthened by CFRP Sheets with and without Fiber Anchors

2.1. ABSTRACT

An experimental program was conducted to examine the seismic performance of flexural beam members strengthened with carbon fiber-reinforced polymer (CFRP) sheet and anchored using carbon fiber splay anchors. This research extends the use of carbon fiber anchors to secure the top and bottom CFRP flexural sheets under cyclic loading. In this study, low strength concrete is examined, with lightly reinforced steel ratio (0.0034) to test full-scale rectangular beams. Five reinforced concrete beams were cast, strengthened, and tested under reversed cycles of four-point bending to failure. The beams were categorized into a control specimen, strengthened specimens with thin sheets with and without fiber anchors, and strengthened specimens with thick sheets with and without fiber anchors. They were tested cyclically under displacement control according to the AC 125 loading protocol (Acceptance Criterion 125, ICC). The failure modes ranged from classical ultimate failure for the control beam to rupture and IC debonding for the beam with unanchored thin CFRP sheets. On the other hand, debonding took place for the thicker sheets with no anchors, while the thicker sheets with fiber anchors underwent cover delamination failure mode despite the fact that the sheets were extended very close to the simple supports. The hysteresis response loops were compared for the different specimens and the analytical envelop curves were predicted resulting in a close agreement to the experimental finding.

Keywords: Seismic performance; CFRP strengthening; Carbon fiber splay anchors; Cyclic response; Modeling backbone curve.

2.2. Introduction

The use of Carbon Fiber Reinforced Polymers (CFRP) has become a well-known technique to strengthen or rehabilitate existing reinforced concrete members, such as beams, columns, and frames. In fact, during the last two decades, the demand of retrofitting and enhancing the load-carrying capacity of existing structures has increased, leading to more research on using CFRP as a strengthening material. Numerous studies have demonstrated the effectiveness of using CFRP in enhancing the flexural behavior of RC beams under monotonic loading (Rasheed and Pervaiz 2002, Tamimi et al. 2011, Saqan et al. 2013, Rasheed and Decker 2015, and Smith et al. 2017). However, using this technique to strengthen (RC) beams located in active seismic zones needs further evaluation to investigate the effects of cyclic loading on the response of strengthened RC beams. Additionally, new anchoring techniques need to be investigated to develop optimized anchoring methods for RC members that significantly improve the cyclic behavior.

The main components of the CFRP-concrete bonded system, which are utilized to externally strengthen RC structures, include CFRP dry fiber sheets, adhesive, and anchors whenever they are applied (Rasheed and Pervaiz 2002). Typically, it is assumed that there is a full composite action between the surface of concrete members such as beams and CFRP materials. However, the degree of bonding directly depends on the shear stiffness and strength of the adhesive, which must be sufficient to transfer the shear forces between CFRP and concrete substrate (Rasheed and Pevaiz 2003, Gao et al. 2012, and Teng 2018). Additionally, the quality of bond is directly impacted by concrete properties and surface preparation. Many studies and design codes reflect that as the compressive strength of the concrete increases, so does the strength of the CFRP-concrete system

(Hollaway et al. 1999, Walraven 2010, Kim 2014, and Fu et al. 2018). Thus, many researchers have investigated how to improve the bond deficiencies by applying different types of mechanical anchoring systems (Chen et al. 2007, Diab and Farghal 2014, Chen et al. 2018, and Alhassan et al. 2021). In fact, using anchoring along with adhesive to secure the CFRP sheets can improve the loading capacity by significant amounts (Alhassan et al. 2021).

Limited studies have investigated the seismic behavior of RC structures strengthened with CFRP. Ceroni (2010) studied the performance of strengthened RC beams with Externally Bonded Reinforcement (EBR) and Near Surface Mounted (NSM) bars under monotonic and cyclic loading. The findings of this study showed that the loading-carrying capacity increased in the range of 26% to 50% in case of low reinforcement ratio and 17% to 33% for higher reinforcement ratios. It was also observed that the ductility was reduced when CFRP is used as externally bonded strengthening material due to the premature debonding of the CFRP sheets. On the other hand, the use of Near Surface Mounted (NSM) bars successfully improved the ductility of the system along with increasing the ultimate failure load. The failure mode changed from debonding when CFRP sheets were used to cover delamination or concrete crushing when NSM bars are used. Additionally, different types of anchors were used along with Externally Bonded Reinforcement (EBR) to investigate their effectiveness towards enhancing the performance of the strengthened system. It was found that an adequate ductility was reached as well as enhancement of ultimate loading capacity when anchoring devices were applied. Finally, according to the author, a redaction of at least 10 % of the ultimate failure load was observed under cyclic compared to monotonic loading.

Laseima et al. (2020) carried out an experimental study to investigate the seismic behavior of exterior RC beam-column joints strengthened with CFRP. According to the authors, the strength, energy dissipation and ductility of the strengthened system were enhanced by 61.7%, 208.9%, and 61.8% respectively compared to the control specimen.

Another study by Saqan et al. (2020) investigated the effectiveness of using CFRP with various anchors on seismic behavior of RC beam-column joint assemblies. The finding of this study demonstrated that the ultimate load-curying capacity increased by 19% to 43.6% compared to the control specimens depending on the anchoring arrangements. It was also evident that all strengthened specimens exhibited higher total energy dissipation and damping ratios compared to the control one.

A more recent study conducted by Karayanniset and Golias (2022) examined full-scale RC beam-column joints that were externally strengthened using CFRP ropes. These joints were strengthened by applying X-shaped ropes, either single or double, at each side of the joint. Additionally, single or double straight ropes were applied at each side of the beam. The specimens that were strengthened in this manner exhibited an enhanced hysteretic response compared to the non-strengthened ones. The improvement was observed in terms of maximum loads per loading step, stiffness, and energy dissipation. The ultimate capacity of the strengthened specimens increased by a range of 20% to 57%, depending on the number of CFRP ropes used.

This study aims to investigate the seismic behavior of full-scale RC simply supported beams strengthened with CFRP sheets of varying thicknesses at their top and bottom surfaces, with and without carbon fiber anchor arrangements, in comparison with a control specimen. All specimens in this study have been designed with low concrete strength to simulate older beams having nearly a minimum steel ratio. The main objective of this strengthening study is to enhance the capability of RC beams, particularly under extreme events like earthquakes. To evaluate their performance, all specimens are subjected to a quasi-static cyclic loading in displacement control. A comparison is made between the strengthened specimens and the control specimen, as well as between specimens with different sheet thickness and anchoring arrangements. Furthermore, the experimental envelope response is accurately predicted using an analytical approach typically suitable for monotonic loading.

2.3. Experimental Campaign

2.3.1. Specimen Matrix and Beam Parameters

Five full-scale RC beam specimens were designed in accordance with ACI 318 building code (American Concrete Institute, 2019). All specimens are identical in geometry, reinforcement steel, ϕ 13 bars in flexure and ϕ 10 bars in shear (#4 bars in flexure and #3 bars in shear), as well as concrete strength but are categorized differently in terms of the level of strengthening, based on the thickness of CFRP layers and their anchoring status, as shown in Table2.1. The dimensions, steel reinforcement layout as well as the supports and loading protocol are shown in Figure 2.1. Furthermore, Figure 2.2. to Figure 2.5. present the geometry of specimens No.2 to No.5 along with the steel reinforcement as well as the strengthening CFRP sheet types and anchors arrangement. Figure 2.6. illustrates the carbon fiber splay anchors that are used to secure the CFRP sheet in beams No.3 and No.5.

Table 2.1. Beams details summary.

Beam No.	Specimen Type	CFRP Sheets	Number of layers	Figure No.	Δy Analysis (μ=1) mm (in)
1	Control	N/A	N/A	1	18.30 (0.72)
2	FRP strenghened	CSS V-Wrap™ C100HM	1 top and bottom	2	19.05 (0.75)
3	FRP strenghened & anchored	CSS V-Wrap™ C100HM	1 top and bottom	3	19.05 (0.75)
4	FRP strenghened	CSS V-Wrap™ C400HM	1 top and bottom	4	20.32 (0.80)
5	FRP strenghened & anchored	CSS V-Wrap™ C400HM	1 top and bottom	5	20.32 (0.80)

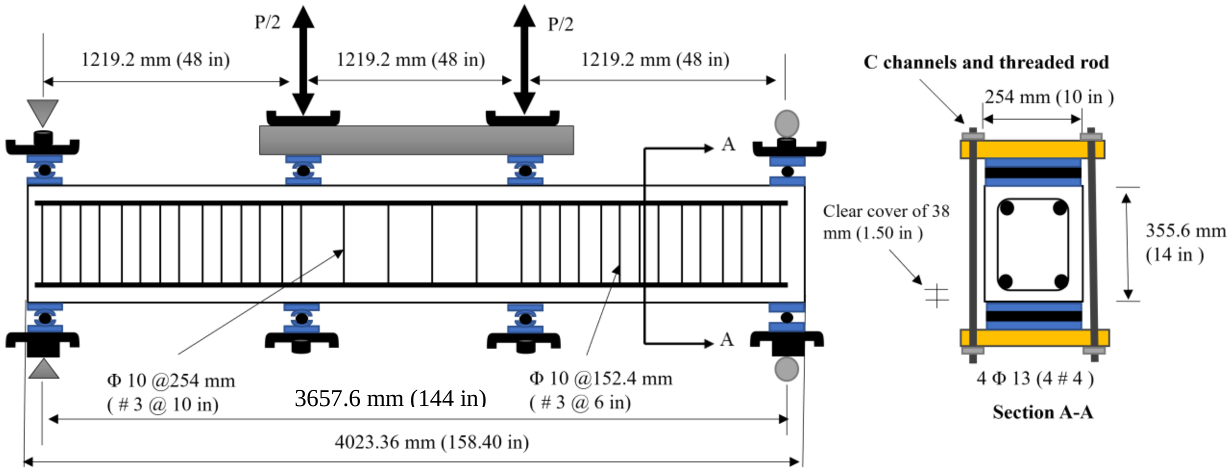

Figure 2.1. Beam No.1 (Control beam)

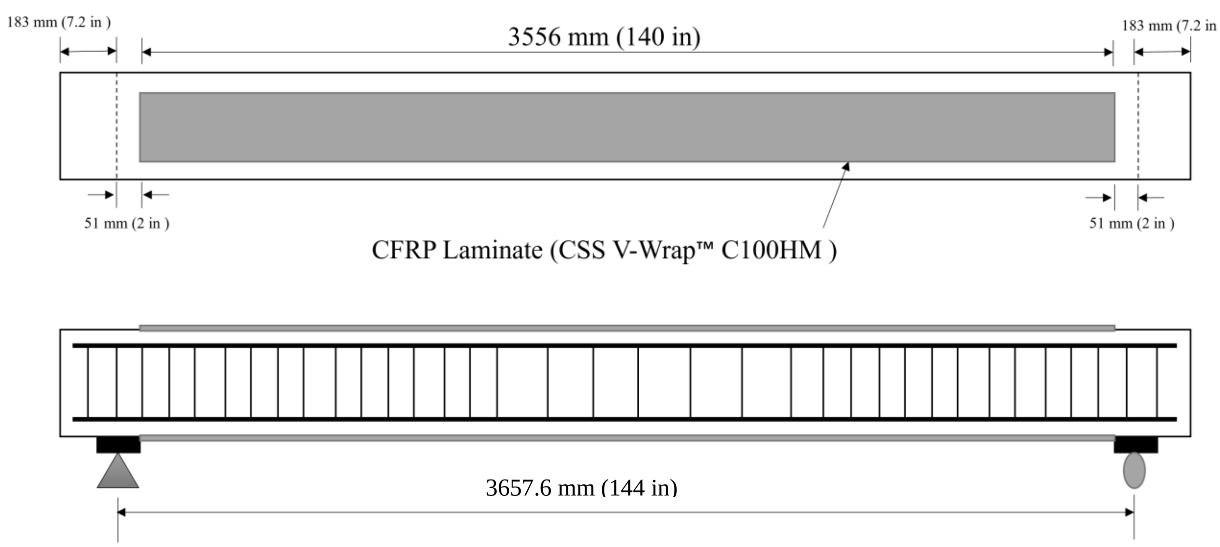

Figure 2.2. Beam No.2

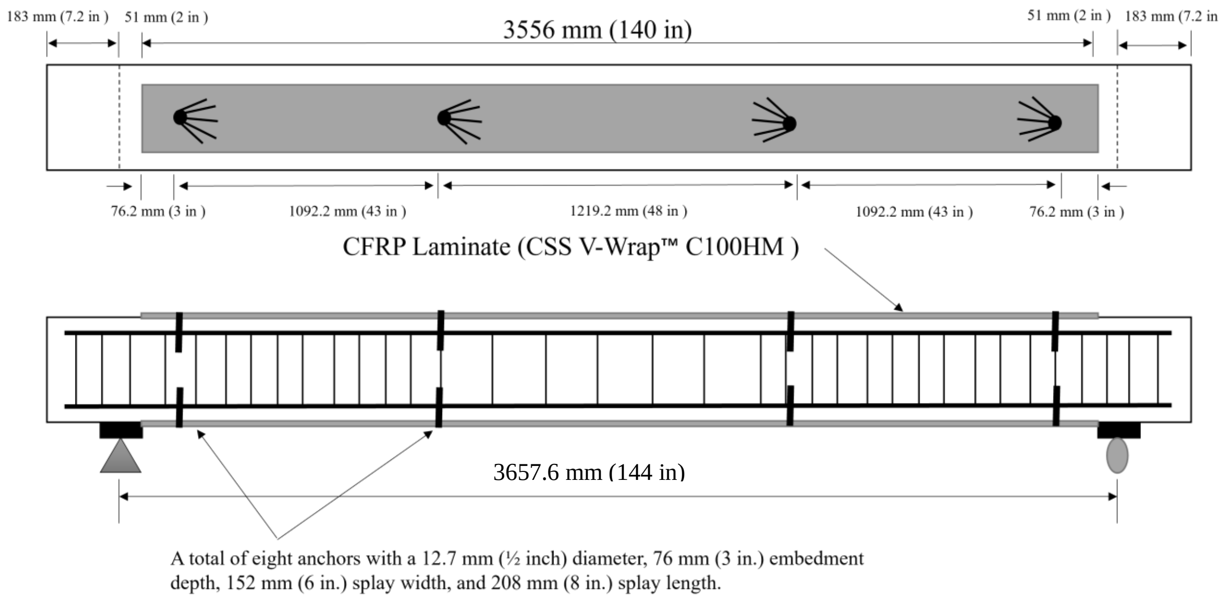

Figure 2.3. Beam No.3

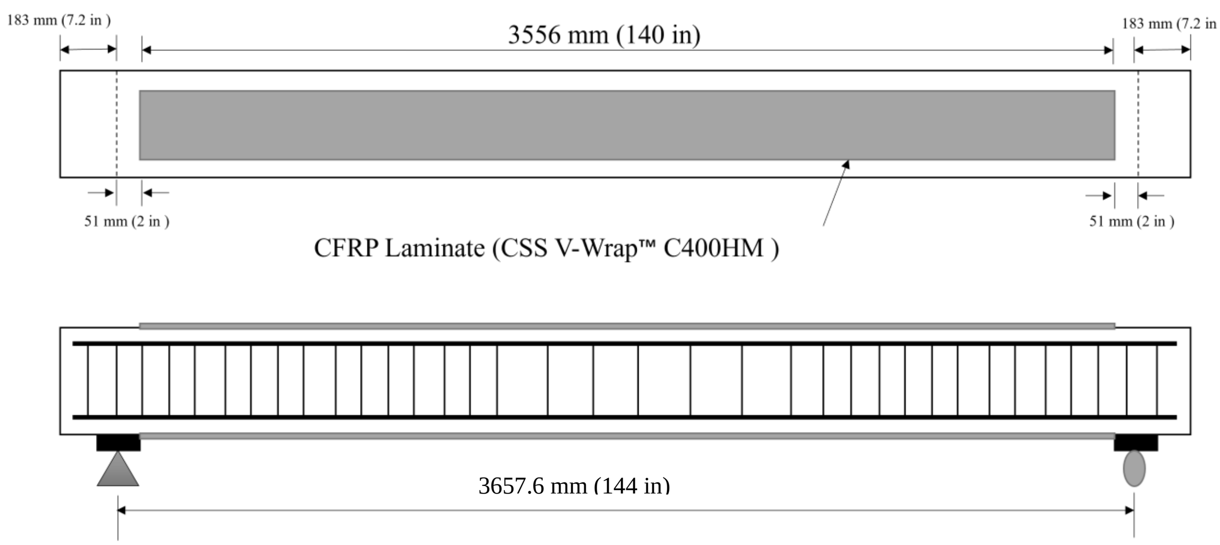

Figure 2.4. Beam N.4

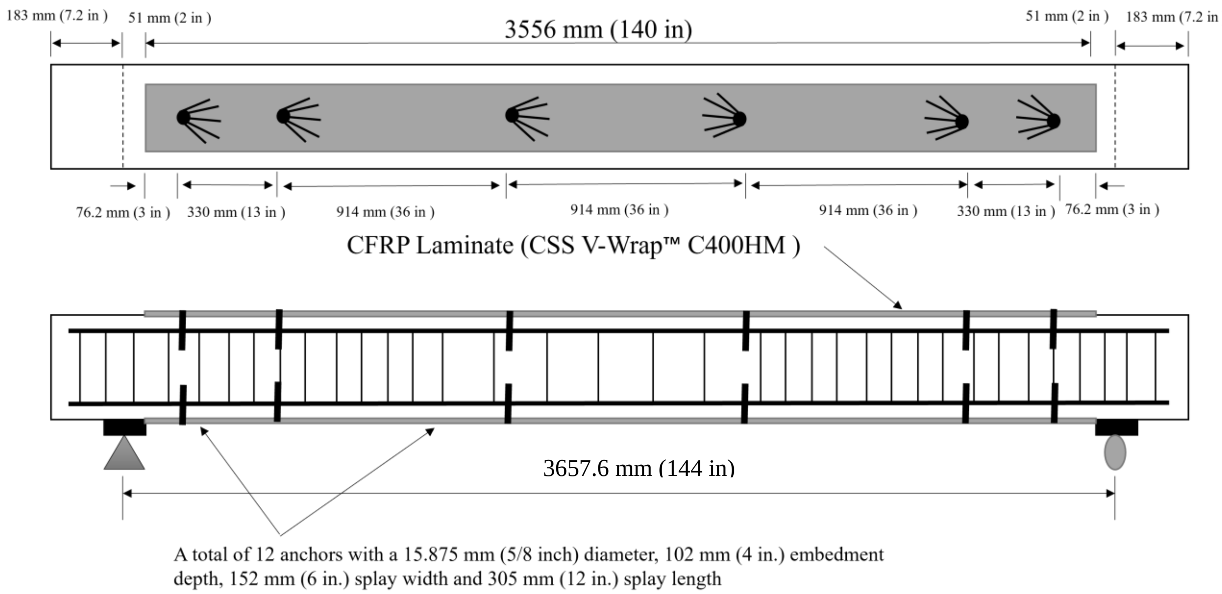

Figure 2.5. Beam No.5

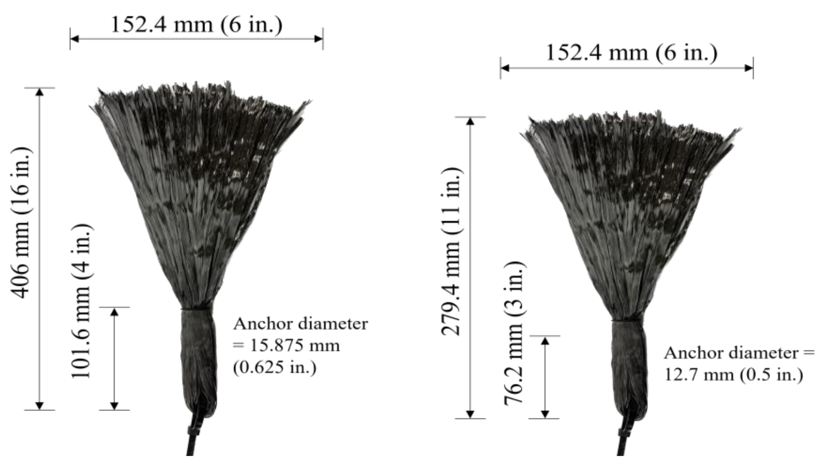

Figure 2.6. Carbon fiber splay anchors.

2.3.2. Materials Characteristics

2.3.2.1. Concrete

The concrete mix was designed to have a 28-day compressive strength of 17.24 MPa (2.5 ksi) with a slump of 75 mm (3 inches). Three concrete cylinders of 100 mm diameter x 200 mm height (4" diameter x 8" height) were tested to determine the 28-day compressive strength of the concrete mixture based on ASTM C39. One additional cylinder was tested on the day of testing beam No. 3 (216 days from the casting date), see Table 2.2. Based on the conducted cylinder tests, the concrete had an average 28-day compressive strength of 21.02 MPa (3.05 ksi). It is interesting to observe that this concrete gained around 4.75 MPa (0.69 ksi) extra strength by the day of testing compared to its standard 28-day strength.

Table 2.2.Concrete Compressive Strength Testing

Specimen	Testing type	Strength MPa (psi)	Average strength MPa (psi)
C1	Compressive at 28-day	21.23 (3,081.00)	21.02 (3,048.50)
C2		20.52 (2,978.00)	
C3		21.30 (3,092.00)	
C4	Compressive at day of testing	25.77 (3,740.00)	25.77 (3,740.00)

2.3.2.2. Steel Reinforcement

The acquired ϕ 13 (#4) steel bars were reported to have a yield strength of 572.95 MPa (83.1 ksi) based on the manufacturer mill certificates. To examine the mechanical properties of these bars in the lab, three rebars were tested in accordance with ASTM A615. The average yielding strength was obtained to be 536.01 MPa (77.74 ksi). The average modulus of elasticity was also measured using stress-strain curves to be 170,489 MPa (24,727.34 ksi), while the typical modulus of elasticity of steel is known to be 200,000 MPa (29,000 ksi). A possible reason for this discrepancy is the use of sacrificial grips, cut from steel sheets, between the re-bar and the hydraulic grips of the Universal Testing Machine where minor slippage might have taken place under a gripping pressure of 27.58 MPa (4000 psi). In addition, the steel bar surface was slightly grinded to allow for mounting the strain gauge on a flat smooth surface causing a very minor reduction in cross section. The mechanical properties of steel according to the experimental testing are shown in Table 2.3.

Table 2.3. Mechanical properties of the tested steel bars.

Specimens	Average Yielding Strength MPa (ksi)	Average Elastic Modulus MPa (ksi)
Rebar ϕ 10 (# 3)	485.54 (70.42)	173,181.67 (25,117.88)
Rebar ϕ 13 (# 4)	536.01 (77.74)	170,489.00 (24,727.34)

2.3.2.3. Carbon Fiber-Reinforced Polymer

Two types of commercially available high-modulus unidirectional carbon fiber fabric sheets were used to strengthen the RC beams. One of the fabrics has a 0.508 mm (0.02 in) thick saturated laminate layer made from 0.165 mm (0.0065 in.) dry fabric sheet (CSS V-Wrap™ C100HM) having 330 g/m^2 (9.73 oz/yd^2) weight. The other one has 2.03 mm (0.08 in) thick saturated laminate layer made from 0.66 mm (0.026in.) dry fabric sheet (CSS V-Wrap™ C400HM) having 1300 g/m2 (38.34 oz/yd2). Table 2.4 illustrates the manufactured data for both of the CFRP types.

Table 2.4. Mechanical Properties of CFRP per Manufacturer.

Type of Carbon fiber fabric	Properties Type	Nominal thickness t, mm (in)	Ultimate tensile strength $f_{fu'}$, MPa (ksi)	Elongation at break $\varepsilon_{fu'}$ %	Modulus of elasticity E, MPa (ksi)
CSS V-Wrap™ C100HM	Dry fiber properties	0.165 (0.0065)	5,440.00 (790.00)	1.90	289,550 (42,000)
	Cured laminate properties	0.508 (0.02)	1,490.00 (216.00)	1.30	115,142 (16,700)
CSS V-Wrap™ C400HM	Dry fiber properties	0.66 (0.026)	5,440.00 (790.00)	1.90	289,550 (42000)
	Cured laminate properties	2.03 (0.08)	1,241.00 (180.00)	1.27	98,181 (14,240)

2.3.3. Specimen Fabrication

Five full-scale beams were manufactured in the Structural Engineering laboratory at Kansas State University using wooden formwork. The specimens were fabricated carefully after placing all required strain gauges on the top and bottom steel rebars at mid-span.

2.3.4. Specimen Strengthening

After the curing of the concrete mixtures, the strengthened specimen surfaces were prepared using a grinder to ensure adequate bonding with CFRP. Two types of CFRP sheets with varying thickness were used, along with anchoring for two of those specimens, see Figure. 2.3 and Figure. 2.5. Figure. 2.7 (a-c) illustrates the surface preparation and CFRP installation phase.

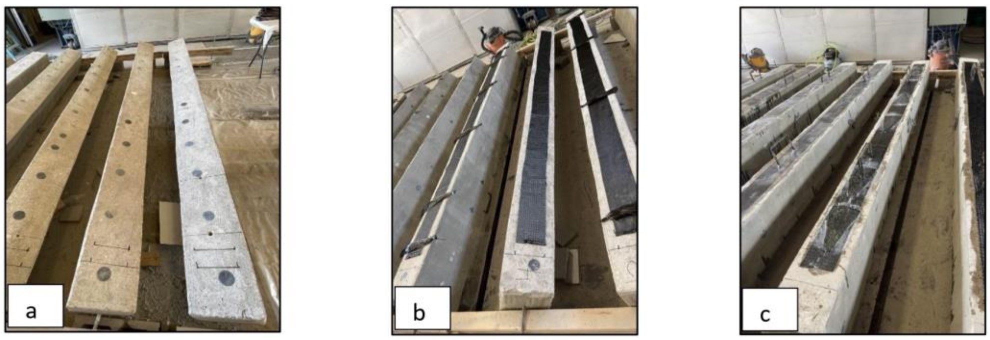

Figure 2.7. (a-c) RC Beams during Surface Preparing and CFRP Installation.

2.3.5. Loading Protocol and Measurement Instrumentation

To simulate the seismic load, a displacement-controlled cyclic four-point loading was employed using a 668 kN (150 kip) hydraulic actuator at Kansas State University's Structural Engineering Lab, see Figure. 2.1. The average rate of applied displacement was 17.78 mm/min (0.7 in/min). To capture the behavior of the tested beams, various instruments were used including, four LVDT's, two at mid-span and one at each support, at least eight strain gauges at mid-span, in addition to extra strain gauges in-between the load point and the nearest anchors to capture any possible debonding scenarios. An 890 kN (200-kips) load cell, to measure the applied load, is also used. According to AC 125 (ICC ES AC125 2021), the displacement-controlled loading protocol followed the variation shown in Figure. 2.8. The entire measured data was collected and stored in a Vishay System 7000 data acquisition equipment having 16-strain gauge channels, 4-LVDT channels, one-load cell channel and one channel for actuator displacement.

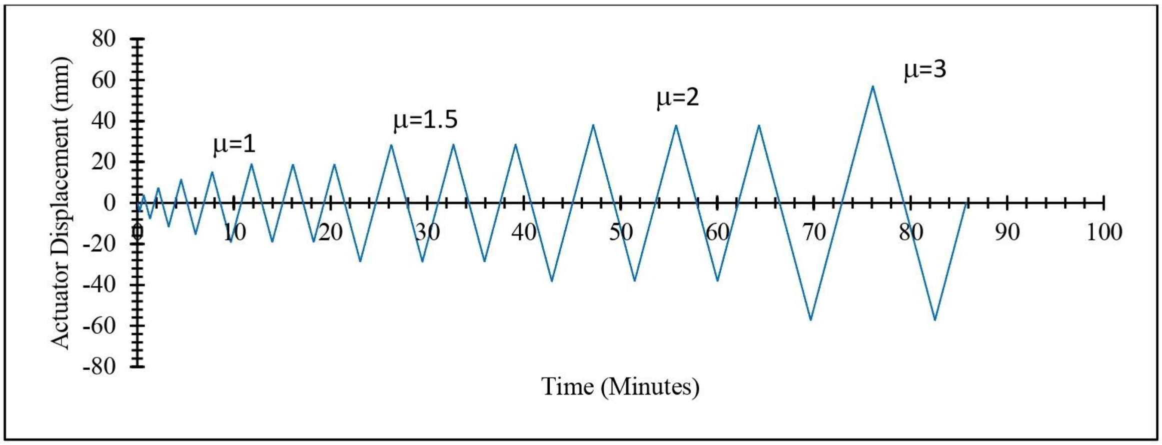

Figure 2.8. Loading Protocol for Beam No.2.

2.3.6. Test Setup

A comprehensive testing setup was applied in this study to examine the flexural behavior of all five beam specimens under reversed cyclic loading. A simply supported setup with a clear span between supports of 3657.6 mm (144inches)[1], and the load applied at the one-third points along the member using a steel spreader beam, see Figure 1. To securely hold the specimens in place during the pull loading, steel C channels with threaded rods on both sides were utilized as shown in Figure. 2.9. Each threaded rod was pre-tensioned to 66.72 kN (15-kips) using a torque wrench allowing for sufficient clamping force during the pull loading direction. It is important to note that under an ultimate pull load of 266.88 kN (60-kips), each threaded rod will pick up an additional 66.72 kN (15-kip) force resulting in a 133.44 kN (30-kip) maximum force. The load required to yield a 1-in threaded rod at 413.69 MPa (60 ksi) yield strength is 209.06 kN (47-kips) leaving a 1.57 factor of safety for the rods used.

[1] The clear span of the RC beams was slightly over 144 in. since the center-to-center distance between the strong floor tie-down was 144.75 in.

Figure 2.9. Standard testing set-up of beam No.2

2.4. Results and Discussions

The results, observations and findings of the experimental tests will be discussed individually for each beam in this section. Additionally, the performance of all five specimens will be compared against each other.

2.4.1. Beam No.1

Based on the obtained results, the control specimen exhibited a ductile behavior. Moreover, the beam was able to survive up to more than 82.55 mm (3.25 in.) of displacement with negligible reduction of strength. During the experiment, the cracking load was 34.75 kN (7.81 kips) in the push direction with a corresponding cycle size of 7.62 mm (0.30 in.) while it was 43.14 kN (9.70 kips) in the pull mode within the same cycle size. The first cracking was followed by several flexural cracks developed within the constant moment region. The yielding occurred around a load of 62.27 kN (13.74 kips) in push with a corresponding cycle of 19.05 mm (0.75 in.) while it was 74.59 kN (16.77 kips) in the pull mode within the same corresponding cycle size. This was accompanied by more flexural crack propagation at the constant moment region along with shear cracking at both points where the loading was applied on the shear span side. The ultimate load at which the failure took place due to excessive yielding was around 89.01 kN (20.01 kips) in push mode with a corresponding cycle size equal to 82.55 mm (3.25 inches). It also took place at around 125.80 kN (28.29 kips) in the pull mode during a similar corresponding displacement cycle level. It is important to observe that the different loads in the pull direction are noticeably higher than the same loads in the push direction for this beam. Part of the reason is the fact that gravity acts in the push direction resulting in higher reported load values for the pull direction in this case. Another reason is the pin-pin boundary conditions used for Beam No.1 that did add extra constraint in the pull direction due to the tightened clamping of the threaded rods. Figure. 2.10. illustrates the hysteretic response of the control specimen. Figure. 2.11. presents the beam setup prior to and after testing.

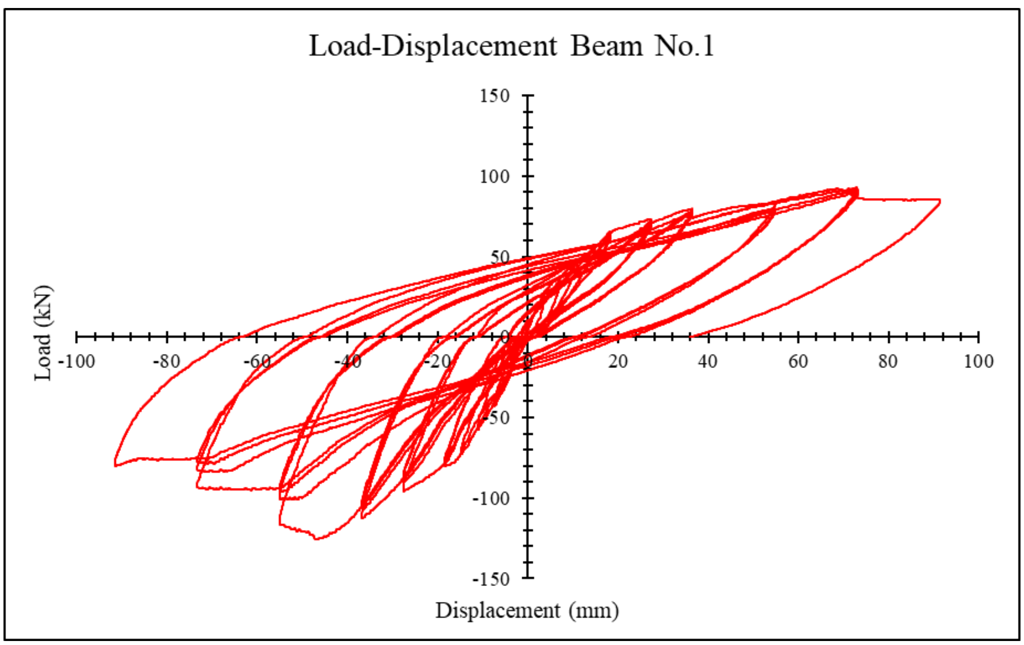

Figure 2.10. Load-displacement response of beam No.10 (1 Kips=4.45 KN)

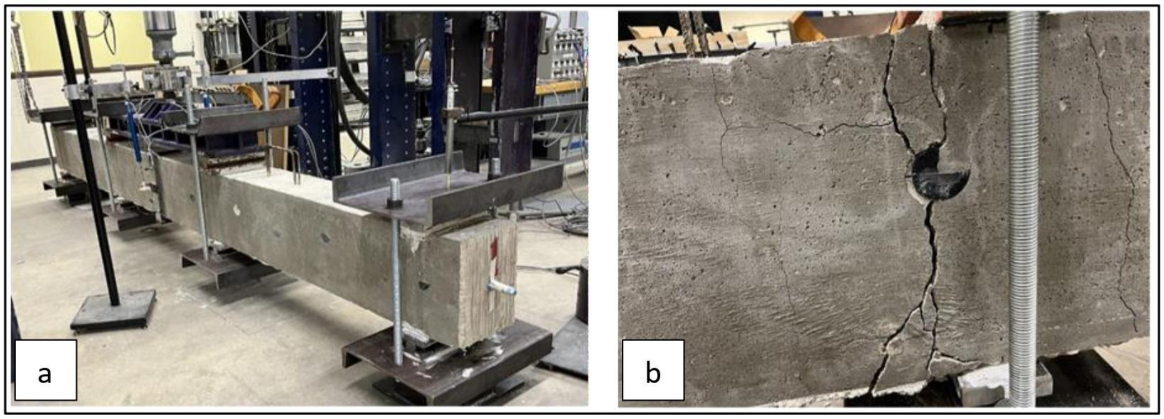

Figure 2.11. Specimen No.1. (a) before testing. (b) at failure

2.4.2. Beam No.2

For the second specimen, some ductility was observed despite the use of CFRP to strengthen the beam since the external sheets applied were of the thin type. Moreover, the beam was able to survive up to more than 34.30 mm (1.35 in.) of displacement with a sudden drop in strength within that cycle due to CFRP fiber rupture, see Figure. 2.12. A cracking load was determined to be 34.33 kN (7.71 kips) on the push side with a corresponding cycle size of 7.62 mm (0.30 in.) while it was 37.68 kN (7.79 kips) on the pull side within a similar cycle size. Subsequently, typical flexural cracks were developed within the constant moment region. Although less than those observed in the control specimen due to the influence of the externally bonded CFRP sheets in restraining and redistributing these cracks. Yielding occurred around a push load of 80.40 kN (18.08 kips) and a corresponding cycle size of 19.07 mm (0.75 in.). On the other hand, yielding happened at a pull load of 81.43 kN (18.30 kips) having the same corresponding cycle size followed by shear-crack propagation at both load points inside the shear span. Evidently, the failure took place due to rupture of the CFRP sheet at both surfaces of the beam, top and bottom, at the loading points but inside the shear span at a push load of approximately 104.80 kN (23.56 kips) and a pull load of 124 kN (28.07 kips) with a corresponding cycle equal to 57.2 mm (2.25 inches). The failure was primarily caused by large diagonal shear cracks adjacent to the load application location in the shear span. Figure. 2.12. illustrates the response of the beam No.2 specimen. Figure. 2.13. presents the beam setup prior to and after testing.

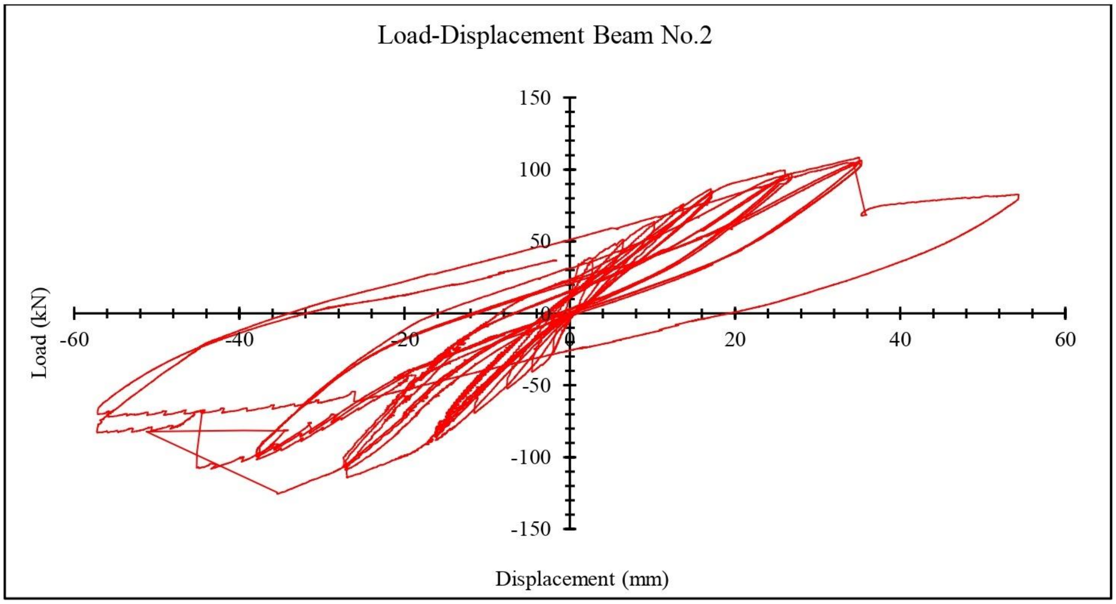

Figure 2.12. Load-displacement response of beam No.2 (1 Kips=4.45 KN)

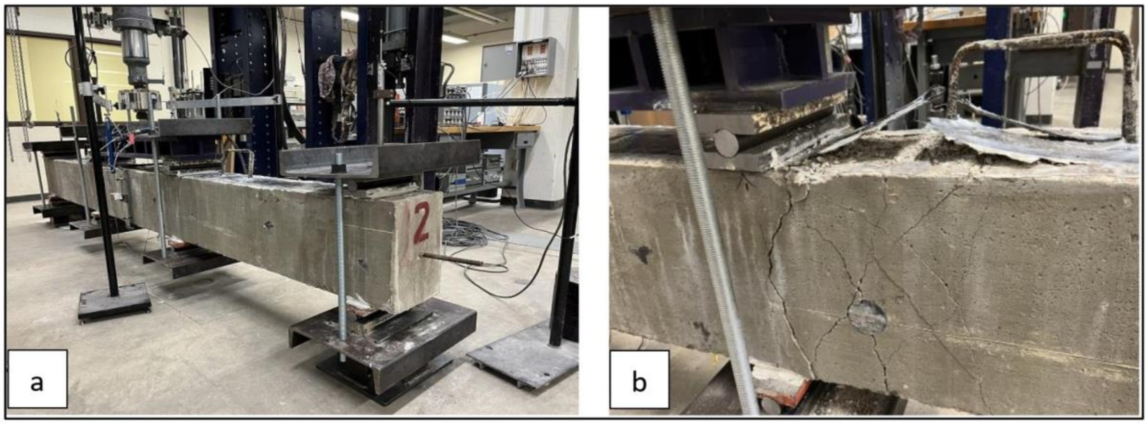

Figure 2.13. Specimen No.2. (a) before testing. (b) at failure

2.4.3. Beam No.3

The third specimen showed a hysteretic response similar to the second specimen until it reached the yield point. After yielding, the behavior of the third specimen differed, as it exhibited a higher ultimate load. The experimental data clearly indicate that specimen No.3 showed ductility until failure, followed by a sudden reduction of the strength that occurred due to the external sheet debonding on the top and CFRP rupture on the bottom sides of the beam at the boundary of the shear span. On the push side, a cracking load of approximately 34.33 kN (7.71 kips) was observed, while on the pull side, a cracking load of approximately 28.23 kN (6.35 kips) was noticed. Both sides exhibited a corresponding cycle size of 7.62 mm (0.30 in.). Yielding occurred at a push load of 83.64 kN (18.81 kips) and a pull load of 75.82 kN (17.05 kips), both corresponding to a cycle size of 19.05 mm (0.75 in.) followed by the propagation of shear cracks at both points where the loading was applied. The failure of the third specimen was caused by the CFRP rupture of the external sheet on the bottom side of the beam (push loading) at the boundary of the shear span. On the other hand, failure of this beam was caused by CFRP debonding of the external sheet on the top side of the beam (pull loading) at the boundary of the shear span as well. Failure occurred at a push load of approximately 119.5 kN (26.81 kips) and a pull load of approximately 109.42 kN (24.6 kips), with a corresponding cycle displacement equal to 57.15 mm (2.25 in.) same for the push and pull loading. The failure was attributed to large diagonal shear cracks at the edge of the shear span, which developed at the location of load application. When investigating the reason for the higher cracking, yielding and ultimate loading for the push direction, the authors realized that the effective depth (d) of the push side was noticeably higher 292 mm (11.5 in.) than the (d) of the pull side which was lower 279 mm (11 in.). Figure. 2.14. illustrates the hysteretic response of beam No.3. Additionally, Figure. 2.15. presents the beam setup prior to and after testing. It is also worth mentioning that the end anchor prevented the thin CFRP sheet from fully separating from the beam in the pull direction.

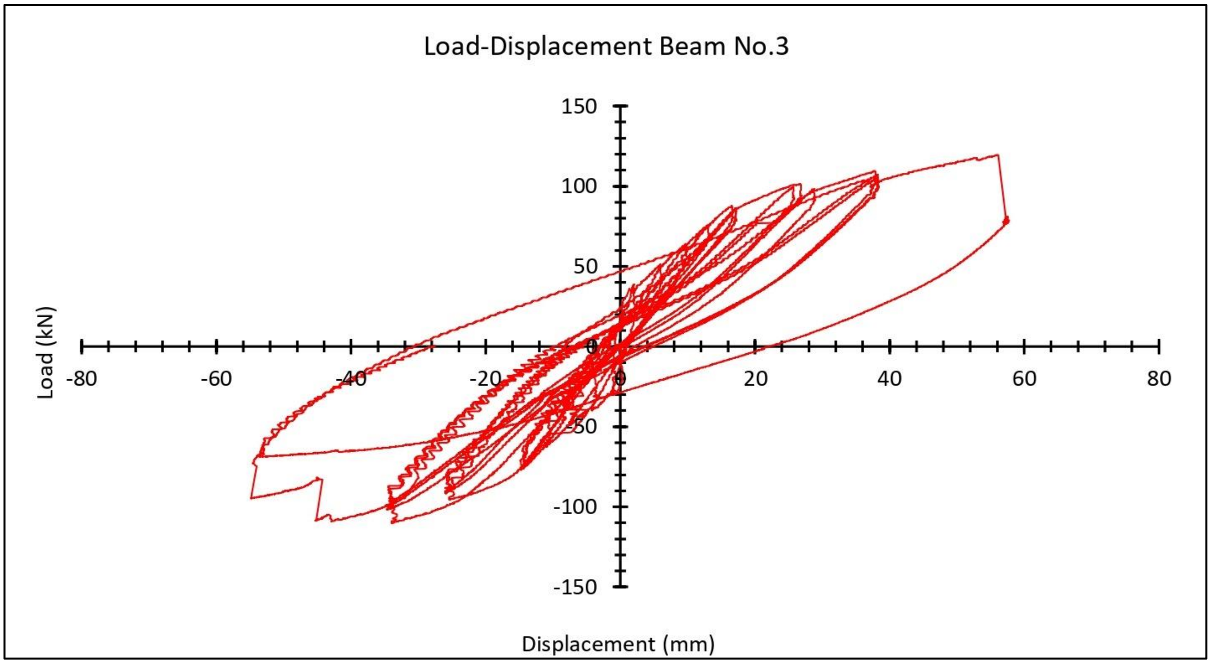

Figure 2.14. Load-displacement response of beam No.3 (1 Kips=4.45 KN)

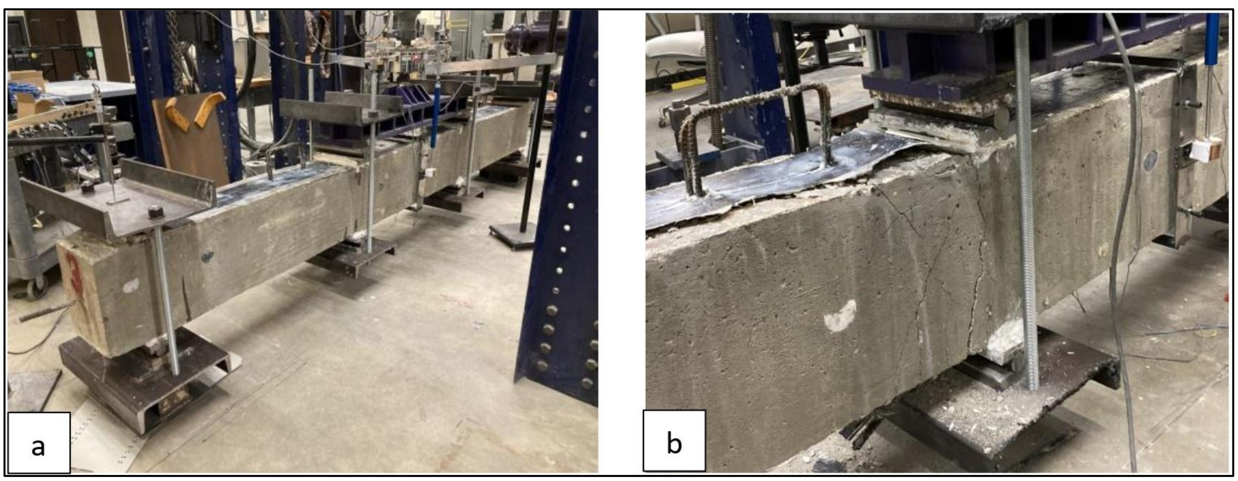

Figure 2.15. Specimen No.3. (a) before testing. (b) at failure

2.4.4. Beam No.4

Specimens No.4 exhibited reduced ductility compared to specimens No.1 to No.3, as it failed by CFRP debonding within the displacement cycle of 40.64 mm (1.60 in.) before experiencing a sudden reduction in strength. Despite the limited ductility, the ultimate capacity of specimen No.4 demonstrated a significant increase. According to the experimental data, the cracking load on the push side was measured at 35.30 kN (7.93 kips), while on the pull side, it was measured at 32.97

kN (7.41 kips). Both of these cracking loads were observed within a corresponding cycle size of 3.81 mm (0.15 in.). Subsequently, normal flexural cracks developed within the fixed moment region. Yielding was observed at a push load of 115.91 kN (26.06 kips) and a pull load of 112.73 kN (25.34 kips), both occurred at a corresponding cycle size of 20.32 mm (0.80 in.). Yielding was followed by the formation of more flexural cracks within the constant moment region and shear cracks within the shear span. The failure occurred as a result of the debonding of the external CFRP sheets on both the top and bottom sides of the beam, specifically at the edge of the shear span. This debonding occurred at a load of approximately 146.34 kN (32.9 kips) on the push side and at a load of around 154.05 kN (34.63 kips) on the pull side, both corresponding to a cycle size of 40.64 mm (1.60 in.). The failure of the beam was primarily attributed to the development of large diagonal shear cracks at the load application location. Figure. 2.16. illustrates the response of beam No.4 reflecting higher hysteresis pinching due to the use of thicker CFRP. Figure. 2.17. presents the beam setup prior to and after testing.

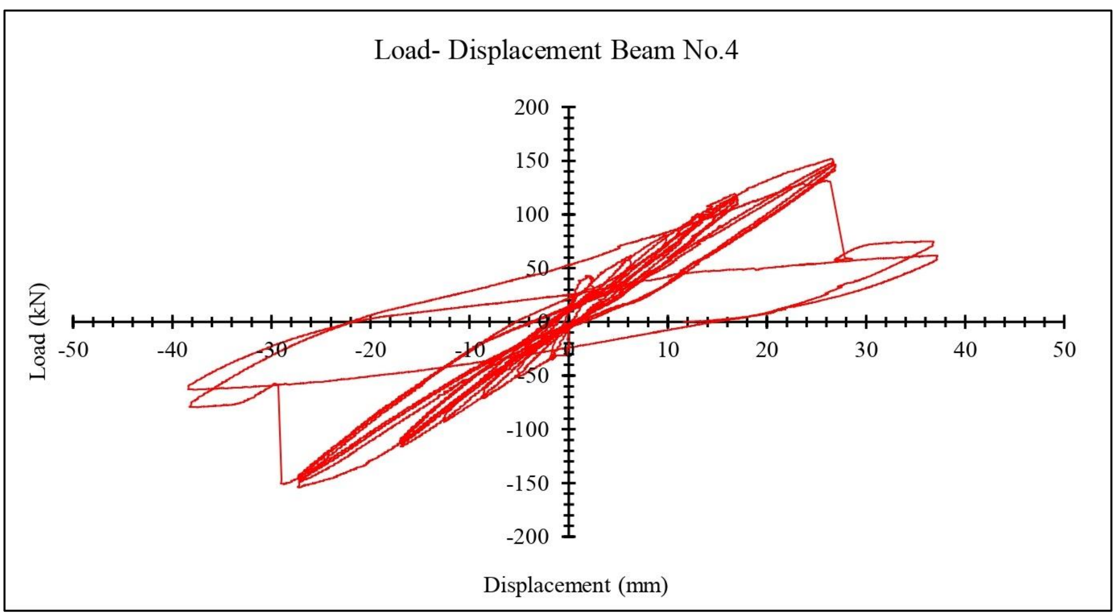

Figure 2.16. Load-displacement response of beam No.4 (1 Kips=4.45 KN)

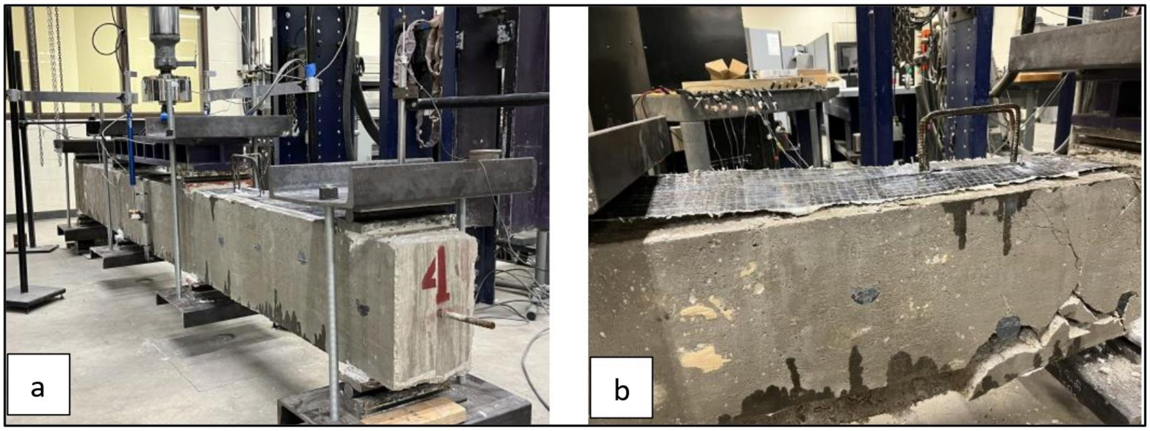

Figure 2.17. Specimen No.4. (a) before testing. (b) at failure

2.4.5. Beam No.5

Beam No.5 showed almost identical results to those obtained from specimen No.4 with slightly higher ultimate capacity at about the same ductility while the energy dissipation seemed a bit more than that of beam No.4, Figure. 2.16. and Figure. 2.18. Similar to specimen No.4, the beam failed within the displacement cycle of 40.64 mm (1.60 in.) before experiencing a sudden reduction in strength due to concrete cover delamination. However, it exhibited the highest ultimate capacity among all five specimens. It is very interesting to observe that the anchors in beam No.5 functioned perfectly forcing the concrete separation to take a path around and below the anchors introducing complete cover delamination failure mode, Figure. 2.19b. Therefore, it is recommended to consider the effect of deeper anchors as a potential reason for improving the response of this beam during future testing. Experimentally, the cracking load on both the push and pull sides of the specimen was measured at 35.35 kN (7.95 kips) and 31.39 kN (7.05 kips) respectively, both occurring at a corresponding cycle of 3.81 mm (0.15 in.). After that, typical flexural cracks developed within the constant moment region between the applied load points. At a cycle size of 28.58 mm (1.125 in.), yielding was reached on both the push and pull sides at a load of 130.35 kN (29.31 kips) and 131.48 kN (29.56 kips) respectively followed by the propagation of shear cracks at both points where the loading was applied, similar to those observed in specimen No.4. The failure took place due to concrete cover separation at both faces of the beam, top and bottom, at the edge of the shear span at a load of approximately 154.8 kN (34.8 kips) on the push side and 160.35 kN (36.05 kips) on the pull side, within a corresponding cycle of 40.64 mm (1.60 in.). Figure. 2. 18. illustrates the hysteretic response of beam No.5 while Figure. 2.19. presents the beam setup prior to and after testing.

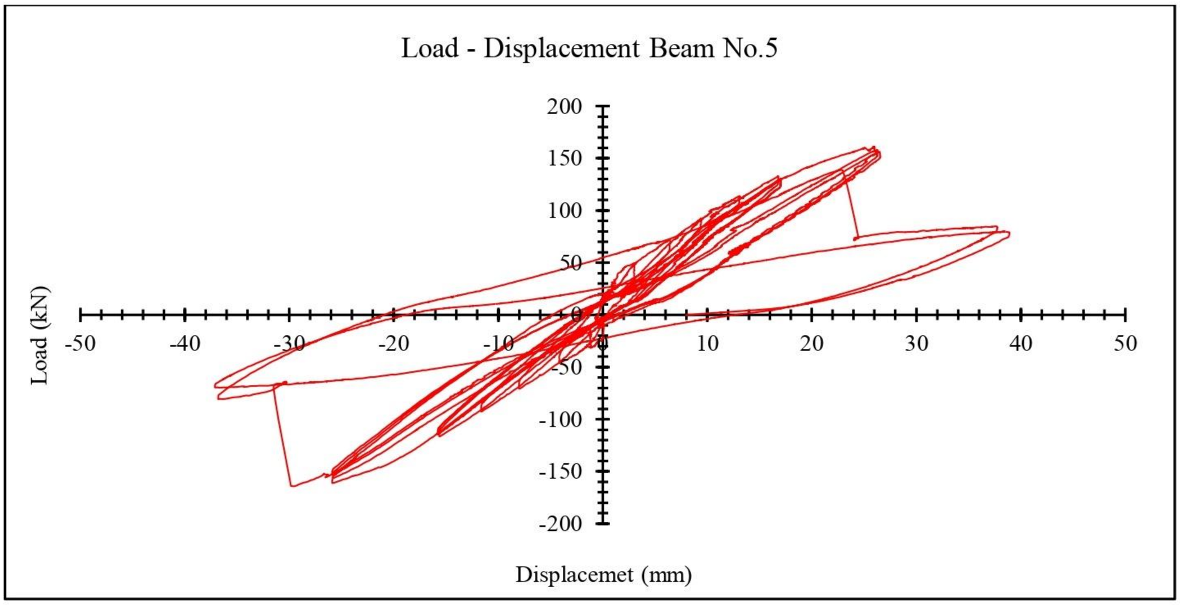

Figure 2.18. Load-displacement response of beam No.5 (1 Kips=4.45 KN)

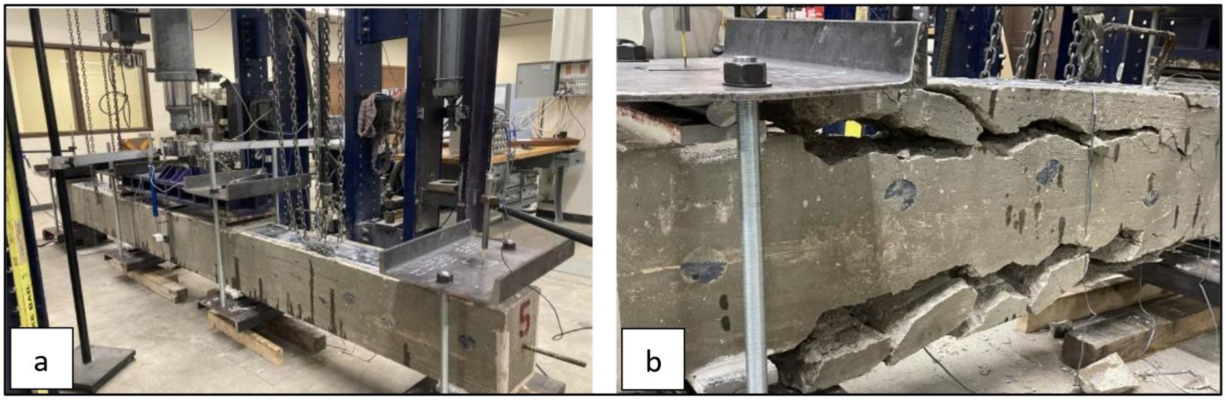

Figure 2.19. Specimen No.5. (a) before testing. (b) at failure

2.5. Comparison of Specimen Responses

2.5.1. Strength and Ductility

The results of the control specimen showed a ductile behavior with significant energy dissipation due to extensive steel yielding, which is expected of un-strengthened RC beams. Specimens No.2 and No.3 still exhibited some noticeable ductility. However, the ultimate capacity on the push side was enhanced when compared to the control one by 17.74% and 33.3%, respectively. The comparison between specimens No.2 and No.3 indicated that both have almost the same cracking and yielding load while the ultimate capacity of the third beam was, on average, 14% higher as results of applying the anchors which delayed the failure as well as shifted the failure mode from top and bottom rupture to a mixed debonding-rupture mode, see Figure. 2.17b. and Figure. 2.18b. As for specimens No.4 and No.5, the ultimate failure load was increased by 64.41% and 73.91% respectively in comparison to the control specimen. Both specimens exhibited very similar responses such that cracking and yielding load were almost the same, with a slight difference in the ultimate failure load as shown in Figure. 2.20. However, the failure mode was changed from debonding of the CFRP sheets to concrete cover delamination due to the carbon fiber splay anchors and the ultimate load for beam No. 5 was 14.75 % higher than beam No. 4 on average. It is evident from Figure. 2.20. that the strength increases, and ductility decreases from the control beam to the beams strengthened with thin CFRP to those strengthened with thick CFRP. The use of fiber anchors in these experiments was mainly concentrated at the sheet ends causing minimal strength benefits. Had there been anchors installed across the whole shear span, the strength and ductility improvement would have been anticipated to be more (Zaki et al. 2020). Also, it is worth mentioning that using deeper fiber anchors would have potentially helped with strength and ductility, as it would have delayed or prevented the cover delamination failure mode observed in beam No.5. Figure. 2.21. shows energy dissipation of all specimens together.

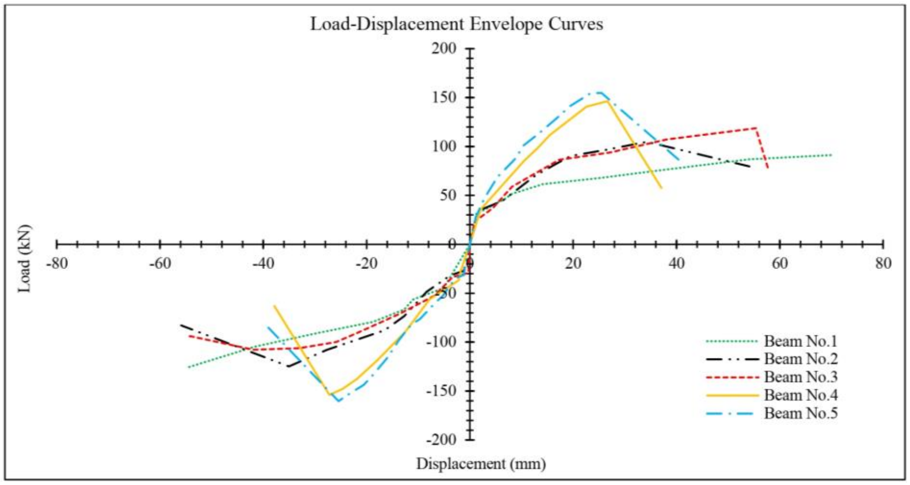

Figure 2.20. Envelope Carves Comparison of all Beams.

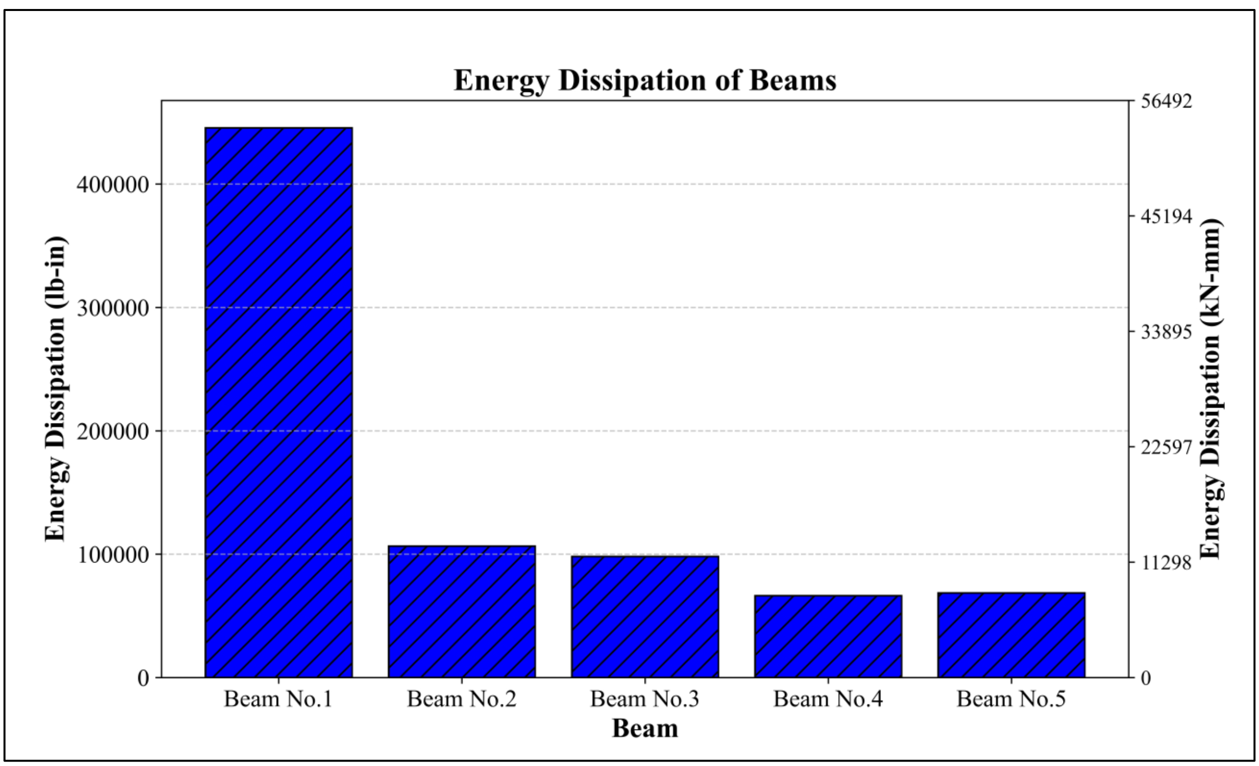

Figure 2.21. Energy dissipation of all beams[2]

[2] Energy dissipation for CFRP strengthened beams is measured up to the failure of the strengthening system and not beyond that.

2.5.2. Stiffness Degradation

Specimens showed various stiffness degradation trends due to the influence of CFRP sheet thickness as well as the use of carbon fiber splay anchors. Based on the collected data, it is evidence that specimen No.1 (control beam) exhibited the highest stiffness reduction after cracking as shown in Figure. 2.20. Specimens No.2 and 3 showed lower stiffness reduction compared to the control beam, but slightly higher reduction compared to beams No.4 and 5. On the other hand, post-peak stiffness drop was highest for thicker CFRP (beams No. 4 and 5) compared to the corresponding stiffness drop for thinner CFRP (beams No.2 and 3), while the control beam did not experience any stiffness drop due to the lack of CFRP strengthening.

2.5.3. Experimental Envelope Curve

The envelope curve was extracted from the hysteresis loops of each specimen for the purpose of comparing it to the analytical envelope curve. Table 2.5 depicts the key points of the envelope curve on the push side at cracking, yielding and ultimate levels for all five beams. It is evident from Table 2.5 that the ultimate strength increases steadily by increasing the beam number (i.e., by using thicker CFRP sheets and applying fiber anchors). Ductility is also seen to reduce as the CFRP sheet thickness increases while it increases when applying anchors to the thin sheet type at ultimate push side. For the thick sheet type, the ductility was almost the same with and without anchors. Table 2.6, on the other hand, is identical to Table 2.5 but it is depicted for the pull side. It can be noted that beams No. 4 and 5 show increase in ultimate load compared to the control while beams No.2 and 3 shows reduction in ultimate capacity, which is attributed to the use of a pin-pin boundary condition for the control beam and beam No.2 while adjusting the boundary condition to a pin-roller for beams No. 3-5, as mentioned earlier. Similar trend can be observed for the ductility on the pull side as that captured for the push side. The only exception is beam

No.3 which failed by rupture on the push side and by debonding on the pull side due to some uneven surface on the latter. Furthermore, Table 2.7 and 2.8 shows the same key loading for the push and pull side, respectively, while reporting the cycle size at which these key loadings took place. Figure. 2.22. and Figure. 2.23. show the peak ultimate load and the peak displacement at failure for all beams, respectively.

Table 2.5. Forward loading against displacement (Push Side).

Specimen	Experimental results						
	Cracking load kN (Kips)	Cracking Displacement mm (in)	Yielding load kN (Kips)	Yielding Displacement mm (in)	Ultimate load kN (Kips)	Ultimate Displacement mm (in)	Percent increase in ultimate load %
Beam No.1	34.75 (7.81)	7.81 (0.15)	62.27 (13.74)	13.74 (0.54)	89.01 (20.01)	69.85 (2.75)	-
Beam No.2	34.33 (7.71)	2.37 (0.09)	80.40 (18.08)	15.24 (0.60)	104.8 (23.56)	34.29 (1.35)	17.74
Beam No.3	34.33 (7.71)	1.59 (0.062)	83.64 (18.81)	15.17 (0.60)	119.50 (26.81)	55.37 (2.18)	33.3
Beam No.4	35.30 (7.93)	1.065 (0.042)	115.91 (26.06)	15.86 (0.62)	146.34 (32.9)	26.67 (1.05)	64.41
Beam No.5	35.35 (7.95)	1.35 (0.05)	130.35 (29.31)	17.07 (0.67)	154.8 (34.8)	25.40 (1.00)	73.91

Table 2.6. Reversed loading against displacement (Pull Side).

Specimen	Experimental results						
	Cracking load kN (Kips)	Cracking Displacement mm (in)	Yielding load kN (Kips)	Yielding Displacement mm (in)	Ultimate load kN (Kips)	Ultimate Displacement mm (in)	Percent increase in ultimate load %
Beam No.1	43.14 (9.70)	6.67 (.26)	74.59 (16.77)	15.31 (0.60)	125.8 (28.29)	54.61 (2.15)	-
Beam No.2	37.68 (7.79)	3.12 (0.13)	81.43 (18.30)	14.71 (0.58)	124 (28.07)	35.05 (1.38)	-1.43
Beam No.3	28.23 (6.35)	1.09 (0.04)	75.82 (17.05)	14.30 (0.56)	109.42 (24.6)	41.91 (1.65)	-14.324
Beam No.4	32.97 (7.41)	1.35 (0.053)	112.73 (25.34)	16.33 (0.64)	154.05 (34.63)	27.18 (1.07)	22.5
Beam No.5	31.39 (7.05)	1.10 (0.044)	131.48 (29.56)	18.43 (0.73)	160.35 (36.05)	25.40 (1.00)	27.46

Table 2.7. Forward loading against cycle size (Push Side).

Specimen	Experimental results						
	Cracking load kN (Kips)	Cracking Cycle Displacement mm (in)	Yielding load kN (Kips)	Yielding Cycle Displacement mm (in)	Ultimate load kN (Kips)	Ultimate Cycle Displacement mm (in)	Percent increase in ultimate load %
Beam No.1	34.75 (7.81)	7.62 (0.30)	62.27 (13.74)	19.05 (0.75)	89.01 (20.01)	82.55 (3.25)	-
Beam No.2	34.33 (7.71)	7.62 (0.30)	80.40 (18.08)	19.05 (0.75)	104.8 (23.56)	57.15 (2.25)	17.74
Beam No.3	34.33 (7.71)	3.81 (0.15)	83.64 (18.81)	19.05 (0.75)	119.50 (26.81)	57.15 (2.25)	33.3
Beam No.4	35.30 (7.93)	3.81 (0.15)	115.91 (26.06)	20.32 (0.80)	146.34 (32.9)	40.64 (1.6)	64.41
Beam No.5	35.35 (7.95)	3.81 (0.15)	130.35 (29.31)	28.575 (1.125)	154.8 (34.8)	40.64 (1.6)	73.91

Table 2.8. Reversed loading against cycle size (Pull Side).

Specimen	Experimental results						
	Cracking load kN (Kips)	Cracking Cycle Displacement mm (in)	Yielding load kN (Kips)	Yielding Cycle Displacement mm (in)	Ultimate load kN (Kips)	Ultimate Cycle Displacement mm (in)	Percent increase in ultimate load %
Beam No.1	43.14 (9.70)	7.62 (0.30)	74.59 (16.77)	19.05 (0.75)	125.8 (28.29)	82.55 (3.25)	-
Beam No.2	37.68 (7.79)	7.62 (0.30)	81.43 (18.30)	19.05 (0.75)	124 (28.07)	57.15 (2.25)	-1.43
Beam No.3	28.23 (6.35)	3.81 (0.15)	75.82 (17.05)	19.05 (0.75)	109.42 (24.6)	57.15 (2.25)	-14.324
Beam No.4	32.97 (7.41)	3.81 (0.15)	112.73 (25.34)	20.32 (0.80)	154.05 (34.63)	40.64 (1.6)	22.5
Beam No.5	31.39 (7.05)	3.81 (0.15)	131.48 (29.56)	28.575 (1.125)	160.35 (36.05)	40.64 (1.6)	27.46

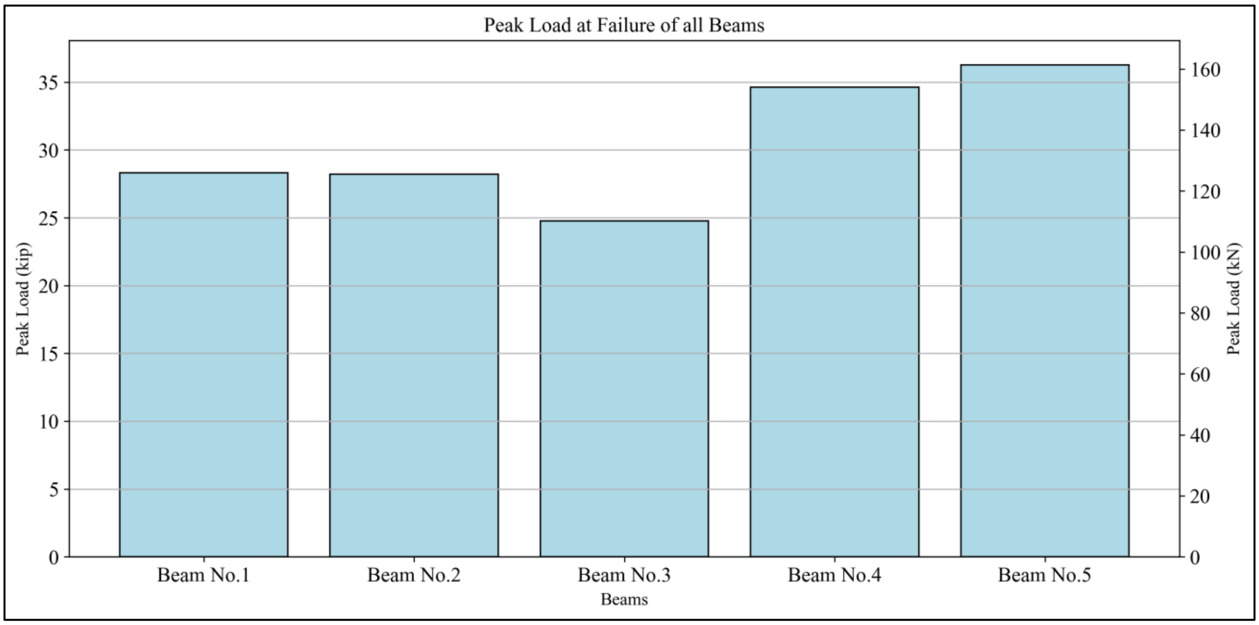

Figure 2.22. Peak ultimate load at failure for all beams

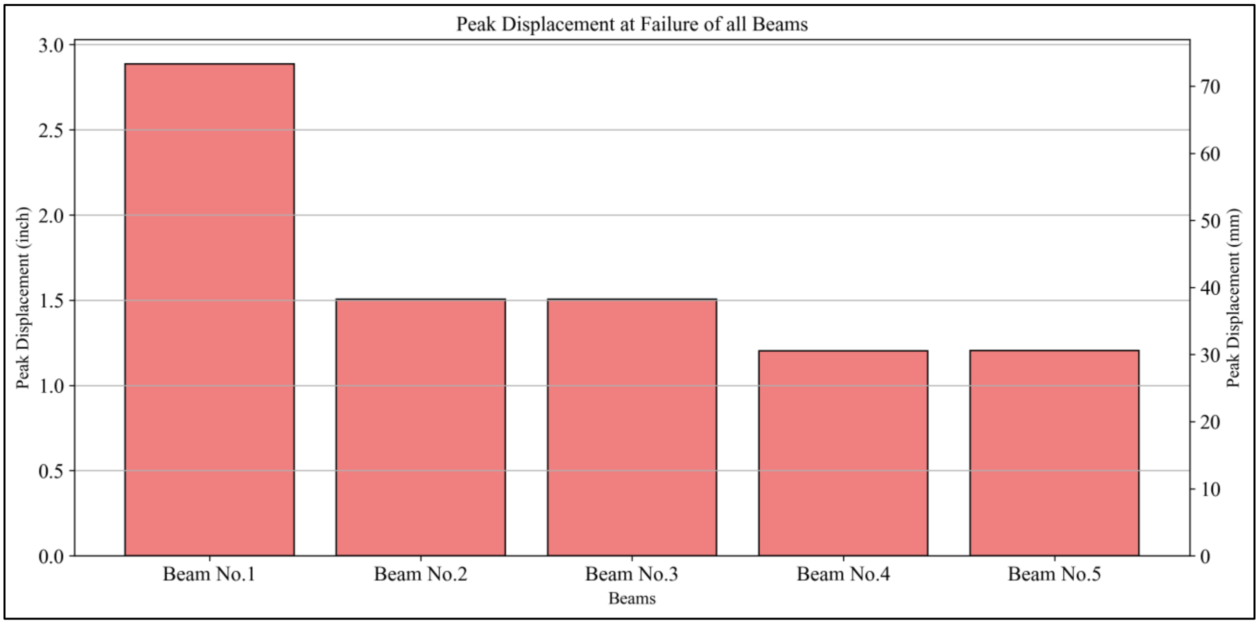

Figure 2.23. Peak displacement at failure for all beams

2.6. Analysis of the Envelope Curves

To predict the envelope curve response of the tested specimens, a trilinear load-displacement model that was developed by Charkas et al. (2003) for monotonic loading was utilized. According to this model, the Moment-Curvature analysis was approximated by a trilinear curve. In fact, this curve is controlled by three key points as follows:

2.6.1. Cracking Point:

The first point of the trilinear curve can be easily computed using the following equations:

$$M_{cr} = \frac{f_r \, I_{gt}}{y_t} \qquad (1)$$

$$\emptyset_{cr} = \frac{f_r}{E_c \, y_t} \qquad (2)$$

Where:

$f_r = 7.5\sqrt{f'_c}$ in psi or $f_r = 0.62\sqrt{f'_c}$ in MPa .

Ec is modulus of elasticity of concrete.

I_{gt} is gross transformed section moment of inertia.

y_t is the centroid depth of the section to the extreme tension fiber.

2.6.2. Yielding Point:

To predict the yielding point of the trilinear curve, the following equations are used:

$$\left[\frac{\frac{\varepsilon_y * c_y}{d-c_y}}{\varepsilon_{\prime c}} - \frac{\left(\frac{\varepsilon_y * c_y}{d-c_y}\right)^2}{3\varepsilon_{\prime c}^2}\right] f'_c\, B\, c_y + A'_s\, E_s\, \frac{\varepsilon_y}{d-c_y}\left(c_y - d'\right) - A_s f_y + A_f E_f \frac{\varepsilon_y}{d-c_y}\left(d_f - c_y\right) = 0 \tag{3}$$

$$M_y = A_s f_y \left(d - \left(0.5\, \hat{\beta}_1\, c_y\right)\right) + A_f E_f \varepsilon_{fe} \left(d_f - \left(0.5\, \hat{\beta}_1\, c_y\right)\right) + A'_s\, E_s\, \varepsilon'_s \left(0.5\, \hat{\beta}_1\, c_y - d'\right) \tag{4}$$

$$\phi_y = \frac{\varepsilon_y}{d - c_y} \tag{5}$$

Where:

$$\varepsilon'_s = \frac{\varepsilon_y}{(d-c_y)(c_y-d\,)} \tag{6}$$

$$\varepsilon_{fe} = \frac{\varepsilon_y}{d-c_y} * \left(d_f - c_y\right) \tag{7}$$

$$\varepsilon_{cf} = \frac{\varepsilon_y * c_y}{d-c_y} \tag{8}$$

$$\alpha = \frac{\varepsilon_{cf}}{\varepsilon_{\prime c}} - \frac{\varepsilon_{cf}^2}{3\varepsilon'^2_{cf}} \tag{9}$$

$$\hat{\beta} = \frac{\frac{1}{3} - \frac{\varepsilon_{cf}}{12 * \varepsilon_{\prime c}}}{1 - \left(\frac{\varepsilon_{cf}}{3 * \varepsilon_{\prime c}}\right)} \tag{10}$$

$$\hat{\beta}_1 = 2 * \hat{\beta} \tag{11}$$

2.6.3. Ultimate Point:

This model was modified to capture the three different failure modes of strengthened RC beams, including crushing, debonding, and rupture failure as demonstrated below. Similar force equilibrium equations, to that presented above for the yielding point, are used to solve for the neutral axis location at the ultimate point based on the various failure modes considered.

2.6.3.1. Crushing failure:

$$M_{nc} = A_s f_y(d - (0.5 * \hat{\beta}_1\, c_{nc})) + A_f E_f \varepsilon_{fe}(df - (0.5 * \hat{\beta}_1\, c_{nc}))) + A'_s E_s \varepsilon'_s((0.5 * \hat{\beta}_1\, c_{nc}) - d')) \qquad (12)$$

$$\phi_{nc} = \frac{\varepsilon_{cu}}{c_{nc}} \qquad (13)$$

2.6.3.2. Debonding failure:

$$M_{nd} = A_s f_y(d - (0.5 * \hat{\beta}_1\, c_{nd})) + A_f E_f \varepsilon_{fu}(df - (0.5 * \hat{\beta}_1\, c_{nd}))) + A'_s E_s \varepsilon'_s((0.5 * \hat{\beta}_1\, c_{nd}) - d')) \qquad (14)$$

$$\phi_{nc} = \frac{\varepsilon_{fu}}{df - c_{nd}} \qquad (15)$$

2.6.3.3. Rupture failure:

$$M_{nr} = A_s f_y(d - (0.5 * \hat{\beta}_1\, c_{nr})) + A_f E_f \varepsilon_{fu}(df - (0.5 * \hat{\beta}_1\, c_{nr}))) + A'_s E_s \varepsilon'_s((0.5 * \hat{\beta}_1\, c_{nr}) - d')) \qquad (16)$$

$$\phi_{nr} = \frac{\varepsilon_{fu}}{df - c_{nr}} \qquad (17)$$

Based on the analytical results, it is worth mentioning that the present model does not account for the extra contribution of carbon fiber splay anchors. Thus, it is expected that the model will yield similar results for specimens No.2, and No.3 as well as No.4 and No.5. However, the expected values have excellent agreement with the experimental ones. This is simply because the fiber anchors in these tests had a minor contribution since they were only applied at the sheet ends. The analytical yielding load for beam No.2 was predicted to be 80.92 kN (18.19kips) while the actual yielding load was measured to be 81.85 kN (18.40 kips) showing an excellent agreement. Furthermore, the expected cracking loads for all specimens showed a strong agreement with experimental data. The observation of the comparison adds further evidence to the precision and consistency of the current model in capturing the envelope curve of cyclic responses of RC beams, both with and without CFRP strengthening. Table 2.9, and Figure. 2.24. to Figure. 2.28. illustrate the comparison between the proposed model and the results obtained from experimental data.

Table 2.9. Comparison of average experimental results against analytical predictions.

Specimen	Average experimental results			Analytical results		
	Cracking load kN (Kips)	Yielding load kN (Kips)	Ultimate load kN (Kips)	Cracking load kN (Kips)	Yielding load kN (Kips)	Ultimate load kN (Kips)
Beam No.1	38.03 (8.55)	67.87 (15.26)	107.41 (24.15)	31.14 (7.00)	57.83 (13.00)	80.07 (18.00)
Beam No.2	34.47 (7.75)	80.92 (18.19)	114.4 (25.72)	33.36 (7.50)	81.85 (18.40)	102.31 (23.00)
Beam No.3	31.26 (7.03)	79.75 (17.93)	114.46 (25.73)	33.36 (7.50)	81.85 (18.40)	102.31 (23.00)
Beam No.4	34.12 (7.67)	114.34 (25.71)	150.20 (33.77)	36.03 (8.10)	116.54 (26.20)	133.45 (30.00)
Beam No.5	33.36 (7.50)	130.93 (29.44)	157.43 (35.39)	36.03 (8.10)	116.54 (26.20)	133.45 (30.00)

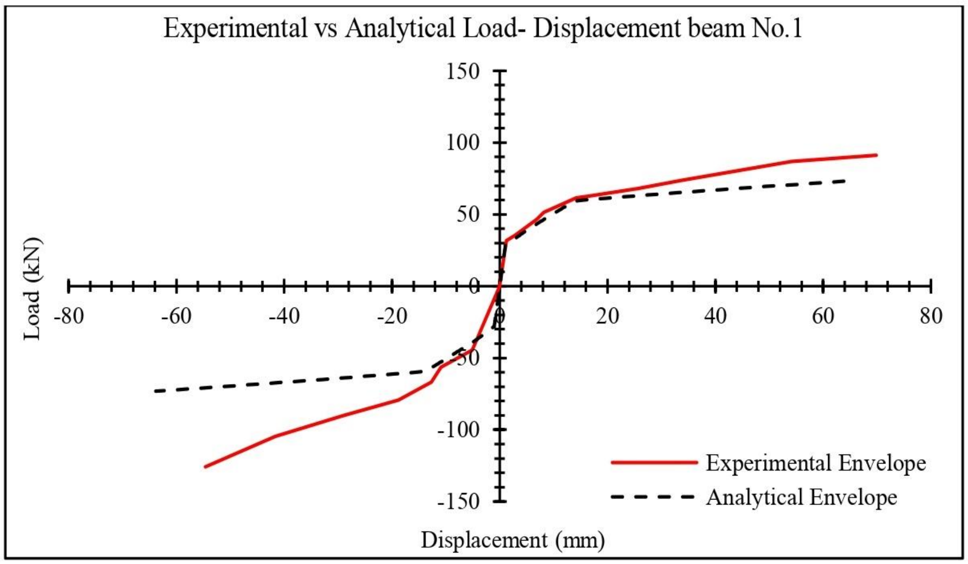

Figure 2.24. Analytical vs. Experimental Envelope Curve Comparison of beam No.1

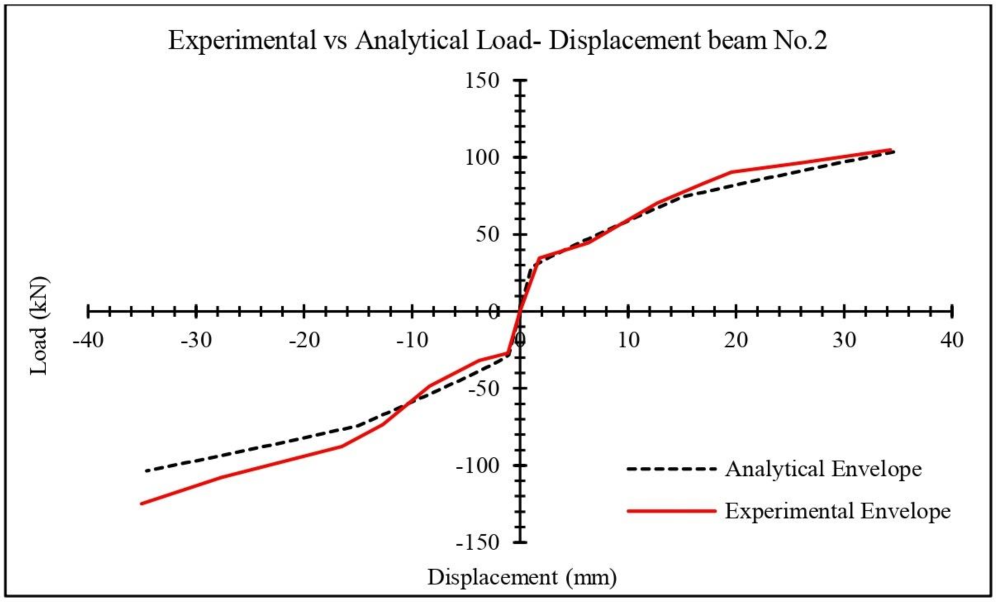

Figure 2.25. Analytical vs. Experimental Envelope Curve Comparison of beam No.2

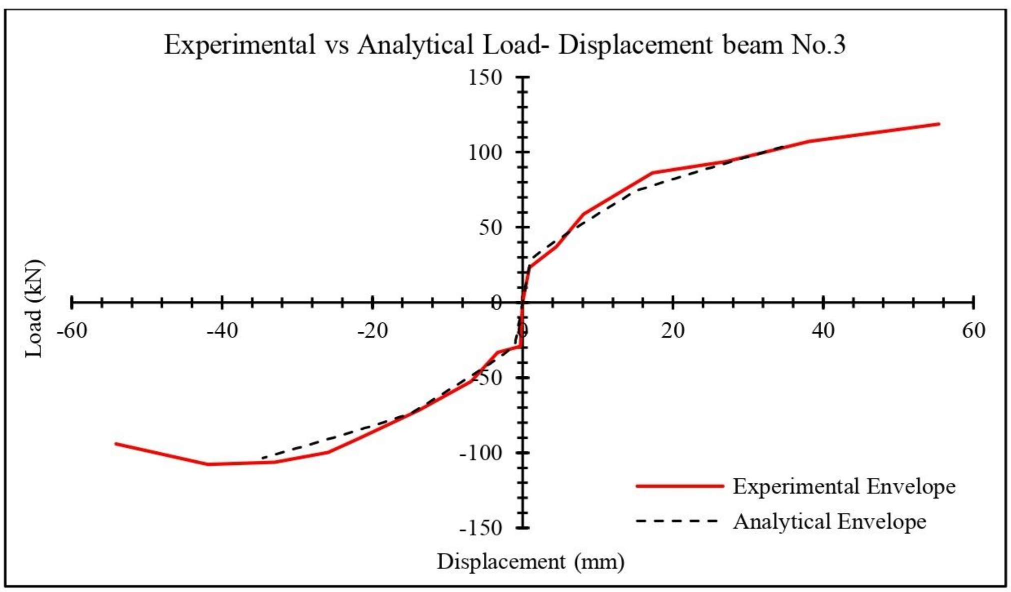

Figure 2.26. Analytical vs. Experimental Envelope Curve Comparison of beam No.3

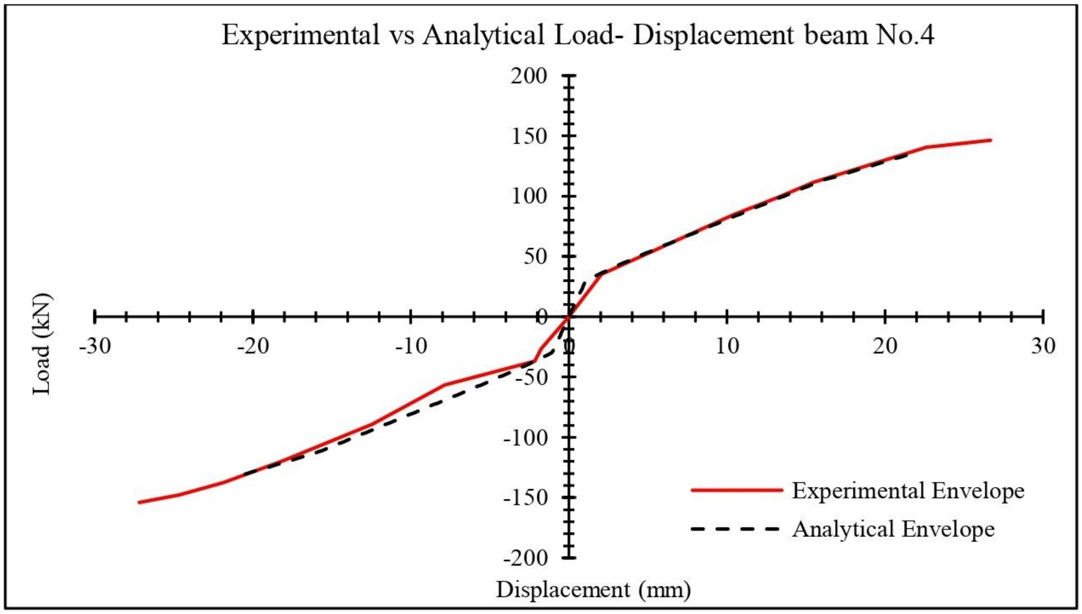

Figure 2.27. Analytical vs. Experimental Envelope Curve Comparison of beam No.4

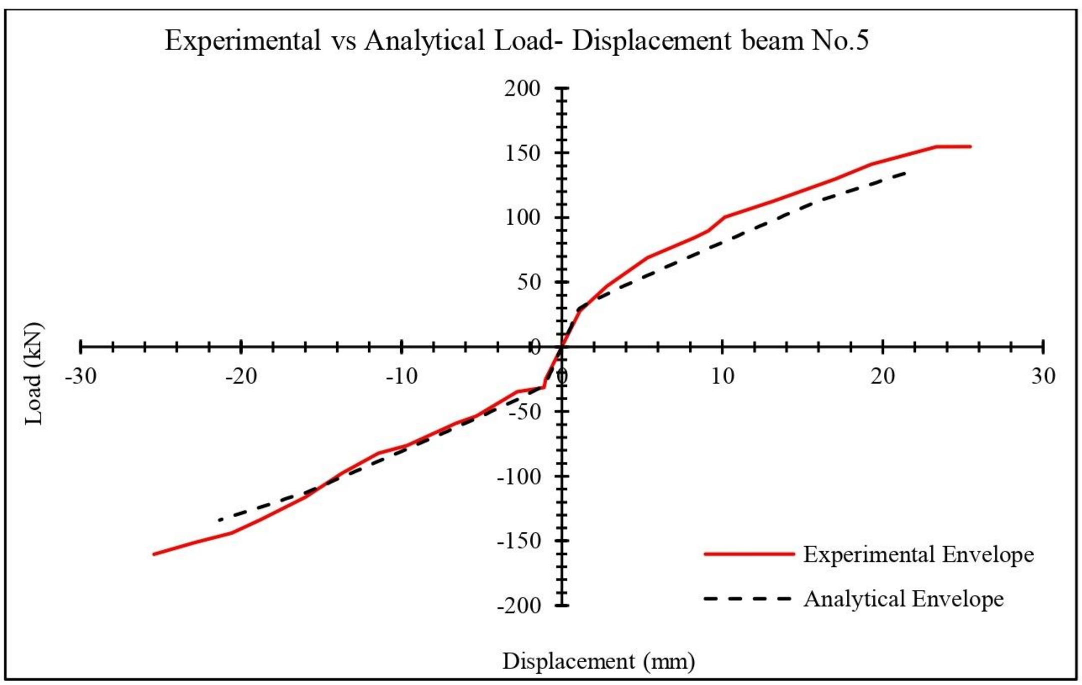

Figure 2.28. Analytical vs. Experimental Envelope Curve Comparison of beam No.5

2.7. Load-Strain and Moment-Curvature Response

Experimental load-strain data was collected for the purpose of extracting the equivalent experimental moment-curvature response for all beams. In this section, the hysteretic load-strain curves for the strain gauges mounted on the FRP sheets are plotted first for beam No.3 to maintain the brevity of presentation in this paper, Figure. 2.29-2.30. These figures clearly show the difference in behavior between the compressive and tensile sides. It is interesting to note that the two graphs are symmetric about the X- axis indicating an accurate measurement protocol. On the other hand, the hysteretic load-strain curves for the strain gauges mounted on the steel bars are plotted next for beam No.3, Figure. 2.31-2.32. These figures show a similar trend to the results plotted for the FRP strain gauges. Figure.2.29-2.30 are used to extract the hysteretic moment -curvature response of that beam for the FRP gauges while Figure. 2.31-2.32 are used to determine the same moment-curvature curve for the steel gauges. Figure. 2.33 shows a comparison between the two independently extracted moment-curvature curves indicating the relevance of the Bernoulli-Navier hypothesis of plane section remine plane after bending. However, the small discrepancy between the two curves might be attributed to some bond slip in the FRP sheets at mid-span causing the FRP strains to be lower than the steel strain especially in the post cracking region. Furthermore, the analytical moment-curvature response derived using section 5 above is also plotted in the same figure. It is evident that the analytical curve perfectly matches the envelope curve of the steel strain gauges. The small discrepancies between the FRP experimental and the analytical moment-curvature curves is expected since these correspond to localized strain measurement that cannot perfectly align with theoretical predictions.

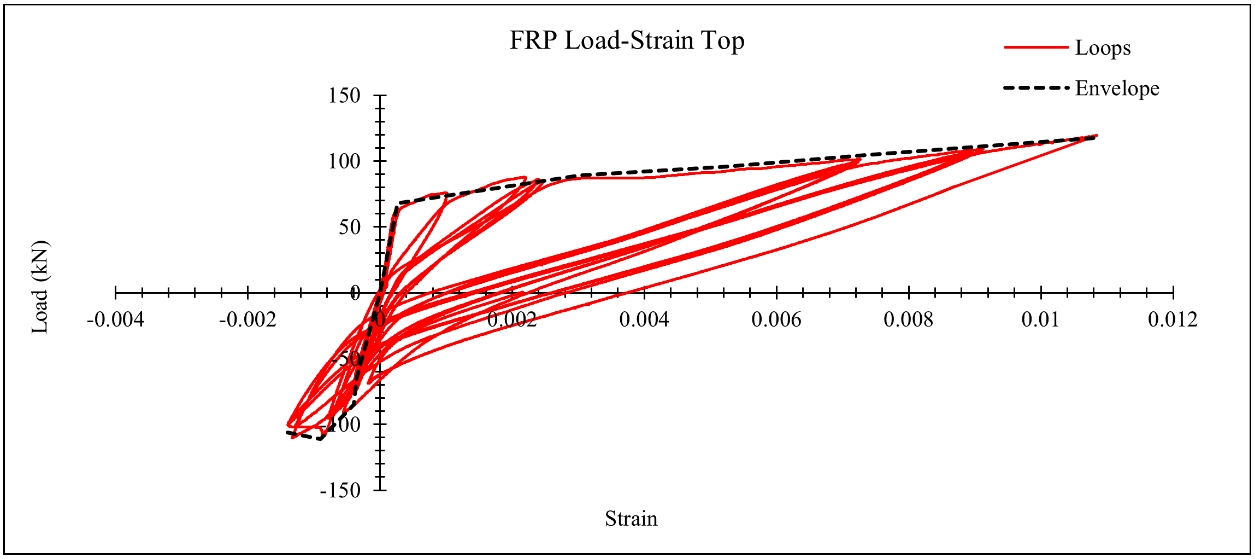

Figure 2.29. Top FRP Load-Strain for Beam No.3

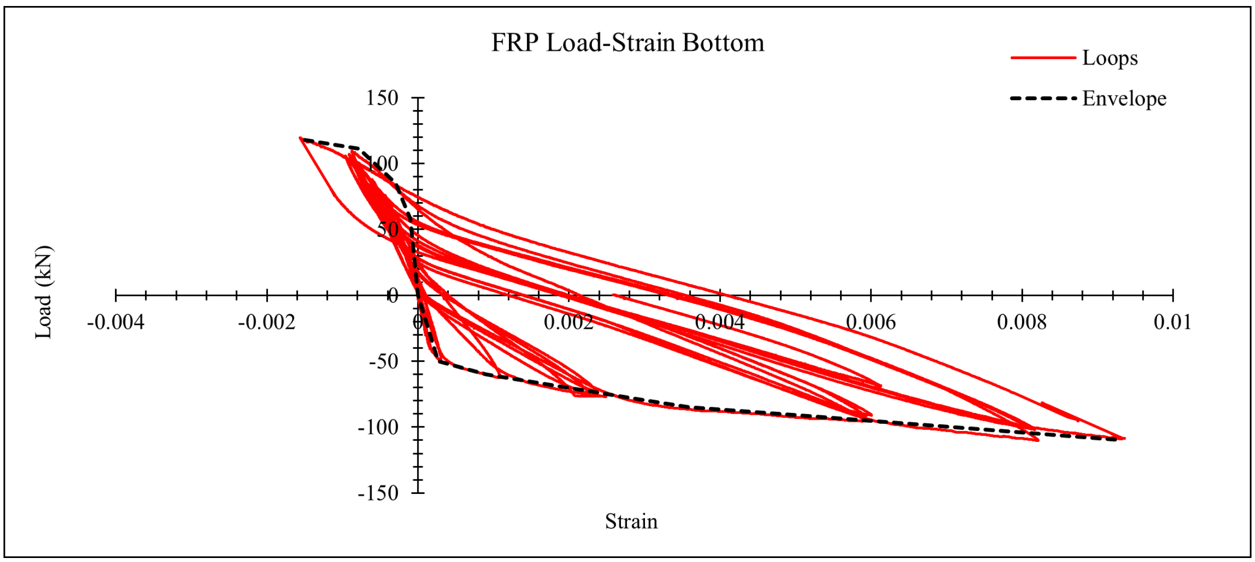

Figure 2.30. Bottom FRP Load-Strain for Beam No.3

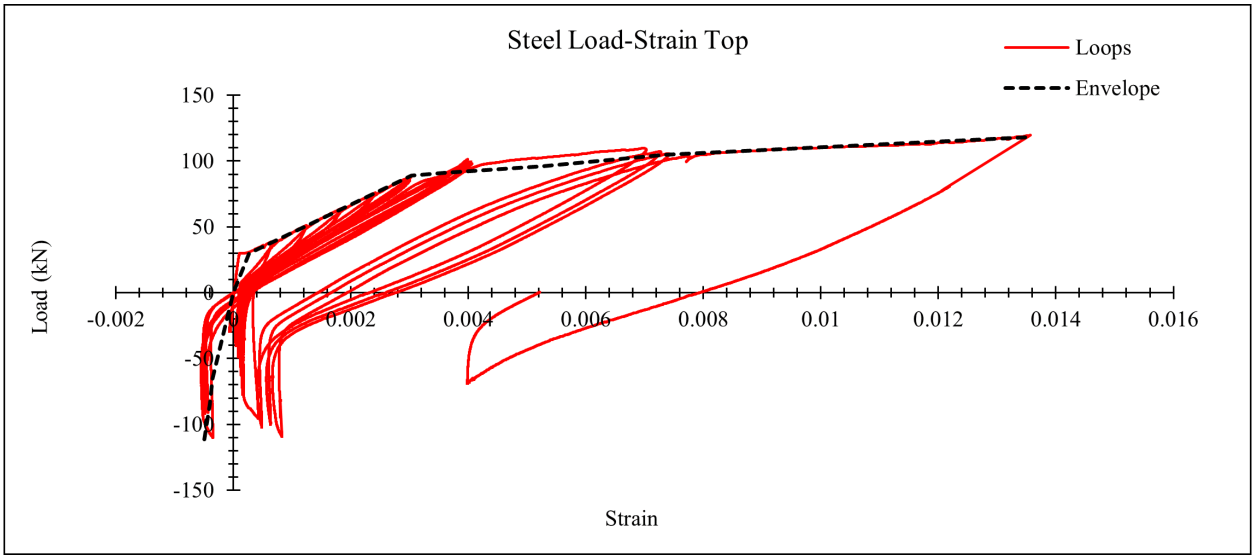

Figure 2.31. Top Steel Rebar Load-Strain for Beam No.3

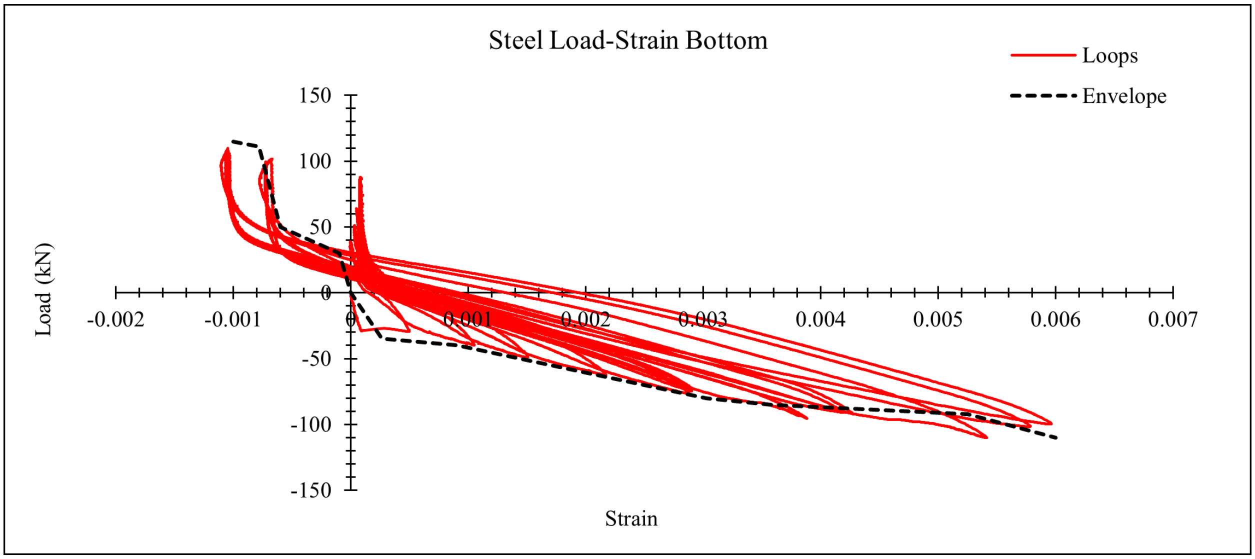

Figure 2.32. Bottom Steel Rebar Load-Strain for Beam No.3

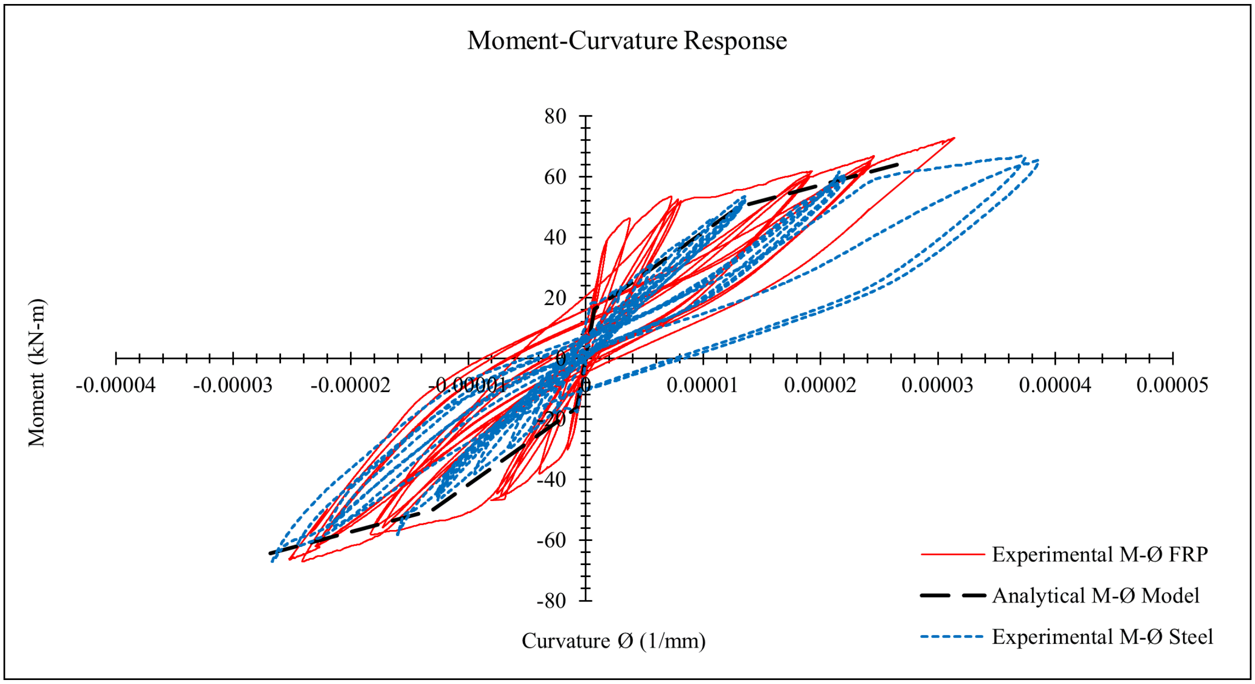

Figure 2.33. Experimental and Modeled Moment-Curvature of Beam No.3

2.8. Conclusions

This study presents detailed results on CFRP strengthened RC beams, with and without fiber anchors, subjected to cyclic displacement-controlled loading protocol up to failure. The use of carbon fiber splay anchors along with thin CFRP sheets had limited effect on the load-displacement response prior to yielding of reinforcing steel compared to the response without anchoring. In contrast, the ultimate capacity was noticeably enhanced due to the fact that anchors delayed the CFRP debonding. The use of carbon fiber splay anchors along with thick CFRP sheets had slight effect on the load-displacement response even after yielding of reinforcing steel compared to the one without anchoring even though the anchors shifted the failure mode to complete cover delamination around the anchor depths as opposed to sheet debonding. This is attributed to the use of no more than two anchors per shear span located back-to-back at the sheet ends with a limited fiber anchor embedment depth. On the other hand, the increase in CFRP thickness positively influenced the ultimate strength while negatively impacting the energy dissipation and ductility for thicker CFRP sheets. It is important to conduct further investigation into the impact of deeper anchors on the failure mode of the beams with thick CFRP, which could potentially mitigate this issue. It is also relevant to examine the impact of multi-layer CFRP system with thick fabric when anchored continuously within the shear span. It should be noted that this aspect will be thoroughly examined and validated in future tests.

Chapter 3 - Flexural Seismic Behavior of Moderate Concrete Strength-Steel Ratio RC Beams Strengthened by CFRP Sheets with and without Fiber Anchors

3.1. ABSTRACT

The behavior of carbon fiber reinforced polymer (CFRP) flexurally-strengthened reinforced concrete beams under reversed cyclic loading is not sufficiently studied. In this paper, normal strength concrete is used, with a typical steel ratio (0.5%), to build full-scale rectangular beams strengthened on top and bottom with flexural unanchored and anchored CFRP sheets. Five identical beams were examined under fully-reversed cycles up to failure following the AC 125 displacement loading protocol (Acceptance Criterion 125, ICC). The first beam was tested as an unstrengthened control specimen. The second and third beams were tested as strengthened specimens using thin sheets with and without fiber anchors. On the other hand, the fourth and fifth beams were tested when strengthened using thick sheets with and without fiber anchors. Specimens with thin sheets underwent higher ductility and lower hysteresis pinching relative to the thick ones. The results are comparatively discussed and compared to a phenomenological cyclic analysis model showing promising correspondence.

Keywords: Seismic strengthening; Carbon fiber anchors; Flexural members; Hysteresis modeling; Backbone curve.

3.2. Introduction

The externally bonded carbon fiber reinforced polymer (CFRP) strengthening technique has been widely established as the method of choice to enhance or retrofit deficient and damaged reinforced concrete structures because of its durability and high strength-to-weight ratio. CFRP is typically used as externally bonded material to the surface of RC members. Due to the premature debonding failure mode of externally bonded CFRP, the response of strengthened elements can be improved using mechanical fiber anchors. Some studies in the literature found that the ultimate failure load was enhanced when mechanical fiber anchors were applied compared to those RC beams without anchors (Ceroni et al. 2008 and Esmaeili et al. 2022). Most of these studies aimed to examine the performance of strengthened RC beams under static monotonic loads (Khalifa et al. 2016, Dias et al. 2018, Jawdhari et al. 2018, Alabdulhady et al. 2022, Liu et al. 2023, Liu et al. 2023, and Li et al. 2023). On the other hand, studies addressing the performance of such members under cyclic loads have been limited (Anil 2008, Capani et al. 2017, Saqan et al. 2018 and Saqan et al. 2020). Thus, there is a lack of knowledge regarding the seismic behavior of these strengthened systems.

Anil (2008) examined the seismic behaviors of RC T-beams strengthened with CFRP and loaded in cyclic shear. It was reported that the performance of the strengthened system could be directly influenced by CFRP layout, the concrete strength, and whether the application of steel bolts (used to anchor the CFRP) was implemented or not. The strength was increased by about 26% without anchor bolts, while the ultimate capacity of the tested RC beam with steel bolts increased by about 147% compared to the control beam. The use of these bolts successfully enhanced the cyclic response including strength and energy dissipation of the strengthened specimens.

Capani et al. (2017) experimentally investigated the cyclic response of RC beam-columns externally repaired with CFRP sheets. The tested specimens were categorized in terms of damage level, magnitude of the axial load, as well as strengthening technique. The results of the experiment showed that the strengthened repaired members exhibited improvement of the overall mechanical behavior compared to the unstrengthened ones. It was also noticed that the usage of CFRP sheets prevented the separation of concrete cover, excessive damage, and bucking of the longitudinal steel rebars. Regarding the number of loading cycles, the strengthened members survived more cycles than the control specimen.

Further research by Saqan et al. (2018) studied the effectiveness of CFRP sheets with full wrap anchorage as well as Near Surface Mounted (NSM) bars on the seismic performance of RC beam-column joint assemblies. It was observed that the use of both strengthening methods enhanced the overall behavior, including stiffness degradation, ultimate failure load, and energy dissipation. The hysteresis response of strengthened specimens was also improved in comparison to the control specimen. Additionally, the energy dissipation of the specimen, strengthened with CFRP sheets, was higher than the specimen strengthened using NSM. According to the authors, this is attributed to the gradual debonding of CFRP sheets. Furthermore, there was no significant improvement of the stiffness after yielding under cyclic loading compared to the stiffness after yielding under monotonic loading. In fact, the load-deflection response flattened and subsequently degraded because of the localized separation of the CFRP and NSM bars.

Alkhawaldeh et al. (2023) conducted an experimental study to investigate the improvement of cyclic response of heat-damaged non-ductile RC joints using CFRP hybrid (sheets and bars) systems. Twelve RC beam-column joints were built and categorized based on the strengthening technique employed. The joints as well as the beams and columns were wrapped with CFRP sheets in addition to NSM-CFRP string. Eight of the specimens were pre-damaged by exposing them to a temperature of 400°C and 600°C, the remaining specimens were kept at room temperature. The use of CFRP hybrid systems enhanced the cyclic response, resulting in higher ultimate load, larger displacement, and higher ductility compared to the control specimens. Furthermore, it was observed that the use of the CFRP hybrid system caused the joints to have superior energy dissipation. It was noted that the crack propagation was delayed due to the use of the CFRP strengthening. When comparing the strengthened specimens against the control ones, it was observed that the average improvement in ultimate capacity was 45%, 62%, and 75% for specimens strengthened with one, two, and three layers of CFRP sheets and strings, respectively.

The focus of this study is to investigate the seismic performance of externally strengthened RC beams using flexural CFRP sheets with different thicknesses and variable anchoring schemes. All tested RC beams were designed and built according to the ACI-318 building code (American Concrete Institute, 2019). Quasi-static cyclic loading in displacement control was applied to all five specimens in order to investigate the effects of using CFRP sheets on the seismic performance of the RC beam loaded by cyclic four-point bending. The load-displacement responses of the tested specimens are presented, the results are compared against each other and discussed. A phenomenological model is developed to predict the hysteresis response and compare it with the experimental data for two of the tested specimens.

3.3. Experimental Program

3.3.1. Specimen Design and geometric properties

A total of five full-scale RC beam specimens were designed based on ACI-318 code (American Concrete Institute, 2019). These specimens share the same dimensions, steel reinforcement, and concrete strength, see Fig. 1. Steel reinforcement was composed of 2 ϕ 16 bars (2 #5 bars) top and bottom in flexure and ϕ 10 bars at 152 mm (#3 bars at 6 in.) for stirrups in the shear span. The tested beams differ in terms of the level of strengthening, categorized based on the thickness of CFRP layers and their anchoring status, see Table 3.1. The vertical actuator mid-span displacement at yielding corresponding to a ductility ratio of 1, is also given in Table 3.1. The layout of steel reinforcement, boundary supports, and loading protocol are shown in Figure. 3.1. Additionally, Figure. 3.2. to Figure. 3.5. provide details on the geometry of specimens No.11 to No.14, including the steel reinforcement, types of CFRP sheets used for strengthening, and arrangement of anchors. Figure. 3.6. presents the carbon fiber splay anchors employed to secure the CFRP sheets in beam No.12 and No.14.

Table 3.1. CFRP strengthening details of all specimens.

Beam No.	Specimen Type	CFRP Sheets	Number of layers	Fig. No.	Δy Analysis (μ=1) mm (in)
10	Control	N/A	N/A	1	18.30 (0.72)
11	FRP strengthened	CSS V-Wrap™ C100HM	1 top and bottom	2	19.05 (0.75)
12	FRP strengthened & anchored	CSS V-Wrap™ C100HM	1 top and bottom	3	19.05 (0.75)
13	FRP strenghened	CSS V-Wrap™ C400HM	1 top and bottom	4	19.05 (0.75)
14	FRP strengthened & anchored	CSS V-Wrap™ C400HM	1 top and bottom	5	19.05 (0.75)

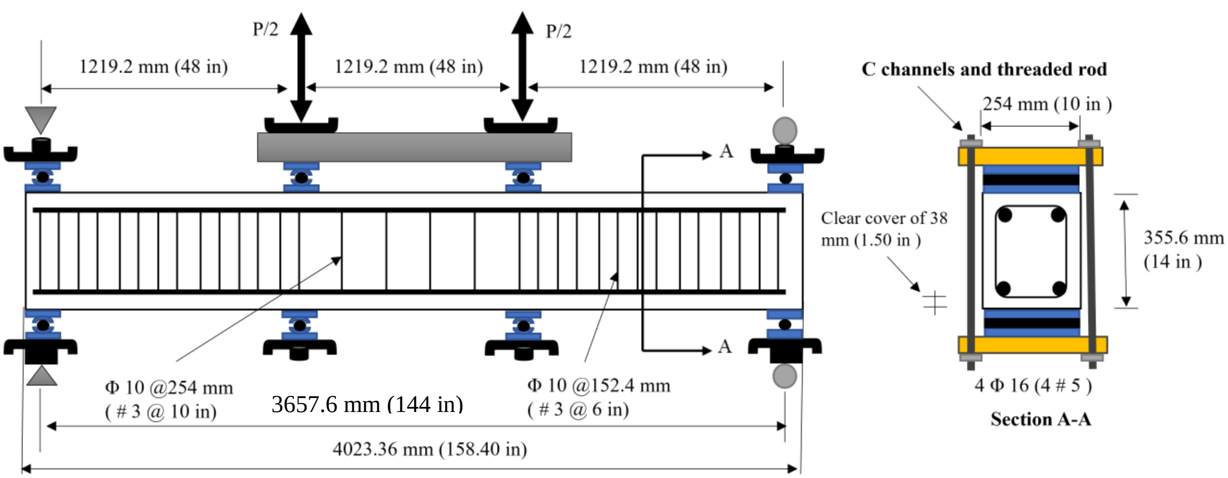

Figure 3.1. Beam No.10 (Control beam)

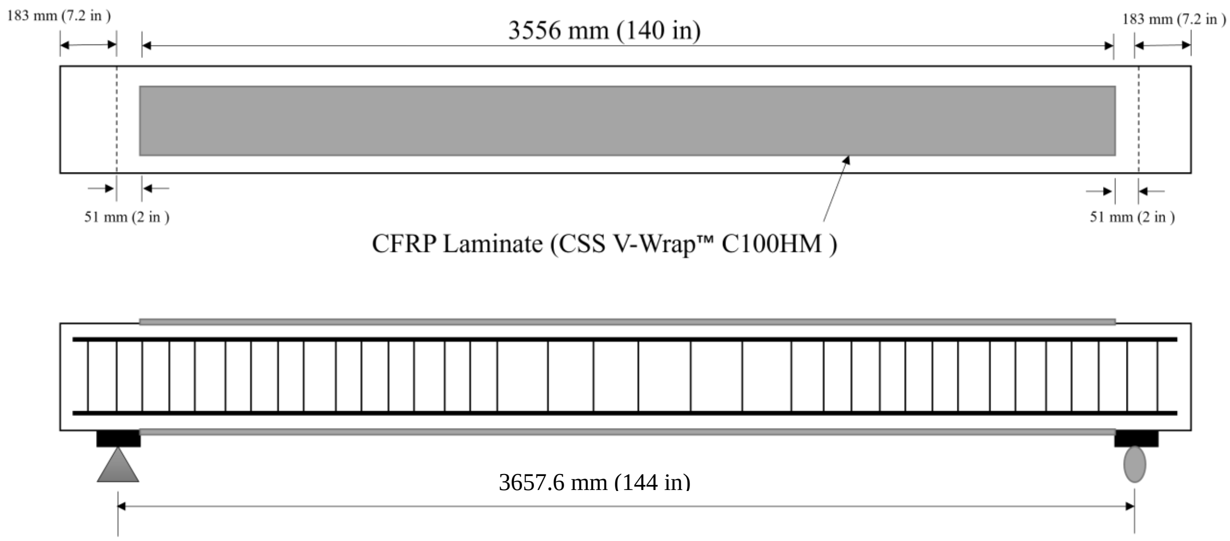

Figure 3.2. Beam No.11

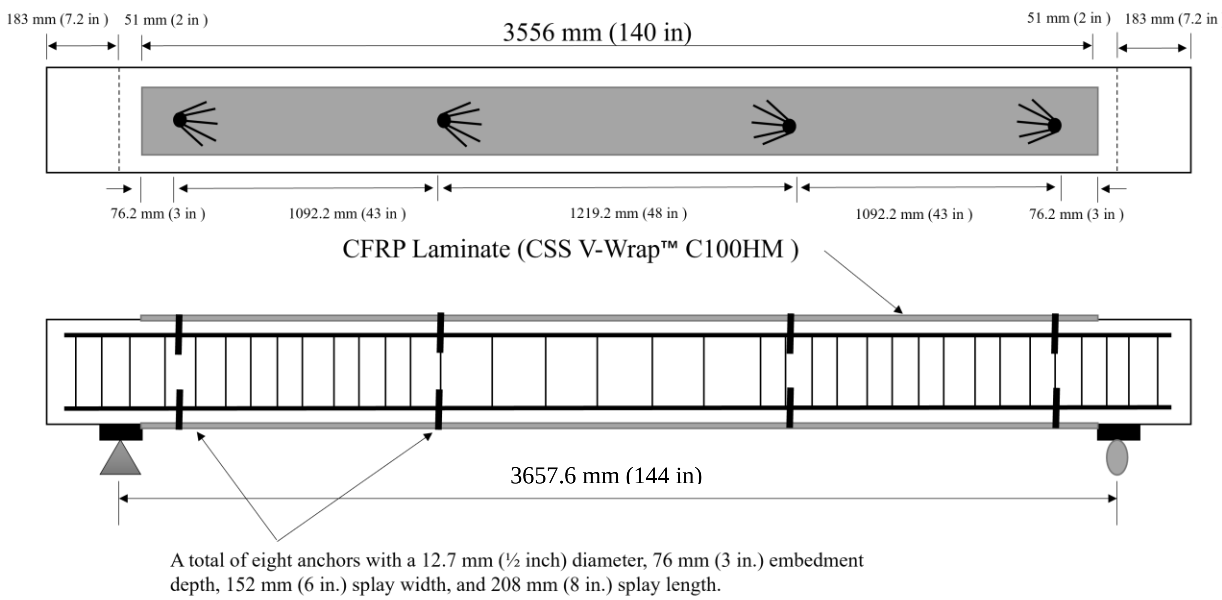

Figure 3.3. Beam N.12

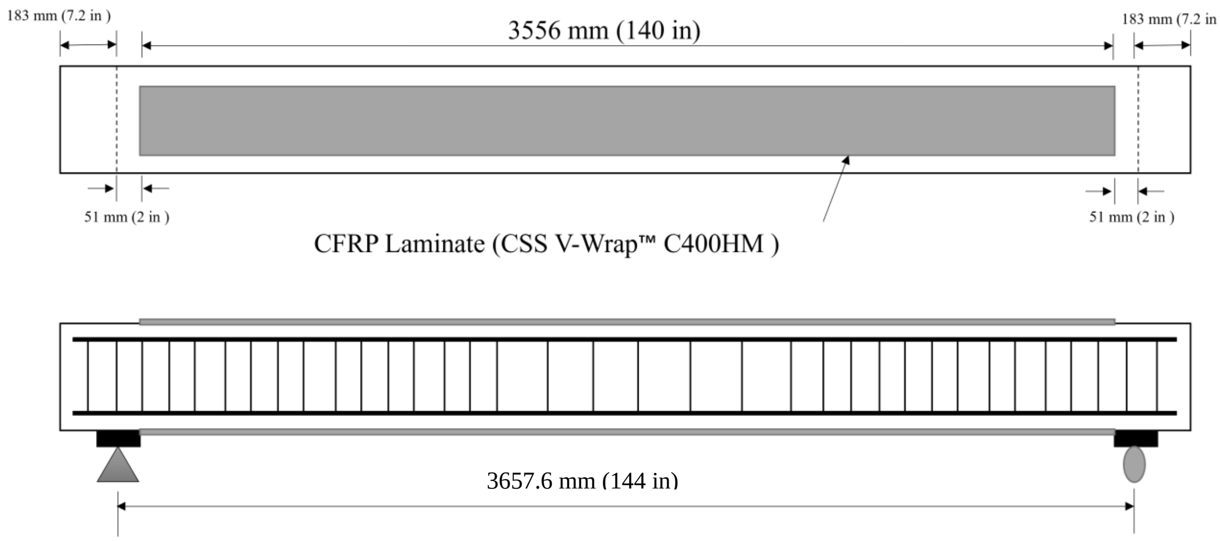

Figure 3.4. Beam N.13

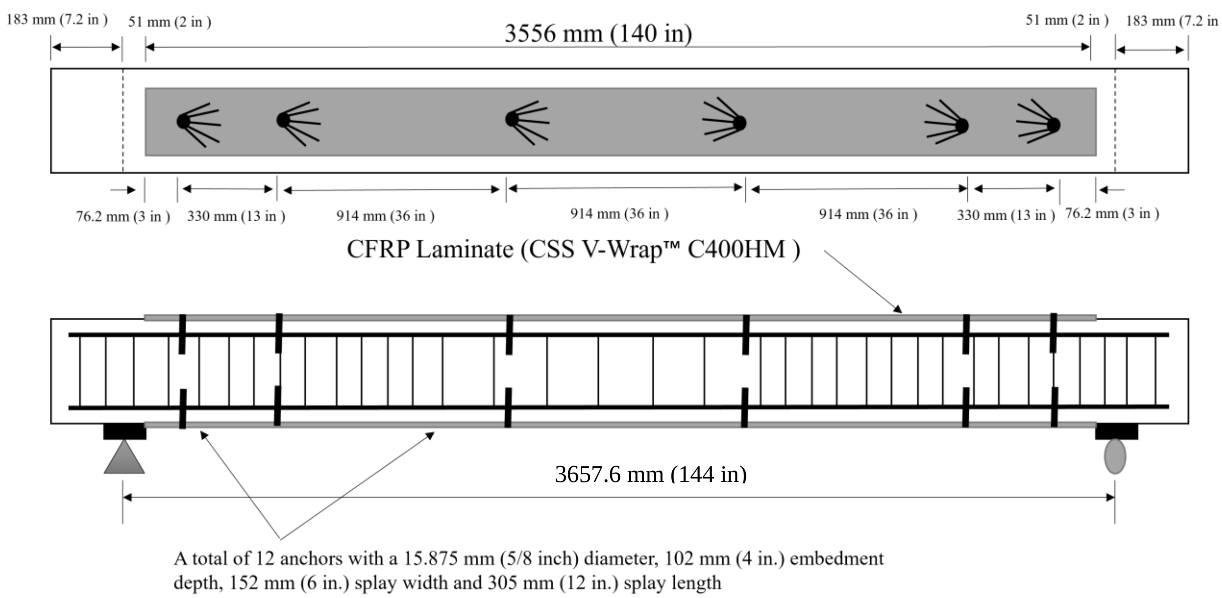

Figure 3.5. Beam No.14

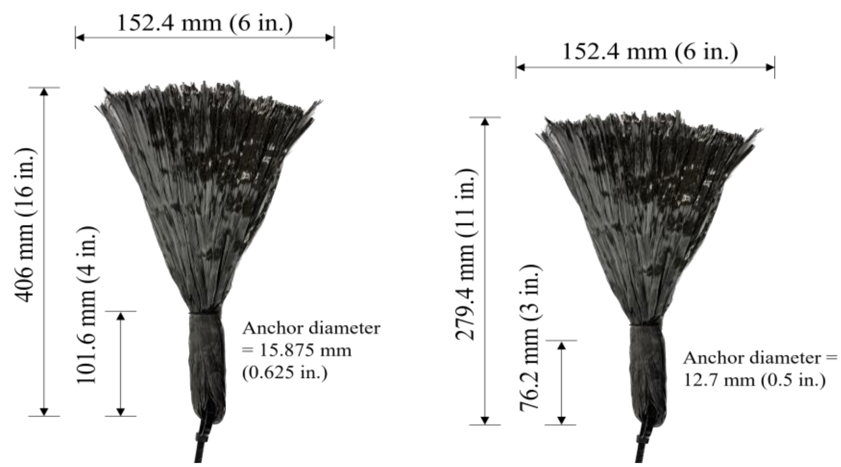

Figure 3.6. Carbon fiber splay anchors

3.3.2. Material Properties

3.3.2.1. Concrete Parameters

The compressive strength of the concrete mixture was initially designed to be 31 MPa (4500 psi) for all five specimens at 28 days. The standard cylinder tests followed in ASTM C39, utilizing four cylindrical specimens measuring 100 mm in diameter and 200 mm in height (4" diameter x 8" height). Since all the beams used the same concrete mix design, four cylinders were made to test the compressive strength of concrete. Three of these specimens (CS1-CS3) were tested at 28-days, while the fourth one (CS4) was tested at the day of beam No.11 testing, which occurred at an age of 230 days from casting, see Table 3.2. Based on the test results, it was determined that the average 28-day compressive strength of the concrete was approximately 39.28 MPa (5.7 ksi), which exceeded the cylinder strength tested after 230 days. Nevertheless, the result of one cylinder is not enough to make a conclusion about that issue. It is worth mentioning that the strength value determined from testing slightly exceeded the target design strength, which is common for commercial concrete mix designs.

Table 3.2. Concrete Compressive Strength Testing

Specimen	Testing type	Strength MPa (psi)	Average strength MPa (psi)
CS1	28-day Compressive Strength	41.60 (6,038)	39.28 (5,700)
CS2		37.87 (5,496)	
CS3		38.36 (5,567)	
CS4	Day of testing	37.95 (5,508)	37.95 (5,508)

3.3.2.2. Steel Reinforcement

ASTM A615 was followed in testing three ϕ 16 (#5) steel rebars to determine the modulus of elasticity and the yield strength of steel reinforcement. The average tested modulus of elasticity was 176.54 GPa (25,623 ksi), and the average yield strength was 513.30 MPa (74.50 ksi). Additional testing was carried out to determine the mechanical properties of shear reinforcement. It is important to note that the manufacturer mill certificates indicate that the ϕ 16 (#5) steel bars have a yield strength of 560.50 MPa (81.30 ksi). It is worth mentioning that the modulus of elasticity of this bar, from laboratory testing, appears to be lower than the typical steel modulus of 200 GPa (29,000 ksi). This difference may be attributed to a slight slippage in the Aluminum sacrificial inserts that fill in the gap between the bar and the hydraulic grips of the universal testing machine. The mechanical properties of longitudinal steel according to the experimental results are presented in Table 3.3 below along with the properties of ϕ 10 (#3) steel stirrups.

Table 3.3. Steel mechanical property testing results.

Rebar Size	Average Yielding Strength MPa (ksi)	Manufacturer Yielding Strength MPa (ksi)	Average Elastic Modulus MPa (ksi)	Manufacturer Elastic Modulus MPa (ksi)
ϕ 16 (No.5)	513.30 (74.50)	560.50 (81.30)	176,542 (25,623)	200 (29,000)
ϕ 10 (No.3)	485.50 (70.40)	470.20 (68.20)	173,182 (25,118)	200 (29,000)

3.3.2.3. Carbon Fiber Reinforced Polymer

Commercial high-modulus carbon fabric sheets were utilized as external strengthening materials with two different thicknesses. The thin fabric has a dry thickness value of 0.165 mm (0.0065 in.) resulting in a typical 0.508 mm (0.02 in) thick saturated laminate (CSS V-Wrap™ C100HM) with 330 g/m^2 (9.73 oz/yd^2) areal weight. The thick fabric has a dry thickness value of 0.66 mm (0.026in.) making the saturated laminate 2.03 mm (0.08 in) (CSS V-Wrap™ C400HM) with a 1300 g/m^2 (38.34 oz/yd^2) areal weight. The manufacturer data and dimensions are shown in Table 3.4 for both CFRP types.

Table 3.4. Mechanical Properties of CFRP per Manufacturer

Type of Carbon fiber fabric	Properties Type	Nominal thickness t, mm (in)	Ultimate tensile strength f_{fu}, , MPa (ksi)	Elongation at break ε_{fu}, %	Modulus of elasticity E, MPa (ksi)
CSS V-Wrap™ C100HM	Dry fiber properties	0.165 (0.0065)	5,440 (790)	1.9	289,550 (42,000)
	Cured laminate properties	0.508 (0.02)	1,490 (216)	1.3	115,142 (16,700)
CSS V-Wrap™ C400HM	Dry fiber properties	0.66 (0.026)	5,440 (790)	1.9	289,550 (42000)
	Cured laminate properties	2.03 (0.08)	1,241 (180)	1.27	98,181 (14,240)

3.3.3. Building and Casting of the Specimens

After formwork and steel caging were finished, the steel strain gauges were installed on the top and bottom longitudinal steel rebars at mid-span before the concrete was cast for all five specimens. The fabricated specimens were sprayed with water for seven days to ensure high quality of concrete curing and control the hydration process.

3.3.4. Preparing and Strengthening Techniques

The surfaces of the top and bottom faces of the beam were prepared by grinding the surface down to the aggregate level to ensure the quality of bond at the interface between concrete and CFRP sheets, see Figure. 3.2 to Figure. 3.5. Different types of strengthening systems were utilized based on the sheet thickness, and the arrangement of the CFRP anchors. Figure. 3.7. **(a-c)** illustrates the surface preparation and CFRP installation phase.

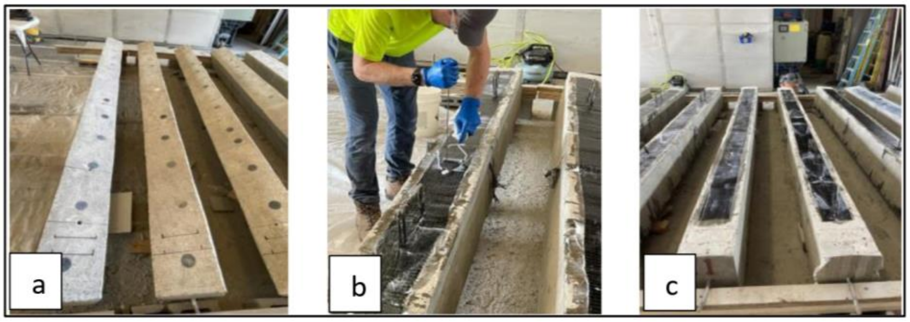

Figure 3.7. (a-c) RC Beams during Surface Preparation and CFRP Installation and Anchoring.

3.3.5. Cyclic Loading and Instrumentation

Displacement-controlled cyclic four-point bending was applied using a 668 kN (150-kip) hydraulic actuator, with an average rate of applied displacement equal to 17.78 mm/min (0.70 in/min), at Kansas State University's Structural Engineering Lab, see Figure. 3.1. Figure. 3.8. presents the displacement-controlled loading procedure. Additionally, to assess the net measured displacement at mid-span, four LVDTs (linear variable differential transformers) were employed. These LVDTs allowed for the measurement of displacement at both end supports (1 LVDT per support) and the mid-span of the specimen (2 LVDT's on both sides of the mid-span). Moreover, a minimum of four pairs of strain gauges were installed on the top and bottom of the beams at the mid-span to obtain the strain data for the steel and CFRP sheets (or for concrete faces in the case of the control beam). Also, CFRP strain gauges were installed on the top and bottom faces within the shear span, halfway between the anchors, to indicate any signs of premature debonding. In addition, an 890 kN (200-kips) load cell was employed to measure the applied load. Regarding the loading protocol, a displacement-controlled scheme followed the variations depicted in AC 125 (ICC ES AC125 2021), see Figure. 3.8. To collect the test data, including strains, displacements, and load, a Vishay

System 7000 data acquisition equipment was used. This data acquisition device consists of 16-strain gauge channels, one-load cell channel, one displacement actuator channel and 4 LVDTs channels.

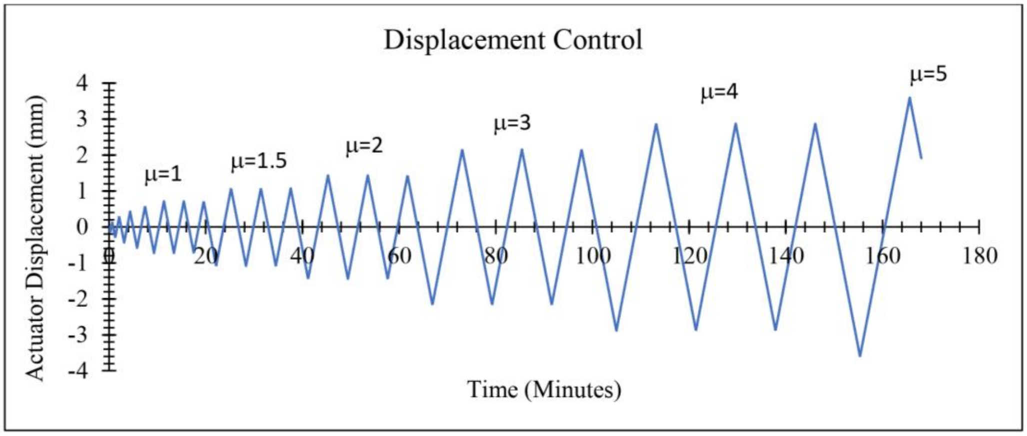

Figure 3.8. Loading Protocol for Beam No.10.

3.3.6. Experimental Setup

To evaluate the performance of the tested specimens subjected to reversed cyclic loading, a unique testing setup was utilized. The support conditions were a pin on one end and a roller on the other end with a clear span of 3657.6 mm (144inches)[3]. The load was applied at the one-third points along the specimen using a steel spreader beam as presented in Figure. 3.1. Additionally, steel C channels with threaded rods on both sides were employed to secure the specimens and prevent the movement during the application of the pull load, see Figure. 3.9. A torque wrench was used to apply a 66.72 kN (15-kips) pre-tensioned force to each of those threaded rods in order to provide adequate clamping force during the pull loading. According to the manufacturer data, the yielding strength of each 1-in threaded rod is reported to be 413.69 MPa (60 ksi). Thus, a load of 209.06 kN (47-kips) is required to cause yielding of each rod. Under an ultimate pull load of 266.88 kN

[3] The clear span of the RC beams was slightly over 144 in. since the center-to-center distance between the strong floor tie-down was 144.75 in.

(60-kips), each threaded rod will pick up an additional 66.72 kN (15-kip) to the pre-tensioned force leading to a 133.44 kN (30-kip) maximum force. Consequently, the threaded rods used have a safety factor of 1.57.

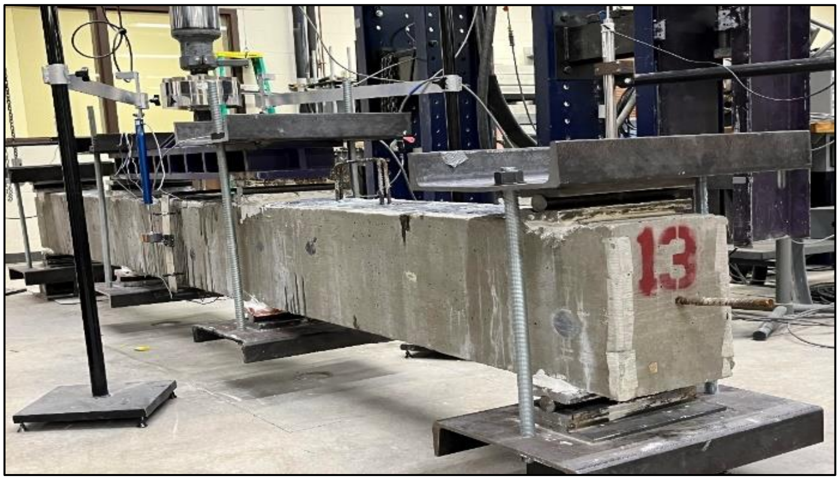

Figure 3.9. Typical testing set-up (Beam No.13).

3.4. Testing Outcomes

This section will discuss the outcomes, observations, and findings of the experimental data for each individual beam as well as a comparison of performance of all beams.

3.4.1. Beam No.10

The control beam showed a very ductile response, represented by a significant energy dissipation in hysteresis loops. The beam withstood sizeable displacement exceeding 57.15 mm (2.25 in.), in the pull direction, with minimal gradual reduction in strength near failure. The initial cracking of the beam occurred at a pushing load of 34.78 kN (7.82 kips) and a pulling load of 34.91 kN (7.85 kips), both at a cycle displacement of 7.62 mm (0.30 in.). As the displacement increased, additional typical flexural cracks formed in the constant moment region, accompanied by propagation of shear cracks underneath the points of load application. Based on strain readings of the steel, yielding was observed at a load of 92.62 kN (20.82 kips) in the push direction and 90.55 kN (20.36

kips) in the pull direction, both corresponding to a cycle displacement of 19.05 mm (0.75 in.). With further displacement, more flexural and shear cracks developed, and the existing ones widened. Failure of the beam occurred at a cycle displacement of 57.15 mm (2.25 in.) due to excessive yielding, which is expected for a typical steel RC beam. The ultimate load was experimentally determined to be 103.20 kN (23.20 kips) in the push direction and 107.14 kN (24.09 kips) in the pull direction. Figure. 3.10. illustrates the hysteretic response of the control specimen, while Figure. 3.11. shows the setup of the beam before and after testing.

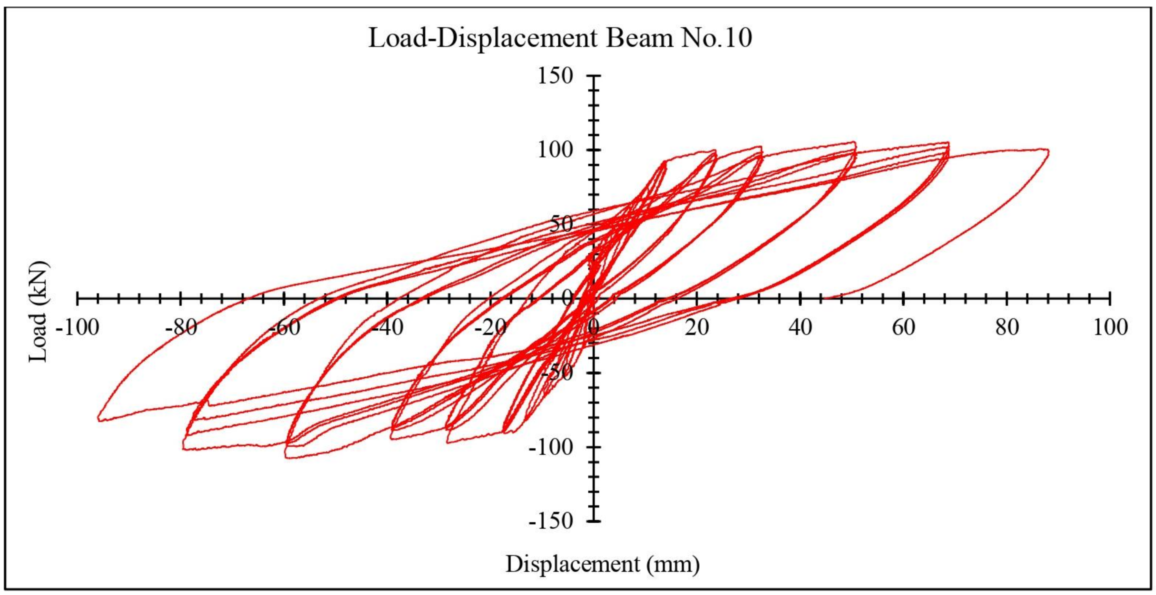

Figure 3.10. Load-displacement response of beam No.10 (1 Kips=4.45 KN)

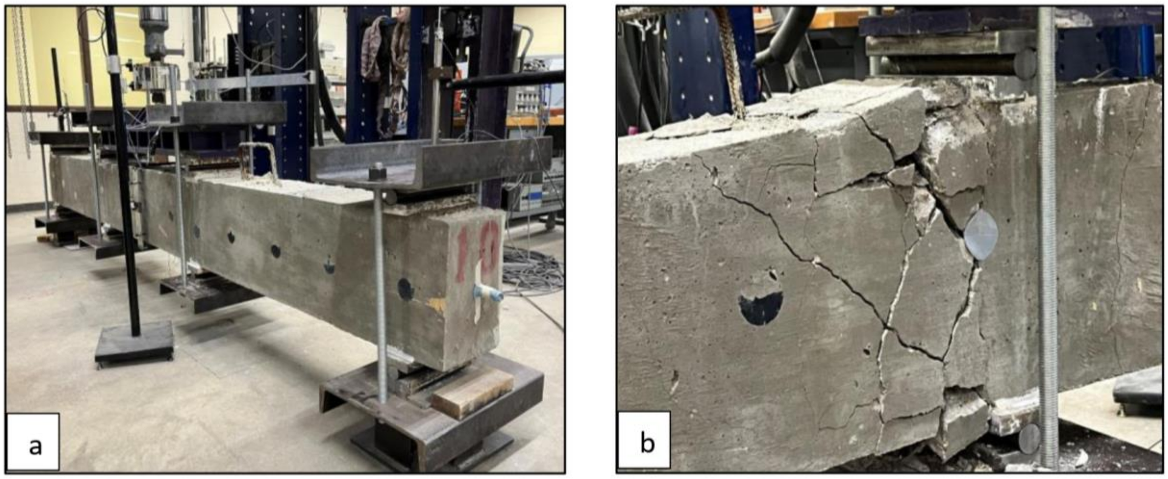

Figure 3.11. Specimen No.10. (a) before testing. (b) at failure

3.4.2. Beam No.11

Despite the use of CFRP sheets to enhance the strength of the second specimen, some level of ductility was notable due to the implementation of the thin sheet. The beam was able to endure displacement of 47.75 mm (1.88 in.), in the pull direction, before experiencing a sudden drop in strength within that cycle, caused by CFRP fiber rupture on the top face of the beam. Debonding of the bottom side, refer to Figure. 3.12, took place at a displacement of 38.11 mm (1.50 in.), in the push direction due to some unevenness in the bottom surface to which the CFRP was attached. The experimental data indicated the cracking load on both sides of the beam, push and pull, to be 53.06 kN (11.93 kips) and 30.87 kN (6.94 kips) respectively with a corresponding displacement cycle of 3.81 mm (0.15 in.). Also, it was observed that the density of flexural cracks increased, and shear cracks formed as displacement cycles increased. However, the cracks were narrower in comparison to the control specimen due to the restraint of the externally bonded CFRP sheets that controlled the distribution of these cracks. Furthermore, yielding was reached at a push load of approximately 108.21 kN (24.22 kips) with a corresponding cycle displacement of 29.21 mm (1.15 in.). In the pull direction, yielding occurred at a load of 106.80 kN (24.01 kips) at the same corresponding cycle displacement. As the applied load passed the yielding value, the shear-crack at the location of the load application, within the shear span, expanded across the height of the beam and became wider. Beam No.11 failed because of CFRP rupture on the top side of the beam (pull loading) at the boundary of the shear span. Failure of this beam was caused by CFRP debonding on the bottom side of the beam (push loading) at the boundary of the shear span. This failure took place at a push load of approximately 136.11 kN (30.60 kips) and a pull load of 132.11 kN (29.70 kips) with a corresponding cycle displacement of 57.2 mm (2.25 in.). Failure was mainly due to large diagonal shear cracks close to the load application location in the shear span. These cracks were attributed to the roller plates clamped by the C channels causing an anchor effect at these locations. Figure. 3.12 illustrates the response of Beam No. 11, while Figure. 3.13 shows the setup of the beam before and after testing.

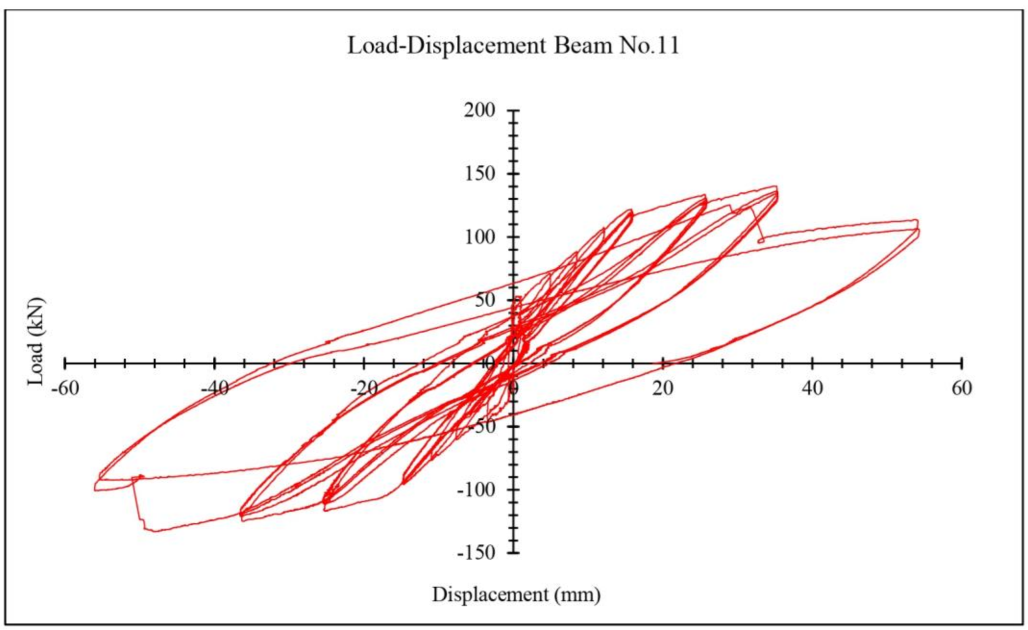

Figure 3.12. Load-displacement response of beam No.11 (1 Kips=4.45 KN)

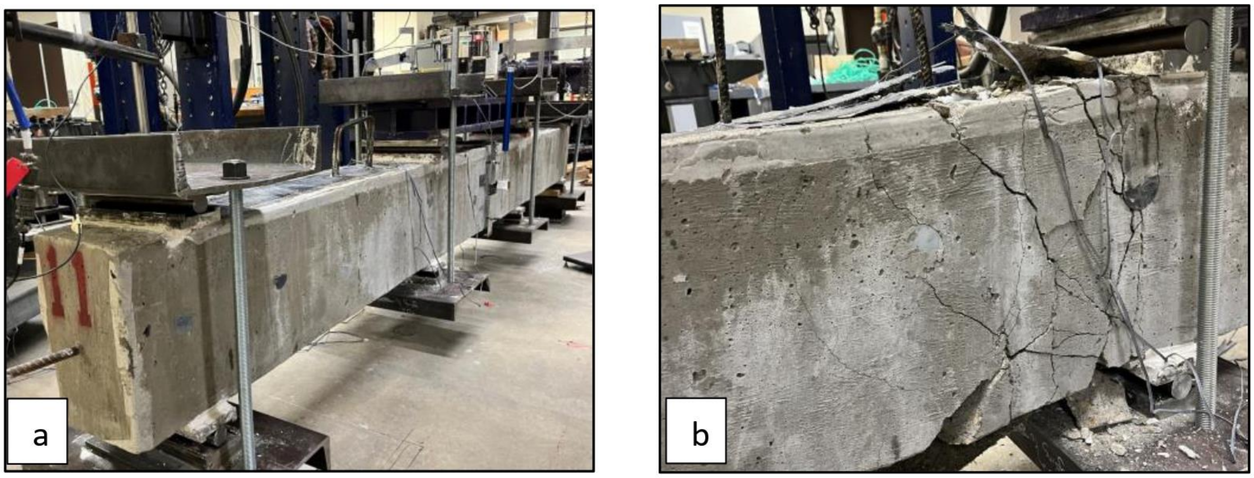

Figure 3.13. Specimen No.11. (a) before testing. (b) at failure

3.4.3. Beam No.12

The hysteretic response of the third specimen is almost the same as the previous specimen (beam No.11) until the ultimate load. Despite the use of carbon fiber splay anchors at the ends of the CFRP sheets of beam No.12, failure took place at the same displacement cycle under a similar strength and displacement. The specimen experienced a sudden reduction of strength that occurred due to CFRP rupture on the top and bottom faces of the beam within the constant moment region at the mid-span. The cracking load was approximately 41.38 kN (9.30 kips) in the push direction and 56.34 kN (12.65 kips) in the pull direction with a corresponding cycle displacement of 7.62 mm (0.30 in.). After the applied load exceeded the cracking load, the density of flexural cracks increased, accompanied by shear crack propagation at the edge of the shear span under the load. The yielding load during testing was determined to be 113.82 kN (25.59 kips) and 107.42 kN (24.15 kips) in the push and pull directions, respectively. These loads corresponded to the same cycle displacement of 29.21 mm (1.15 in.). After reaching the yielding load, both shear and flexural cracks increased. Specifically, shear cracks became wider and more noticeable, especially at the location of the load application. Unlike beam No. 11 that failed at the end of the shear span, beam No. 12 experienced failure at its mid-span, specifically within the constant moment region. This failure was attributed to the rupture of the external CFRP sheet on both top and bottom surfaces of the member. Failure load, in push and pull directions, was 129.62 kN (29.11 kips) and 135.91 kN (30.56 kips), respectively, with a corresponding cycle displacement of 38.10 mm (1.50 in.). Figure. 3.14 illustrates the hysteretic response of beam No.12. Figure. 3.15 presents the beam setup prior to and after testing. It is also worth mentioning that the end anchor prevented the thin CFRP sheet from completely separating from the beam.

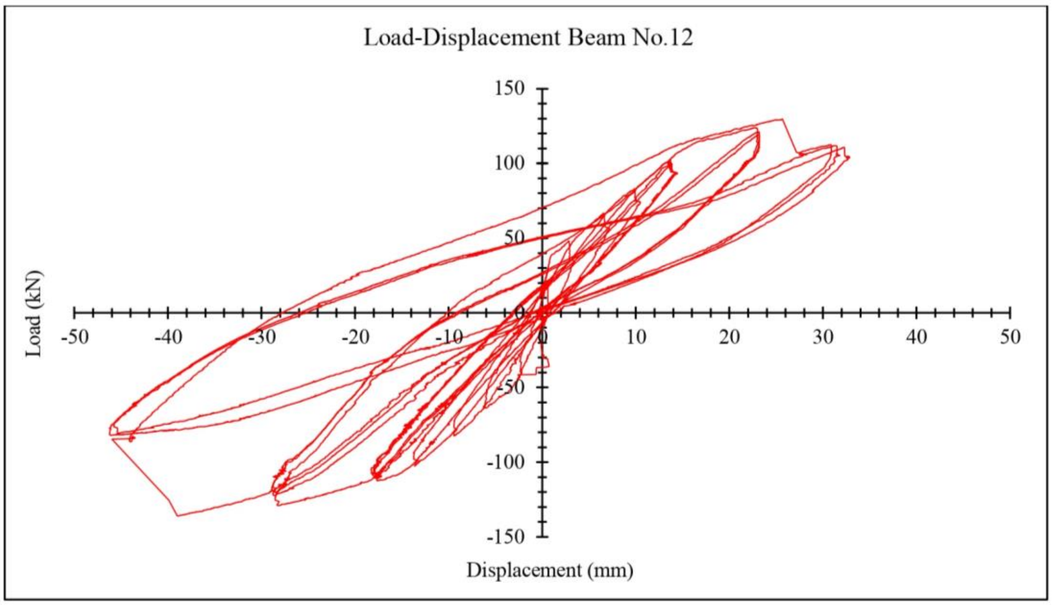

Figure 3.14. Load-displacement response of beam No.12 (1 Kips=4.45 KN)

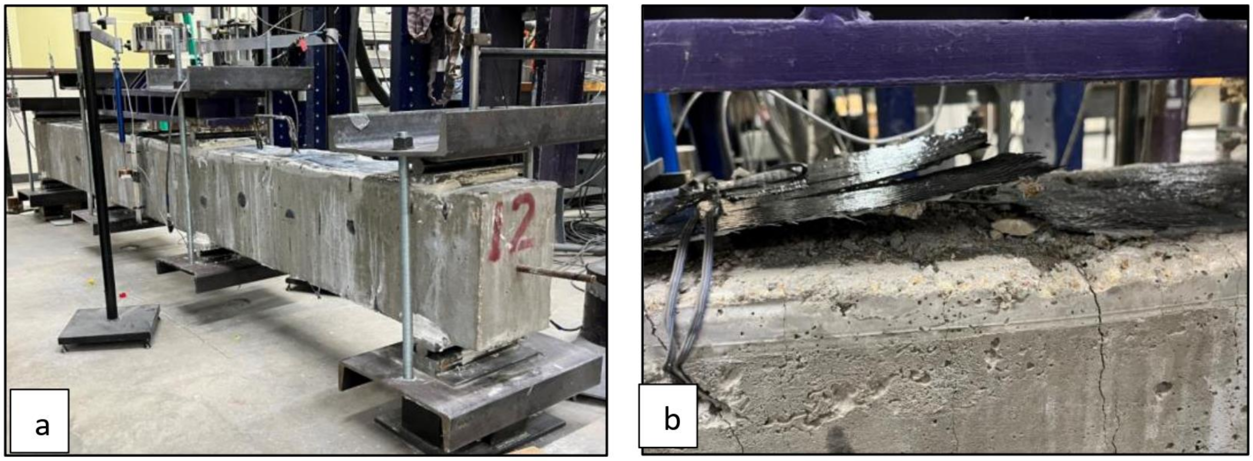

Figure 3.15. Specimen No.12. (a) before testing. (b) at failure

3.4.4. Beam No.13

A reduction in ductility was observed in beam No. 13 due to the use of a thicker CFRP sheet compared to the previous two specimens. The experimental data indicates that, on average, the beam only reached a displacement of 30.00 mm (1.18 in.) at the maximum load, which is 43 % less than the maximum displacement of beam No. 11. Additionally, a sudden drop of strength occurred at the failure, which was mainly caused by CFRP sheets debonding within the shear span at top and bottom faces of the member as shown in Figure. 3.16. The cracking loads on both faces of the beam, in push and pull directions, were 52.94 kN (11.90 kips) and 32.18 kN (7.24 kips) respectively. Furthermore, the corresponding displacement cycle for the push mode was 3.81 mm (0.15 in.), while for the pull direction, it was 7.62 mm (0.30 in.). It was observed that the flexural cracks became denser and increased while shear cracks developed as displacement cycles increased. The cracks present in beam No. 13 are narrower than the cracks in beam No. 11. This can be attributed to using thicker CFRP sheets, which provided more restraint and redistribution of the cracks. Moreover, the yielding was reached at a push load of approximately 133.35 kN (29.98 kips) with a corresponding cycle displacement of 29.21 mm (1.15 in.). In the pull direction, yielding occurred at a load of 127.67 kN (28.70 kips) having the same corresponding cycle displacement. The shear-crack at the location of the load application expanded within the height of the beam and became wider as flexural rebar yielded. The failure took place because of the debonding of the external CFRP sheets on both the top and bottom faces of the beam, specifically at the outer edge of the shear span. This debonding occurred at 173.79 kN (39.07 kips) on the push direction and at 177.41 kN (39.89 kips) in the pull direction, both corresponding to a cycle displacement of 38.10 mm (1.50 in.). Figure. 3.16 illustrates the response of beam No.13 reflecting lower energy dissipation and higher hysteresis pinching due to the use of thicker CFRP. Figure. 3.17 presents the beam specimen prior to and after testing.

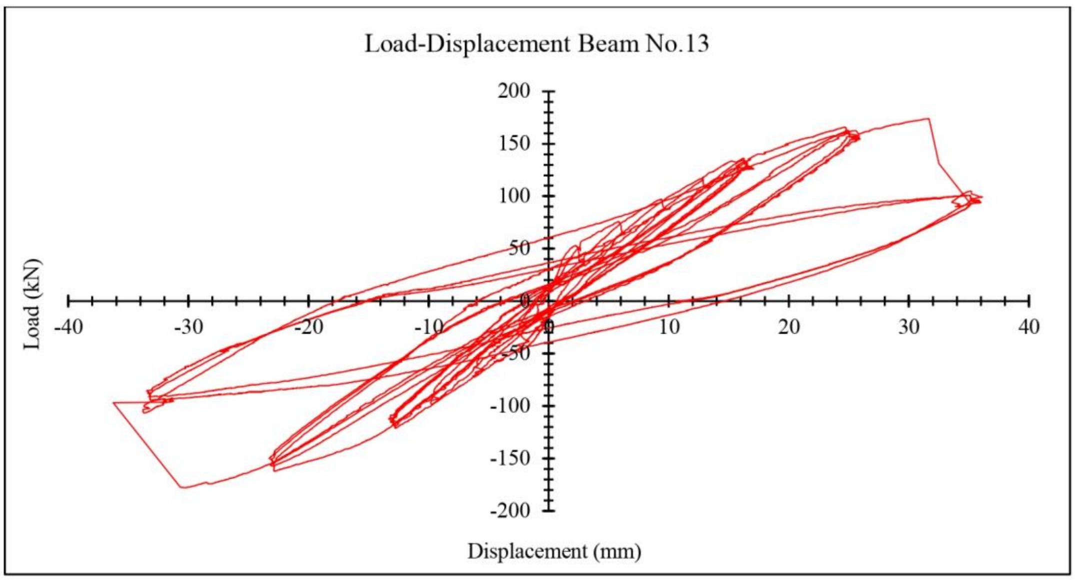

Figure 3.16. Load-displacement response of beam No.13 (1 Kips=4.45 KN)

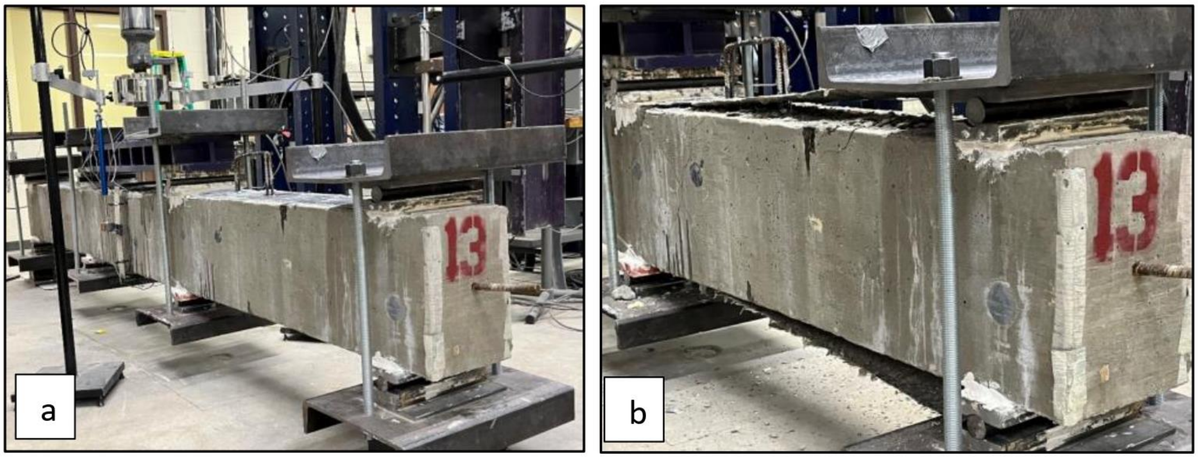

Figure 3.17. Specimen No.13. (a) before testing. (b) at failure

3.4.5. Beam No.14

The fifth specimen, beam No.14, assumed a similar hysteretic response to that of the fourth specimen, beam No.13, prior to yielding. However, it showed a higher ultimate capacity specifically in the push direction. The ultimate capacity of beam No.14 was enhanced by 23% and 5 % in the push and pull direction, respectively. Additionally, the energy dissipation appeared to be greater than that of beam No.13. The ductility of beam No.14 was also greater than that of beam No. 13 because of the use of anchors, see Figure. 3.16 and Figure. 3.18. Similar to all strengthened specimens, a sudden reduction of strength was observed after failure of the CFRP strengthening system. The failure occurred due to a partial cover delamination of the CFRP sheets along with the end anchor on one side of the bottom face of the beam close to the support. Failure was caused by rupture and debonding of CFRP sheets on the top side close to the load at that end of the shear span. In the push direction, a cracking load of 77.42 kN (17.41 kips) was observed, while in the pull direction, a cracking load was 49.78 kN (11.19 kips). Both sides exhibited a corresponding cycle displacement of 7.62 mm (0.30 in.). Also, it was observed that the width of flexural cracks and the appearance of shear cracks were minimal in beam No.14 compared to all other tested specimens. This result was attributed to the use of thicker CFRP sheets with anchors, which positively influenced crack restraint and redistribution. Yielding occurred at a push load of 154.97 kN (34.84 kips) and a pull load of 152.16 kN (34.21 kips), both corresponding to a cycle size of 29.21 mm (1.15 in.) followed by the propagation of shear cracks at both points where the loading was applied. The failure took place at a push load of approximately 214.70 kN (48.27 kips) and a pull load of 186.76 kN (41.99 kips) with a corresponding cycle displacement of 57.2 mm (2.25 in.). Figure. 3.18 illustrates the response of Beam No.14, while Figure. 3.19 presents the setup of the beam before and after testing.

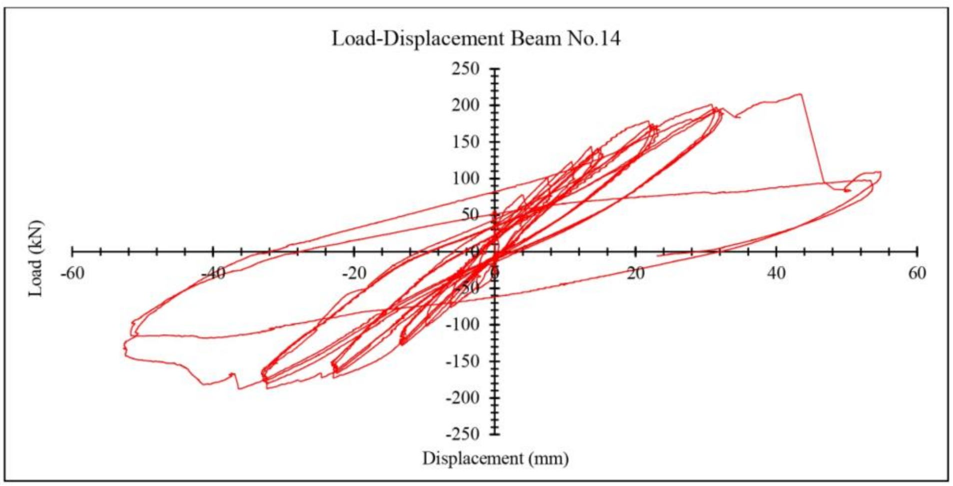

Figure 3.18. Load-displacement response of beam No.14 (1 Kips=4.45 KN)

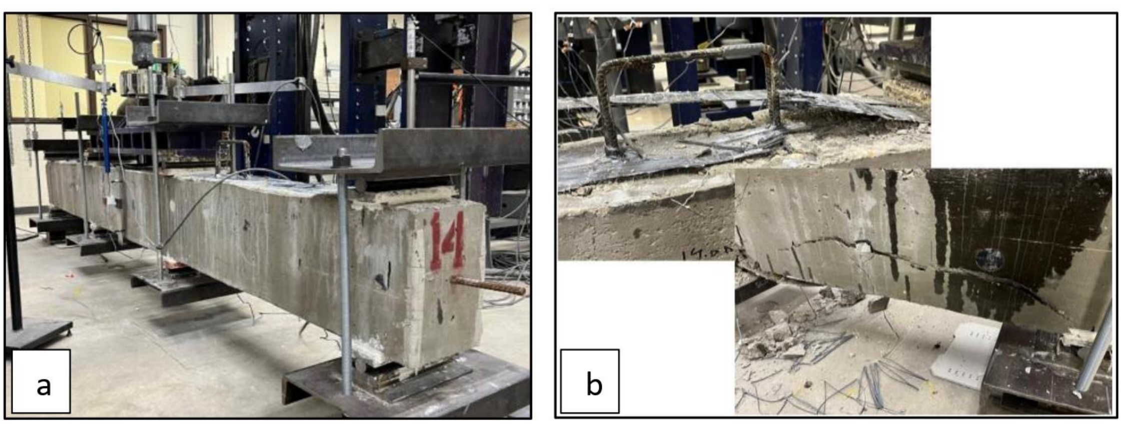

Figure 3.19. Specimen No.14. (a) before testing. (b) at failure

3.5. Performance Comparison of Specimens

In this research, a comprehensive comparison has been conducted between experimental results for all beams. The purpose of this comparison was to evaluate the structural behavior of these beams under various strengthening levels. The key parameters investigated in this section included strength, ductility, as well as stiffness degradation and envelope curves. These parameters were analyzed to gain insights into the performance and structural integrity of the tested beams.

3.5.1. Strength and Ductility

Comparing the strength and ductility of the tested specimens, the control beam (beam No.10) demonstrated the highest ductility and most significant energy dissipation due to extensive steel yielding. This can be attributed to the absence of CFRP strengthening. Based on the experimental results, specimens No.11 and No.12 exhibited some ductility, with beam No.11 displaying the highest level of ductility among the strengthened beams. On average, the ultimate capacity of beams No.11 and No.12 increased by 32% and 26%, respectively. Both specimens (No.11 and No.12) exhibited similar behavior, but different failure modes. Beam No.11 failed due to CFRP sheet debonding on the bottom face and CFRP sheet rupture on the top face, while beam No.12 failed as a result of CFRP sheet rupture at the mid-span within the constant moment region on both sides of the beam (top and bottom), Figure. 3.13(b) and Figure. 3.15(b). Regarding specimens No.13 and No.14, the use of carbon fiber splay anchors resulted in a different response. The cracking, yielding, and ultimate load for beam No.14 were higher, on average, by 49%, 18%, and 14%, respectively, compared to beam No.13. When comparing the ultimate capacity of these specimens to the control (No.10), it was found that the ultimate load capacity was enhanced by 67% and 90% for beam No.13 and No.14, respectively, see Figure. 3.20. The failure mode of beam No.13 occurred due to CFRP sheet debonding on both faces of the specimen, while for beam

No.14, the failure was caused by CFRP sheet debonding and rupture on the top side and concrete cover delamination on the bottom side near the support. It is important to note that the use of anchoring allowed for more deformation capacity, resulting in improved ductility and ultimate capacity of the strengthened beams with the CFRP sheet and anchors. In the present study, however, it should be noted that the locations of these anchors were concentrated at the ends, close to the supports, resulting in minimal benefits. Figure. 3.20 and Figure. 3.21 show the envelope load-displacement responses and energy dissipation of all specimens together.

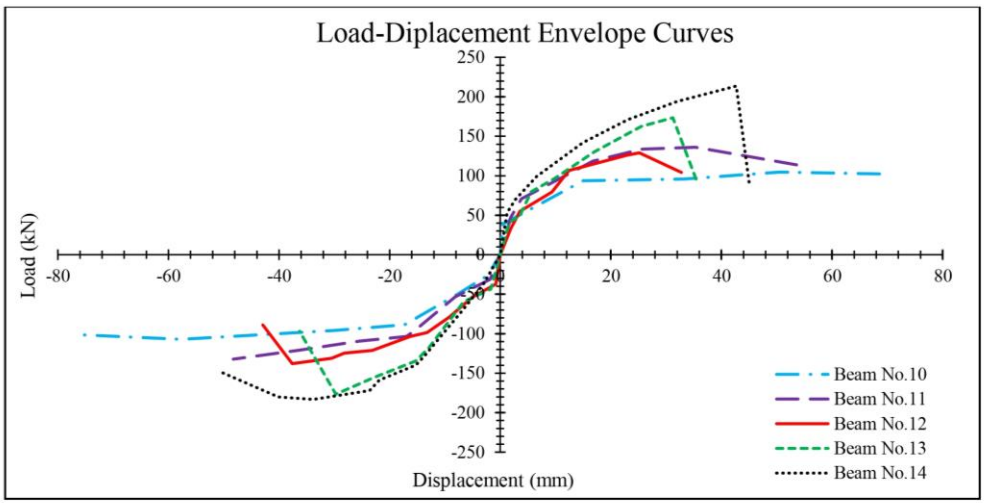

Figure 3.20. Envelope Carves Comparison of all Beams (1 Kips=4.45 KN)

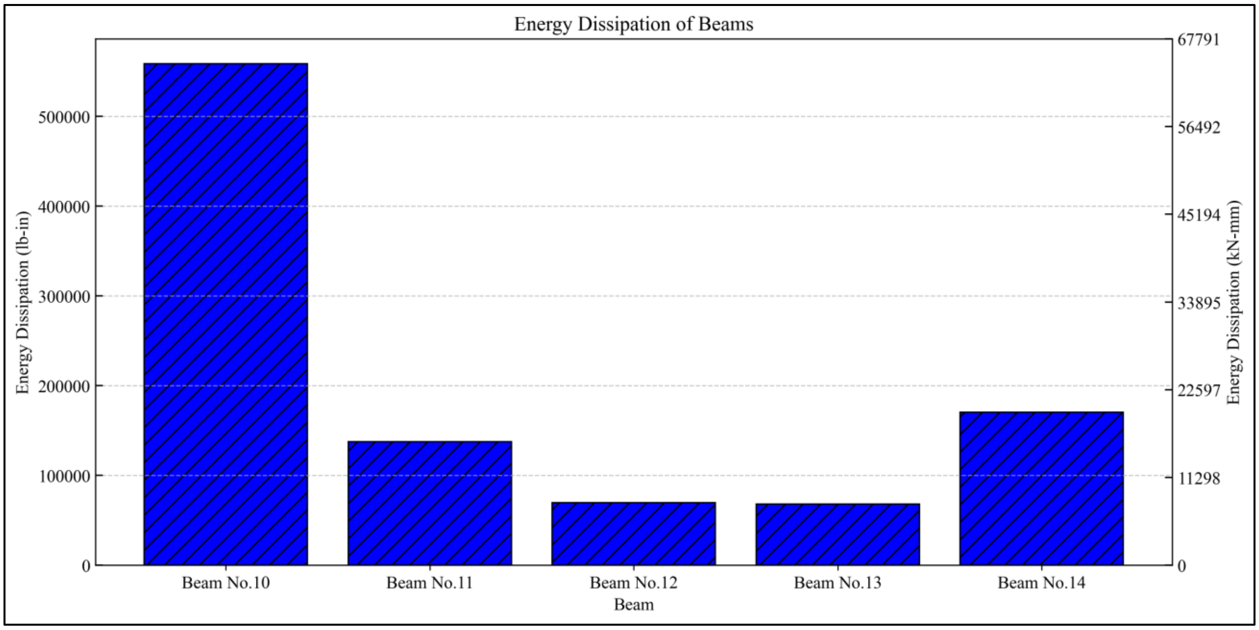

Figure 3.21. Energy dissipation of all beams[4]

3.5.2. Stiffness Degradation

When comparing the stiffness degradation of the beams tested under cyclic loading conditions, it is evident that each specimen exhibited a different level of degradation due to the use of varying thicknesses of CFRP sheets and different arrangements of carbon fiber splay anchors. Beam No.10 (control beam) demonstrated the highest stiffness degradation among all beams after cracking due to the absence of CFRP strengthening restraint, see Figure. 3.10. In contrast, beams No.11 and 12 showed less stiffness degradation compared to the control beam because of the CFRP strengthening. Beams No.13 and 14 exhibited a minimal reduction in stiffness due to the use of thicker CFRP sheets. Beams No.13 and 14 experienced the highest post-peak drop in stiffness due to the use of thick CFRP sheets. Beams No.11 and 12 also showed a drop in stiffness, but it is less pronounced compared to beams No.13 and 14, as the thinner sheets provide less stiffness

[4] Energy dissipation for CFRP strengthened beams is measured up to the failure of the strengthening system and not beyond that.

contribution. As expected, the control beam, lacking CFRP strengthening, did not exhibit any post-peak stiffness drop. To facilitate the reproduction of results in future studies, the key parameters of the response curves are summarized in Tables 3.5 to Table 3.8. Figure. 3.22 to Figure 3.23 show the peak displacement and the peak ultimate load at failure for all beams, respectively.

Table 3.5. Forward loading against displacement (Push direction).

Specimen	Experimental results						
	Cracking load kN (Kips)	Cracking Displacement mm (in)	Yielding load kN (Kips)	Yielding Displacement mm (in)	Ultimate load kN (Kips)	Ultimate Displacement mm (in)	Percent increase in ultimate load %
Beam No.10	34.78 (7.82)	3.81 (0.15)	92.62 (20.82)	13.72 (0.54)	103.2 (23.20)	50.7 (2.00)	-
Beam No.11	53.06 (11.93)	3.43 (0.135)	108.21 (24.22)	16.92 (0.67)	136.11 (30.60)	38.11 (1.50)	31.89
Beam No.12	41.38 (9.30)	6.07 (0.24)	113.82 (25.59)	15.29 (0.60)	129.62 (29.11)	25.40 (1.00)	25.26
Beam No.13	52.94 (11.90)	3.30 (0.13)	133.35 (29.98)	17.97 (0.71)	173.79 (39.07)	31.69 (1.25)	68.40
Beam No.14	77.42 (17.41)	7.11 (0.28)	154.97 (34.84)	19.75 (0.78)	214.70 (48.27)	43.33 (1.71)	108.04

Table 3.6. Reversed loading against displacement (Pull direction).

Specimen	Experimental results						
	Cracking load kN (Kips)	Cracking Displacement mm (in)	Yielding load kN (Kips)	Yielding Displacement mm (in)	Ultimate load kN (Kips)	Ultimate Displacement mm (in)	Percent increase in ultimate load %
Beam No.10	34.91 (7.85)	3.30 (.13)	90.55 (20.36)	16.76 (0.66)	107.14 (24.09)	57.36 (2.26)	-
Beam No.11	30.87 (6.94)	3.68 (0.145)	106.8 (24.01)	19.05 (0.75)	132.11 (29.70)	47.75 (1.88)	23.31
Beam No.12	56.34 (12.65)	5.84 (0.23)	107.42 (24.15)	15.16 (0.60)	135.91 (30.56)	39.00 (1.50)	26.85
Beam No.13	32.18 (7.24)	4.83 (0.19)	127.67 (28.70)	14.23 (0.56)	177.41 (39.89)	30.05 (1.18)	65.60
Beam No.14	49.78 (11.19)	7.34 (0.289)	152.16 (34.21)	17.40 (0.69)	186.76 (41.99)	38.84 (1.41)	74.31

Table 3.7. Forward loading against cycle displacement (Push direction).

Specimen	Experimental results						
	Cracking load kN (Kips)	Cracking Cycle Displacement mm (in)	Yielding load kN (Kips)	Yielding Cycle Displacement mm (in)	Ultimate load kN (Kips)	Ultimate Cycle Displacement mm (in)	Percent increase in ultimate load %
Beam No.10	34.78 (7.82)	7.62 (0.30)	92.62 (20.82)	19.05 (0.75)	103.2 (23.20)	57.15 (2.25)	-
Beam No.11	53.06 (11.93)	3.81 (0.15)	108.21 (24.22)	29.21 (1.15)	136.11 (30.60)	57.15 (2.25)	31.89
Beam No.12	41.38 (9.30)	7.62 (0.30)	113.82 (25.59)	29.21 (1.15)	129.62 (29.11)	24.40 (1.50)	25.26
Beam No.13	52.94 (11.90)	3.81 (0.15)	133.35 (29.98)	29.21 (1.15)	173.79 (39.07)	24.40 (1.50)	68.40
Beam No.14	77.42 (17.41)	7.62 (0.30)	154.97 (34.84)	29.21 (1.15)	214.70 (48.27)	57.15 (2.25)	108.04

Table 3.8. Reversed loading against cycle displacement (Pull direction).

Specimen	Experimental results						
	Cracking load kN (Kips)	Cracking Cycle Displacement mm (in)	Yielding load kN (Kips)	Yielding Cycle Displacement mm (in)	Ultimate load kN (Kips)	Ultimate Cycle Displacement mm (in)	Percent increase in ultimate load %
Beam No.10	34.91 (7.85)	7.62 (0.30)	90.55 (20.36)	19.05 (0.75)	107.14 (24.09)	57.15 (2.25)	-
Beam No.11	30.87 (6.94)	3.81 (0.15)	106.8 (24.01)	29.21 (1.15)	132.11 (29.70)	57.15 (2.25)	23.31
Beam No.12	56.34 (12.65)	7.62 (0.30)	107.42 (24.15)	29.21 (1.15)	135.91 (30.56)	24.40 (1.50)	26.85
Beam No.13	32.18 (7.24)	7.62 (0.30)	127.67 (28.70)	29.21 (1.15)	177.41 (39.89)	24.40 (1.50)	65.60
Beam No.14	49.78 (11.19)	7.62 (0.30)	152.16 (34.21)	29.21 (1.15)	186.76 (41.99)	57.15 (2.25)	74.31

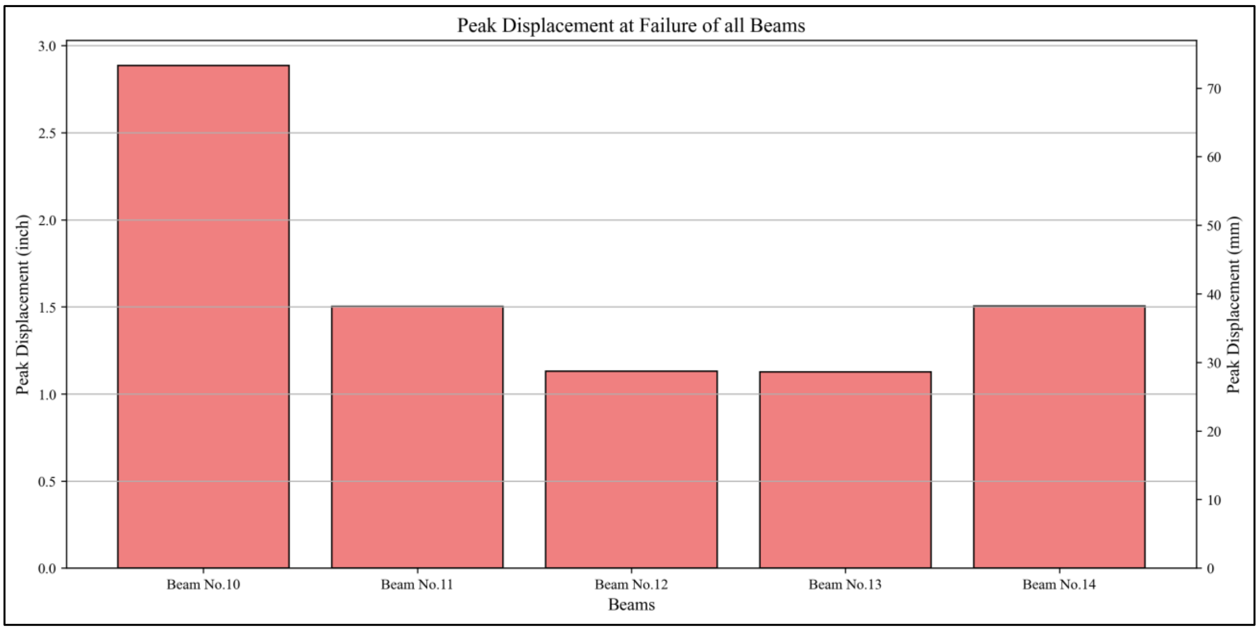

Figure 3.22. Peak displacement at failure for all beams

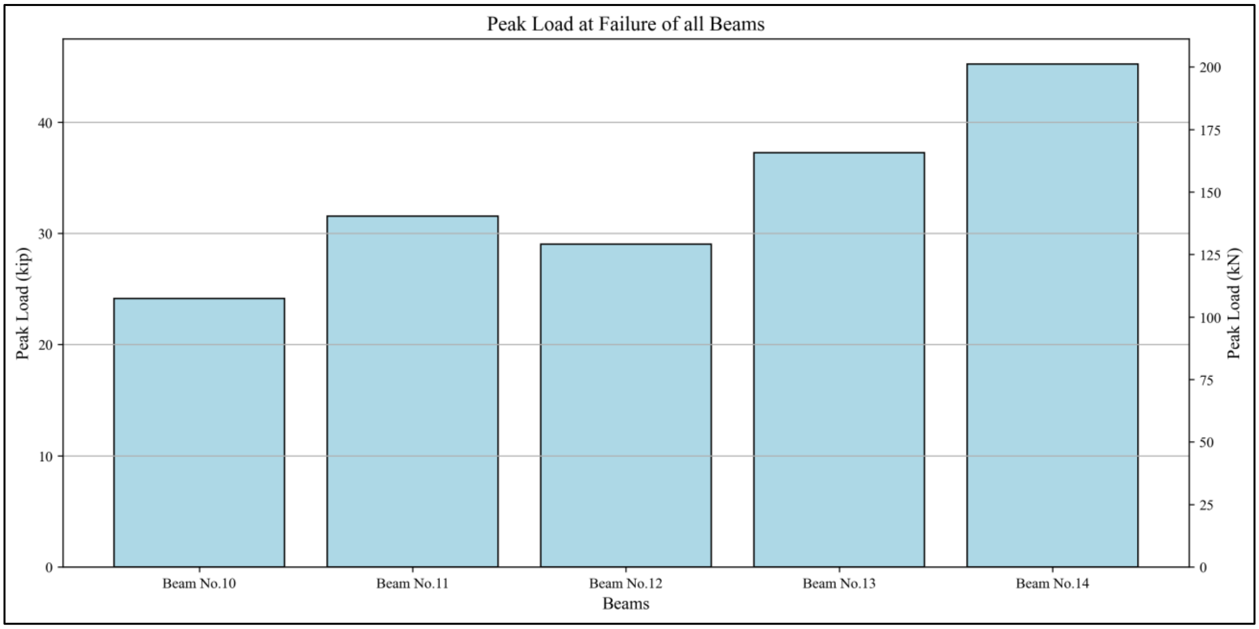

Figure 3.23. Peak ultimate load at failure for all beams

3.6. Phenomenological Modeling of Hysteresis Loops

This section provides information on the modeling of the hysteresis loops of beams No.11 and 12. A phenomenological model is developed based on the observations of the experimental data to simulate the hysteresis response of RC beams strengthened with longitudinal CFRP sheets. Various assumptions have been made to adequately predict the seismic behavior.

3.6.1. Assumptions

When modeling the hysteresis loops:

1. Each cycle is broken down into three linear regions in the unloading and reloading paths, respectively.
2. These linear regions are named push, inflection range, and pull direction in the unloading path and the reloading path, see Figure. 3.24.

3. The unloading push path has a similar slope to the reloading pull path. Accordingly, these two-line slopes are averaged together in the present model and are referred to as Region A, Figure. 3.24.
4. The unloading pull path has a comparable slope to the reloading push path, and they are, therefore, averaged together in this model and referred to as Region C, Figure. 3.24.
5. The inflection range, indicated as Region B, has similar slopes in the unloading and reloading bounds. Therefore, these two bounds are averaged.
6. To automate the model, curves correlating the ratio of slope variations of each region to the initial backbone curve slope on the x-axis vs. the backbone curve drift ratios at the envelope curve to that drift ratio at yielding on the y-axis are generated for all cycles throughout the response, Figure. 3.25. These three curves define the rules that the hysteresis loops behave in accordance with.

Using the assumptions above with the graphs of the three regions shown in Figure. 3.25, the complete set of hysteresis loops are defined for beam No.11, Figure. 3.26, and are used to reproduce the hysteretic response of beam No. 12 using the rules and graphs established for beam No. 11, Figure. 3.25. It is evident that the analytical hysteresis loops predicted in Figure. 3.26-Figure 3.27 are in agreement with the corresponding experimental loops.

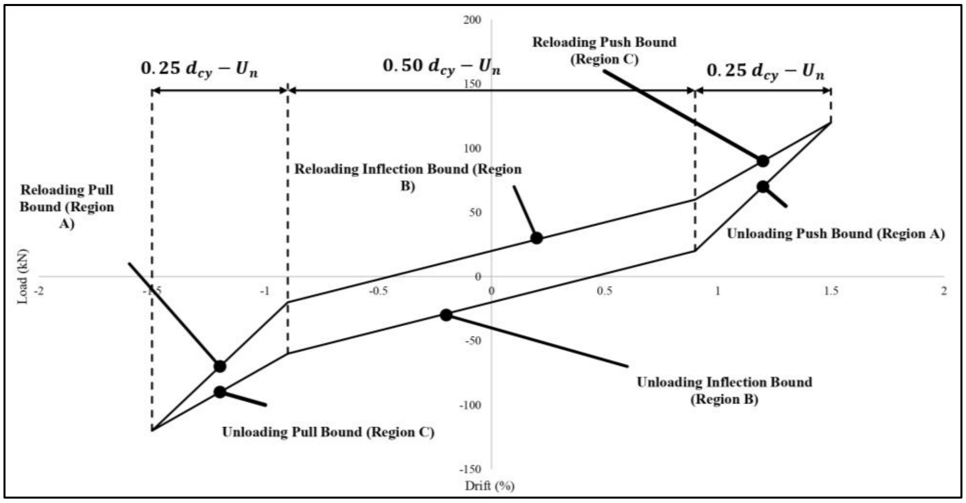

Figure 3.24. Three linear regions of the hysteresis loop model.

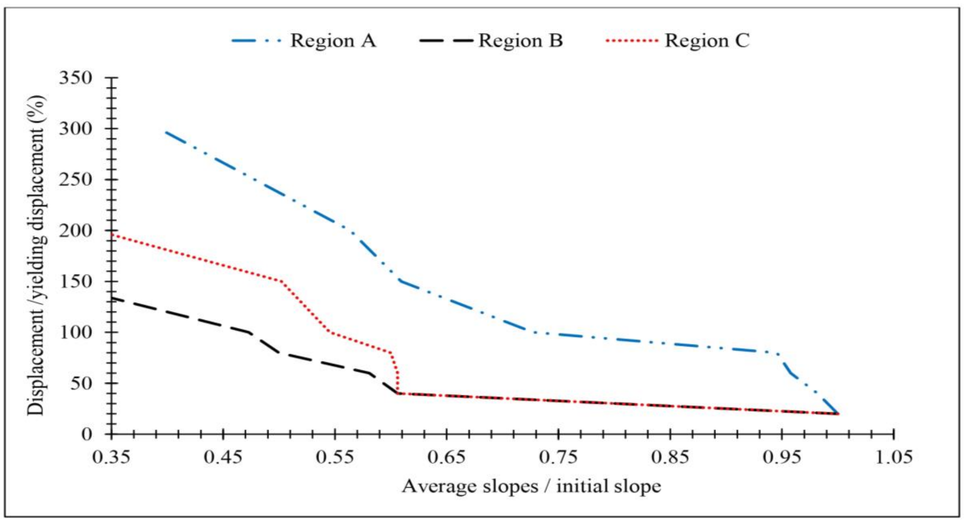

Figure 3.25. Regions a, b, c graphs to characterize the hysteresis loops beam No.11

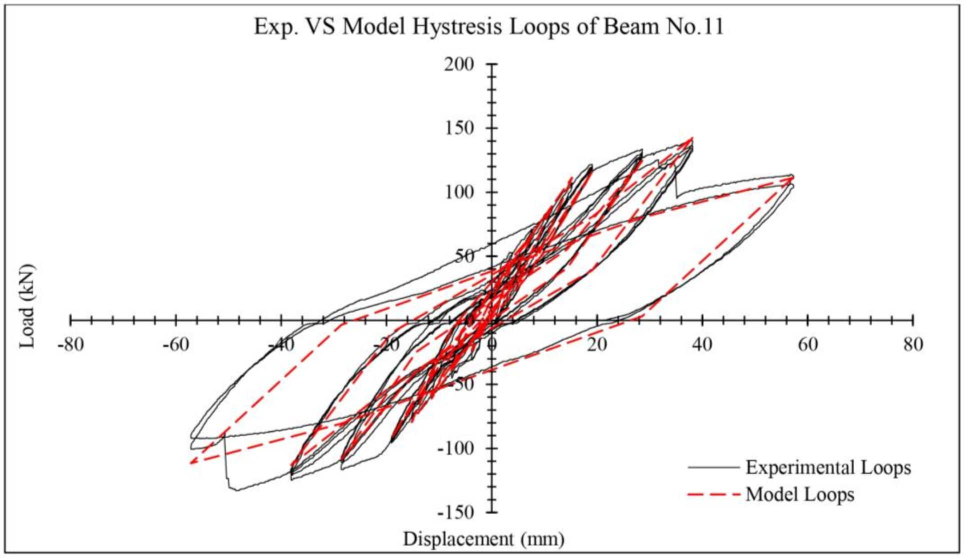

Figure 3.26. Experimental vs. modeled hysteresis loops for beam No.11 (1 Kips=4.45 KN)

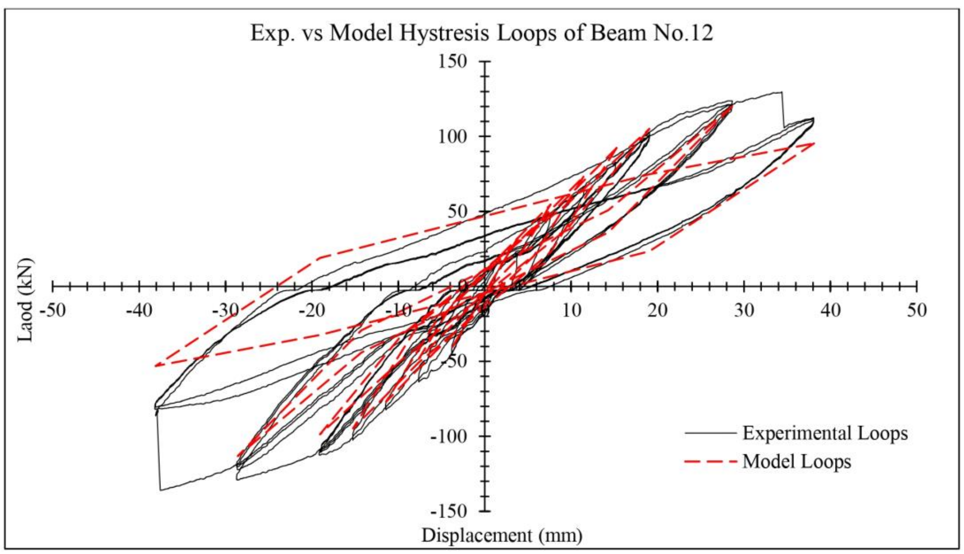

Figure 3.27. Experimental vs. modeled hysteresis loops for beam No.12 (1 Kips=4.45 KN)

3.7. Conclusions

In this chapter, a seismic investigation was performed on rectangular RC beams strengthened with thin and thick CFRP sheets to failure. Carbon fiber splay anchors were applied to twin beams with those of no anchors to determine the improvement in cyclic response, if any. The following conclusions may be drawn from this study:

1. The higher the CFRP thickness applied, the less energy dissipation and the more pinching is observed, leading to the conclusion that heavily strengthened RC beams with externally bonded CFRP will behave less favorably to anticipated seismic response.
2. The higher the CFRP thickness applied, the higher the ultimate loading capacity experienced, especially with the application of CFRP anchors. Conversely, the use of anchors with the thin CFRP layer resulted in no tangible benefit compared to the twin beam with no anchors.
3. Failure modes were controlled by CFRP rupture or debonding on the shear span side of the load point due to the current experimental setup forcing the clamped C channels above and below the beam at the load points to behave as rigid anchors.
4. The control beam had the highest ductility while the beam with an unanchored thin CFRP sheets had the second highest ductility. The beam with an unanchored thick CFRP sheets demonstrated the least ductility. It is important to note that the use of end anchors in the thin CFRP sheet beam reflected no benefit in behavior, while the use of two end anchors per shear span in the thick CFRP sheet beam illustrated a noticeable improved performance over the beam's unanchored twin.
5. In future testing, it will be important not to clamp the CFRP sheets at the load point with C clamps, but rather, bridge the CFRP sheets so they may debond freely.
6. The shear span must be strengthened with intermediate anchors to realize significant improvements in ultimate capacity, ductility, energy dissipation, and stiffness degradation compared to the twin specimens without anchors.

Chapter 4 - Analytical Modeling of the Envelope Curve and Phenomenological Depiction of Hysteretic Loops.

4.1. Introduction

The seismic response of reinforced concrete strengthened with FRP composites is an attractive research topic that has drawn significant attention of researchers during the last thirty years. Several research studies have been conducted and found that cyclic response of RC members can be enhanced by the application of FRP materials (Al-Salloum et al. 2007, Alsayed et al. 2010, Saqan et al. 2018, Saqan et al. 2020, and Alshamrani et al. 2024).

Nehdi and Said (2005) studied the performance of RC frames with hybrid reinforcement (steel and GFRP) under reversed cyclic loading. Joints reinforced with GFRP and subjected to reversed cyclic loading exhibited a significant reduction in plasticity features and low energy dissipation compared to joints with hybrid and steel reinforcement. The hybrid specimens resulted in stiffness lower than the typically reinforced joints but higher than those strengthened using GFRP only.

Golias et al. (2021) studied the application of X-Shaped CFRP ropes for structural upgrading of reinforced concrete beam–column joints under cyclic loading. Both the strength and seismic characteristics of specimens strengthened with CFRP ropes were improved when compared to the control specimen. Furthermore, the density of cracks as well as the width were reduced within the joints due to the use of CFRP ropes. At a drift ratio of 1.00%, all the strengthened specimens showed higher energy dissipation by about 60% compared to the control one. In summary, the use of CFRP ropes can enhance the ultimate load, energy dissipation under a small drift ratio, and overall seismic performance.

A more recent study conducted by Sawant and Jadhav (2022) examined the response of strengthened RC beams under cyclic loading. It was found that the use of CFRP strengthening technique can increase the ultimate load capacity in both directions of loading (forward and reverse loading).

However, there is a lack of available modeling to simulate the behaviors under cyclic load. A limited literature has been carried out to develop a suitable modeling technique to mimic such responses. Dowell et al. (1998) conducted a research study to predict the non-linear behavior of RC columns by developing a pivot hysteresis model. Based on the available experimental literatures, the model was established. The outputs of the experimental investigations observed that the unloading path returns to zero from any displacement level, extending to a singular point on the force-displacement graph known as the primary pivot point. Moreover, all force-displacement curves were found to meet at one pinching pivot point on the force-displacement graph as well. The study presented two parameters, $\boldsymbol{\alpha}$ and β, related to the primary pivot point and pinching pivot point, respectively, to regulate unloading stiffness and pinching characteristics.

An additional model was developed by Sharma et al. (2013) to predict the cyclic response of RC frame subjected to reversed cyclic load. Similar to Dowell et al. (1998) mode, this model utilized $\boldsymbol{\alpha}$ and β parameters from Dowell et al. model after an improvement in order to increase the ability and accuracy of the model in capturing the seismic response. According to the authors, $\boldsymbol{\alpha}$ and β are parameters that account for the influence of the transfer steel reinforcement as well as the amount of the applied axial load at the tip of the column on the pinching behavior of the frame. Further parameters were presented in order to consider the impacts of the exterior joints that are not seismically reinforced. The comparison of the model prediction to the experimental showed very good agreement.

In this chapter, a trilinear load-displacement model that was developed by Charkas et al. (2003) for monotonic loading was utilized for the strengthened beams from chapters 3 and 4 to capture the load-displacement envelope curve and showed an excellent agreement compared to the experimental response. Furthermore, a phenomenological hysteresis loop model developed by (Alshamrani et al. 2024) for RC frame assembly was used in order to predict the cyclic response of RC beams strengthened with CFRP with and without fiber anchors. The phenomenological model was based on careful observations of the experimental results leading to identifying 3 distinct zones of the hysteresis cycles. The decrease in stiffness during unloading and reloading, as a percentage of the initial stiffness, is compared to the drift ratio, expressed as a percentage of the drift ratio at the yielding point. The boundaries of the three zones were identified based on experimental observations as well. This treatment resulted in a simplified yet unique cyclic response model for reinforced concrete beams strengthened with CFRP that was applied blindly to other specimens with similar strengthening features reflecting good correspondence.

4.2. Analysis of the Envelope Curves

To predict the envelope curve response of the tested specimens, a trilinear load-displacement model that was developed by (Charkas et al. 2003) for monotonic loading was utilized. According to this model, the Moment-Curvature analysis was approximated by a trilinear curve. In fact, this curve is controlled by three key points as follows:

4.2.1. Cracking Point:

The first point of the trilinear curve can be easily computed using the following equations:

$$M_{cr} = \frac{f_r \, I_{gt}}{y_t} \tag{18}$$

$$\emptyset_{cr} = \frac{f_r}{E_c \, y_t} \tag{19}$$

Where:

$f_r = 7.5\sqrt{f'_c}$ in psi or $f_r = 0.62\sqrt{f'_c}$ in MPa .

Ec is modulus of elasticity of concrete.

I_{gt} is gross transformed section moment of inertia.

y_t is the centroid depth of the section to the extreme tension fiber.

4.2.2. Yielding Point:

To predict the yielding point of the trilinear curve, the following equations are used:

$$\left[\frac{\frac{\varepsilon_y * c_y}{d-c_y}}{\varepsilon\prime_c} - \frac{\left(\frac{\varepsilon_y * c_y}{d-c_y}\right)^2}{3\varepsilon\prime_c^2}\right] f'_c\, B\, c_y + A'_s\, E_s\, \frac{\varepsilon_y}{d-c_y}\left(c_y - d'\right) - A_s f_y + A_f E_f \frac{\varepsilon_y}{d-c_y}\left(d_f - c_y\right) = 0 \tag{20}$$

$$M_y = A_s f_y \left(d - \left(0.5\,\hat{\beta}_1\, c_y\right)\right) + A_f E_f \varepsilon_{fe} \left(d_f - \left(0.5\,\hat{\beta}_1\, c_y\right)\right) + A'_s\, E_s\, \varepsilon'_s \left(0.5\,\hat{\beta}_1\, c_y - d'\right) \tag{21}$$

$$\phi_y = \frac{\varepsilon_y}{d - c_y} \tag{22}$$

Where:

$$\varepsilon'_s = \frac{\varepsilon_y}{(d-c_y)(c_y-d\,)} \tag{23}$$

$$\varepsilon_{fe} = \frac{\varepsilon_y}{d-c_y} * \left(d_f - c_y\right) \tag{24}$$

$$\varepsilon_{cf} = \frac{\varepsilon_y * c_y}{d-c_y} \tag{25}$$

$$\alpha = \frac{\varepsilon_{cf}}{\varepsilon\prime_c} - \frac{\varepsilon_{cf}^2}{3\varepsilon'^2_{cf}} \tag{26}$$

$$\hat{\beta} = \frac{\frac{1}{3} - \frac{\varepsilon_{cf}}{12 * \varepsilon\prime_c}}{1 - \left(\frac{\varepsilon_{cf}}{3 * \varepsilon\prime_c}\right)} \tag{27}$$

$$\hat{\beta}_1 = 2 * \hat{\beta} \tag{28}$$

4.2.3. Ultimate Point:

This model was modified to capture the three different failure modes of strengthened RC beams, including crushing, debonding, and rupture failure as demonstrated below. Similar force equilibrium equations, to that presented above for the yielding point, are used to solve for the neutral axis location at the ultimate point based on the various failure modes considered.

4.2.3.1. Crushing failure:

$$M_{nc} = A_s f_y(d - (0.5 * \hat{\beta}_1\, c_{nc})) + A_f E_f \varepsilon_{fe}(df - (0.5 * \hat{\beta}_1\, c_{nc}))) + A'_s E_s \varepsilon'_s((0.5 * \hat{\beta}_1\, c_{nc}) - d')) \quad (29)$$

$$\phi_{nc} = \frac{\varepsilon_{cu}}{c_{nc}} \quad (30)$$

4.2.3.2. Debonding failure:

$$M_{nd} = A_s f_y(d - (0.5 * \hat{\beta}_1\, c_{nd})) + A_f E_f \varepsilon_{fu}(df - (0.5 * \hat{\beta}_1\, c_{nd}))) + A'_s E_s \varepsilon'_s((0.5 * \hat{\beta}_1\, c_{nd}) - d')) \quad (31)$$

$$\phi_{nc} = \frac{\varepsilon_{fu}}{df - c_{nd}} \quad (32)$$

4.2.3.3. Rupture failure:

$$M_{nr} = A_s f_y(d - (0.5 * \hat{\beta}_1\, c_{nr})) + A_f E_f \varepsilon_{fu}(df - (0.5 * \hat{\beta}_1\, c_{nr}))) + A'_s E_s \varepsilon'_s((0.5 * \hat{\beta}_1\, c_{nr}) - d')) \quad (33)$$

$$\phi_{nr} = \frac{\varepsilon_{fu}}{df - c_{nr}} \quad (34)$$

Based on the analytical results, it is worth mentioning that the present model does not account for the extra contribution of carbon fiber splay anchors. Thus, it is expected that the model will yield similar results for specimens No.2, and No.3 as well as No.4 and No.5. Likewise, beams No. 11 and No. 12, along with No. 13 and No. 14, are expected to exhibit identical predictions. However, the expected values have excellent agreement with the experimental ones. This is simply because the fiber anchors in these tests had a minor contribution since they were only applied at the sheet ends. The analytical yielding load for beam No.2 was predicted to be 80.92 kN (18.19kips) while the actual yielding load was measured to be 81.85 kN (18.40 kips) showing an excellent agreement.

Furthermore, the expected cracking loads for all specimens showed a strong agreement with experimental data. The observation of the comparison adds further evidence to the precision and consistency of the current model in capturing the envelope curve of cyclic responses of RC beams, both with and without CFRP strengthening. Table 2.9, and Figure. 4.1. to Figure. 4.10. illustrate the comparison between the proposed model and the results obtained from experimental data.

Table 4.1. Comparison of average experimental results against analytical predictions.

Specimen	Average experimental results			Analytical results		
	Cracking load kN (Kips)	Yielding load kN (Kips)	Ultimate load kN (Kips)	Cracking load kN (Kips)	Yielding load kN (Kips)	Ultimate load kN (Kips)
Beam No.1	38.03 (8.55)	67.87 (15.26)	107.41 (24.15)	31.14 (7.00)	57.83 (13.00)	80.07 (18.00)
Beam No.2	34.47 (7.75)	80.92 (18.19)	114.4 (25.72)	33.36 (7.50)	81.85 (18.40)	102.31 (23.00)
Beam No.3	31.26 (7.03)	79.75 (17.93)	114.46 (25.73)	33.36 (7.50)	81.85 (18.40)	102.31 (23.00)
Beam No.4	34.12 (7.67)	114.34 (25.71)	150.20 (33.77)	36.03 (8.10)	116.54 (26.20)	133.45 (30.00)
Beam No.5	33.36 (7.50)	130.93 (29.44)	157.43 (35.39)	36.03 (8.10)	116.54 (26.20)	133.45 (30.00)
Beam No.10	34.85 (7.83)	91.86 (20.65)	105.17 (23.64)	35.67 (8.02)	95.77 (21.53)	103.64 (23.30)
Beam No.11	41.97 (9.44)	107.51 (24.17)	134.11 (30.15)	35.94 (8.08)	115.92 (26.06)	151.60 (34.08)
Beam No.12	48.86 (10.86)	110.62 (24.87)	132.37 (29.76)	35.94 (8.08)	115.92 (26.06)	151.60 (34.08)
Beam No.13	52.46 (11.79)	130.61 (29.36)	175.60 (39.48)	37.81 (8.50)	162.05 (36.43)	196.03 (44.07)
Beam No.14	63.60 (14.30)	153.57 (34.52)	200.73 (45.13)	37.81 (8.50)	162.05 (36.43)	196.03 (44.07)

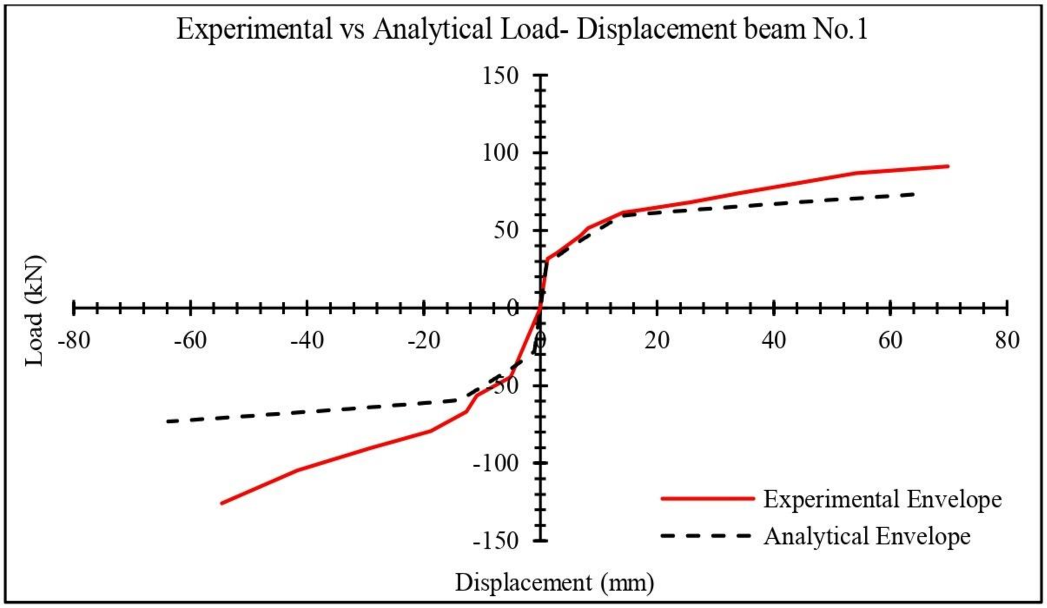

Figure 4.1. Analytical vs. Experimental Envelope Curve Comparison of beam No.1

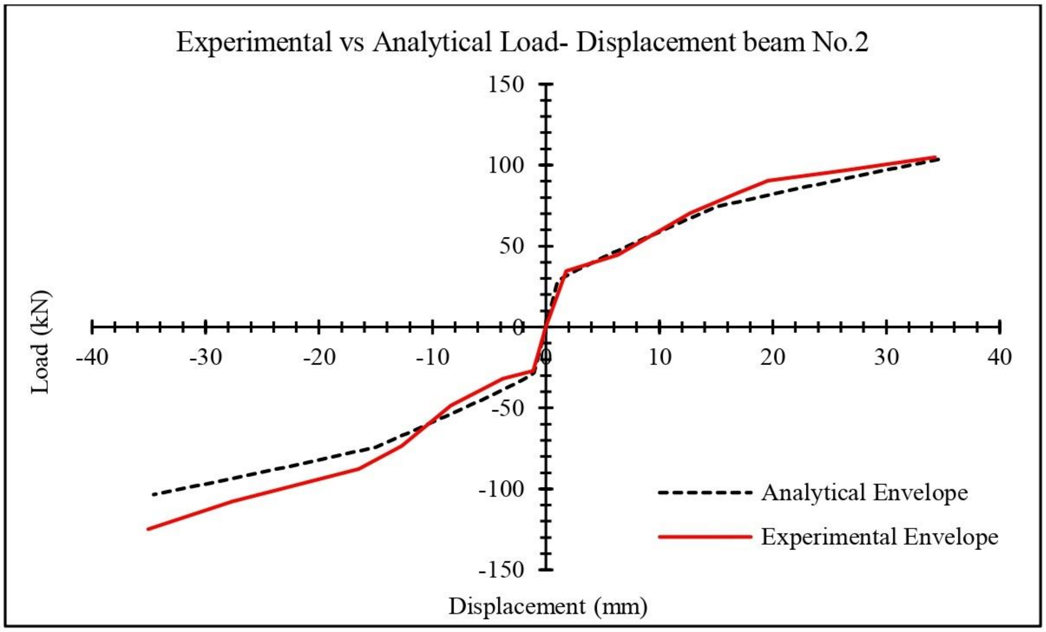

Figure 4.2. Analytical vs. Experimental Envelope Curve Comparison of beam No.2

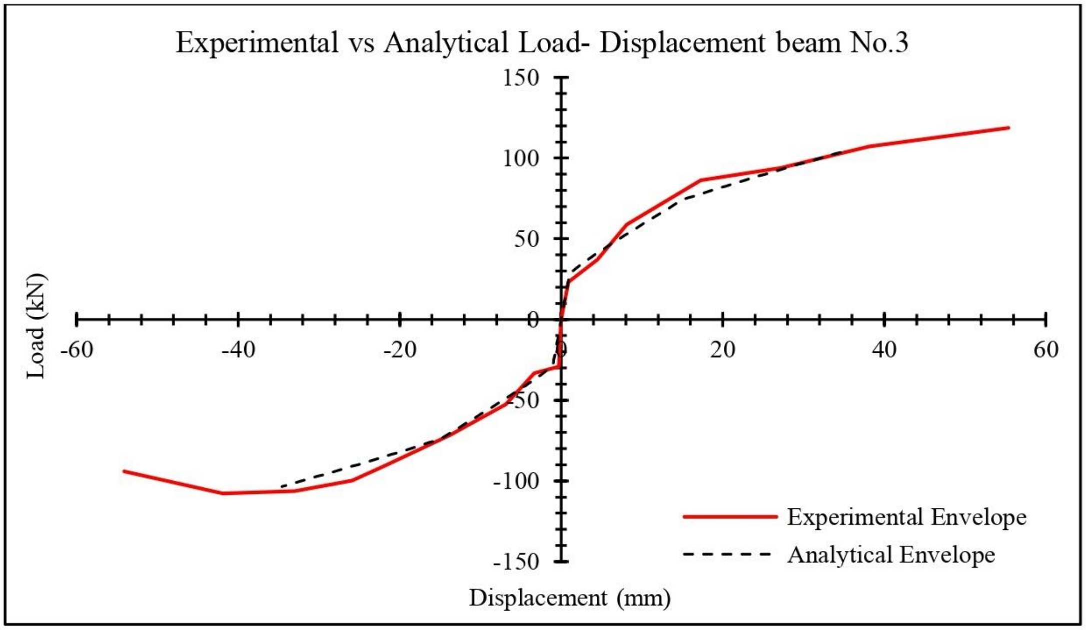

Figure 4.3. Analytical vs. Experimental Envelope Curve Comparison of beam No.3

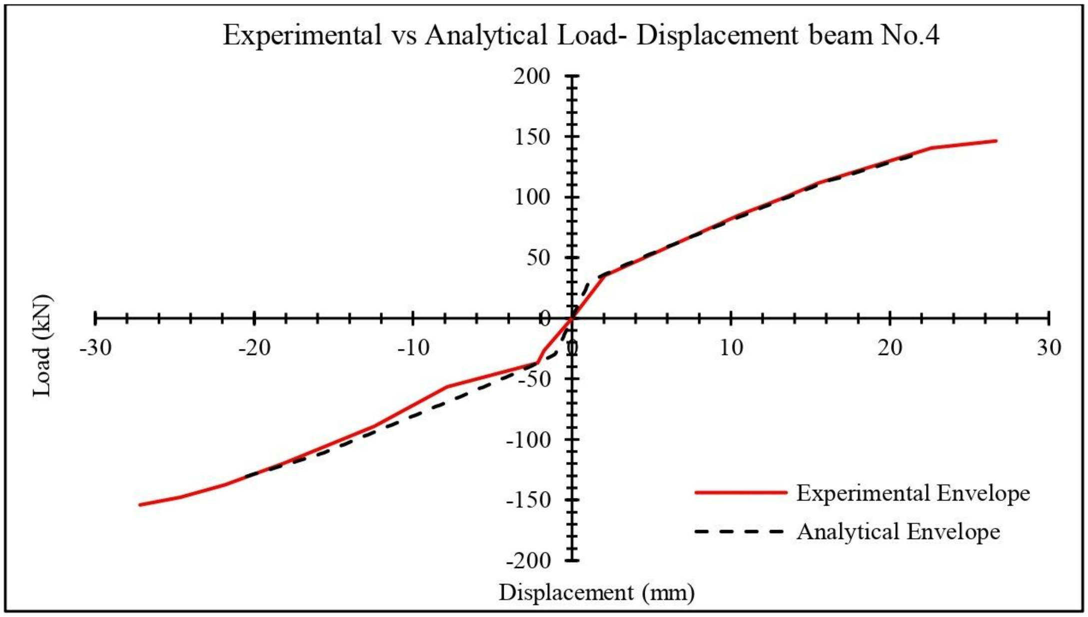

Figure 4.4. Analytical vs. Experimental Envelope Curve Comparison of beam No.4

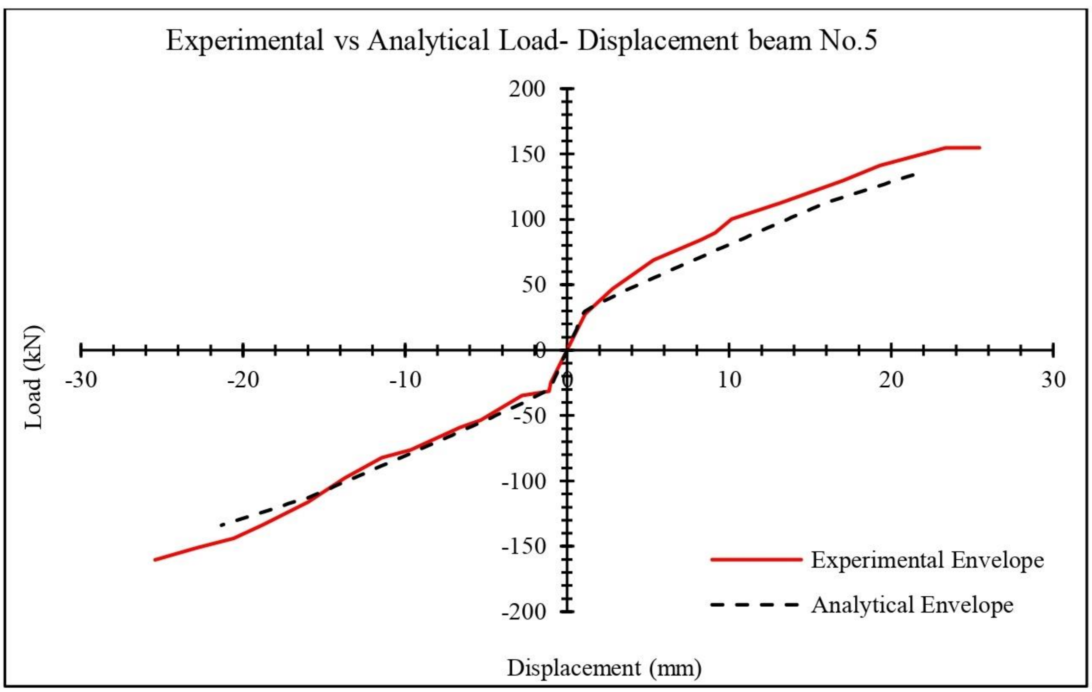

Figure 4.5. Analytical vs. Experimental Envelope Curve Comparison of beam No.5

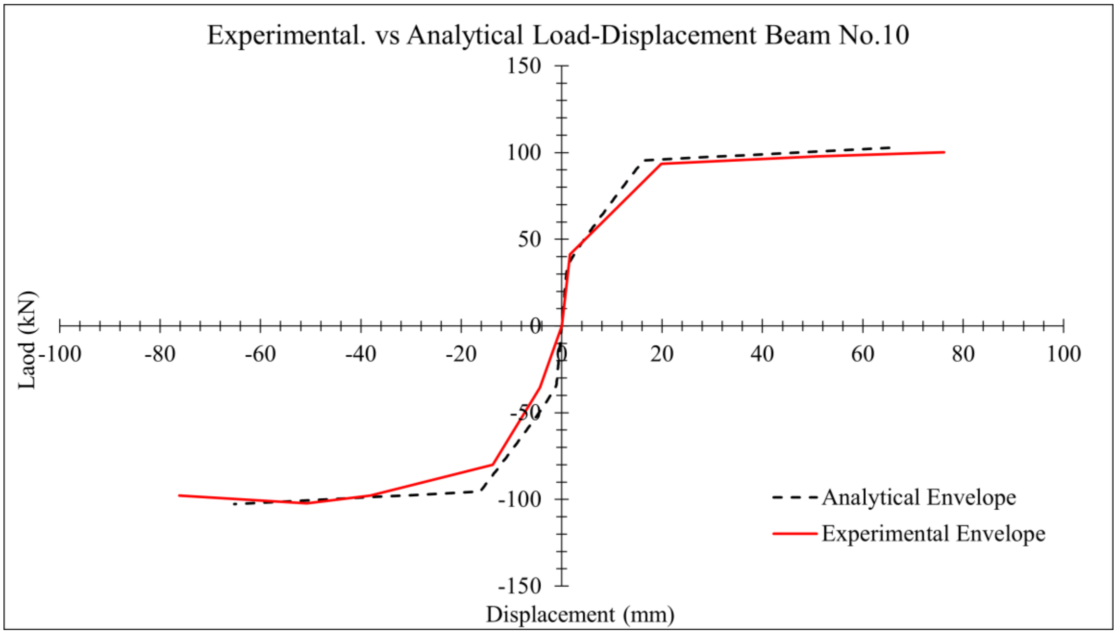

Figure 4.6. Analytical vs. Experimental Envelope Curve Comparison of beam No.10

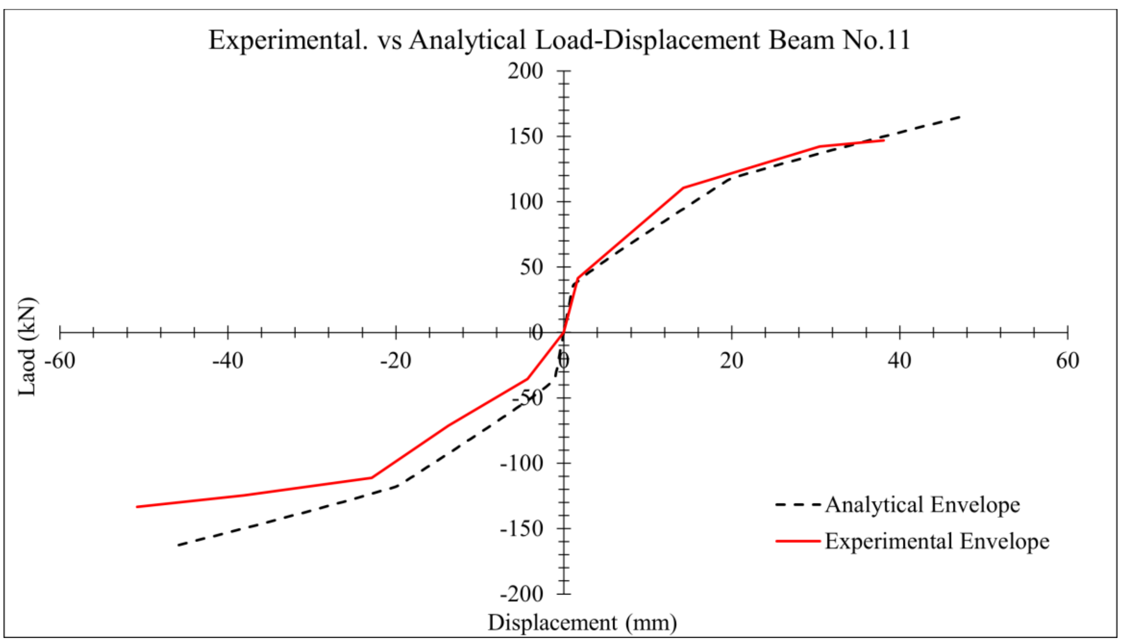

Figure 4.7. Analytical vs. Experimental Envelope Curve Comparison of beam No.11

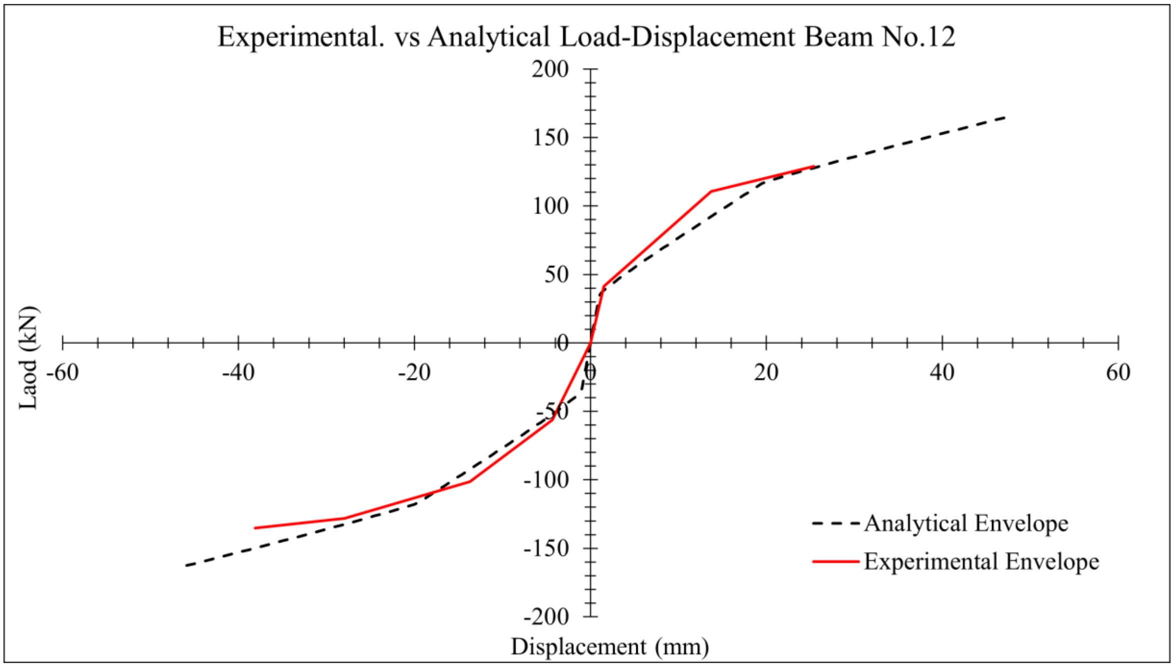

Figure 4.8. Analytical vs. Experimental Envelope Curve Comparison of beam No.12

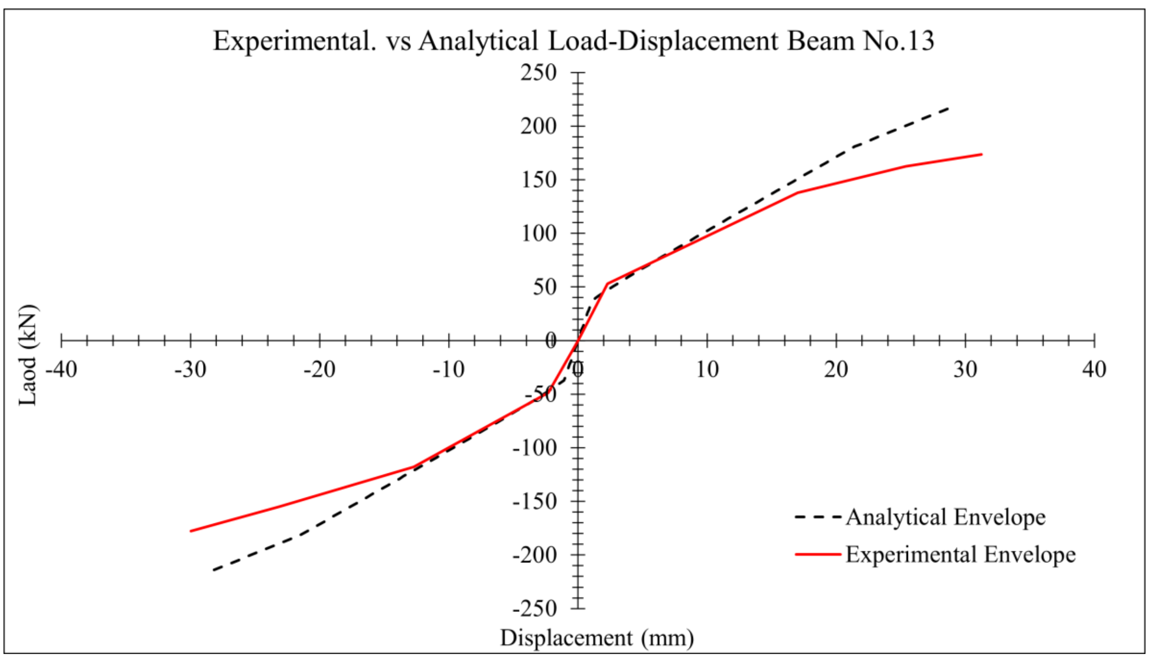

Figure 4.9. Analytical vs. Experimental Envelope Curve Comparison of beam No.13

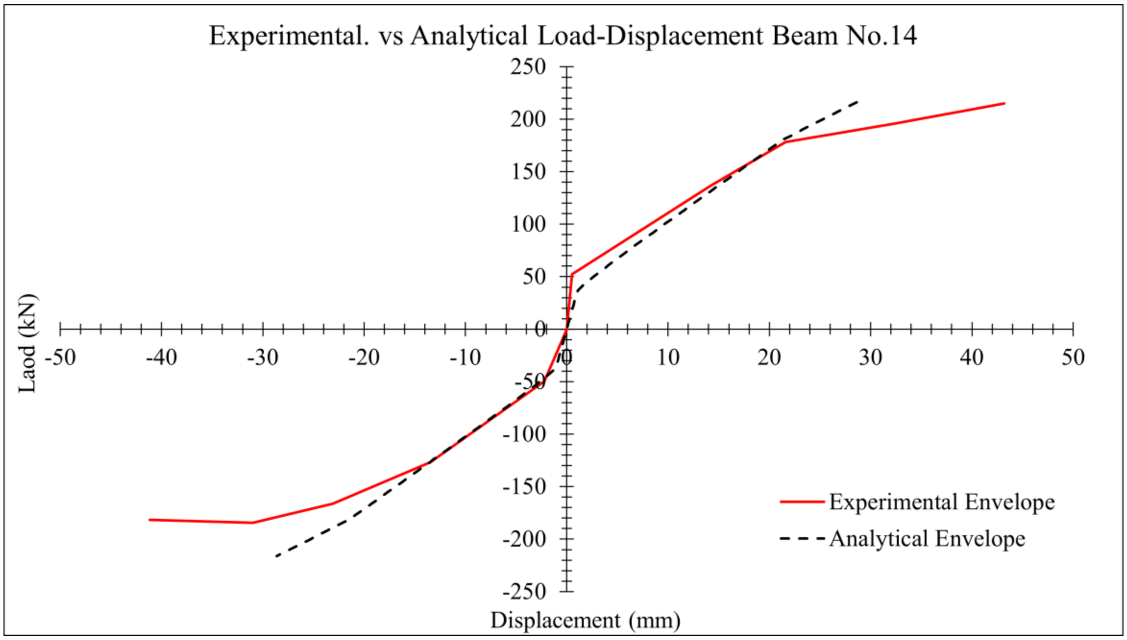

Figure 4.10. Analytical vs. Experimental Envelope Curve Comparison of beam No.14

4.3. Hysteresis Loops Model

When modeling the hysteresis loops, each cycle is broken down into three linear regions in the unloading and reloading paths, respectively. These linear regions are named push, inflection range, and pull side in the unloading path as well as the reloading path, see Figure 4.11. It is observed that the unloading push path has a very similar slope to the reloading pull path. Accordingly, these two-line slopes are averaged together in the present model and are referred to as Region A, Figure 4.12. Similarly, the unloading pull path has a comparable slope to the reloading push path, and they are, therefore, averaged together in this model and referred to as Region C, Figure 4.12. Also, the inflection range, indicated as Region B, has similar slopes in the unloading and reloading bounds. Therefore, these two bounds are averaged here as well. To automate the model, curves correlating the ratio of unloading and reloading push slope variations to the initial backbone curve slope on the x-axis vs. the backbone curve drift ratios at the envelop curve to that drift ratio at yielding on the y-axis are generated for all cycles throughout the response, Figure 4.13. These three curves define the rules that the hysteresis loops behave in accordance with. For example, the drift ratio of the yielding point on the envelope curve (100% value of the y-axis) corresponds to a 0.75 slope ratio for region A, 0.47 slope ratio for region B and 0.55 slope ratio for region C, Figure 4.13. This formulation is used consistently for all cycles of load-drift ratio when reconstructing the hysteresis loops of specimen No.11. Likewise, specimen No.13 has similar graphs developed for that calibration in Figure 4.14. Finally, the three-line slopes extracted from Figure 4.13 or Figure 4.14 extend to drift ratio pivot points (on the drift axis) based on the following equations, Figure 4.11 and Figure 4.12:

$$d_{push-Un} = d_{pull-Re} = 25\% \; of \; d_{cy-Un} \tag{35}$$

$$d_{ir-Un} = d_{ir-Re} = 50\% \; of \; d_{cy-Un} \tag{36}$$

$$d_{push-Re} = d_{pull-Un} = 25\% \; of \; d_{cy-Un} \tag{37}$$

Where:

$d_{push-Un}$ *is* Unloading push side shift on the x − axis (drift axis) of the hysterisis loop.

$d_{pull-Re}$ *is* Reloading pull side shift on the x − axis (drift axis) of the hysterisis loop.

d_{cy-Un} *is* the total drift width on the x − axis (drift axis) of the hysterisis loop.

d_{ir-Un} *is* Unloading Inflection range shift along the x − axis (drift axis) of the hysterisis loop.

d_{ir-Re} *is* Reloading Inflection range shift along the x − axis (drift axis) of the hysterisis loop.

$d_{pull-Un}$ *is* Unloading pull side shift along the x − axis (drift axis) of the hysterisis loop.

$d_{push-Re}$ *is* Reloading push side shift along the x − axis (drift axis) of the hysterisis loop.

By using these formulations, the hysteresis loop responses of beam No.11 and No.13 were accurately reconstructed for the entire cyclic loading range.

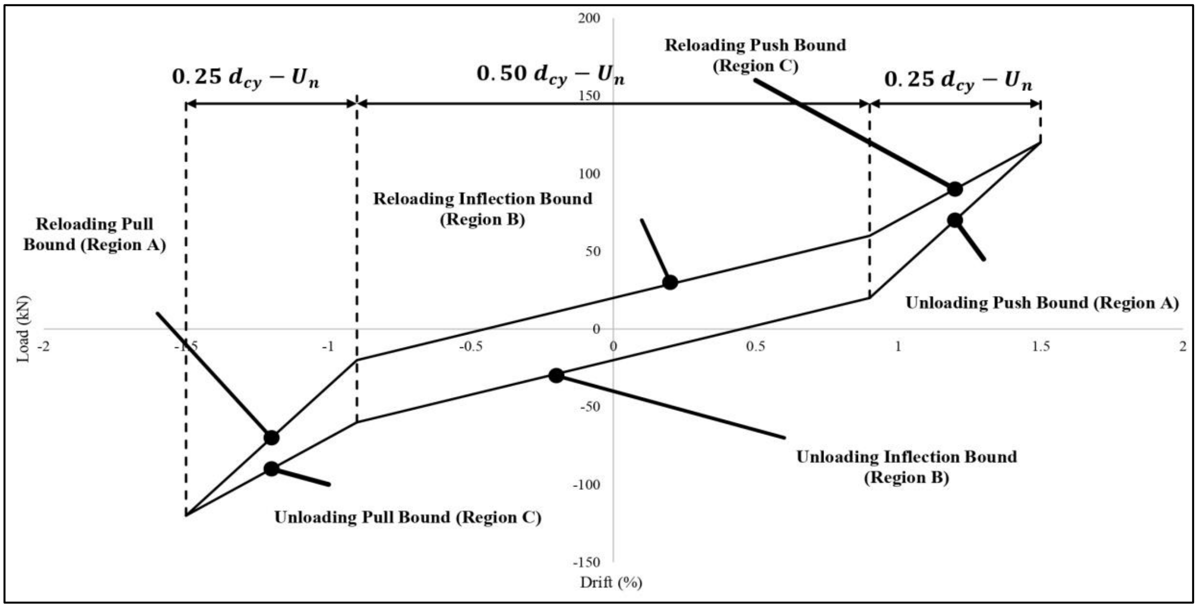

Figure 4.11. Three Linear Regions of The Hysteresis Loop Model.

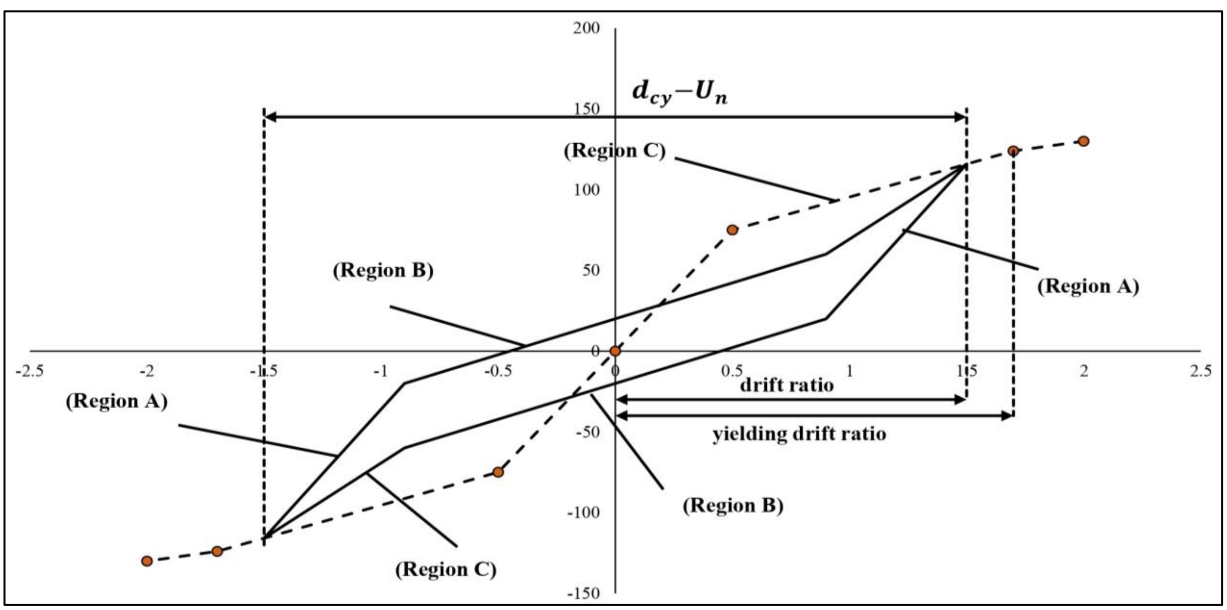

Figure 4.12. Hysteresis Regions Relative to The Backbone Curve.

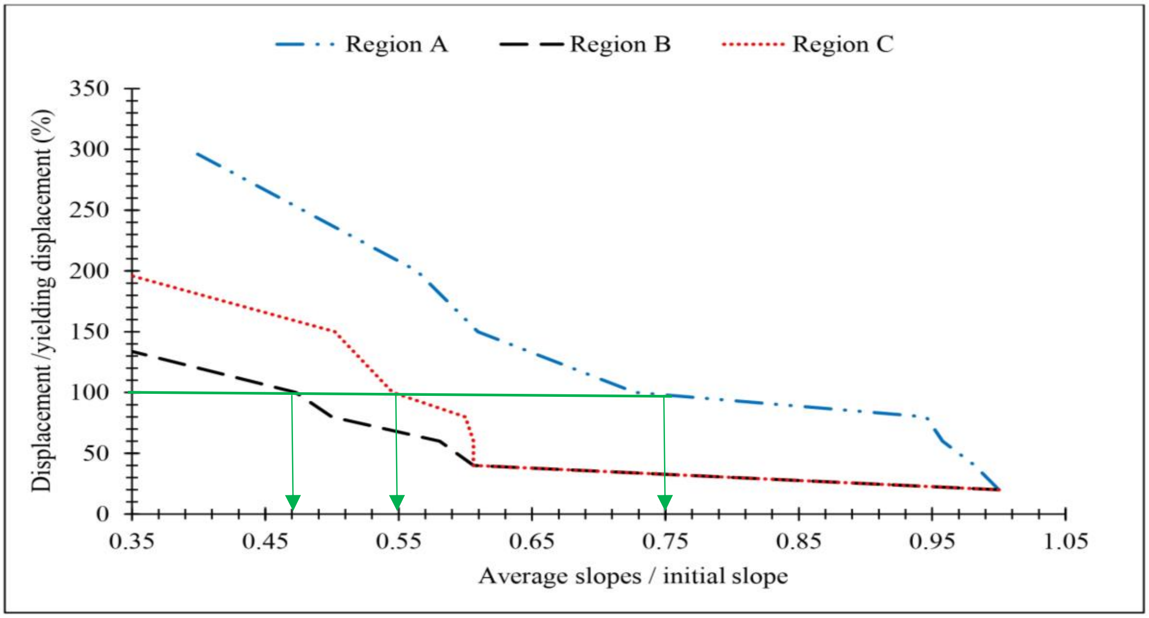

Figure 4.13. Regions A, B, C Graphs to Characterize the Hysteresis Loops beam No.11.

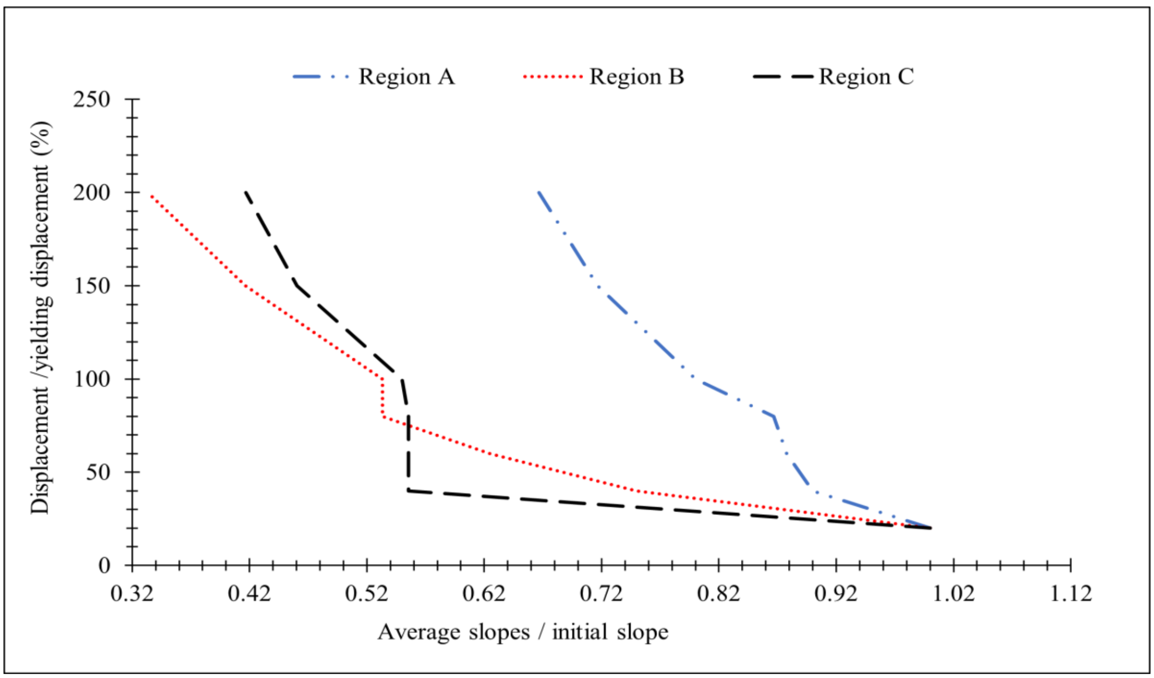

Figure 4.14. Regions A, B, C Graphs to Characterize the Hysteresis Loops beam No.13.

4.3.1. Analysis Steps

The synthesis of the hysteresis loops can be re-produced based on the following steps for a single hysteretic cycle:

1. Identify the departure point from the envelope curve of the load-deflection response on the push side, which is assumed on average to be similar to that on the pull side.
2. Use Figure 4.13 or Figure 4.14 to extract the slope of the unloading line on the push side, which is the same as the reloading line of the pull side (region A), see Figure 4.11.
3. Use Figure 4.13 or Figure 4.14 to extract the slope of the inflection unloading bound on the push side, which is the same as the inflection reloading bound of the pull side (region B), see Figure 4.11.
4. Use Figure 4.13 or Figure 4.14 to extract the slope of the unloading push bound, which is the same as the reloading pull bound (region C), see Figure 4.11.
5. Define the boundaries of each region using vertical lines drawn at the inflection points shown in Figure 4.11.

4.3.2. Model Calibration

The hysteresis model rules, developed herein based on the phenomenological formulation of RC frame assemblies strengthened with CFRP, produced a load-drift ratio hysteresis loop curves using the data in Figure 4.13 and Figure 4.14. Therefore, the hysteresis loops of beam No.11 were derived based on the slope variations in Figure 4.13 resulting in good agreement to the ones obtained experimentally as reflected in Figure 4.15. It can be observed that the hysteresis loops in the post-cracking region show excellent correspondence to the experimental loops while the analytical loops in the post-yielding region reflect a very slight deviation. Similarly, the hysteresis loops of beam No.13 were derived based on the slope variations in Figure 4.14 resulting in good agreement to the ones obtained experimentally as reflected in Figure 4.16. It can also be observed that the hysteresis loops in the post-cracking region show excellent correspondence to the experimental loops while the analytical loops in the post-yielding region reflect a very slight deviation.

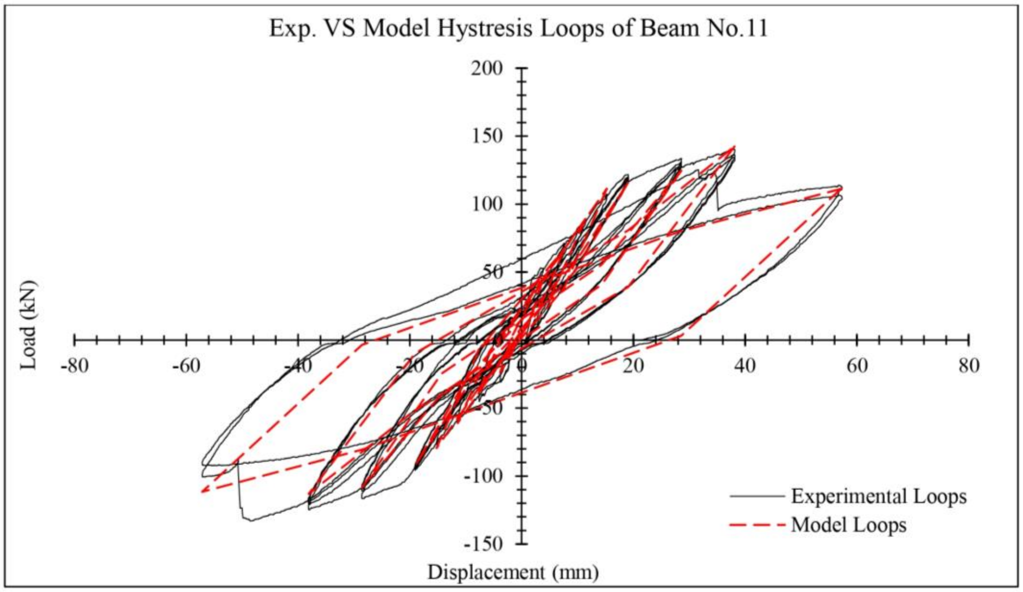

Figure 4.15. Experimental vs. modeled hysteresis loops for beam No.11 (1 Kips=4.45 KN)

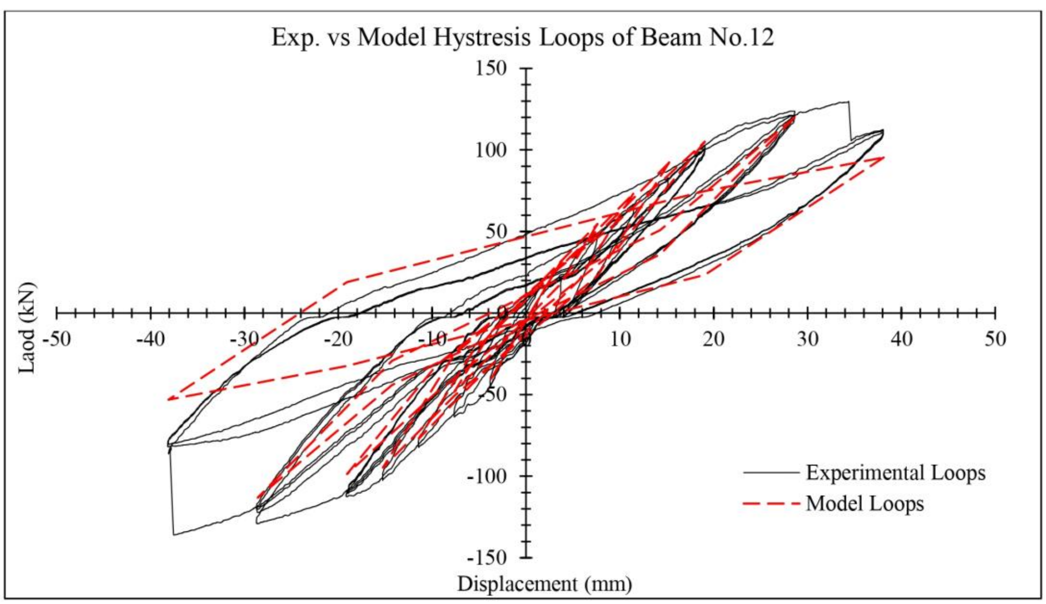

Figure 4.16. Experimental vs. modeled hysteresis loops for beam No.12 (1 Kips=4.45 KN)

4.3.3. Model Verification

The hysteretic behavior model used to predict the hysteresis loops is then used to predict its blind applicability on other sets of experimental data. For this purpose, the load-drift ratio for beam No.12 and No.14 are used to compare against the phenomenological predictions of beam No.11 and No.13 from Figure 4.13 and Figure 4.14, respectively, and showed an excellent agreement as reflected in Figure 4.17 and Figure 4.18 . Accordingly, the present phenomenological model is benchmarked against other experiments sharing general features. Further validations were carried out to investigate the accuracy of the present model by calculating the experimental and analytical energy dissipation of each beam. The results showing an excellent agreement between the experimental and analytical energy dissipation, see Figure 4.19.

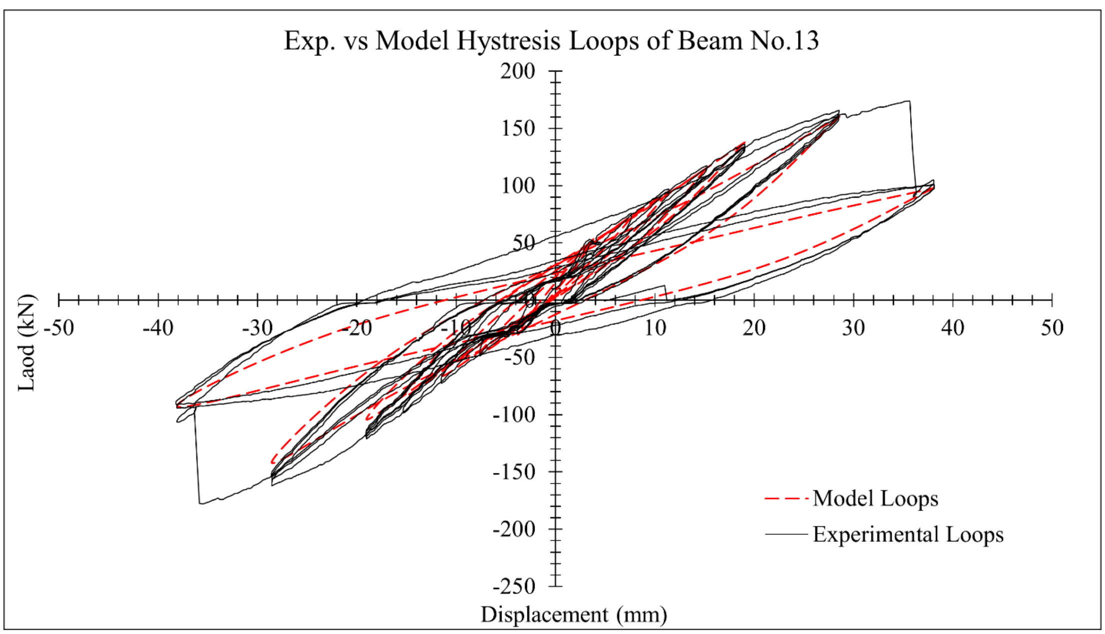

Figure 4.17. Experimental vs. modeled hysteresis loops for beam No.11 (1 Kips=4.45 KN)

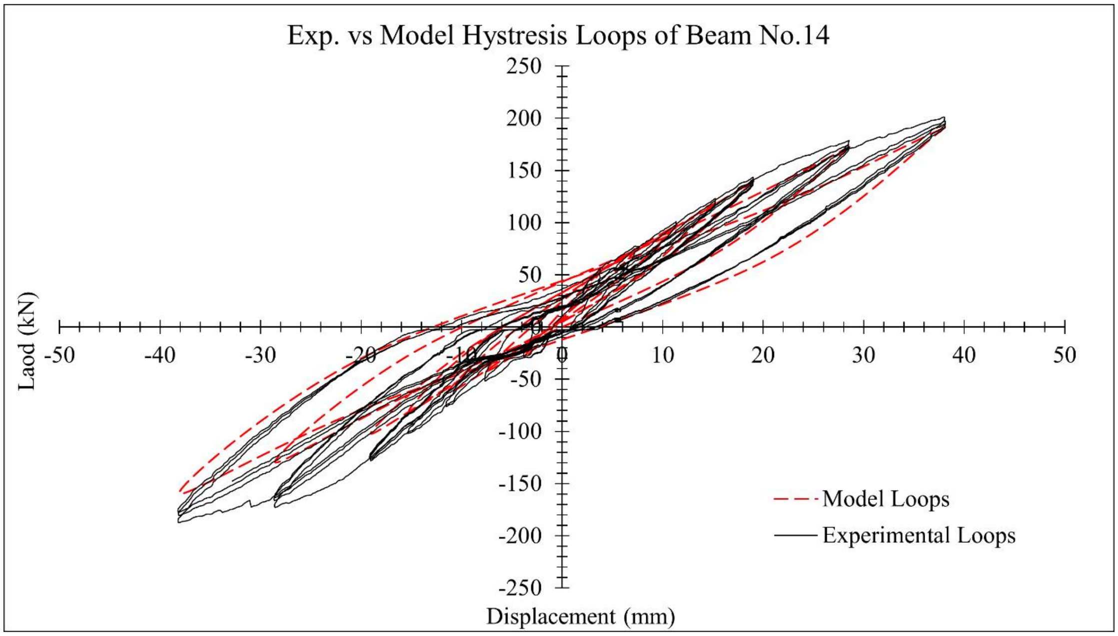

Figure 4.18. Experimental vs. modeled hysteresis loops for beam No.11 (1 Kips=4.45 KN)

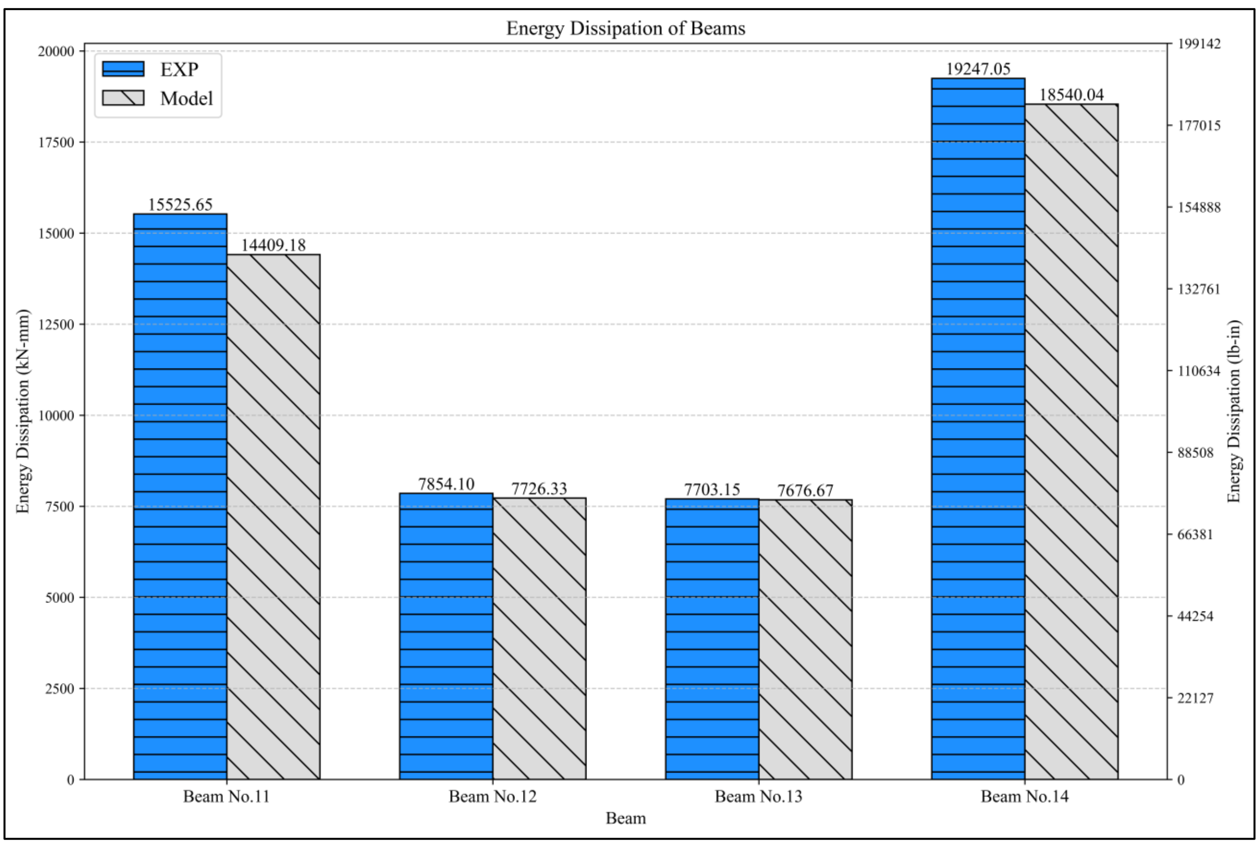

Figure 4.19. Experimental vs. modeled energy dissipation for all beams.

4.4. Conclusions

In this chapter, a trilinear moment-curvature approach, developed by (Charkas et al. 2003), is used to determine the full nonlinear load-deflection response for reinforced concrete beams strengthened with CFRP. Excellent agreement was observed between the envelope curves developed for these beams and the experimental envelope curves. Furthermore, a phenomenological hysteretic load-deflection model is postulated in this work using observations of the experimental hysteresis loops for two beams to calibrate the key parameters controlling the model layout. It was observed that hysteresis loops were very accurately depicted by applying a three-region model while building master curves for the degradation in the slopes of these regions as the load increases. Furthermore, it was noted that the drift span within each cycle can be made of 25%-50%-25% of the entire cycle drift range for the unloading-inflection-reloading regions, which was implemented as an integral part of the current model. This model was applied to two other two beams sharing similar strengthening features to those used in model calibration illustrating excellent correspondence after blind comparisons. The verifications performed reflect very good promise for this model in capturing the shape of the envelope curve as well as the hysteresis loops at different levels of loading, which may be easily extended to other structural systems. Being a phenomenological hysteresis model, it may be only possible to extend to other structural systems and applications after some general or basic modifications or improvements. This is anticipated to be true for almost all models built upon experimental data. It is expected that the calibrated normalized slope degradation curves for region A-C to be applicable to case of similar CFRP flexural ratio ($\rho_f = \frac{A_f}{bd}$). This poses a limitation on the applicability of these degradation graphs to the range of CFRP ratios covered by the present experiments.

Chapter 5 - Cyclic Response of RC Beams Strengthened and Anchored Using CFRP with and without Steel Fuse.

5.1. ABSTRACT

CFRP strengthening with fiber anchors has been recently proven to be an effective technique for seismic upgrades. However, the use of multiple layers of thick CFRP sheets may pose questionable applicability in seismic strengthening due to the limited ductility and energy dissipation characteristics of this solution. A recent patent concept suggests the use of a small steel plate as a ductility fuse by sandwiching it in between two layers of FRP at the critical plastic hinge region. This study applies the proposed technique herein to cyclic testing of RC beams to allow for more ductile seismic response. This steel ductility fuse approach was compared with an identical control strengthened beam without the steel fuse to highlight the benefit of this solution. Comparisons are performed experimentally for low and high concrete strength with low and moderate steel ratios. The results are comparatively discussed.

Keywords: Seismic strengthening; Carbon fiber anchors; CFRP sheets; Steel fuse; Backbone curve; Energy dissipation.

5.2. Introduction

The behavior of reinforced concrete (RC) structures strengthened with carbon fiber reinforced polymer (CFRP) under reversed cyclic loading has received limited research attention and understanding. The majority of previous studies have focused on the behaviors of RC members strengthened with CFRP under monotonic loading (Dong et al. 2012, Dias et al. 2018, Zaki et al. 2020, Alabdulhady et al. 2022, Abdalla et al. 2022, Liu et al. 2023 and Codina et al. 2024).

Therefore, there is a need to better understand the seismic response of these strengthened RC members, as cyclic loading conditions, such as those induced by earthquakes, can significantly affect the structural performance and durability of RC elements.

There is a growing interest in investigating the effectiveness of strengthening techniques, with carbon fiber reinforced polymer emerging as a promising material for stabilizing and enhancing the performance of RC structures. CFRP offers advantages such as a high strength-to-weight ratio, corrosion resistance, and ease of installation, making it a suitable candidate for strengthening applications (Lee and Jain 2009, Siddika et al. 2020, Sbahieh et al. 2022a, Sbahieh et al. 2022b, Vijayan et al. 2023). Furthermore, there is a lack of studies investigating the effectiveness of using fiber anchors as mechanical securing devices that can transfer forces from the CFRP sheet to the concrete substrate beyond debonding strain levels. As a result, guidelines for installing fiber anchors are limited (Sbahieh et al. 2022b). Factors such as anchor layout, hole inclination, depth and area of the anchor hole, anchor radius, amount of CFRP materials, anchor fan length, fan angle, and anchor reinforcement influence the anchorage system (Garcia et al. 2014).

Several studies have investigated the cyclic response of strengthened RC members. Realfonzo et al. (2014) examined the seismic behaviors of RC beam-column joints strengthened with FRP systems. Two sets of exterior RC beam-column joints were designed for the experimental program: subassemblies with a strong column and subassemblies with a weak column. The application of CFRP sheets and steel plates enhanced the ultimate capacity of the system by a range of 16% to 73% based on the strengthening scheme. Additionally, the strengthened specimens showed more ductility compared to the control ones, with an increase ranging from 10% to 102%. The failure mode changed from joint shear failure in un-strengthened specimens to FRP debonding followed by joint shear failure, flexural beam failure, and slight FRP debonding followed by flexural beam failure in the subassemblies with weak columns. For the subassemblies with strong columns, the failure changed from joint shear failure to slight FRP debonding followed by joint shear failure.

Qazi et al. (2019) experimentally investigated the cyclic response of an RC short shear wall strengthened with externally bonded CFRP strips with fiber anchors. The stiffness and strength of the wall were enhanced by using CFRP strengthening. The ultimate capacity of the strengthened wall increased within a range of 23% to 30% when compared to the un-strengthened wall. Additionally, it was observed that the use of the CFRP system improved deformability and reduced the propagation of cracks. Furthermore, it was noted that the specimen with a lower number of fiber anchors improved elastic energy but not energy dissipation compared to the control wall. On the other hand, using denser fiber anchors successfully increased both elastic energy and energy dissipation.

Further research by Chalot et al. (2021) studied the mechanical behavior of a full-scale RC wall-slab connection reinforced with FRP under cyclic loading. Two specimens were tested, one was a control and the other was strengthened with a combination of CFRP, GFRP, and carbon mesh. According to the experimental data, the ductility of the FRP-strengthened specimen was improved by 30%, and the ultimate failure load was increased by 80% compared to the control specimen. The use of FRP composites enhanced the energy dissipation by 385%. Additionally, the failure mode changed from a bending failure of the wall to joint shear failure.

Razavi et al. (2021) experimentally investigated the behavior of RC columns and those strengthened with FRP composite under an innovative reversing cyclic eccentric axial loading. It was found that for columns strengthened with longitudinal FRP sheets employed via the grooving method, there was a reduction in the ductility by 50% and in energy dissipation by 83% to 227%.

On the other hand, the columns strengthened using FRP wraps exhibited higher ductility of 35% compared to the reference column, but there was no improvement in the ultimate load capacity.

Saeed et al. (2022) studied the seismic flexural strengthening of RC columns with EB-CFRP sheets and NSM-CFRP rods and ropes. According to the authors, the use of externally bonded CFRP sheets and near-surface-mounted (NSM) CFRP rod systems improved the lateral resistance of columns by 37% and 44%, respectively. The reduction of the lateral resistance after failure was less in columns with NSM-CFRP compared to CFRP sheets. Additionally, it was observed that the ultimate capacity was increased by 60% when NSM-CFRP ropes were applied, but a non-ductile response and sudden strength reduction were exhibited.

Mei et al. (2023) studied the seismic behavior of shear critical square RC columns strengthened by large rupture strain FRP and CFRP with different Axial Load Ratios (ALRs). A total of 10 specimens were built, including two control columns, six Polyethylene Terephthalate (PET) FRP-strengthened columns, and two CFRP-strengthened columns. The results of this study concluded that the use of PET FRP as a strengthening material improved the ductility ratio by 350%, 470%, and 520.8% for 1, 2, and 3 layers respectively, while the improvement was about 300% when using 1 layer of CFRP compared to the control column in the case of an axial load ratio to the lateral load of 0.17. In contrast, when the ALR ratio was increased to 0.40, the enhancement of the ductility ratio was observed at 163.5%, 205.6%, and 272.6% when the PET FRP was applied for 1, 2, and 3 layers respectively. On the other hand, the use of CFRP with 1 layer increased the ductility ratio by 179.2%. Additionally, it was found that the energy dissipation of the strengthened columns was higher compared to the control one, ranging from 1981.8% to 6498.3%, depending on the number of layers and the FRP material types.

This chapter focuses on the behavior of CFRP-strengthened beams under reversed cyclic loading, aiming to assess the effectiveness of different CFRP strengthening schemes with and without a short steel fuse in improving the structural performance. The experimental investigation involves subjecting identical beams to fully reversed loading cycles until failure, with one beam serving as a control and the others strengthened using various CFRP configurations per group. These configurations include CFRP sheets and fiber anchors, with additional reinforcement in the constant moment region, consisting of two layers of CFRP and a thin ductility steel fuse. The results of experimental testing provide a comprehensive understanding of the behavior and performance of CFRP-strengthened beams, aiding in the development of reliable design guidelines for concrete members subjected to cyclic loading. The findings of this research contribute to the advancement of performance and resilient infrastructure by highlighting the significance of CFRP based strengthening methods. By enhancing the structural performance of RC beams under reversed cyclic loading, these techniques have the potential to extend the service life of concrete members, reduce maintenance costs, and improve the resistance of structures in the face of cyclic loading events, ultimately ensuring the safety of occupants and preserving valuable assets.

5.3. Testing Program

5.3.1. Design and Casting of Specimens

To conduct the experiment, six full-scale reinforced concrete beams were constructed, meeting the ACI 318 building code (American Concrete Institute, 2019) requirements. These beams were divided into groups A and B; both are identical in terms of the geometry, flexural and shear reinforcement. Each beam had a height of 355.6 mm (14 in.), a length of 4023.4 mm (158.4 in.), and a width of 254 mm (10 in.). In terms of stirrups, ϕ 10 (#3) rebars are used for the stirrups, placed at @ 152.4 mm (6 in.) within the shear span and @ 254 mm (10 in.) within the constant moment region. However, there was a variation in internal flexural steel bars, such that group A was reinforced with 2 ϕ 13 (2#4) rebars top and bottom, while group B utilized 2 ϕ 16 (2#5) rebars top and bottom. Additionally, group A utilized a low strength concrete while group B used a higher concrete compressive strength. Figures 5.1 to 5.2 show the dimensions, steel reinforcement layout, supports, and loading protocol of the two control beams (beams No.1 and No.10). Figures 5.3 to 5.6 demonstrate the geometry of specimens No.6, 7, 15, and 16 along with the short steel ductility fuse and the strengthening CFRP sheet types and anchors arrangement. Furthermore, Figure 5.7 (a-b) presents the cross-section of beam No.7 and beam No.16. as well as the carbon fiber anchor, respectively. As illustrated in these Figures, beams No.7 and No.16 were strengthened in shear within the shear span to avoid shear failure, which took place in their twins counterparts, beam No.6 and beam No.15, as it is going to be discussed later in the strengthening and results section.

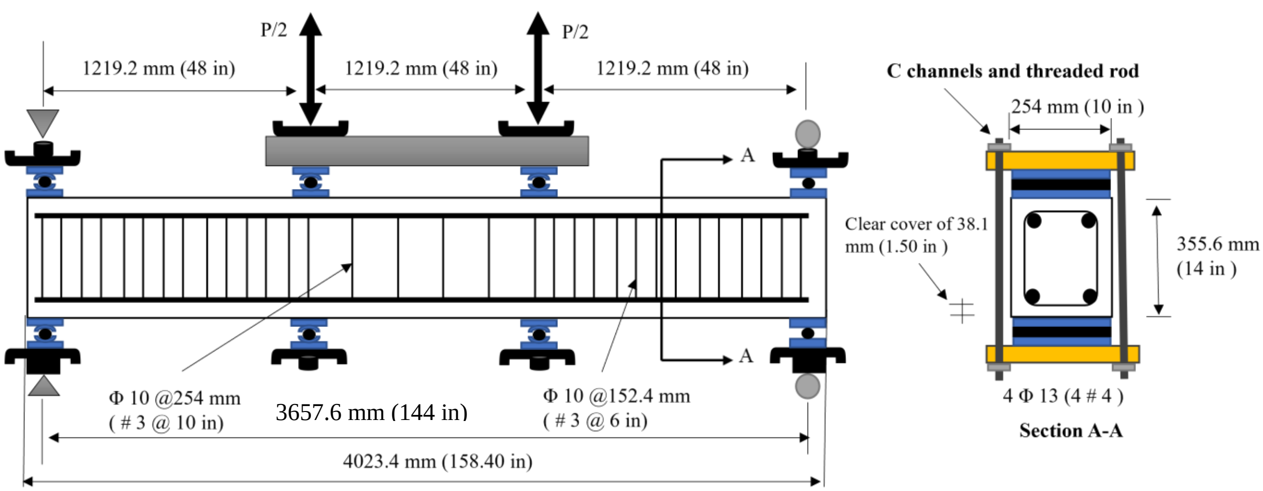

Figure 5.1. Beam No.1

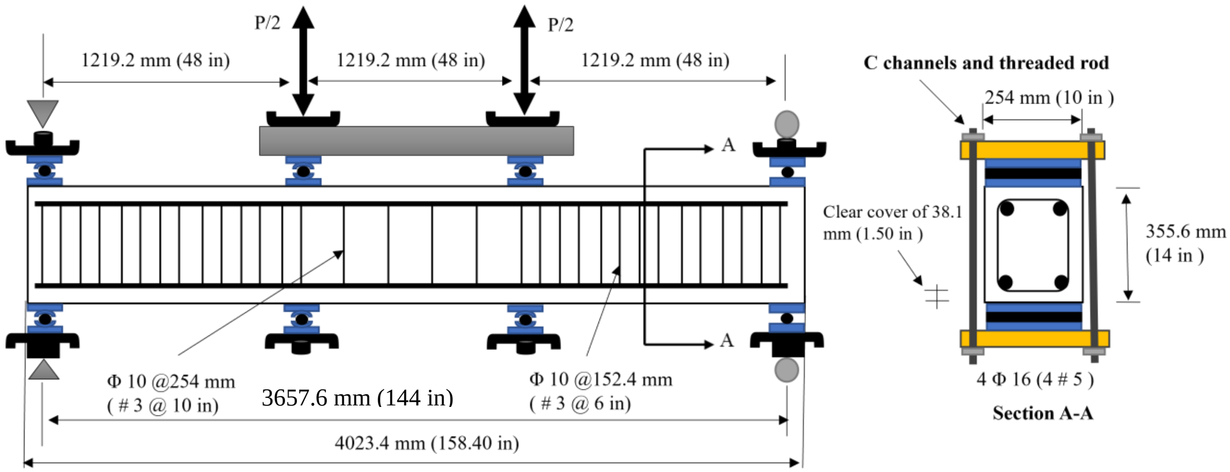

Figure 5.2. Beam No.10

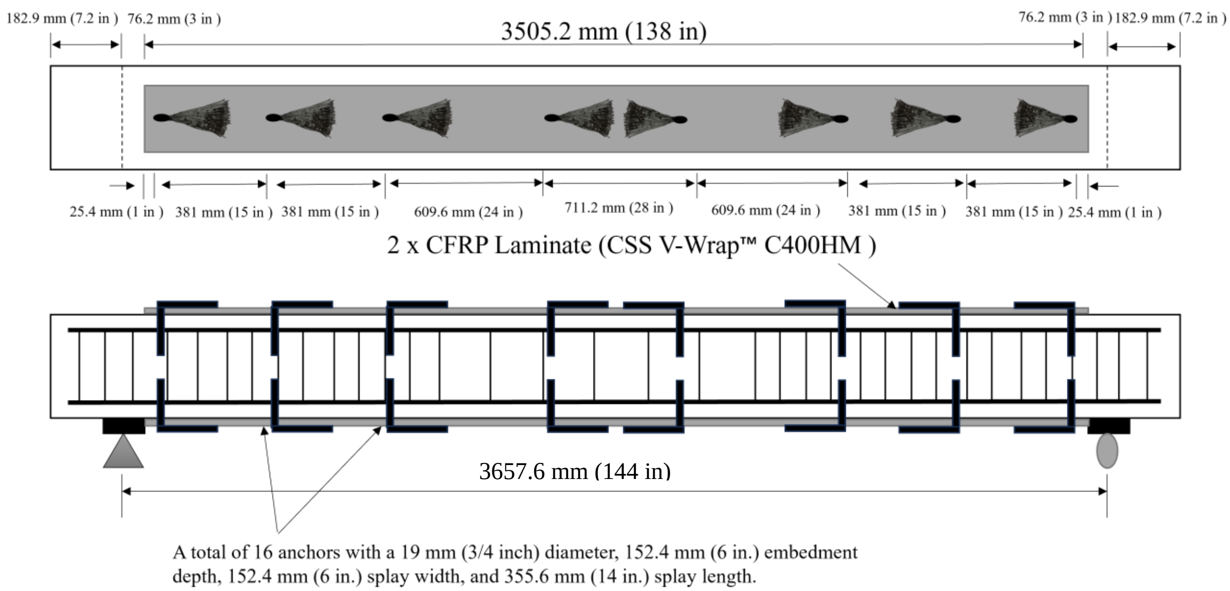

Figure 5.3. Beam No.6

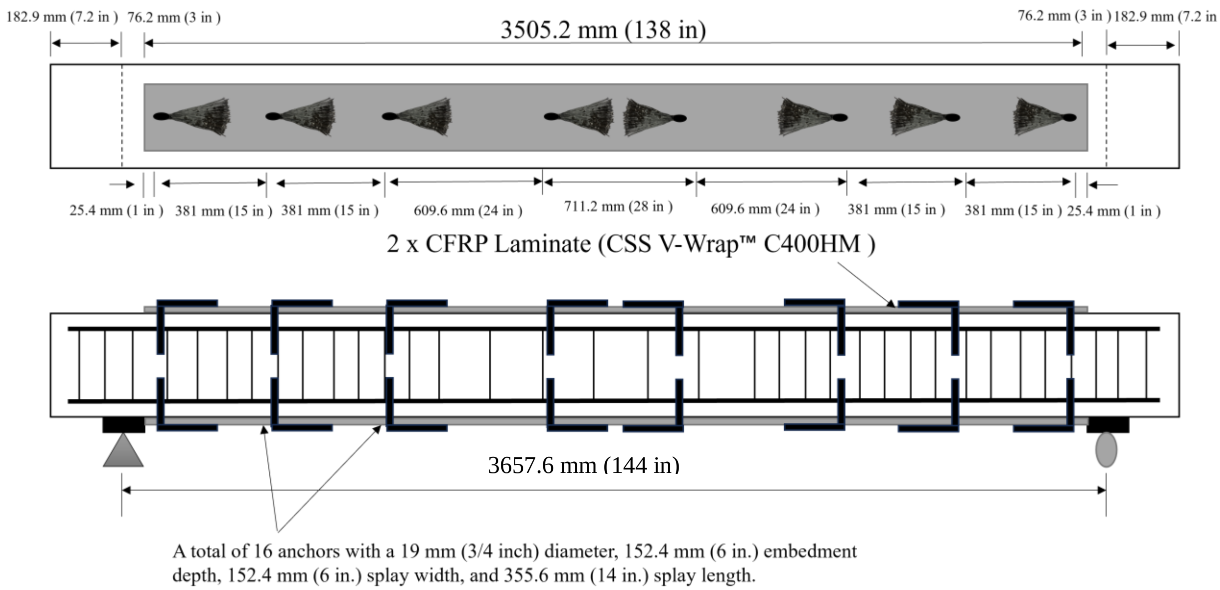

Figure 5.4. Beam No.15

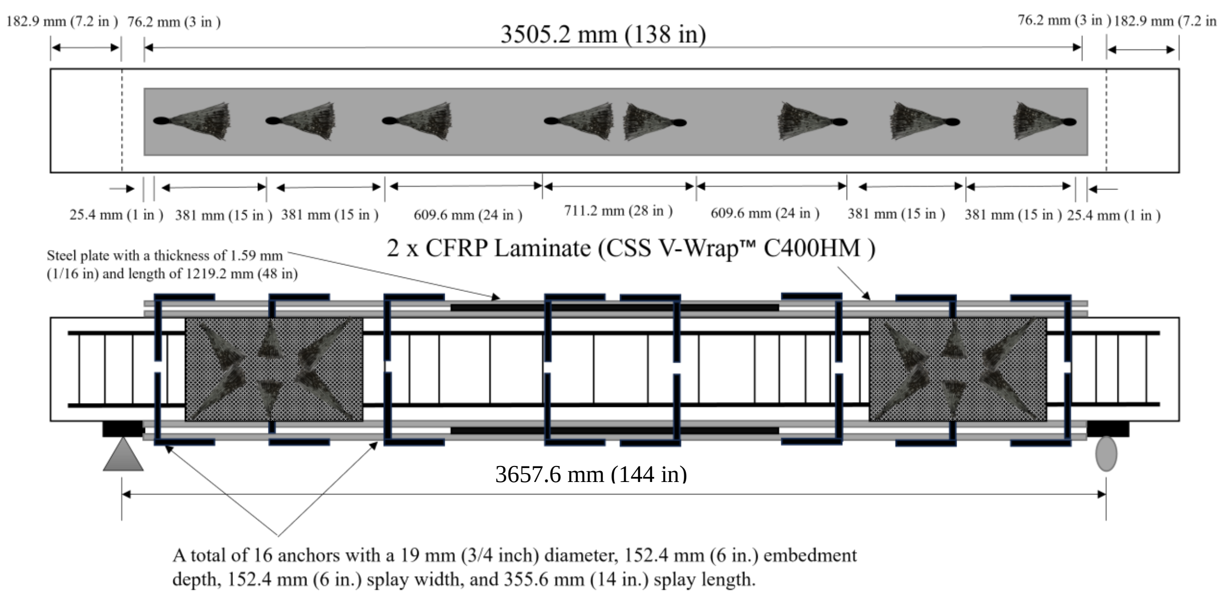

Figure 5.5. Beam No.7

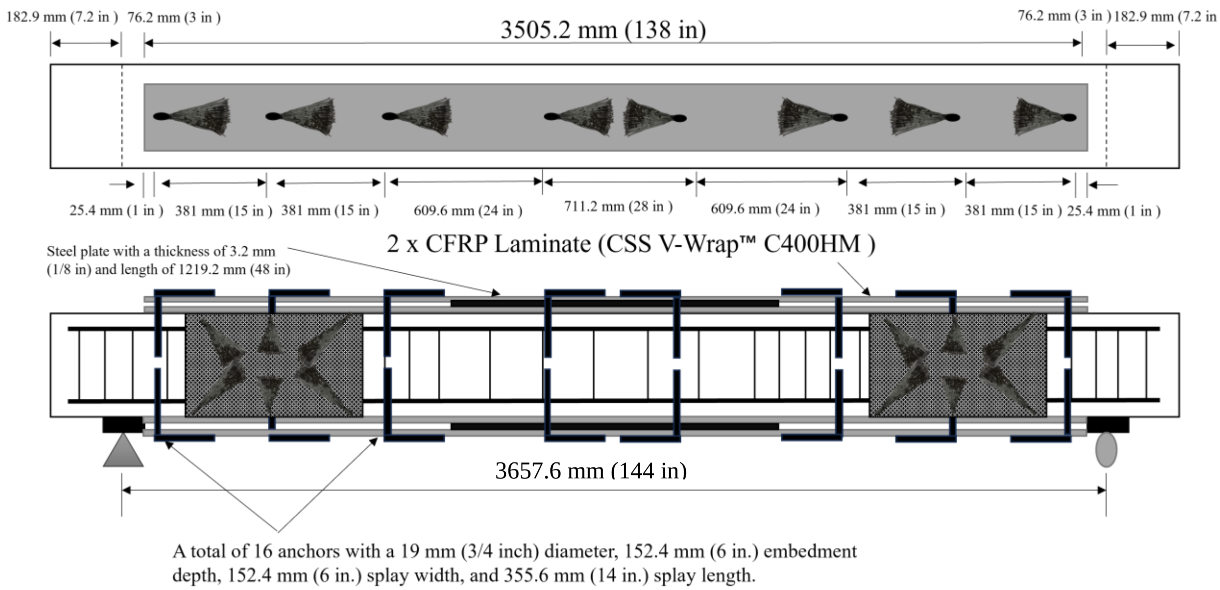

Figure 5.6. Beam No.16

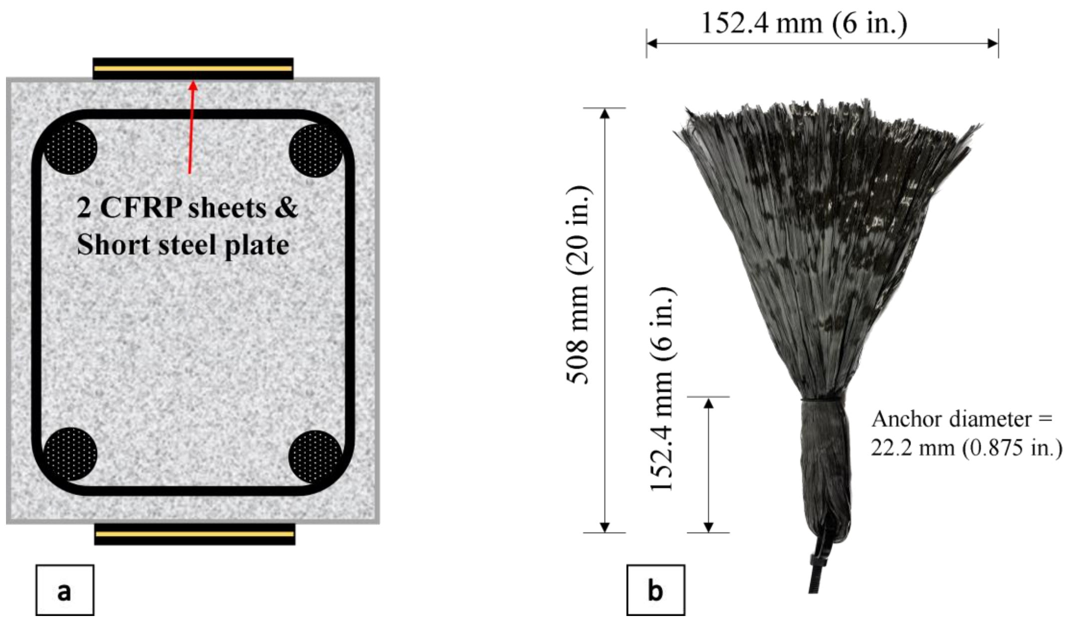

Figure 5.7. Cross section of beam No.7, beam No.16, and the carbon fiber anchor.

5.3.2. Material Properties

5.3.2.1. Concrete

Two concrete mixes were used to cast the tested beams; each group has a different concrete strength. The concrete of group A was designed to have a 28-day compressive strength of 17.2

MPa (2.5 ksi) with a slump of 76.2 mm (3 in.). On the other hand, group B was designed to have a concrete compressive strength of 31 MPa (4.5 ksi). Experimentally, the average concrete compressive strength was evaluated by testing three concrete cylinders of 101.6 mm diameter x 203.2 mm height (4″ diameter x 8″ height) following ASTM C39. The average 28-day concrete compressive strength of group A was found to be 21 MPa (3.0 ksi) while it was 39.28 MPa (5.7 ksi). Additionally, the compressive strength for each group was determined on the day of beam testing by examining two additional cylinders at the time of loading beams No.6 and No.15 and found to be 25.56 MPa (3.71 ksi) and 42.87 MPa (6.22 ksi), respectively. Table 5.1 shows the summary of the results of concrete testing.

Table 5.1 Concrete Compressive Strength Testing

Group	Specimen	Testing type	Strength MPa (psi)	Average strength MPa (psi)
A	ACS1	28-day Compressive Strength	21.2 (3,081.00)	21.0 (3,048.50)
	ACS2		20.5 (2,978.00)	
	ACS3		21.3 (3,092.00)	
	ACS4	Day of Testing	25.56 (3,708.00)	25.56 (3,708.00)
B	BCS1	28-day Compressive Strength	41.60 (6,038)	39.28 (5,700)
	BCS2		37.87 (5,496)	
	BCS3		38.36 (5,567)	
	BCS4	Day of Testing	42.87 (6,218)	42.87 (6,218)

5.3.2.2. Steel Reinforcement

Three specimens of each size of steel, used in the reinforcement of the examined beams, were tested in accordance with ASTM A615. For the stirrup steel, it was found that the average yielding strength was recorded to be 485.50 MPa (70.40 ksi), while the manufacturer yielding strength was reported to be 470.20 MPa (68.20 ksi). The rebars of size ϕ 13 (#4), and ϕ 16 (#5) had an experimentally average yielding strength of 536.01 MPa (77.74 ksi) and 560.50 MPa (81.30 ksi) respectively. Table 5.2 below shows the testing summary along with the manufacturer value of all three sizes of steel rebars. Further testing was conducted to determine the mechanical properties of steel plates used to strengthen two of the strengthened beams (beams No.7 and No.16). A total of ten steel coupons were tested, five specimens for each plate since they are varied in terms of thickness, such that 1.6 mm (1/16 in.) and 3.2 mm (1/8 in.). Testing results and manufacturer data are presented in Table 5.3.

Table 5.2 Steel mechanical property testing results.

Rebar Size	Average Yielding Strength MPa (ksi)	Manufacturer Yielding Strength MPa (ksi)	Average Elastic Modulus MPa (ksi)	Manufacturer Elastic Modulus MPa (ksi)
ϕ 16 (No.5)	513.30 (74.50)	560.50 (81.30)	176,542 (25,623)	200,000 (29,000)
ϕ 13 (No.4)	536.01 (77.74)	559.20 (83.10)	170,489.00 (24,727)	200,000 (29,000)
ϕ 10 (No.3)	485.50 (70.40)	470.20 (68.20)	173,182 (25,118)	200,000 (29,000)

Table 5.3 Mechanical testing results for the short steel plates.

Plate Thickness mm (in.)	Average Yielding Strength MPa (ksi)	Manufacturer Yielding Strength MPa (ksi)	Average Elastic Modulus MPa (ksi)	Manufacturer Elastic Modulus MPa (ksi)
1.6 (1/16)	300.50 (43.59)	275.79 (40.00)	204,319 (29,637)	200,000 (29,000)
3.2 (1/8)	278.08 (40.34)	275.79(40.00)	204,193 (29,619)	200,000 (29,000)

5.3.2.3. Carbon Fiber Reinforced Polymer (CFRP) Sheet

A commercially-available high-modulus unidirectional carbon fiber fabric sheet was used to strengthen four RC beams in flexure. The fabric sheet has a dry thickness of 0.7 mm (0.026 in.) and a 2.0 mm (0.08 in) thick saturated laminate layer (CSS V-Wrap™ C400HM) with 1300 g/m^2 (38.34 oz/ yd^2). Additionally, a further type of fabric sheet with a dry thickness of 0.61 mm (0.024 in.) and 1.02 mm (0.04 in) thick, saturated laminate layer (CSS V-Wrap™ C200HM) having 600 g/m^2 (17.7 oz/ yd^2) was utilized to strengthen two of the tested beams in shear. Table 5.4 demonstrates the mechanical properties of the CFRP sheets.

Table 5.4 Mechanical properties of CFRP sheet and anchor per Manufacturer specifications.

Type of Carbon fiber fabric	Properties Type	Nominal thickness t, mm (in)	Ultimate tensile strength f_{fu}, , MPa (ksi)	Elongation at break ε_{fu}, %	Modulus of elasticity E, MPa (ksi)
CSS V-Wrap HMCA-CV-HMCA75X	Dry fiber properties	NA	5,440 (790)	1.9	289,550 (42,000)
	Cured laminate properties	NA	1,138 (165)	1.1	103,420 (15,000)
CSS V-Wrap HMCA-CV-HMCA50X	Dry fiber properties	NA	5,440 (790)	1.9	289,550 (42,000)
	Cured laminate properties	NA	1,138 (165)	1.1	103,420 (15,000)
CSS V-Wrap™ C400HM	Dry fiber properties	0.66 (0.026)	5,440 (790)	1.9	289,550 (42,000)
	Cured laminate properties	2.03 (0.08)	1,241 (180)	1.27	98,181 (14,240)
CSS V-Wrap™ C200HM	Dry fiber properties	0.61 (0.024)	5,440 (790)	1.9	289,550 (42,000)
	Cured laminate properties	1.02 (0.04)	1,241 (180)	1.27	98,181 (14,240)

5.3.2.4. Carbon Fiber Anchors

For fiber anchors, a commercially-available high-modulus unidirectional carbon was used, including (CSS V-Wrap HMCA-CV-HMCA75X) with a diameter of 19.05 mm (0.75 in.) for flexural strengthening and (CSS V-Wrap HMCA-CV-HMCA50X) with a diameter of 12.70 mm (0.50 in.) for shear strengthening. The manufacturer data for fiber anchors are listed in Table 5.4.

5.3.3. Strengthening Procedure

5.3.3.1. Flexural Strengthening

The strengthening procedure follows several steps to ensure adequate strength, including surface preparation, drilling holes for anchors, application of CFRP sheets, and installation of anchors. All surfaces of the strengthened beams were prepared using a wheel grinder to ensure a good bond between CFRP sheets and the concrete soffit. Then, the locations of fiber anchors were determined following the provided design, the holes were drilled, and any dust was removed. A structural epoxy adhesive resin was applied to the prepared concrete surface as well as the anchor holes were primed with the same epoxy. CFRP sheets were placed and bonded to the concrete surface according to the layout design, the anchor holes were filled with epoxy thickened with fumed silica, the anchors were then inserted using a steel stick tool, and the anchor fan was splayed on the top of the sheets. In addition to the use of a CFRP sheet, a short steel plate was used to add more ductility to two of the strengthened beams, one from each group. Furthermore, each strengthened beam was provided with a total of sixteen fiber anchors (eight for each face) as depicted in Figures 5.3 to 5.6. Table 5.5 summarizes the flexural strengthening details of the tested beams. Moreover, Figures 5.8 (a-c) show the beams during preparation and CFRP installation.

Table 5.5 Beams flexural strengthening details.

Group	Beam No.	Specimen Type	CFRP Sheets	Steel Plate	Number of CFRP layers	Number of steel plate layers
A	1	Control	N/A	N/A	N/A	N/A
	6	FRP strengthened & anchored	CSS V-Wrap™ C400HM	N/A	2 per side, top and bottom	N/A
	7	FRP strengthened, steel plate & anchored	CSS V-Wrap™ C400HM	A36 Steel	2 per side, top and bottom	1 per side, top and bottom
B	10	Control	N/A	N/A	N/A	N/A
	15	FRP strengthened & anchored	CSS V-Wrap™ C400HM	N/A	2 per side, top and bottom	N/A
	16	FRP strengthened, steel plate & anchored	CSS V-Wrap™ C400HM	A36 Steel	2 per side, top and bottom	1 per side, top and bottom

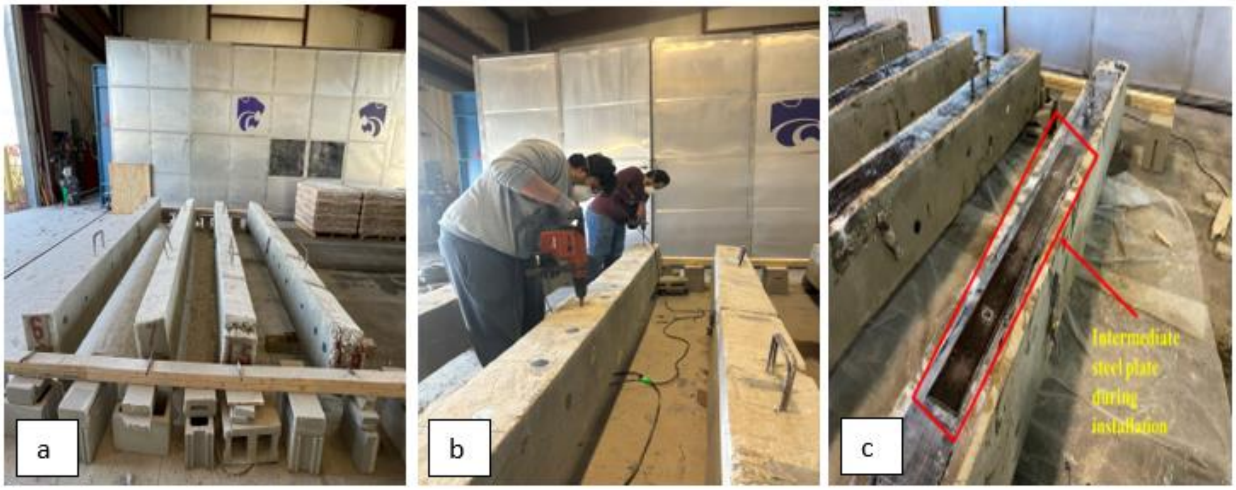

Figure 5.8. Beams during surface preparation and CFRP installation phase.

5.3.3.2. Shear Strengthening

To avoid shear failure of two of the tested beams (beams No.7 and No.16), a single layer of CFRP (CSS V-Wrap™ C200HM) secured with a total of six through-the-width fiber anchors with a diameter of 12.70 mm (0.50 in.) was used within the shear span, as shown in Figures 5.5 to 5.6 for beams No.7 and No.16, respectively. Table 5.6 below summarizes the shear strengthened details of the tested beams.

Table 5.6 Beams shear strengthening categories.

Group	Beam No.	Shear CFRP Sheets	Number of CFRP layers	Number of fiber anchors
A	1	N/A	N/A	N/A
	6	N/A	N/A	N/A
	7	CSS V-Wrap™ C200HM	1 per side, left and right	6 through-the-width
B	10	N/A	N/A	N/A
	15	N/A	N/A	N/A
	16	CSS V-Wrap™ C200HM	1 per side, left and right	6 through-the-width

5.3.4. Test setup and Instrumentation.

Four-point bending, reversed cyclic loading was applied to investigate the seismic flexural behavior of the beams using a hydraulic actuator with an ultimate capacity of 1112 kN (250-kip), refer to Figures. 5.9 to 5.10 for the testing setup as well as the cross section of loading points with CFRP sheet kept without any contact by specifically designed bridge-spacer to allow CFRP debonding freely. A displacement-controlled protocol was performed following AC125 (ICC ES AC125 2021) with an average rate of 17.8 mm/min (0.7 in/min), see Figure 5.11. Beams were tested with a simply supported boundary condition with a clear span of 3657.6 mm (144 in.)[5]. The midspan deflection was collected using four LVDTs, two at mid-span and one at each support. To measure the strain at the extreme fiber, four strain gauges were installed on the CFRP sheets at the mid-span of the beams. Four more CFRP strain gauges were installed within the shear span top and bottom in between the first two anchors closer to the loading points. Additionally, the top and bottom strain of longitudinal steel was collected using four strain gauges, two at the top and two at the bottom rebars, refer to Figure 5.9 for more details.

[5] The clear span of the RC beams was slightly over 144 in. since the center-to-center distance between the strong floor tie-down was 144.75 in.

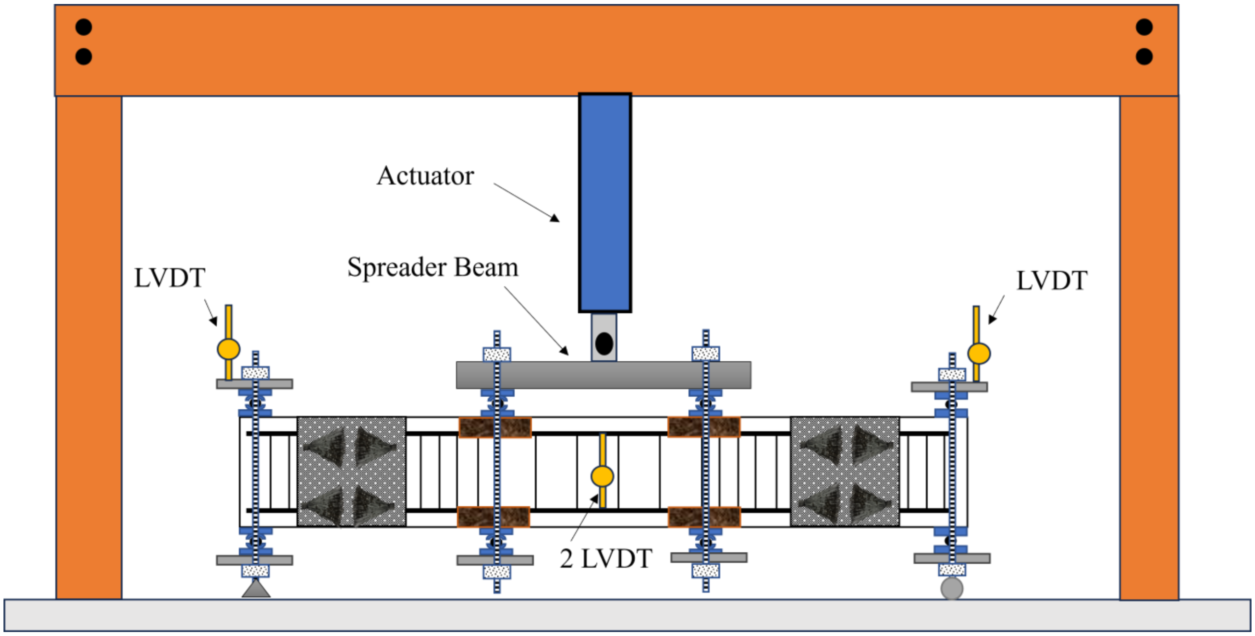

Figure 5.9. Loading frame and testing setup

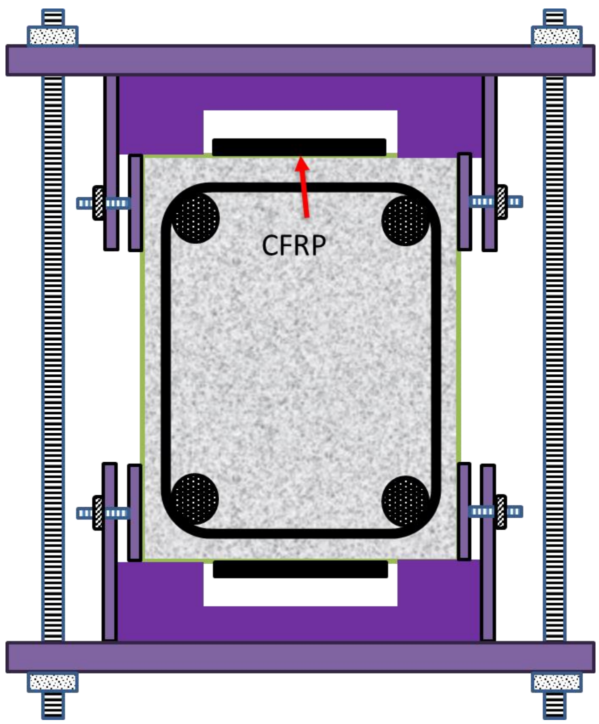

Figure 5.10. Loading points cross section

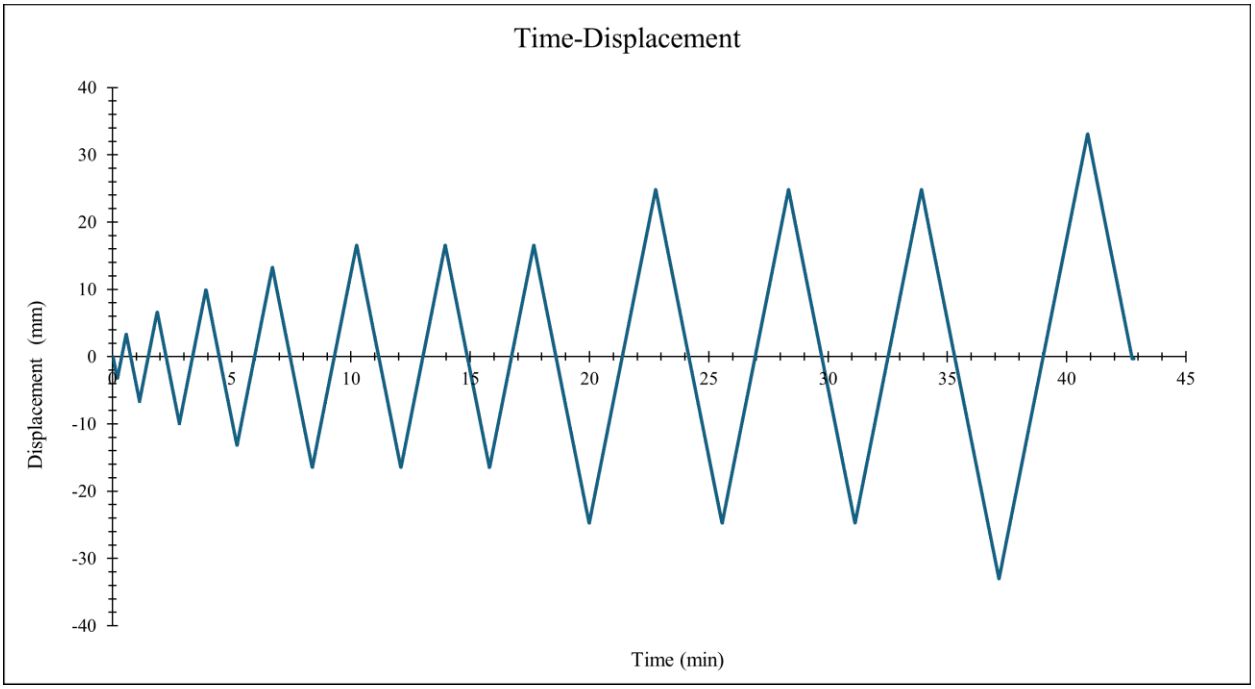

Figure 5.11. Loading Protocol for Beam No.6.

5.4. Experimental Results

5.4.1. Load-Deflection Response

To evaluate the performance of the tested specimens subjected to reversed cyclic loading, a unique setup was developed specifically for this study, see Figures 5.9 to 5.10. Displacement-controlled cyclic four-point bending was applied using a 1112 kN (250-kip) hydraulic actuator. The response of the tested specimens varied as follows.

Beam No.1

Beam No.1 of group A was tested as a control beam. Upon analysis of the results, it was observed that the control specimen displayed ductile behavior. It was able to withstand a displacement of over 82.55 mm (3.25 in.) without significant reduction in strength. The cracking load was measured to be 34.75 kN (7.81 kips) in the push direction with a corresponding cycle size of 7.62 mm (0.30 in.) while it was 43.14 kN (9.70 kips) in the pull direction within the same cycle size. The first cracking was followed by several flexural cracks developed within the constant moment region. According to the experimental data, the yielding occurred around a load of 62.27 kN (13.74 kips) in the push side with a corresponding cycle of 19.05 mm (0.75 in.) while it was 74.59 kN (16.77 kips) in the pull side within the same corresponding cycle size. This was associated by more flexural crack propagation at the constant moment region along with shear cracking at both points where the loading was applied on the shear span side. The ultimate load at which the failure took place due to excessive yielding was around 89.01 kN (20.01 kips) in push direction with a corresponding cycle size equal to 82.55 mm (3.25 inches). It also took place at around 125.80 kN (28.29 kips) in the pull direction during a similar corresponding displacement cycle level. It is important to observe that the different loads in the pull direction are noticeably higher than the same loads in the push direction for this beam. Part of the reason is the fact that gravity acts in the push direction resulting in higher reported load values for the pull direction in this case. The main reason is the pin-pin boundary conditions used for Beam No.1 that did add extra constraint in the pull direction due to the tightened clamping of the threaded rods. Test setup of the beam is shown in Figure 5.12. Figure 5.13 illustrates the hysteretic response of the control specimen while Figure 5.14 presents the failure mode of the beam.

Figure 5.12 Specimen No.6. setup before testing.

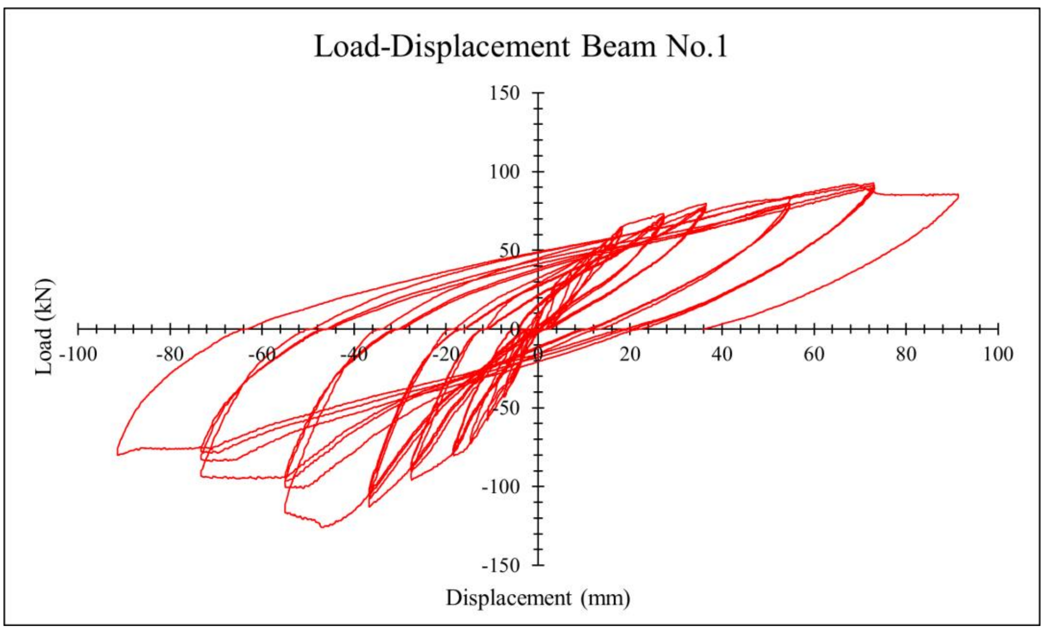

Figure 5.13. Load-displacement response of beam No.10 (1 Kips=4.45 KN)

Figure 5.14. Specimen No.1 at failure.

Beam No.6

The load-deflection of beam No.6, reinforced with CFRP, initially shows a linear behavior with reduced deflections due to the stiffness provided by CFRP compared to its twin, beam No.1. The cracking load was reported at a load of 52 kN (11.69 kips) in pull direction and 54.5 kN (12.25 kips) in push direction with an associated cycle size of 3.30 mm (0.13 in.). The density of the cracks within the constant moment region was very minimal in comparison with the control beam due to the restrain of the use of the CFRP sheets. At midspan displacement of 16.52 mm (0.65 in.), the CFRP sheets started debonding from the concrete substrate. However, the use of distributed fiber anchors prevented the entire debonding and kept the beam continuing to carry more load beyond the capacity if these fiber anchors were absent. The longitudinal steel yielded at a load of 189 kN (42.48 kips) and corresponding cycle size of 16.52 mm (0.65 in.) in the pull direction while in the push direction, the yielding occurred at load of 200 kN (44.96 kips) within the same cycle size. The failure of the beams occurred at a load of 240 kN (53.95 kips) and cycle size of 33.02 mm (1.30 in.) in pull direction and a load of 260 kN (58.45 kips) within the same cycle in push direction due to the lack of sufficient steel shear reinforcement and the low compressive strength of the concrete. In fact, the specimen experienced a shear failure within the shear span. The ultimate load was increased by 250% when compared to the control beam, even though the expected load of 380 kN had not been achieved. Figures 5.15 to 5.16 showcase the test setup and the load-deflection response of beam No.6, respectively, while Figure 5.17 illustrates the specimen failure within the shear span.

Figure 5.15. Specimen No.6. setup before testing.

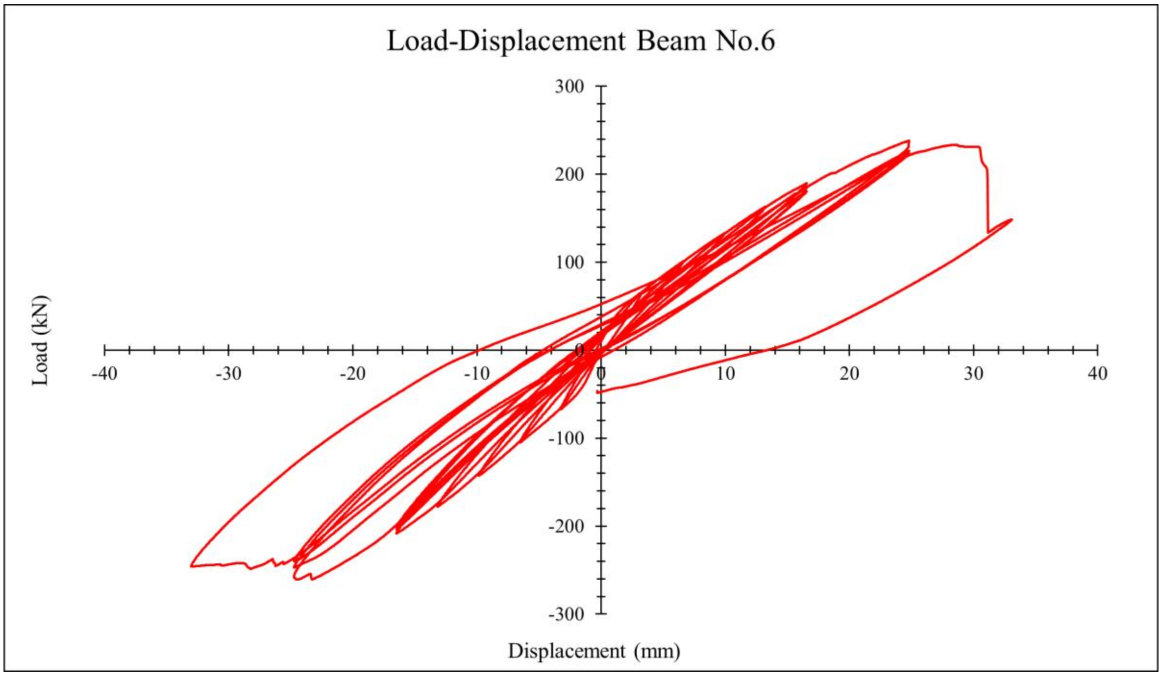

Figure 5.16. Load-displacement response of beam No.6 (1 Kips=4.45 KN)

Figure 5.17. Failure Mode of beam No.6 due to shear cracks.

Beam No.7

When analyzing the outputs of beam No.7, it was observed that the load-displacement response experienced a higher ultimate capacity and ductility compared to its twin (beam No.6), see Figure 5.18 for the load-displacement response of beam No.7. That improvement was due to the use CFRP sheet secured with fiber anchors as a shear strengthening within the shear span to avoid shear failure mode that beam No.6 exhibited as well as the implementation of the sandwiched steel plate within the constant moment region, see Figure 5.19 for shear strengthening of beam No.7. The initial cracking load was recorded at 45.55 kN (10.24 kips) with a corresponding displacement cycle size of 3.30 mm (0.13 in.) in the push direction while in the pull direction the load was 50.5 kN (11.53 kips) within the same cycle size, indicating micro-cracking within the constant moment region. As the load increased, the yielding load was reached at the amounts of 225.3 kN (50.65 kips) and 220.22 kN (49.51 kips) in the push and pull direction, respectively, within the displacement cycle size of 24.89 mm (0.98 in.). The ultimate capacity was achieved at a load of 290.12 kN (65.22 kips) in the push direction, accompanied by a displacement cycle size of 33.02 mm (1.30 in.). On the other hand, the ultimate capacity of the beam in the pull direction was reported to be 244.60 kN (54.94 kips), corresponding to the same cycle size of 33.02 mm (1.30 in.). It is evident that the push direction showed higher capacity when compared to the pull direction. This can be attributed to the fact that the displacement cycle starts with push direction then goes to the pull side, at which one side of the CFRP sheet already debonded due to the preload. The failure of beam No.7 was caused by vertical shear cracks which found their way through the vertical direction between fiber anchors (weak direction) within the CFRP sheet, see Figure 5.20. It is very important to note that all beams in groups A and B have a proper pin-roller boundary condition unlike the pin-pin support initially adopted for the control beam.

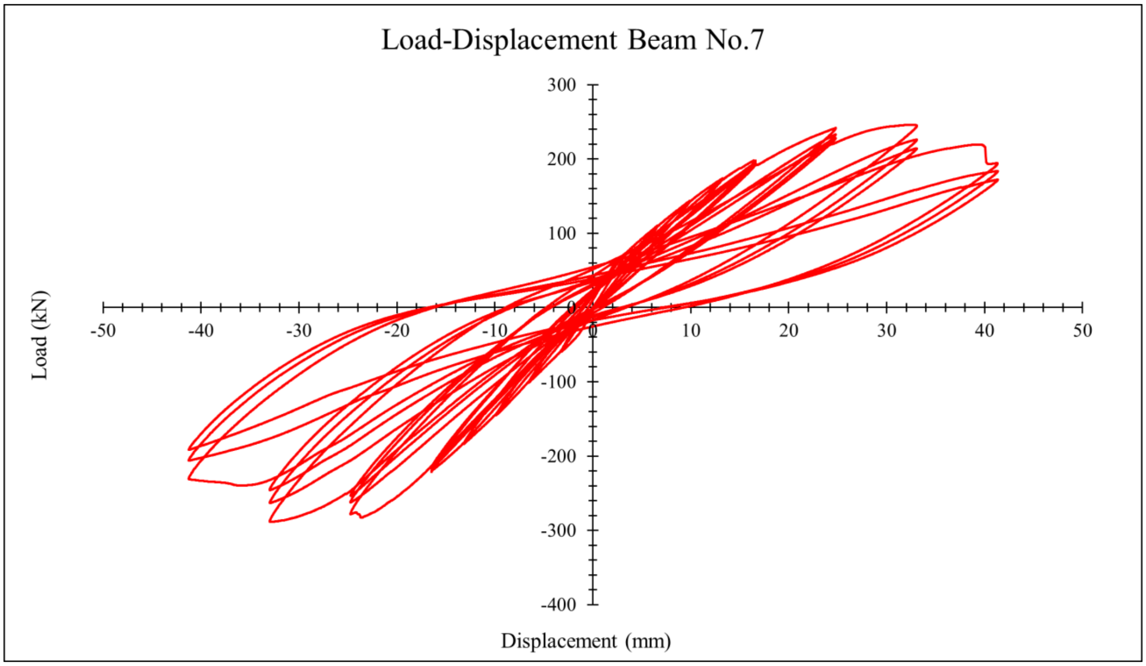

Figure 5.18. Load-displacement response of beam No.7 (1 Kips=4.45 KN)

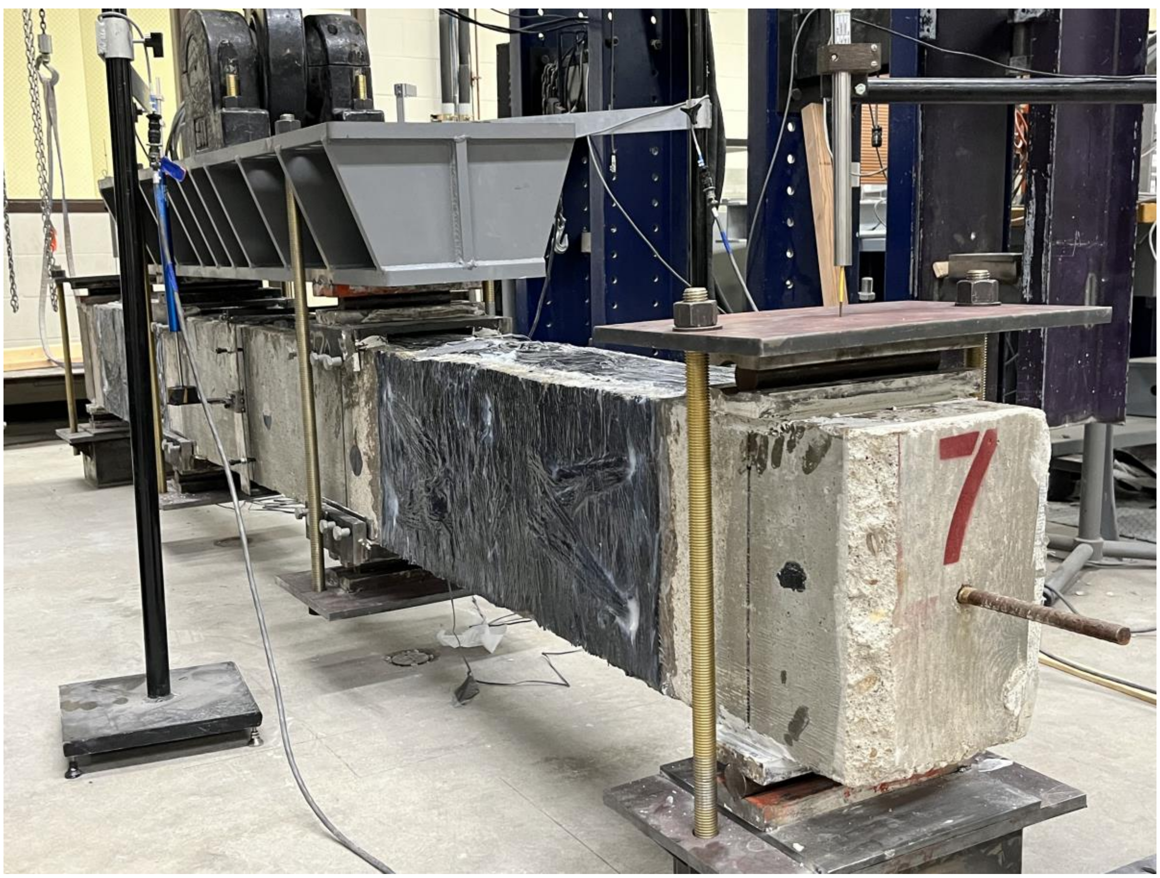

Figure 5.19. Test setup of beam No.7 before testing

Figure 5.20. Specimen No.7 after failure

Beam No.10

The control beam of group B exhibited a highly ductile response, characterized by a significant energy dissipation within the hysteresis loops. The beam endured a substantial displacement of over 57.15 mm (2.25 in.) in the pull direction, with minimal gradual decrease in strength approaching failure. The initial cracking of the beam occurred at a pushing load of 34.78 kN (7.82 kips) and a pulling load of 34.91 kN (7.85 kips), both at a cycle displacement size of 7.62 mm (0.30 in.). As the displacement increased, additional typical flexural cracks formed in the constant moment region, accompanied by propagation of shear cracks underneath the points of load application on the side of the shear span. Based on the strain readings of the steel, yielding was observed at a load of 92.62 kN (20.82 kips) in the push direction and 90.55 kN (20.36 kips) in the pull direction, both corresponding to a cycle displacement of 19.05 mm (0.75 in.). With further displacement, more flexural and shear cracks developed, and the existing ones widened. Failure of the beam occurred at a cycle displacement of 57.15 mm (2.25 in.) due to excessive yielding, which is expected for a typical steel-reinforced concrete beam. The ultimate load was experimentally determined to be 103.20 kN (23.20 kips) in the push direction and 107.14 kN (24.09 kips) in the pull direction. Figures 5.21 and 5.22 illustrate the test setup and the hysteretic response of the control specimen, while Figure 5.23 shows the failure mode of that beam.

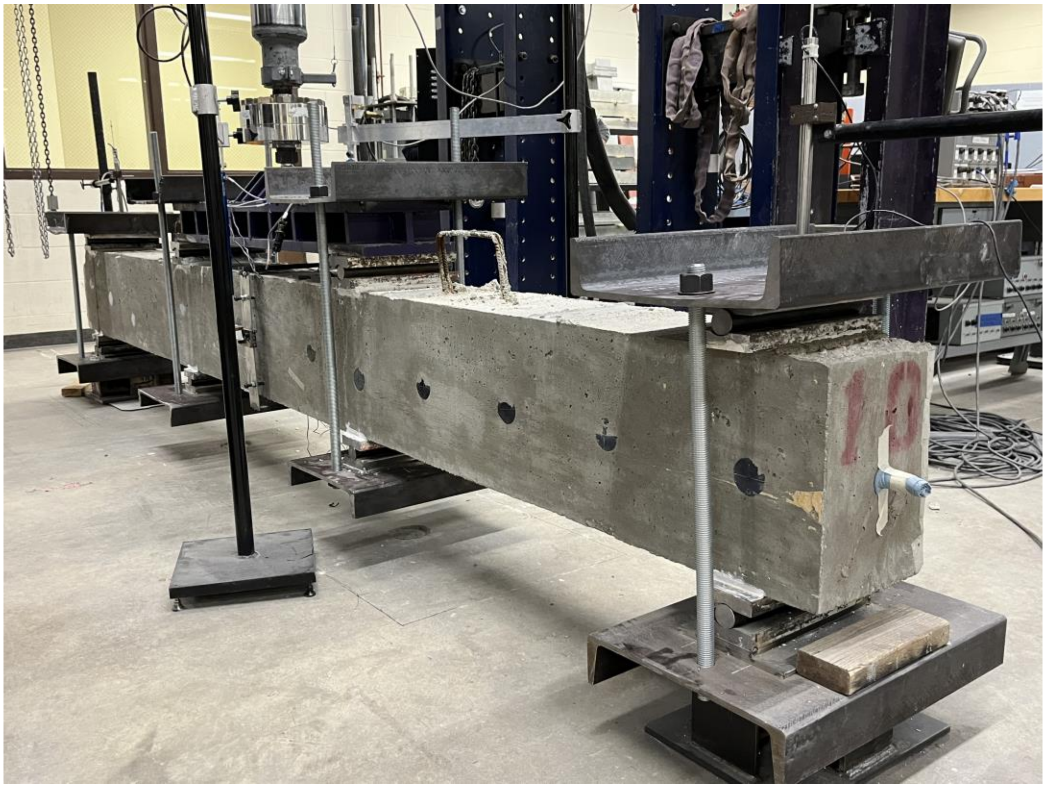

Figure 5.21. Test setup of beam No.10 before testing

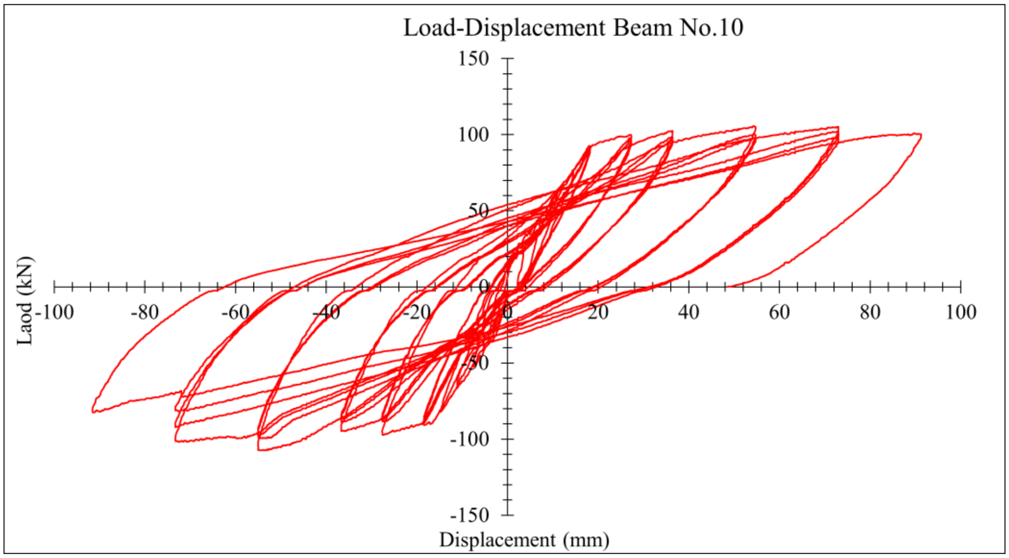

Figure 5.22. Load-displacement response of beam No.10 (1 Kips=4.45 KN)

Figure 5.23. Specimen No.10 after failure

Beam No.15

The response of beam No.15 exhibited higher ultimate capacity in comparison to its twin, beam No.6, because of the use of larger longitudinal rebars and the higher concrete compressive strength of 39.28 MPa (5700.0 psi) instead of 21.00 MPa (3048.5 psi). The setup of beam No.15 before testing and the hysteresis response are shown on Figures 5.24 to 5.25, respectively. The results showed that, in pull direction, the cracking load was about 74.07 kN (16.65 kips) with a displacement cycle size of 3.30 mm (0.13 in.). In the push direction, however, the cracks occurred at a load of 45.39 kN (10.20 kips) under the same cycle size of the pull direction. The density and width of flexural cracks in the constant moment region were significantly lower than those observed in the control specimen, beam No.10, because of the use CFRP sheets bridging the flexural crack formation. The yielding load was achieved at an amount of 211.00 kN (47.43 kips) and 219.00 kN (49.23 kips) in pull and push direction, respectively, both associated with a cycle size of 16.52 mm (0.65 in.). Failure occurred due to a combination of shear cracks within the shear span and concrete cover separation, see Figures 5.26 to 5.27. However, the use of deep fiber anchors prevented the entire cover delamination of concrete and kept the beam curing capacity from sudden reduction. The ultimate capacity was 287.00 kN (64.52 kips) with a cycle size of 33.00 mm (1.30 in.) in pull direction while in push direction, the load was 350.00 kN (78.68 kips) within the similar cycle size. The variation between the ultimate capacity of the pull and push direction was attributed to the occurrence of concrete cover separation at the top face of the beam along with shear cracks, see Figure 5.27.

Figure 5.24. Specimen No.15. before testing.

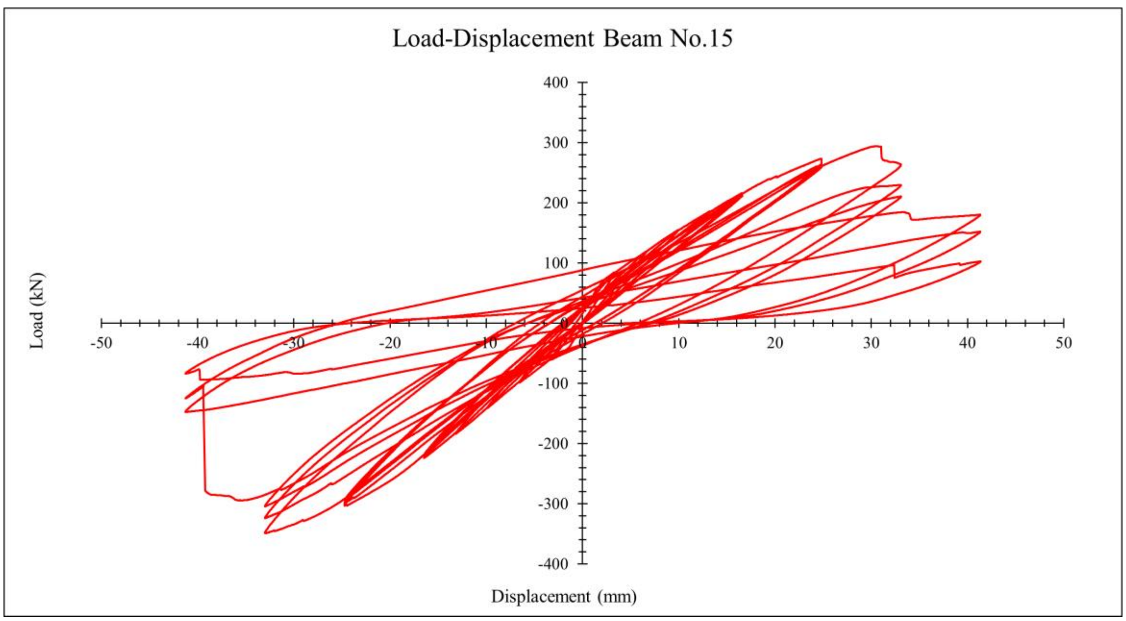

Figure 5.25. Load-displacement response of beam No.15 (1 Kips=4.45 KN)

Figure 5.26. Failure Mode of beam No.15.

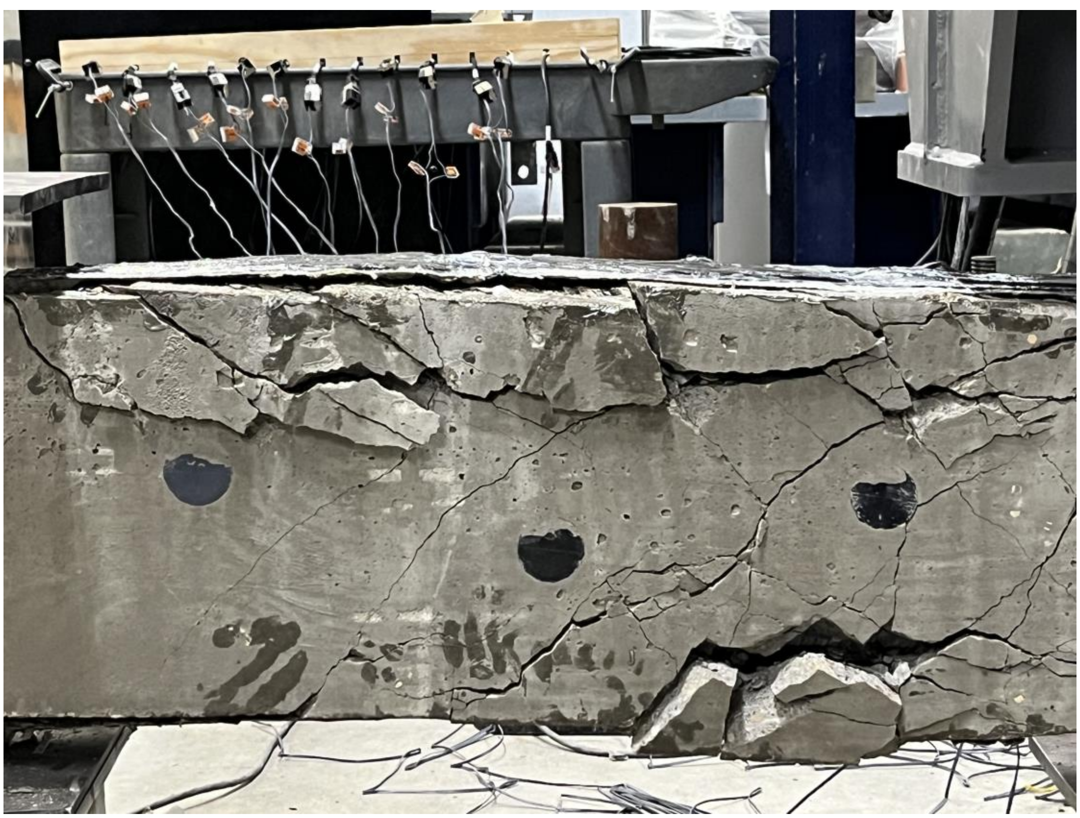

Figure 5.27. Formulation of concrete cover delamination and shear cracks of beam No.15 during testing

Beam No.16

Unlike beam No.15, beam No.16 was strengthened in shear using a single layer of CFRP sheet (**CSS V-Wrap™ C200HM)** secured with total of six through-the-width fiber anchors within each shear span, see Figure 5.28, and additional flexure strengthening was provided using a sandwiched short steel plate within the constant moment region. Thus, the load-deflection response of beam No.16 showed an enhancement in the ultimate capacity and energy dissipation, as well as a slight improvement in the ductility compared to its twin beam No.15. The cracking load in the push direction was reported at 60.13 kN (13.52 kips) with an associated displacement cycle size of 3.30 mm (0.13 in.). In the pull direction, the cracking load was 60.02 kN (13.49 kips) within the exact same displacement cycle size of 3.30 mm (0.13 in.). At a midspan displacement cycle size of 24.89 mm (0.98 in.), the longitudinal steel reinforcement began to yield at a load of 290.00 kN (65.19 kips) and 289.30 kN (65.04 kips) in the push and pull direction, respectively. The failure of the beam occurred at an ultimate load of 375.00 kN (84.30 kips) and 320.20 kN (71.98 kips) in the push and pull direction, respectively, with a corresponding displacement cycle size of 41.28 mm (1.625 in.). It is worth mentioning that the beam failed due to CFRP rupture at the top face under the pull load and end fiber anchor rupture at the bottom face during push load. Figure 5.28 below shows the beam test setup and side shear strengthening. The load-displacement response is depicted in Figure 5.29, and the failure of the beam is demonstrated in Figure 5.30.

Figure 5.28. Specimen No.15. before testing.

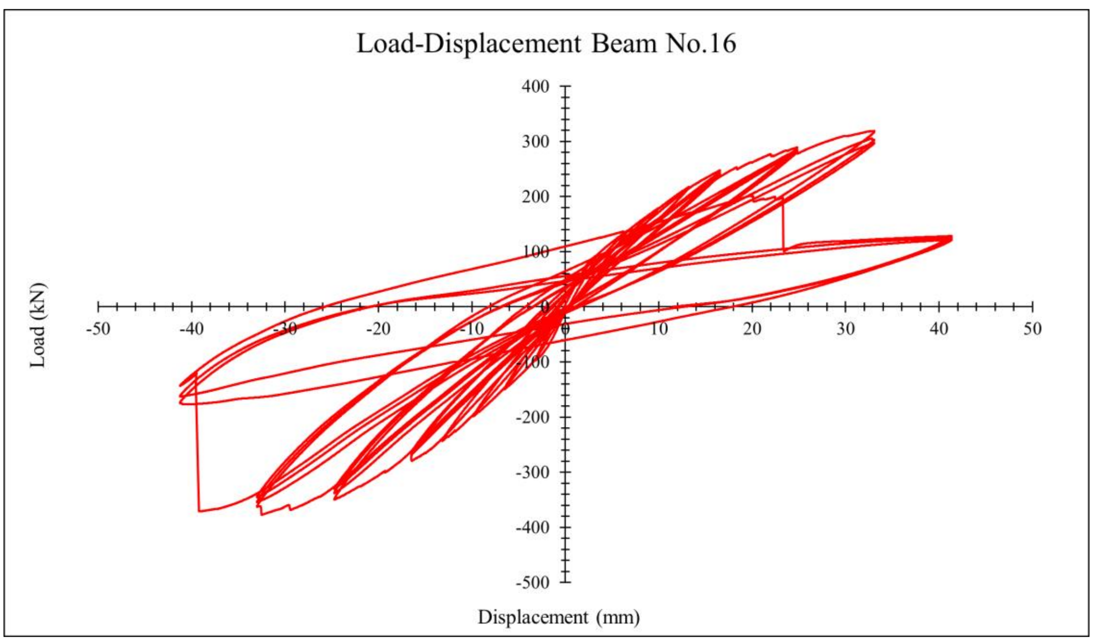

Figure 5.29. Load-displacement response of beam No.16 (1 Kips=4.45 KN)

Figure 5.30. Failure mode of beam No.16.

5.4.2. Failure Modes

The tested beams exhibited various failure modes, ranging from excessive yielding to CFRP sheet rupture. An excessive yielding failure was observed in the response of the control specimens, beam No.1 and No.10, as was expected since there was an absence of the CFRP strengthening material, Figures 5.14 and 5.23. Additionally, beam No.6 experienced a shear failure within the shear span, attributed to both low concrete compressive strength and the lack of sufficient shear reinforcement, as shown in Figure 5.17. According to a study conducted by (Arslan. 2012), concrete contribution to the ultimate shear capacity is negligible under reversed cyclic load after the occurrence of first X-shaped shear crack, leading to the failure of beam No.6 at a load of approximately 260.00 kN (58.45 kips), nearly equal to the predicted shear capacity of transverse steel using the ACI method. On the other hand, Beam No. 7 experienced a different failure mode due to the provided shear strengthening. As evident from Figure 5.20, unlike beam No. 6, beam No. 7 failed due to the propagation of vertical cracks which occurred within the shear strengthening of the CFRP sheet, in-between the fiber anchors. Although the beam did not fail in flexure, there was a significant enhancement in its ultimate capacity compared to its twin, beam No. 6, as a result of the provided shear strengthening as well as short steel fuse within the plastic hinge region.

Furthermore, beam No.15 failed due to a combination of shear and concrete cover separation within the shear span, as illustrated in Figure 5.26. Despite expectations of a similar failure mode to its twin, beam No.6, beam No.15 demonstrated a higher ultimate capacity. This was attributed to the use of larger rebar sizes and double the concrete compressive strength, resulting in a noticeable contribution of concrete to its ultimate capacity. Future research could explore concrete contribution to the shear capacity of strengthened RC beams under reversed cyclic load.

Beam No. 16 exhibited a unique failure mode, failing due to the rupture of the CFRP sheet on the top face at the loading point in the pull direction and the rupture of the end fiber anchor on the bottom face of the beam in the push direction, see Figure 5.30. Although beam No. 16 was provided with shear strengthening as well as a sandwiched steel plate, it showed only a slight improvement in ductility, energy dissipation, and ultimate capacity compared to beam No. 15. However, after failure, the advantages of using a short steel plate became evident: the hysteresis loops were wider, and the beam was able to sustain a load higher than the ultimate capacity of beam No. 10 (control beam).

5.4.3. Strength and Ductility

Control beams of both groups demonstrated the highest ductility and lowest ultimate capacity among all beams, see Figures 5.31 to 5.32 for the load-displacement envelope curves and peak displacement at failure of all specimens, respectively. It is important to notice that the use of low strength concrete as well as low steel ratio has a very clear effect on the overall performance of the tested specimens. Group A, with low concrete strength and low steel ratio, experienced less ultimate capacity as well as ductility; see Figures 5.32 and 5.33, respectively. It was also observed that the enhancement in the loading ultimate capacity was higher in group B than A due to the use of higher concrete strength and moderate steel ratio. For instance, when comparing beams No.6 and No.7 to the control beam (beam No.1), the load capacity was increased by 111% and 130%, respectively. In contrast, the ultimate loading capacity of beams No.15 and No.16 were enhanced by 223% and 252% compared to the control beam (beam No.10), respectively. Furthermore, the use of shear strengthening, and the sandwiched short steel plate had a noticeable impact on the load-displacement response of beams No.7 and No.16 in comparison with their twin beams No.6 and No.15. In fact, ultimate capacity and ductility of beam No.7 in comparison to beam No.6 were increased by about 8.3% and 33.33% respectively, see Figures 5.32 and 5.33. Likewise, beam No.16 exhibited improvement in the ultimate capacity by about 9% compared to beam No.15, but with a slight improvement in the ductility, see Figures 5.32 and 5.33. Additionally, Figures 5.34 and 5.35 demonstrate the hysteresis response comparisons between beams No.6 and No.7 as well as beams No.15 and No.16, respectively.

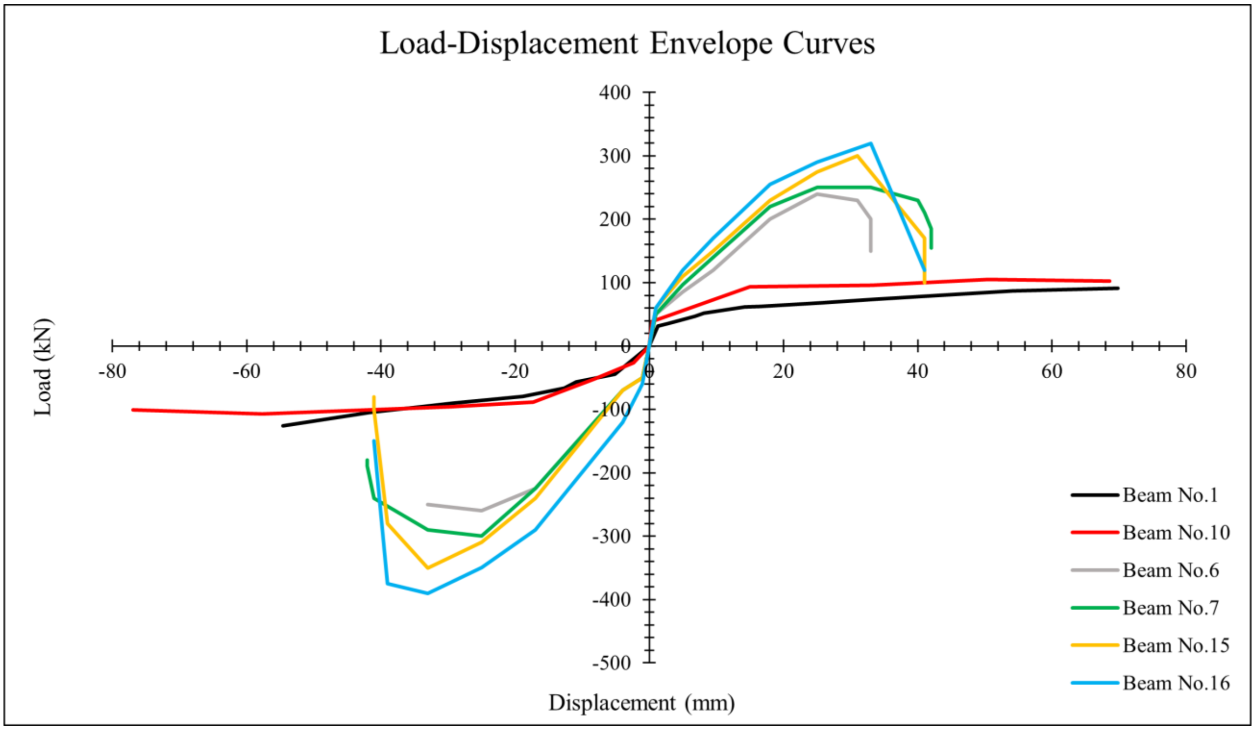

Figure 5.31. Load-displacement envelope curves of all specimens

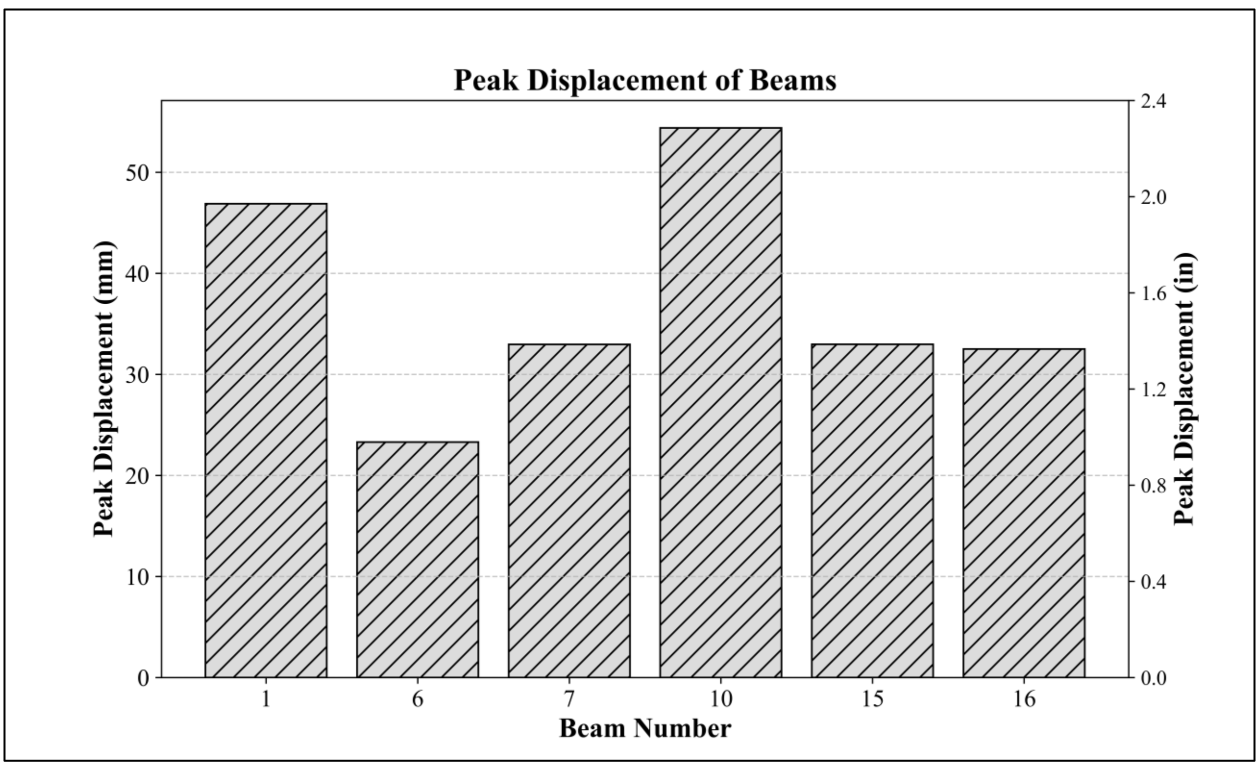

Figure 5.32. Peak displacement at failure of all specimens

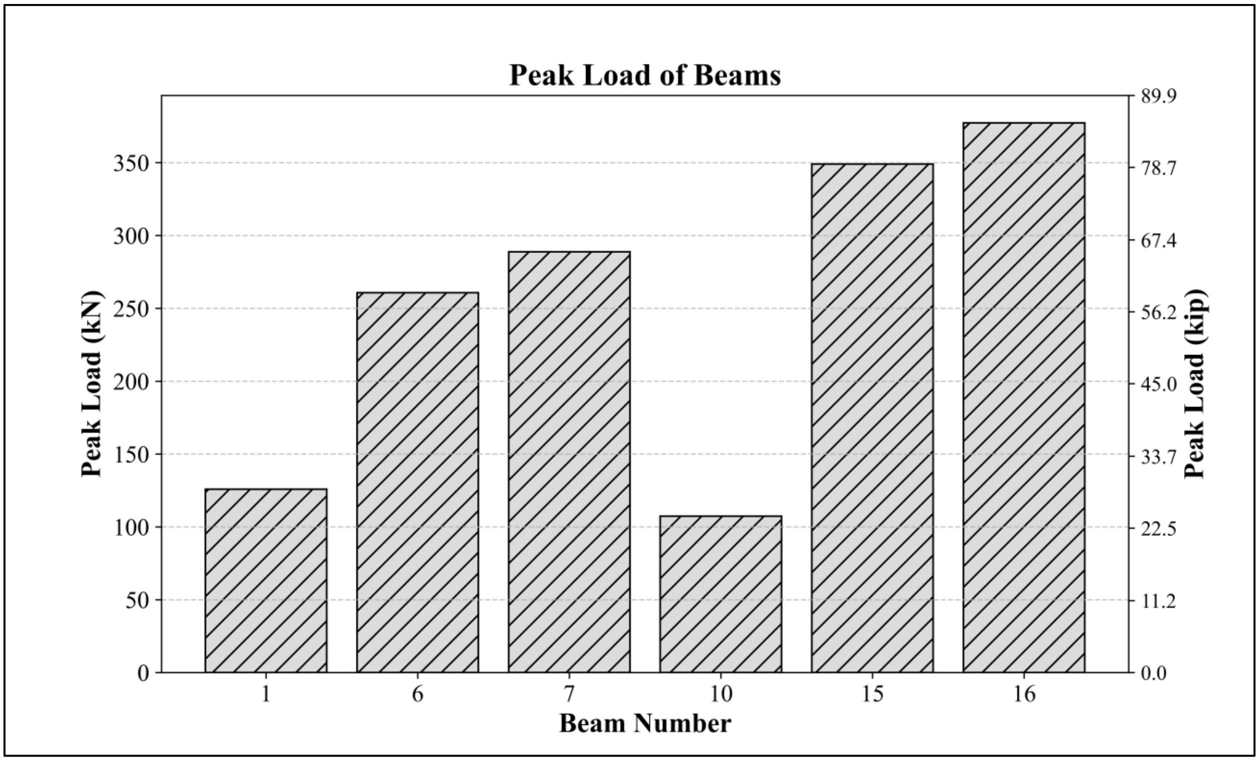

Figure 5.33. Peak load comparison of all specimens.

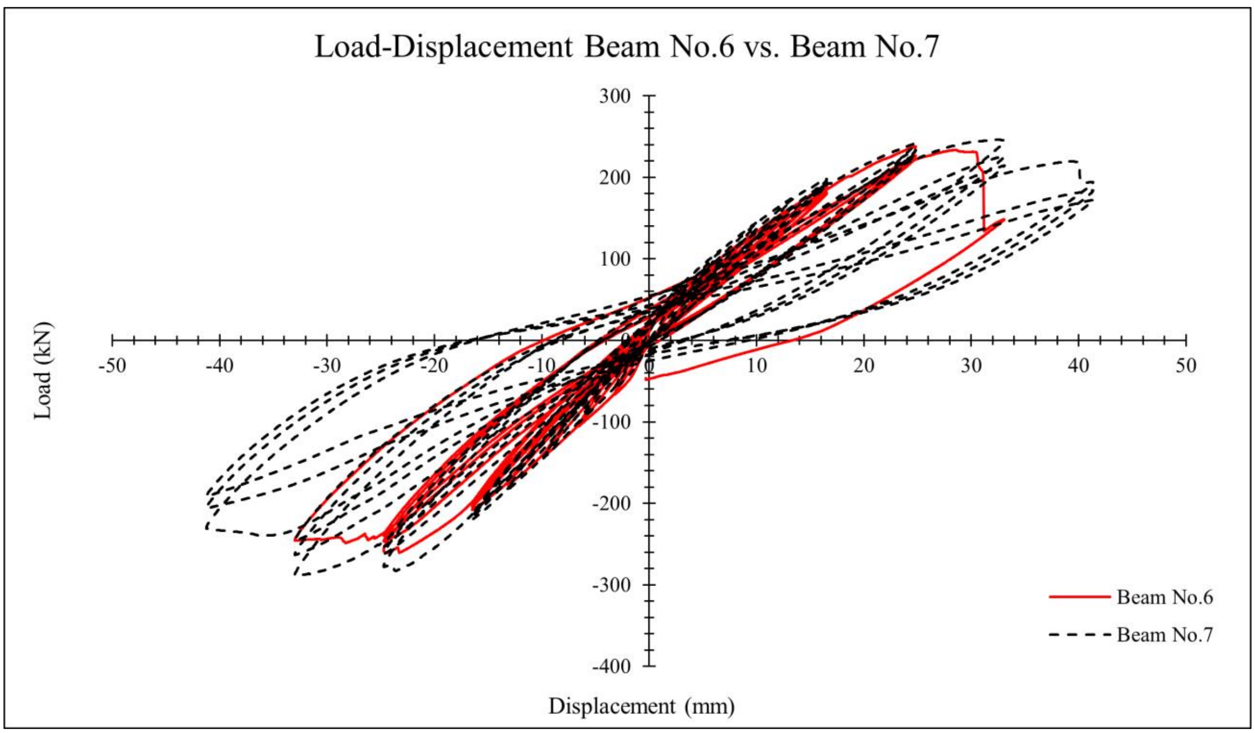

Figure 5.34. Hysteresis response of beams No.6 and No.7

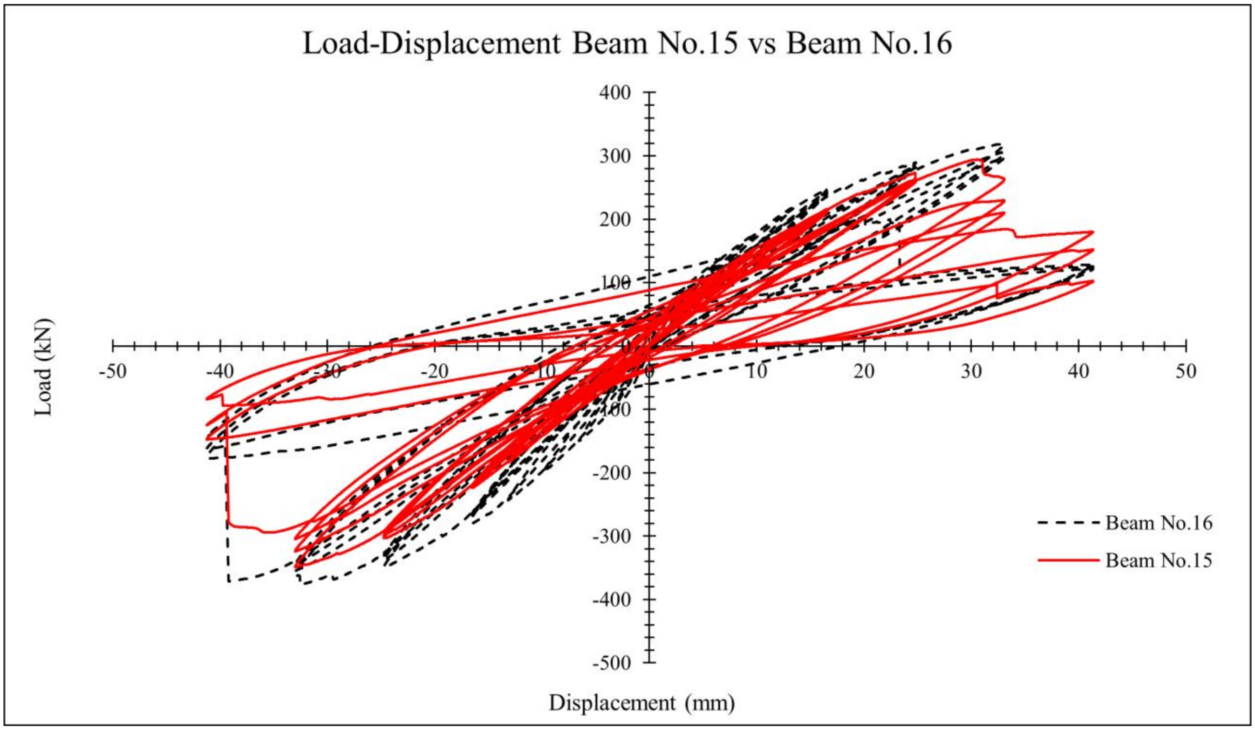

Figure 5.35. Hysteresis response of beams No.15 and No.16

5.4.4. Energy Dissipation

Control beams, beam No.1 and beam No.10, demonstrated energy dissipations of approximately 53,492.00 kN-mm (473,444.08 lb-in) and 67,791.00 kN-mm (600,000.00 lb-in), respectively, with beam No.10 exhibiting the highest energy dissipation among all tested beams, Figure 5.36. Beams No.6 and No.15, strengthened with two layers of CFRP secured with fiber anchors, displayed energy dissipations of approximately 11,298 kN-mm (100,000.00 lb-in) and 43,000 kN-mm (380,582.00 lb-in), respectively. Beams 7 and 16, which were strengthened with both CFRP and steel plates as well as shear strengthening, exhibited intermediate energy dissipation capacities, with beam No.7 achieving approximately 34,895.00 kN-mm (308,846.00 lb-in) and beam No.16 about 47,000.00 kN-mm (415,985.00 lb-in). These results highlight the fact that the control beams and the beams with combined CFRP and steel plate reinforcement exhibit significant energy dissipation capabilities. The use of CFRP and the sandwiched short steel plate to strengthen beams No.7 and No.16 provides a robust seismic strengthening solution, enhancing the structural performance of RC beams under cyclic loading. This combination can be particularly advantageous in applications requiring improved load-bearing capacity and energy absorption, contributing to the endurance and performance of structural elements. Figure 5.36 shows a comparison of energy dissipation of all tested specimens.

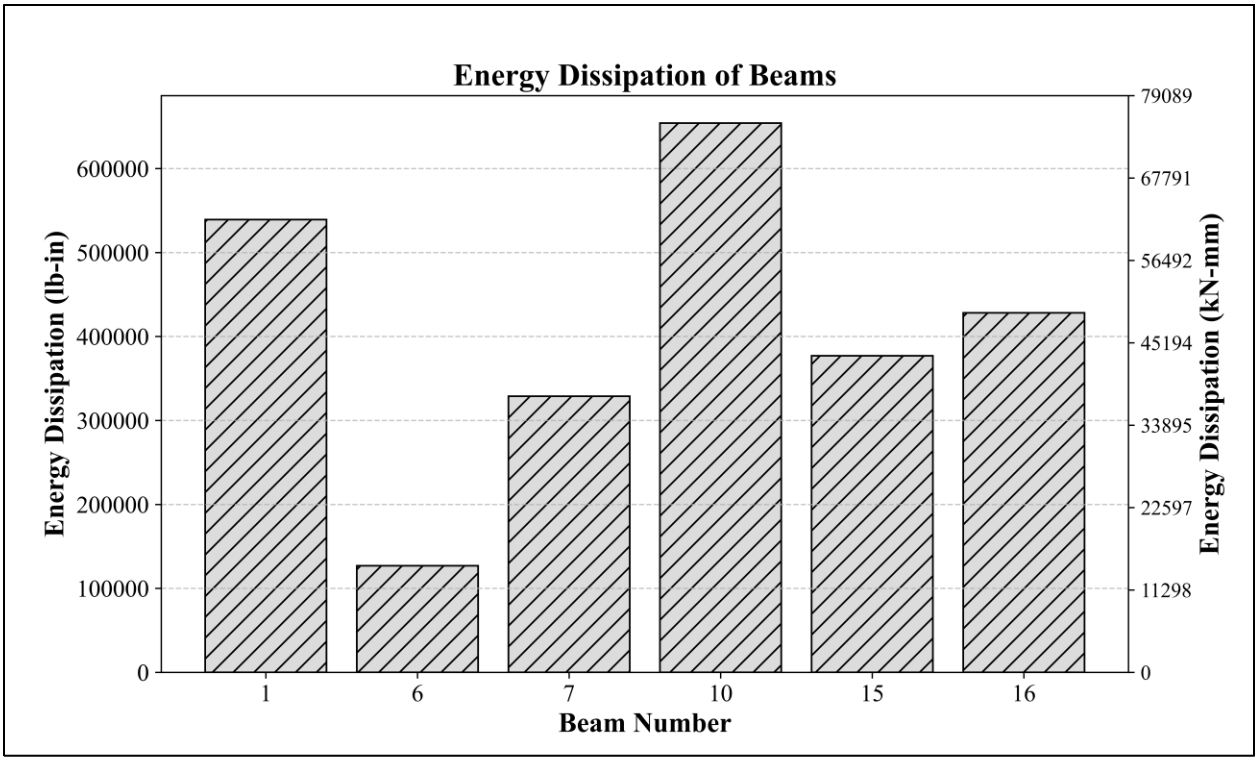

Figure 5.36. Energy dissipation comparison of all specimens[6].

5.4.5. Strains in CFRP Laminates and Steel Reinforcements

For the purpose of the analysis of the load-strain data, the strain data from CFRP sheets and steel reinforcements were collected using mid-span strain gauges, with each beam equipped with four

[6] Energy dissipation for CFRP strengthened beams is measured up to the failure of the strengthening system and not beyond that.

gauges for steel (top and bottom) and four for FRP (top and bottom). In this section, the load-strain results are investigated for beams No.6 and No.7 to distinguish the effect of using fused steel plate as well as shear strengthening on the strain responses. It was observed that the implementation of a sandwiched steel plate led to higher strain in both steel and FRP sheet, see Figures 5.37 to 5.44. Also, it is worth mentioning that the strain-load curve of reinforced steel shifts to positive strain after yielding under cyclic load due to the accumulation of plastic deformation or ratcheting effect. Initially, the steel deforms elastically, but once the load exceeds the yield point, it undergoes plastic deformation, causing permanent strain (Desayi et al. 1979 and Carrillo et al. 2023). On the other hand, in CFRP, the strain-load curve shifts to positive strain under cyclic loading primarily due to damage accumulation rather than plastic deformation (Paimushin et al. 2022). Unlike steel, which plastically deforms and ratchets under cyclic loading, CFRP accumulates micro-damage in the matrix and fibers. This damage leads to an increase in residual strain and a progressive shift of the strain-load curve towards positive strain, indicating internal material degradation and permanent deformation even if the external load is removed. Similar conclusions have been drawn regarding the load-strain responses of beams No.15 and No.16.

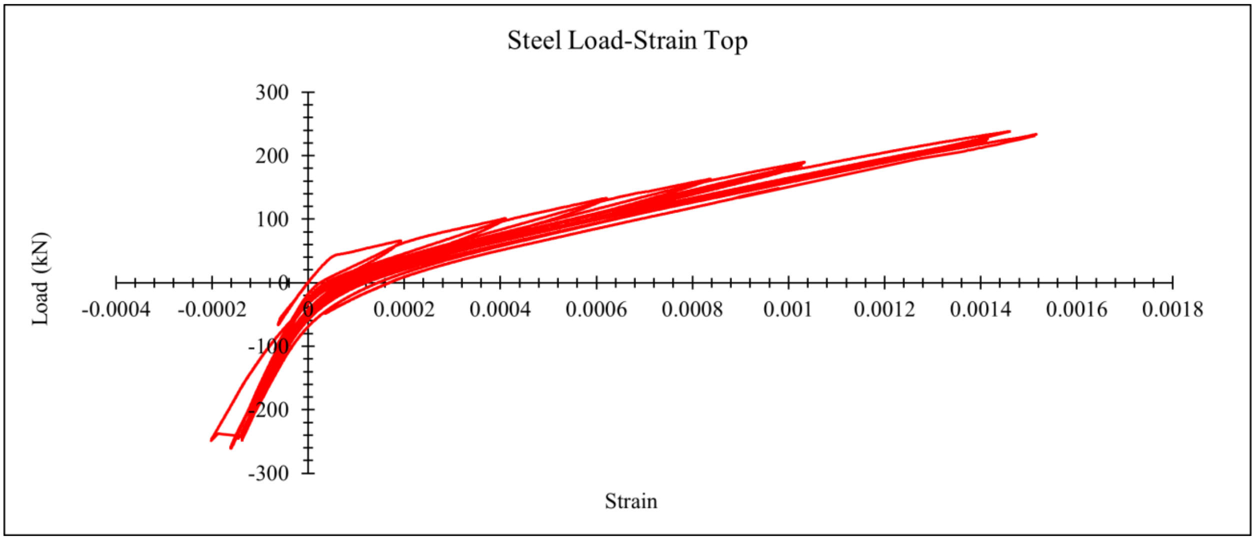

Figure 5.37. Load-strain response of top steel rebars of beam No.6

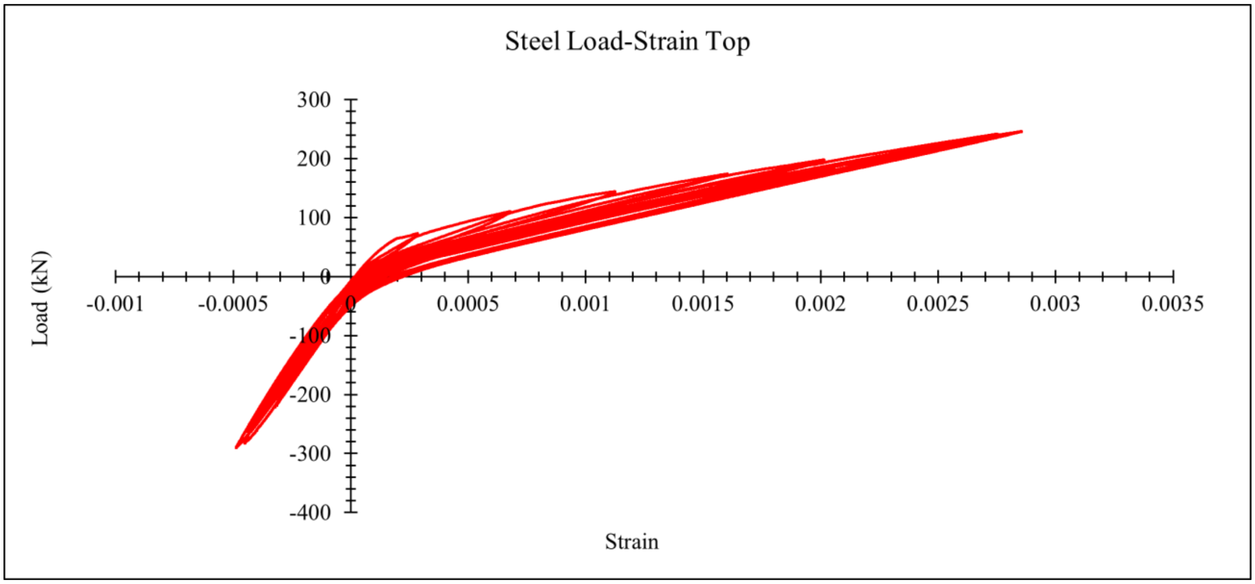

Figure 5.38. Load-strain response of top steel rebars of beam No.7

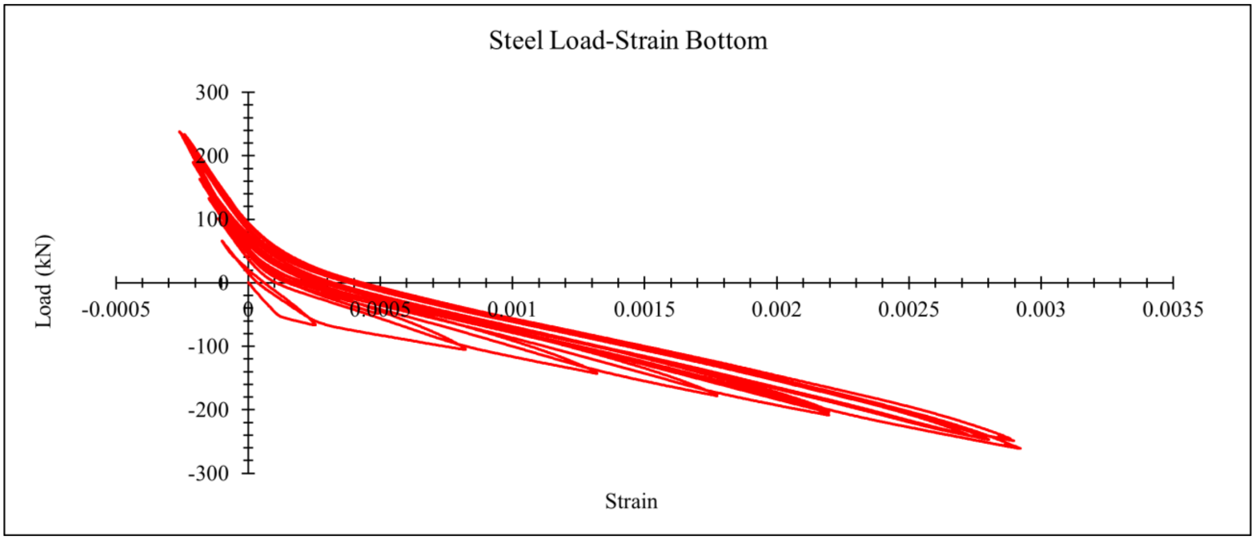

Figure 5.39. Load-strain response of bottom steel rebars of beam No.6

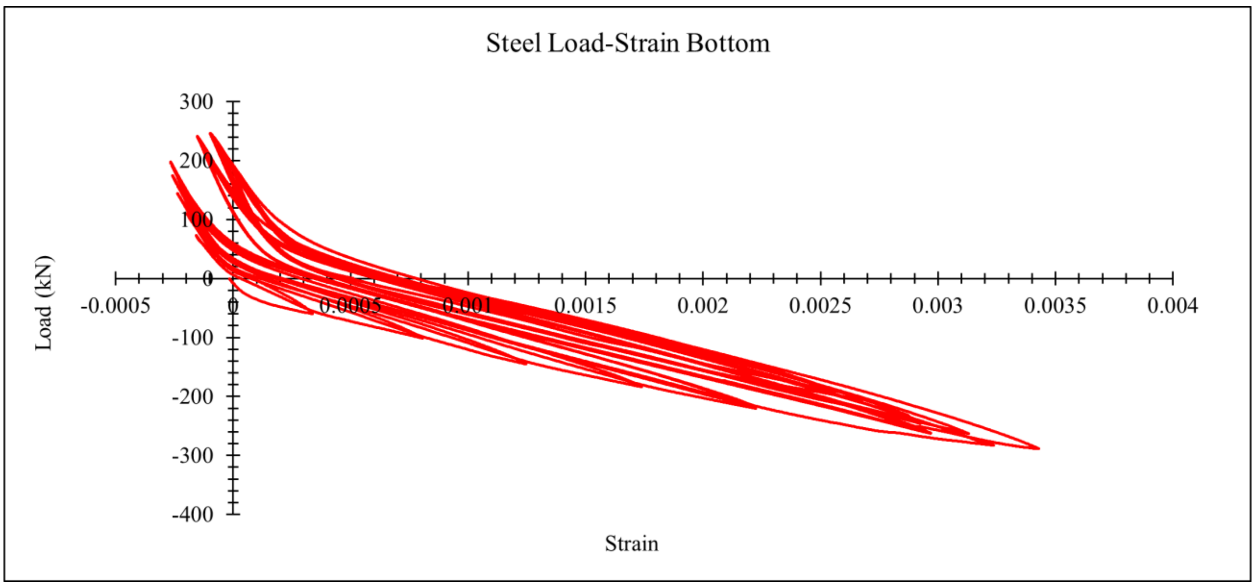

Figure 5.40. Load-strain response of bottom steel rebars of beam No.7

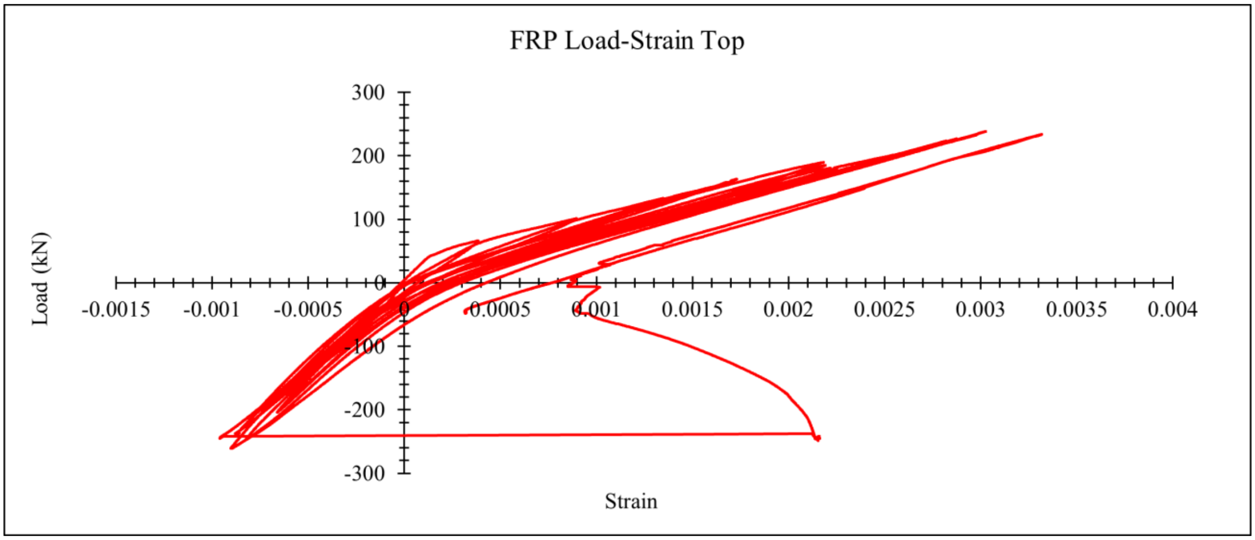

Figure 5.41. Load-strain response of top FRP sheet of beam No.6

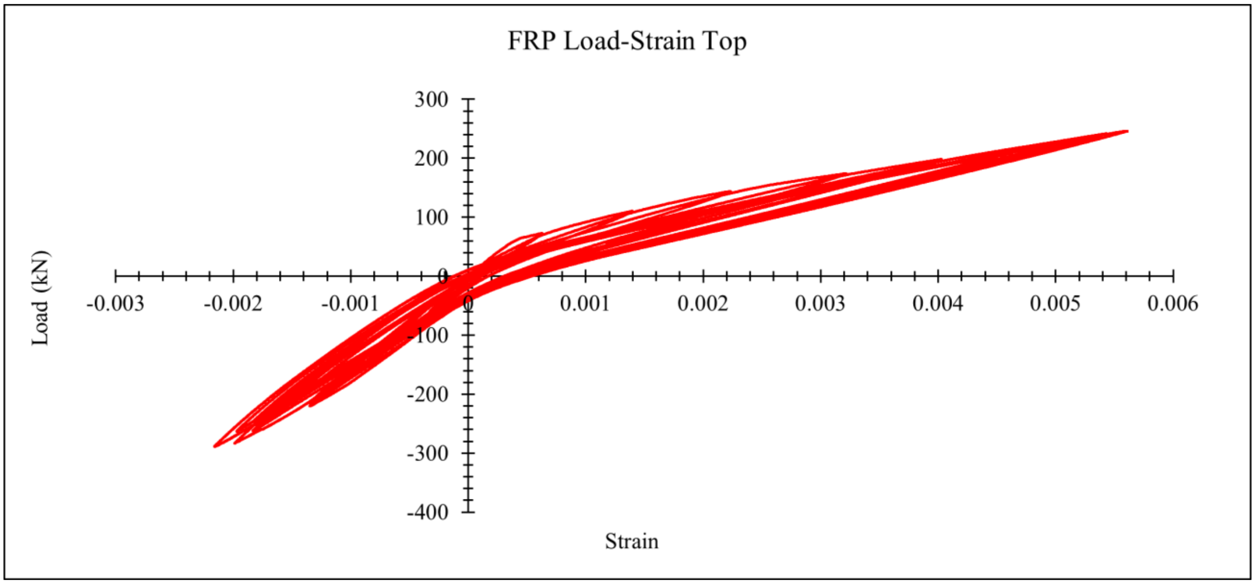

Figure 5.42. Load-strain response of top FRP sheet of beam No.7

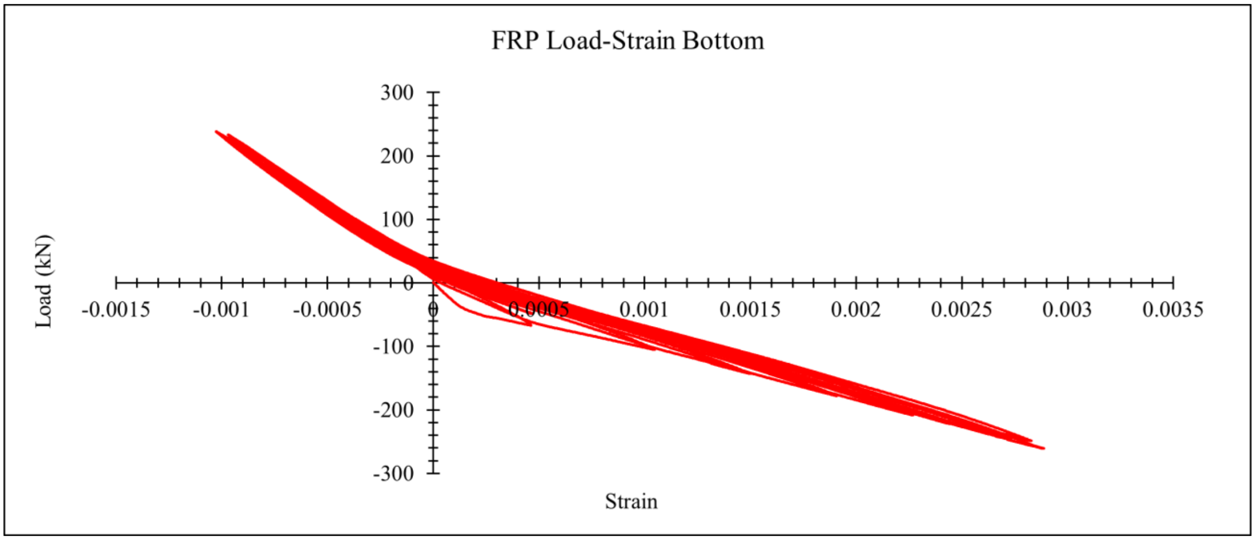

Figure 5.43. Load-strain response of bottom FRP sheet of beam No.6

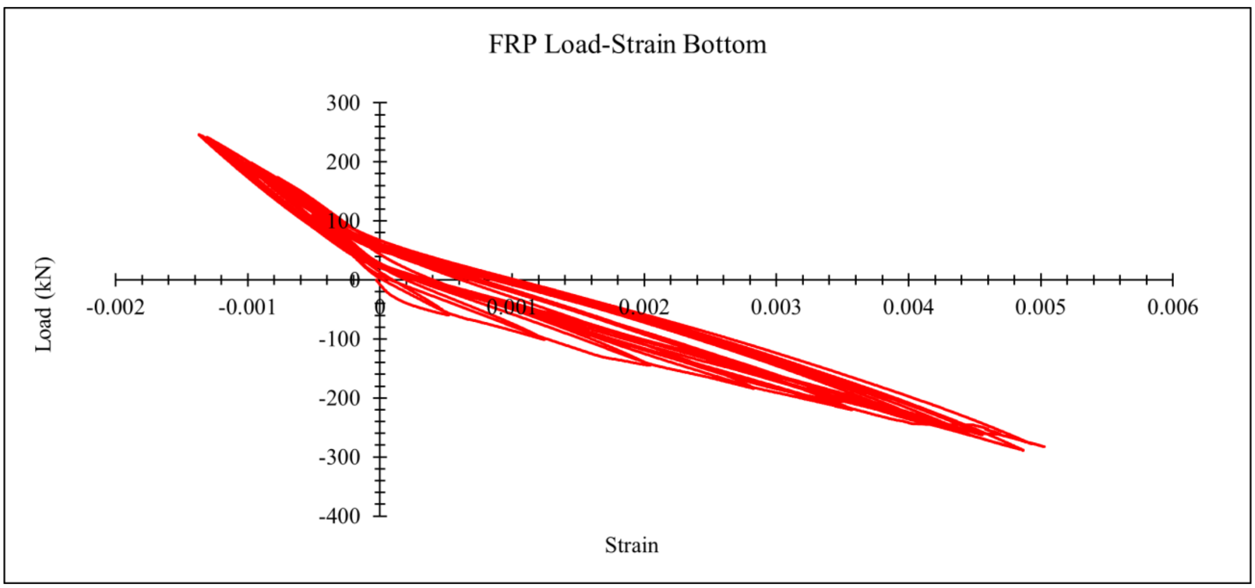

Figure 5.44. Load-strain response of bottom FRP sheet of beam No.7

5.5. Conclusions

In this chapter, a seismic investigation was performed on two groups of rectangular RC beams strengthened with double-thick CFRP sheets secured with fiber anchors to failure. Fuse steel plates were applied to twin beams with those of no plates to determine the improvement in cyclic response, if any. The following conclusions may be drawn from this study:

1- The higher the concrete compressive strength and reinforcement steel ratios, the higher the improvement in terms of energy dissipation, ultimate carrying capacity, and ductility compared to control beams.
2- For both groups, the use double-thick CFRP sheets significantly increased the ultimate capacity, but notably reduced the energy dissipation and ductility.
3- The utilization of shear strengthening, and the implementation of fuse stale plates Substantially improved the energy dissipation and moderately enhanced the ultimate capacity compared to the twin beams.
4- The use of fuse steel plate along with normal concrete strength and typical steel ration as well as shear strengthening was able to switch the failure mode from shear to flexural.
5- Failure modes were controlled by CFRP rupture within the shear span combined with fiber anchor rupture, excessive yielding of control beams, or shear failure within the shear span due to the lack of shear reinforcement.
6- For each group, the control beam had the highest ductility while the beam with a double-thick CFRP sheets combined with steel plate had the second highest ductility.
7- In future testing, it is recommended that extending the shear strengthening CFRP sheets to cover the area underneath the loading points to avoid failure at that point.

Chapter 6 - Experimental Observations for Future Analytical Modeling.

6.1. Introduction

Reinforced concrete (RC) beams are fundamental elements in structural engineering, providing essential support in various construction systems. Enhancing the performance and durability of these beams, especially under cyclic loading conditions, is a critical area of research. One effective method for improving the strength and ductility of RC beams is by externally bonding carbon fiber-reinforced polymer (CFRP) sheets. This chapter investigates the experimental observations that form the basis for future analytical modeling of the moment-curvature relationship of RC beams strengthened with CFRP under reversed cyclic loading, which can be integrated into analytical load-deflection response.

The primary focus of this chapter is investigating four distinct types of beams, each subjected to different CFRP reinforcement configurations, including thin CFRP, thick CFRP, double thick CFRP, and double thick CFRP with an additional sandwiched steel plate. By analyzing the load-strain curves of both steel and CFRP, as well as the moment-curvature and load-deflection responses of the beams, this investigation aims to provide a comprehensive understanding of the structural behavior of these enhanced beams under reversed cyclic loading conditions.

Through careful investigations, the load-strain relationships for steel and CFRP were examined to distinguish the material responses under cyclic loads. These observations are crucial for developing accurate and predictive analytical models of RC beam behavior. Additionally, the moment-curvature curves were inspected to understand how different CFRP configurations affect the bending performance of the beams.

The load-deflection responses of the beams were also thoroughly investigated. These measurements offer insights into the overall stiffness, ductility, and energy dissipation capabilities of the CFRP-strengthened beams.

By exploring these aspects, this chapter aims to contribute valuable data and insights for future computational or analytical models that can predict the moment-curvature behavior of RC beams with CFRP reinforcements under cyclic loading. Such models are essential for designing more resilient and efficient structural elements of reinforced concrete strengthened with FRP, ensuring safety and longevity in real-world applications.

6.2. Load-Strain Curves

Load-strain curves were carefully investigated to identify the local material behaviors of RC beams strengthened with various configurations of CFRP sheets, including main longitudinal steel and CFRP sheets within the midspan.

6.2.1. Steel Response

The load-strain responses of the longitudinal steel were constructed using the collected experimental data for the selected specimens (Beams No.3, No.4, No.6 and No.7). The following observations were found.

6.2.1.1. Thin FRP Sheet (Beam No.3)

According to the obtained data from analyzing the load-strain of beam No.3, which was strengthened with a thin singular CFRP sheet on top and bottom, it is clear that after the applied load reached the yielding value, the strain hysteretic loops shifted to a positive strain, see Figures

6.1 to 6.2 for top and bottom steel, respectively. The strain-load curve of reinforcing steel shifts to positive strain after yielding under reversed cyclic load due to the accumulation of plastic deformation or ratcheting effect. Initially, the steel deforms elastically, but once the load exceeds the yielding point, it undergoes plastic deformation, causing permanent strain (Desayi et al. 1979 and Carrillo et al. 2023). Under cyclic loading, the material experiences progressive accumulation of plastic strain or ratcheting, especially in asymmetric cycles. This leads to an increase in residual strain, causing the strain-load curve to shift to positive strains, indicating that the material has undergone permanent deformation even when the load is removed. According to the literature, metallic materials exhibit four different behaviors depending on the stress limits: elastic, elastic shakedown, plastic shakedown, and ratcheting, see Figure 6.3. (Coleman 2014, Dirks 2015, and Dollevoet 2010)

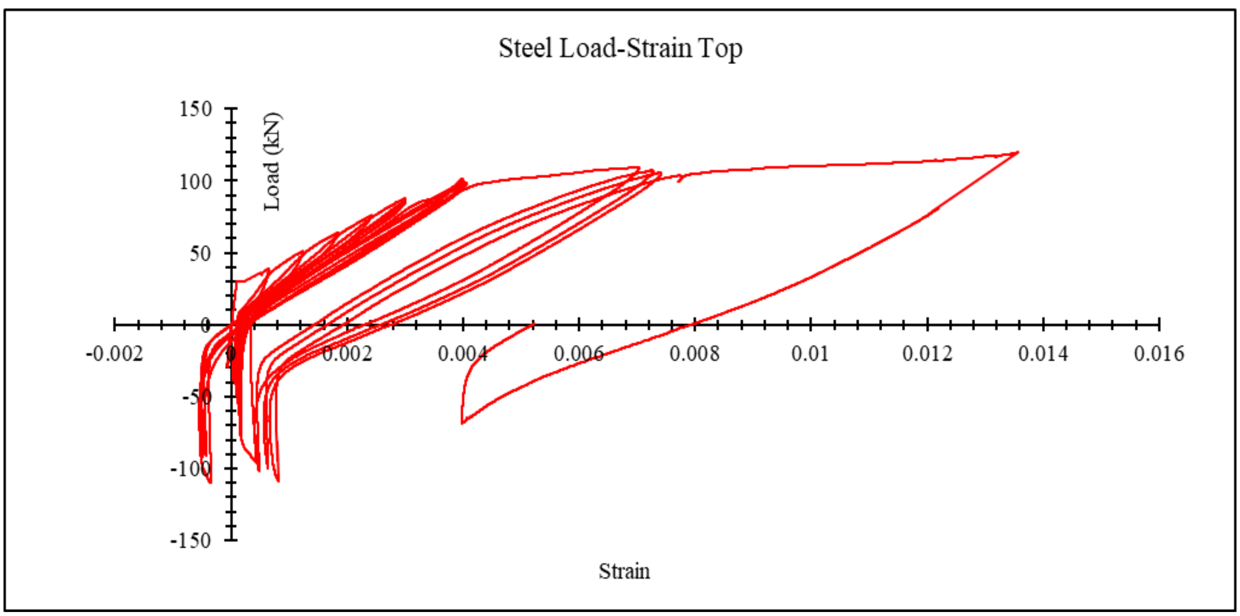

Figure 6.1. Load-strain response of top steel rebars of beam No.3

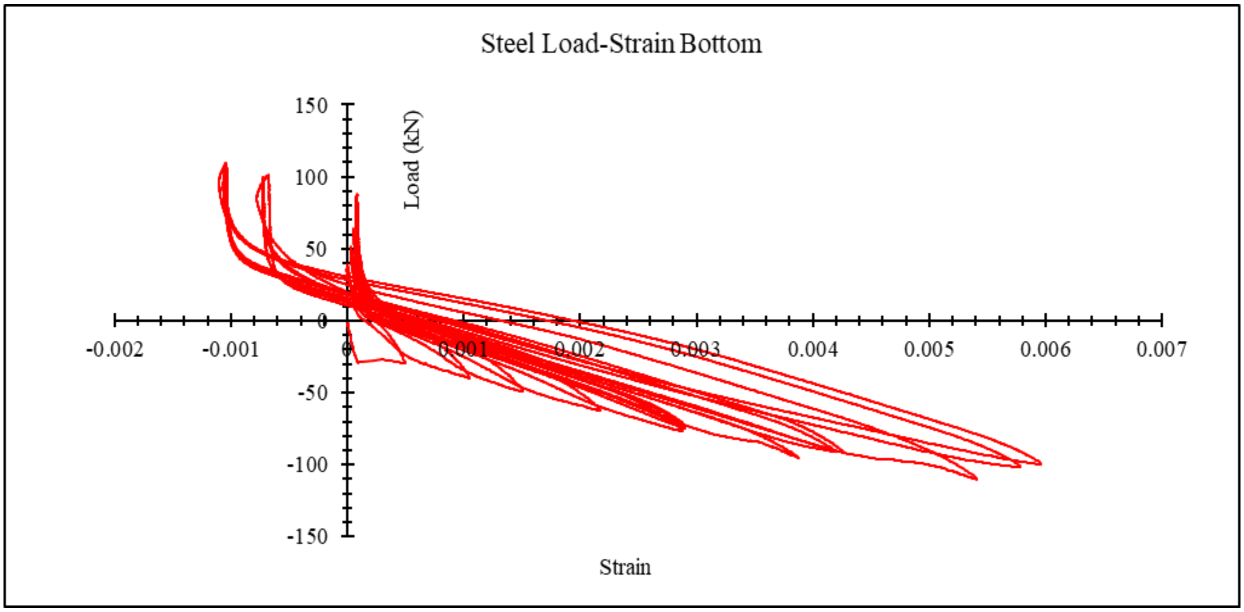

Figure 6.2. Load-strain response of bottom steel rebars of beam No.3

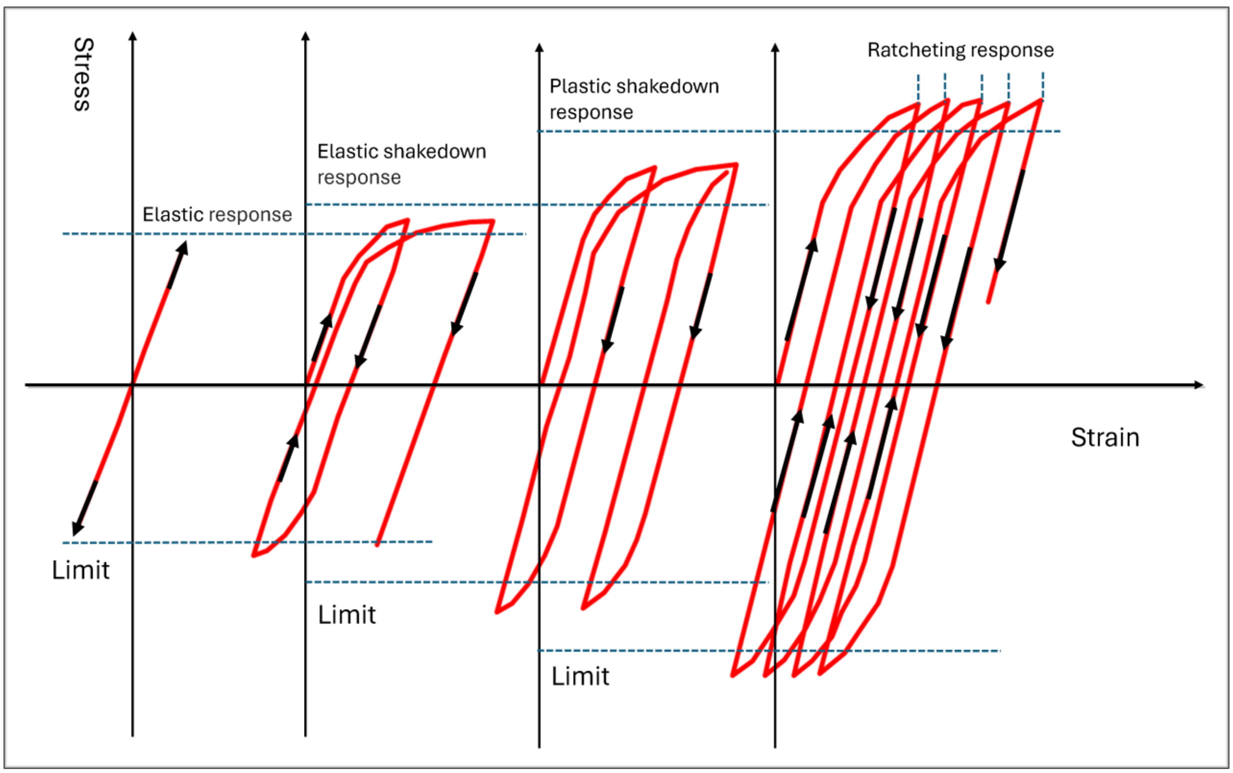

Figure 6.3. Material response to cyclic loading: (a) purely elastic deformations, (b) elastic shakedown, (c) plastic shakedown and (d) ratchetting adapted from (Dollevoet, 2010).

6.2.1.2. Thick FRP Sheet (Beam No.4)

The application of thick CFRP sheets had a clear impact on the longitudinal steel load-strain curve of beam No.4. Based on the experimental data, the use of thick CFRP caused the steel to experience less strain prior to yielding and significant plastic deformation compared to the use of thin CFRP, as shown in Figures 6.1 to 6.2 versus Figures 6.4 to 6.5, respectively. As a result, the application of thick CFRP sheets allowed the beams to withstand a higher load capacity beyond yielding, which led to substantial plastic deformation, see Figures 6.4 to 6.5. Moreover, this plastic deformation was significant, leading to a noticeable shift of the load-strain loops towards the positive side, as depicted in Figures 6.4 to 6.5.

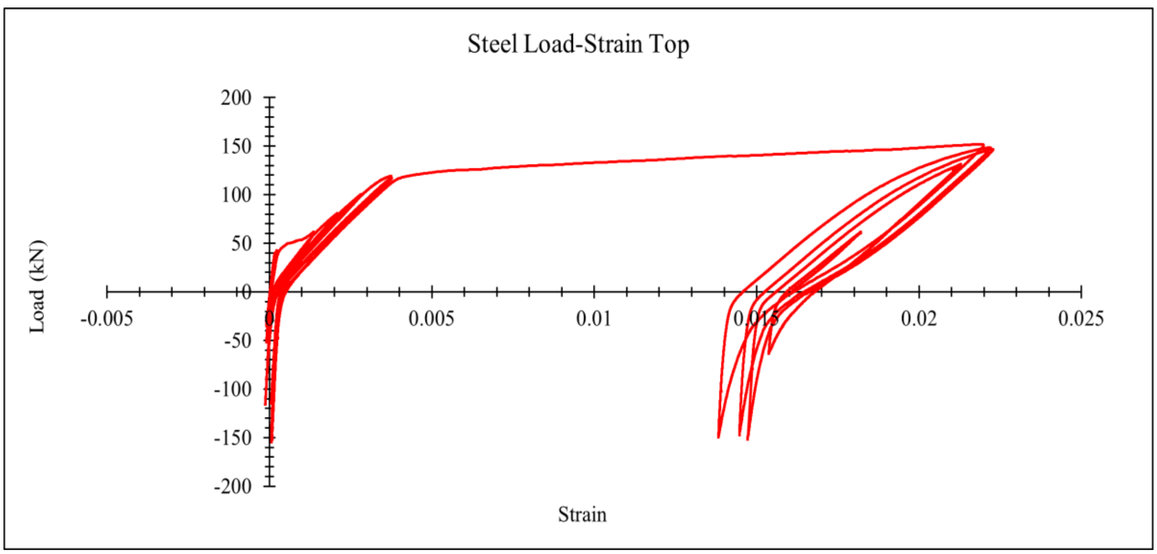

Figure 6.4. Load-strain response of top steel rebars of beam No.4

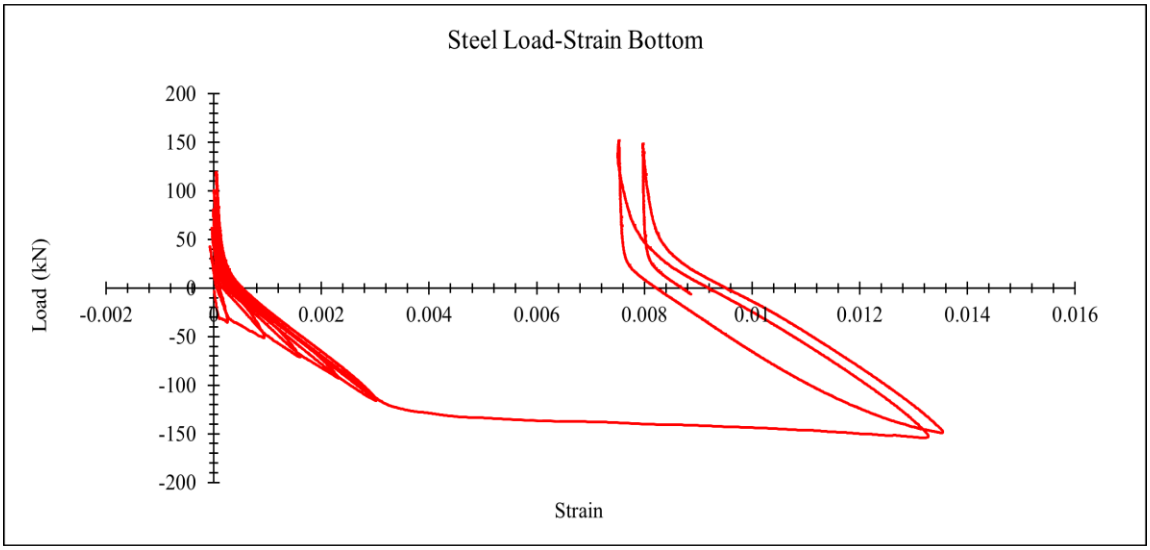

Figure 6.5. Load-strain response of bottom steel rebars of beam No.4

6.2.1.3. Double-Thick FRP Sheet (Beam No.6)

Using multiple layers of thick CFRP sheets instead of a single layer had a clear effect on the load-strain response of longitudinal steel. As Figures 6.6 to 6.7 demonstrate, both the top and bottom steel layers exhibited lower strain compared to a single thin or thick CFRP sheet. This is due to the constraints provided by the double CFRP sheets, which help to distribute the load more effectively and reduce the strain on the steel. Additionally, the CFRP loading points in phase one testing act as equivalent anchors, providing further restraint. Consequently, beams No. 3 and No. 4 withstood higher loads than expected. Additionally, the top steel layer did not reach the yielding strain of 0.00282, while the bottom steel layer nearly yielded. This asymmetry could be attributed to the variable clear cover of the top and bottom steel, which were 2 inches and 1.5 inches, respectively. Moreover, no significant plastic deformation was observed, as indicated by the low strain values.

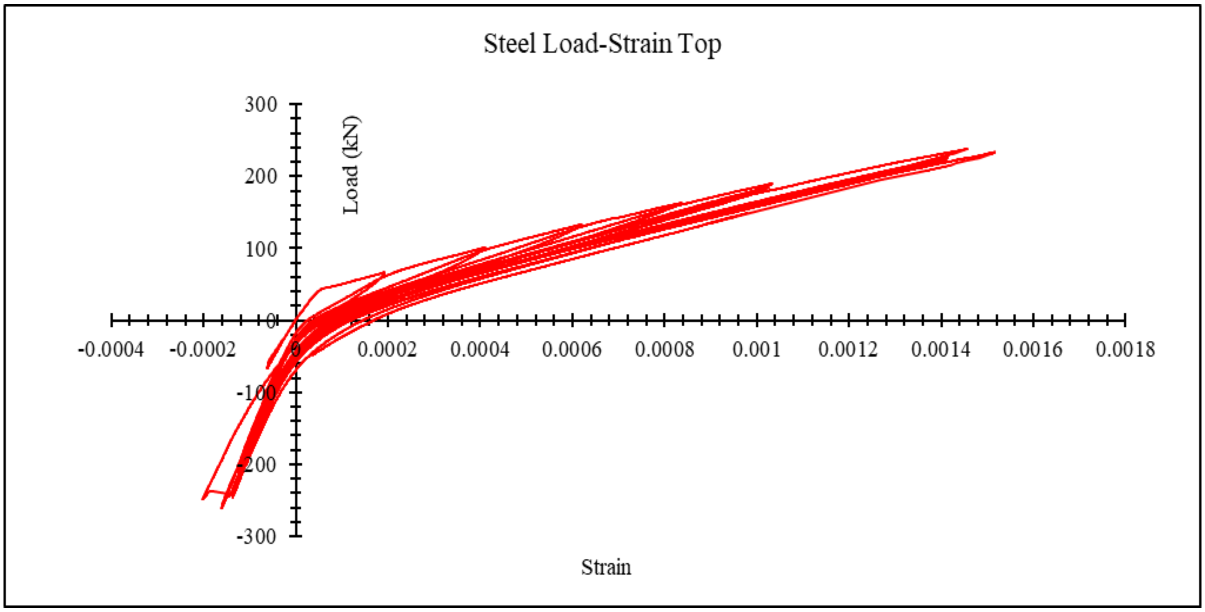

Figure 6.6. Load-strain response of top steel rebars of beam No.6

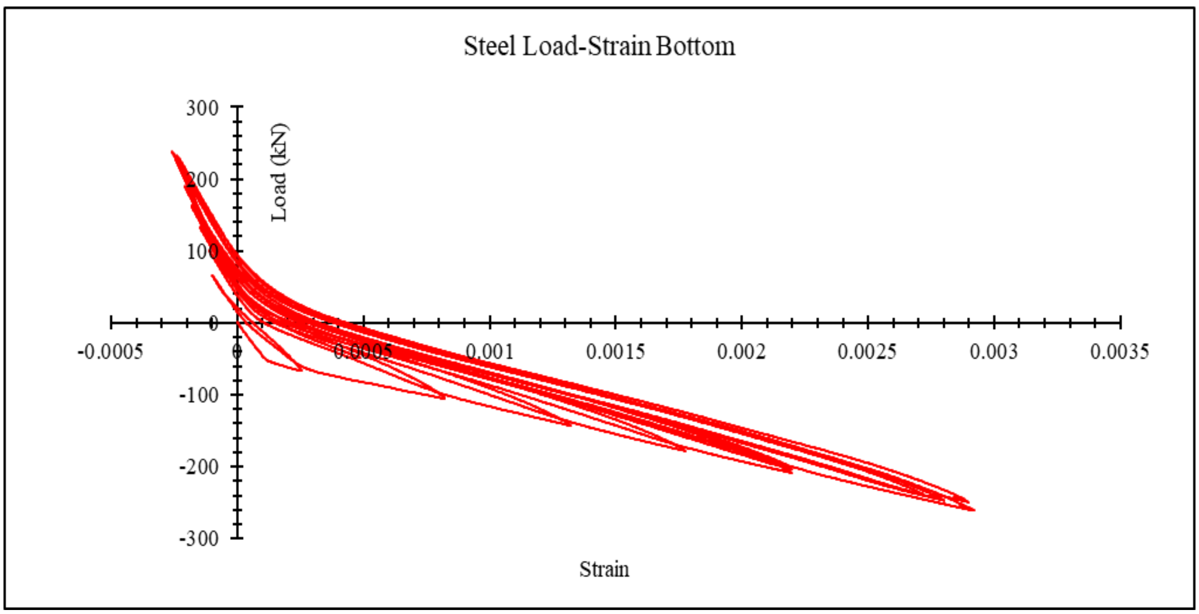

Figure 6.7. Load-strain response of bottom steel rebars of beam No.6

6.2.1.4. Double-Thick FRP Sheet with Sandwiched Steel Plate (Beam No.7) Plus CFRP Shear Strengthening

Unlike the impact of using double-thick CFRP sheets, the implementation of fused steel within the constant moment region affected the strain of the longitudinal steel in the opposite way due to extending the response by using CFRP shear strengthening. In fact, according to the load-strain data, it was observed that steel experienced higher strain when compared to the use of a double-thick sheet without fused steel, see Figures 6.6 to 6.9. That can be attributed to the fact that the utilization of sandwiched steel plate provided the beam with more ductility which eventually increased the strain in the presence of shear strengthening in the shear span. Conversely, similar conclusions have been drawn regarding the relationship between the thickness of the CFRP sheet and the plastic deformation of the steel, such that the larger the thickness, the higher the plastic deformation.

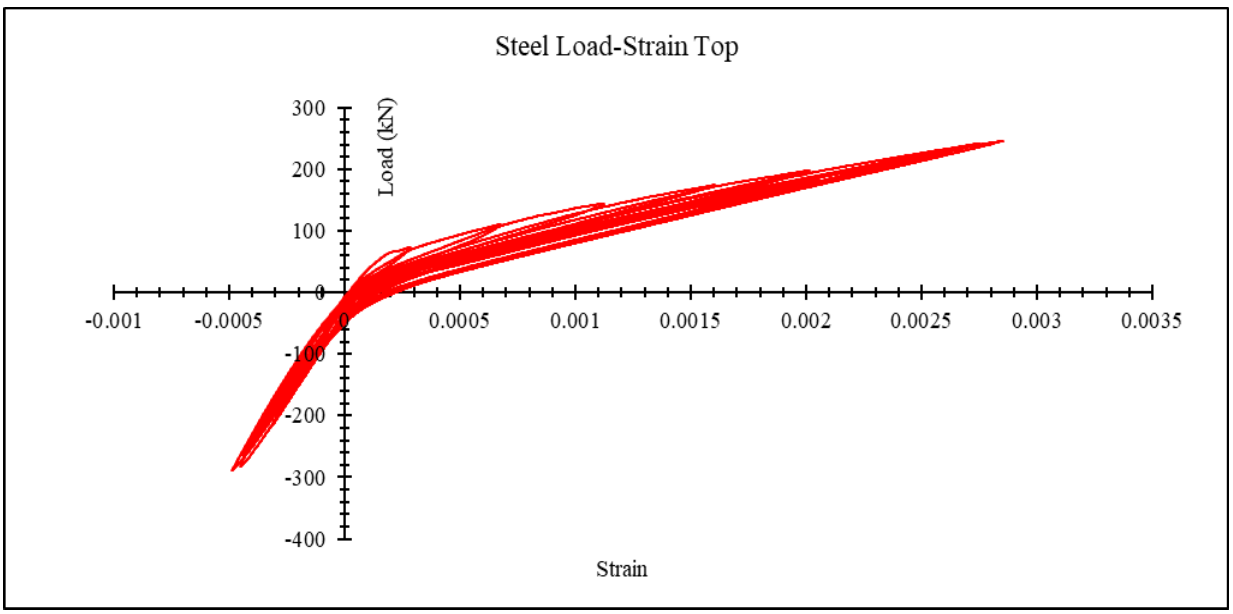

Figure 6.8. Load-strain response of top steel rebars of beam No.7

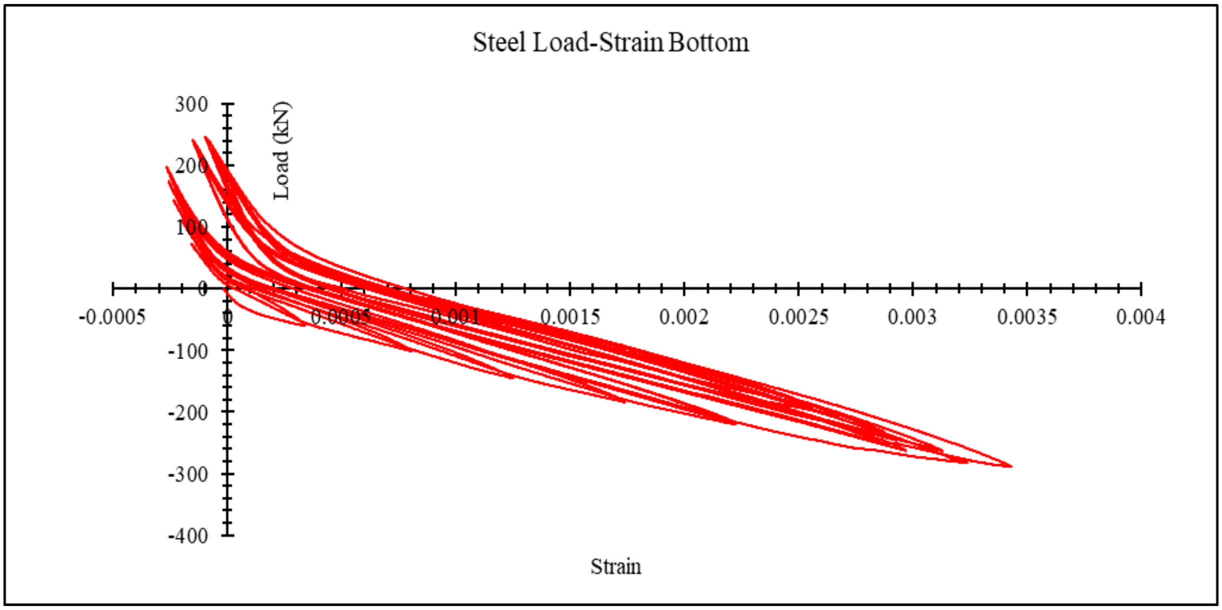

Figure 6.9. Load-strain response of bottom steel rebars of beam No.7

6.2.2. FRP Response

The load-strain curves of CFRP are presented in detail below.

6.2.2.1. Thin FRP Sheet (Beam No.3)

Similar observations were indicated when the CFRP load-strain data were analyzed. The strain of the CFRP sheet shifted to the positive direction as the applied load increased, see Figures 6.10 to 6.11 for top and bottom CFRP, respectively. In CFRP, the strain-load curve shifts to positive strain under cyclic loading primarily. The reason for that is the plastic deformation of internal steel that forces the CFRP to stretch more due to the intact bond at these levels rather than plastic deformation. Unlike steel, which plastically deforms and ratchets under cyclic loading, CFRP accumulates micro-damage in the matrix and fibers. This damage leads to an increase in residual strain and a progressive shift of the strain-load curve towards positive strain caused by steel rebars forcing the FRP to follow, indicating internal material degradation and permanent deformation even if the external load is removed.

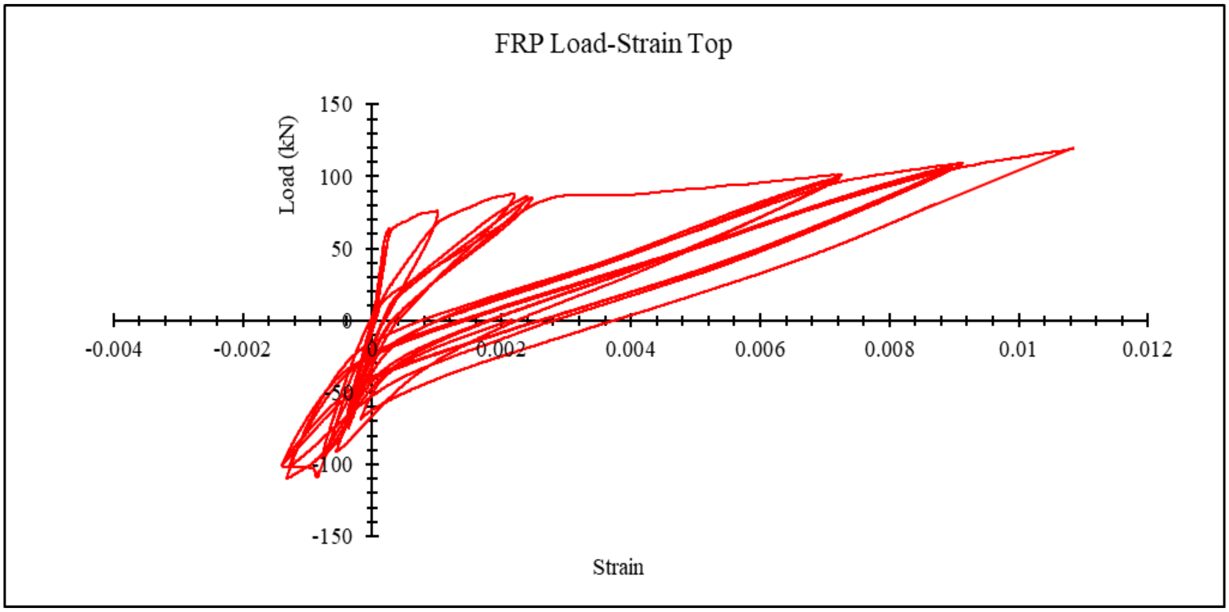

Figure 6.10. Load-strain response of top FRP sheets of beam No.3

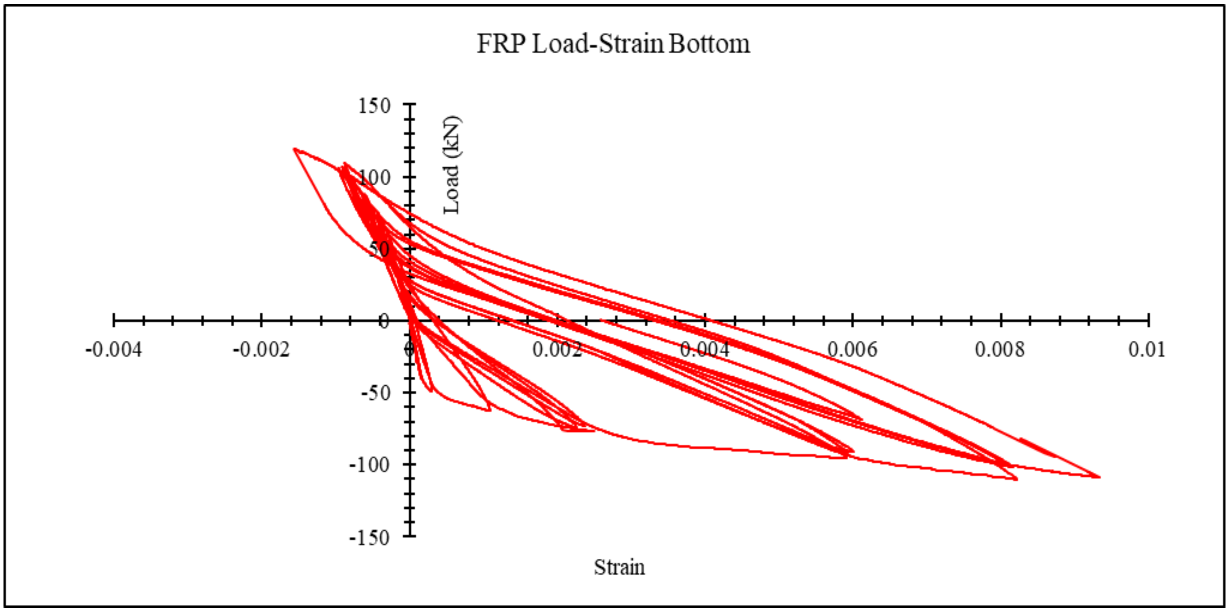

Figure 6.11. Load-strain response of bottom FRP sheets of beam No.3

6.2.2.2. Thick FRP Sheet (Beam No.4)

The implementation of thick CFRP sheets notably influenced the load-strain curve of beam No.4. Analyzing the experimental data showed that the thick CFRP sheets exhibited lower strain levels in comparison to the application of a thin CFRP, as indicated in Figures 6.10 to 6.11 versus Figures

6.12 to 6.13, respectively. This reduction in strain can be credited to the noticeable stiffness restraint offered by the thicker CFRP sheet. Similar to the behavior observed with thin CFRP sheets, the strain shifted towards the positive side of the load-strain curve which caused by the plastic deformation of internal steel that forces the CFRP to stretch more due to the intact bond at these levels.

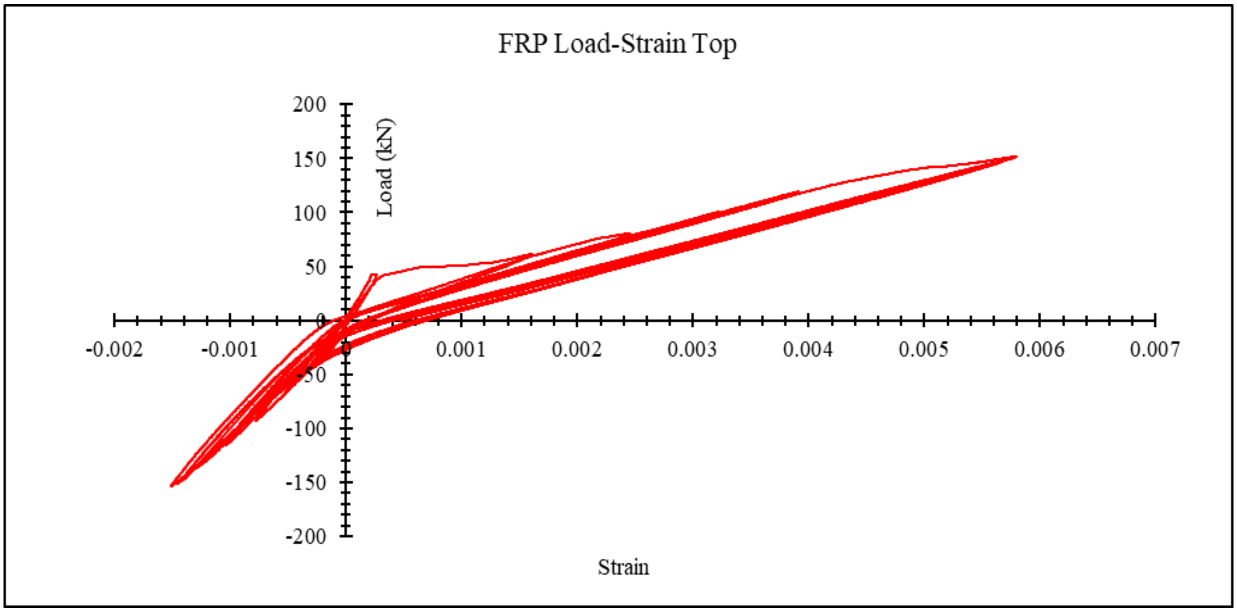

Figure 6.12. Load-strain response of top FRP sheets of beam No.4

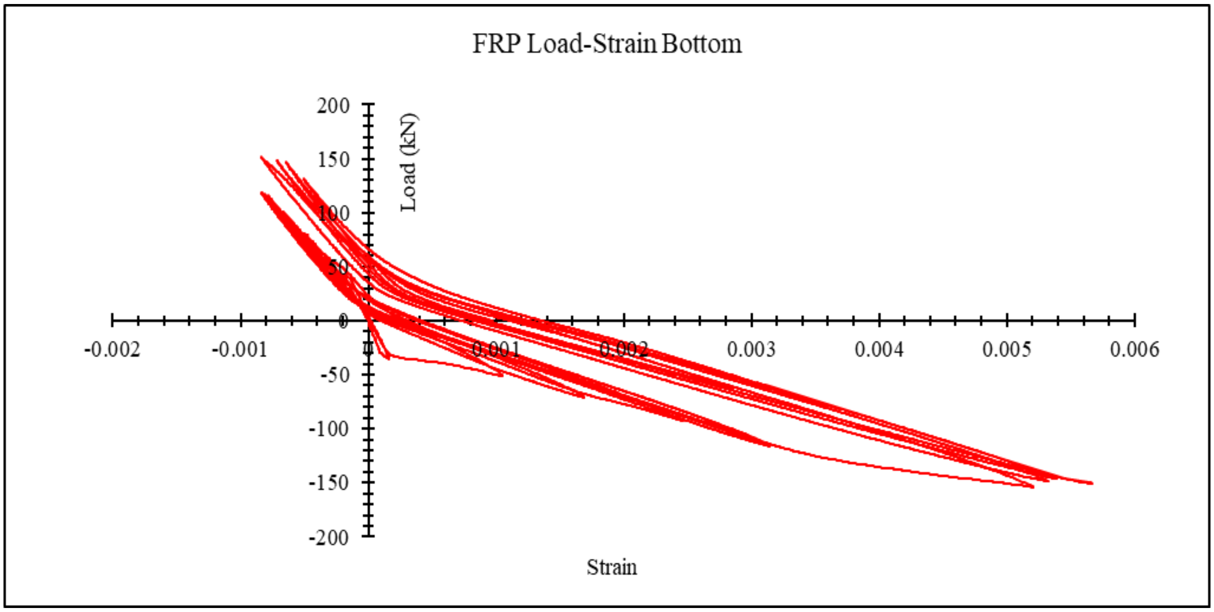

Figure 6.13. Load-strain response of bottom FRP sheets of beam No.4

6.2.2.3. Double-Thick FRP Sheet (Beam No.6)

The load-strain curves generated from FRP data showed that the strain at the extreme fiber of the beam strengthened with double-thick CFRP sheets was less than that of beams strengthened with single thin and thick CFRP sheets, as seen in Figures 6.14 to 6.15. It is evident that both CFRP and steel exhibited lower strain when multiple layers of thick CFRP sheets were implemented. Another observation related to the size of the strain hysteresis loops indicated that the thicker the sheets, the narrower the loops.

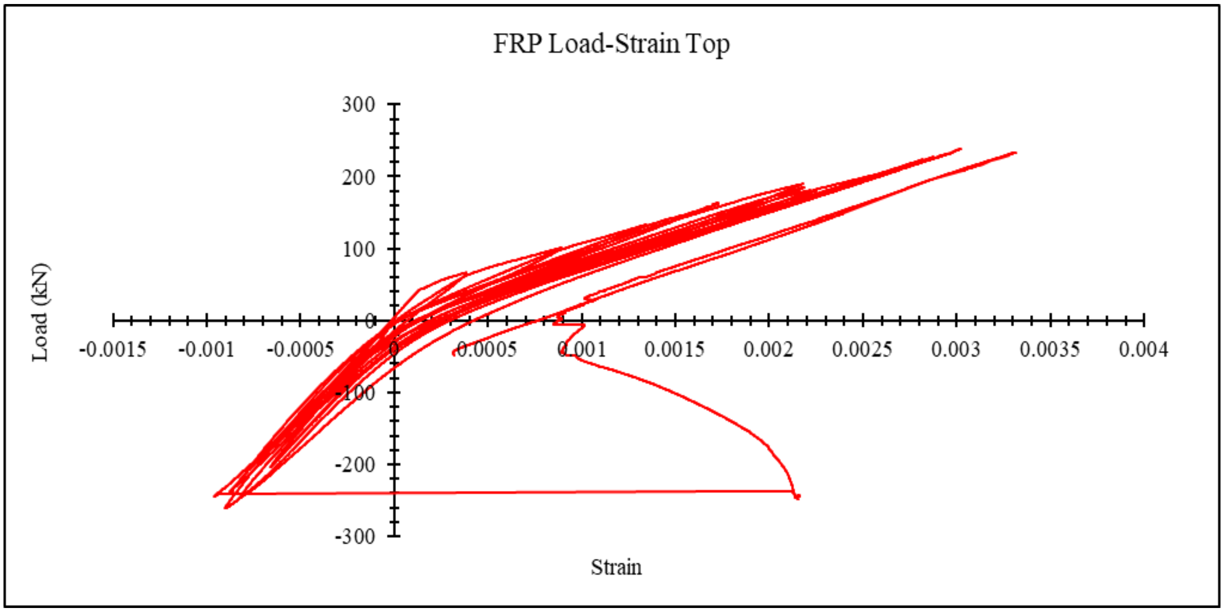

Figure 6.14. Load-strain response of top FRP sheets of beam No.6

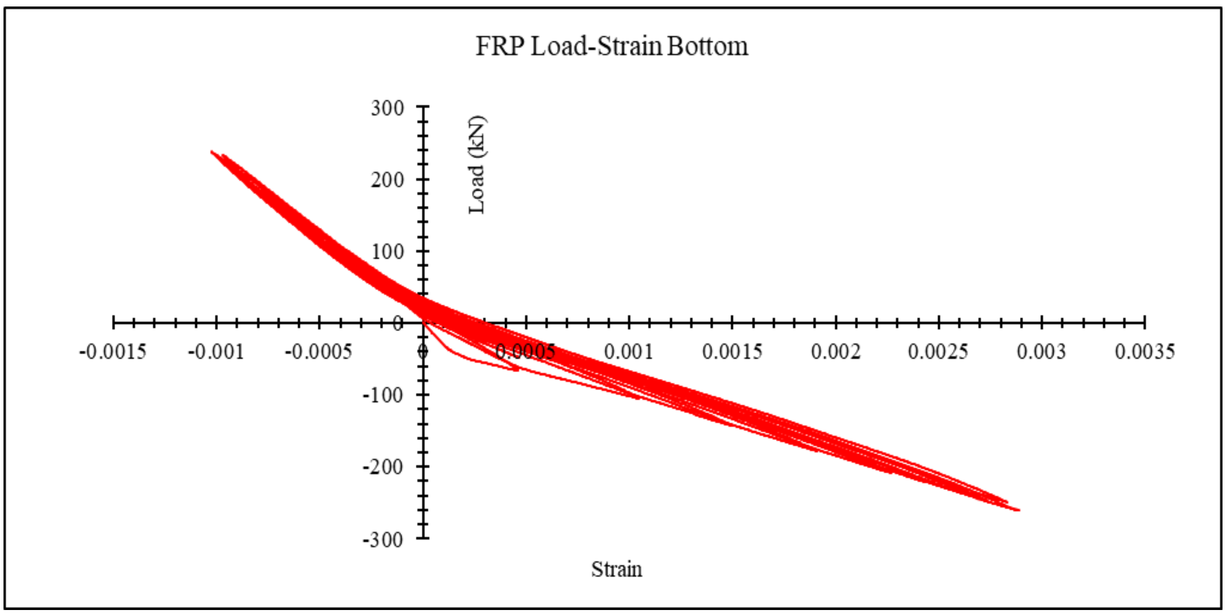

Figure 6.15. Load-strain response of bottom FRP sheets of beam No.6

6.2.2.4. Double-Thick FRP Sheet with Sandwiched Steel Plate (Beam No.7) Plus Shear Strengthening

Similar conclusions have been drawn regarding the load-strain response of CFRP sheets compared to longitudinal steel. Higher strain values were observed at the extreme fiber when compared to the use of double-thick CFRP sheets without a sandwiched steel plate, refer to Figures 6.16 and 6.17. Another important finding highlighted the impact of the steel plate on the width of the load-strain loops. Beam No.7, which was strengthened with a steel plate, exhibited wider loops compared to beam No.6.

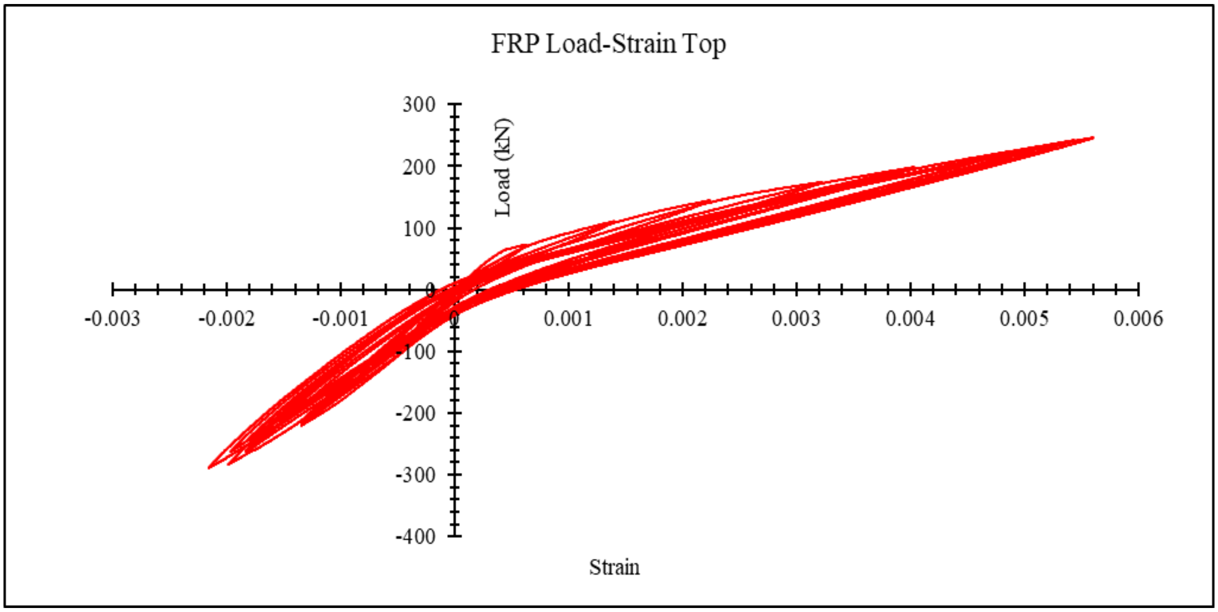

Figure 6.16. Load-strain response of top FRP sheets of beam No.7

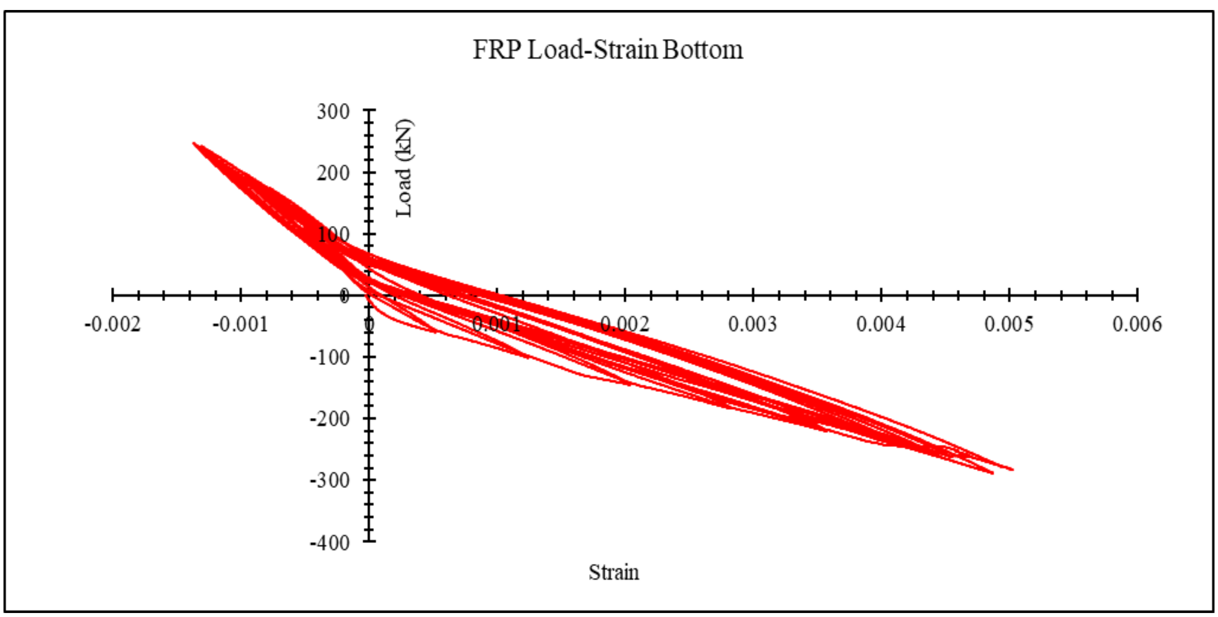

Figure 6.17. Load-strain response of bottom FRP sheets of beam No.7

6.3. Moment-Curvature Curves

The moment-curvature responses of the four RC strengthened beams were generated using the strain data collected from steel and CFRP. Subsequently, an analysis of the moment-curvature curves was conducted.

6.3.1. Steel Response

6.3.1.1. Thin FRP Sheet (Beam No.3)

Figures 6.18 to 6.19 illustrate the moment-curvature response of beam No.3 for several cycles before and after yielding. It was observed that there were no inflection points or flip points within the moment-curvature loops prior to the yielding of steel rebars, as shown in Figure 6.18. Additional observation was concluded, the hysteresis loops became narrower, and their shape varied post-yielding, as depicted in Figure 6.19. It is evident that the loops were no longer linear but became curved. This phenomenon could be attributed to the interaction between the yielding steel and the continuous restraint from CFRP, which could result in a curved moment-curvature relationship as the steel undergoes plastic deformations while the CFRP consistently and elastically resists forces.

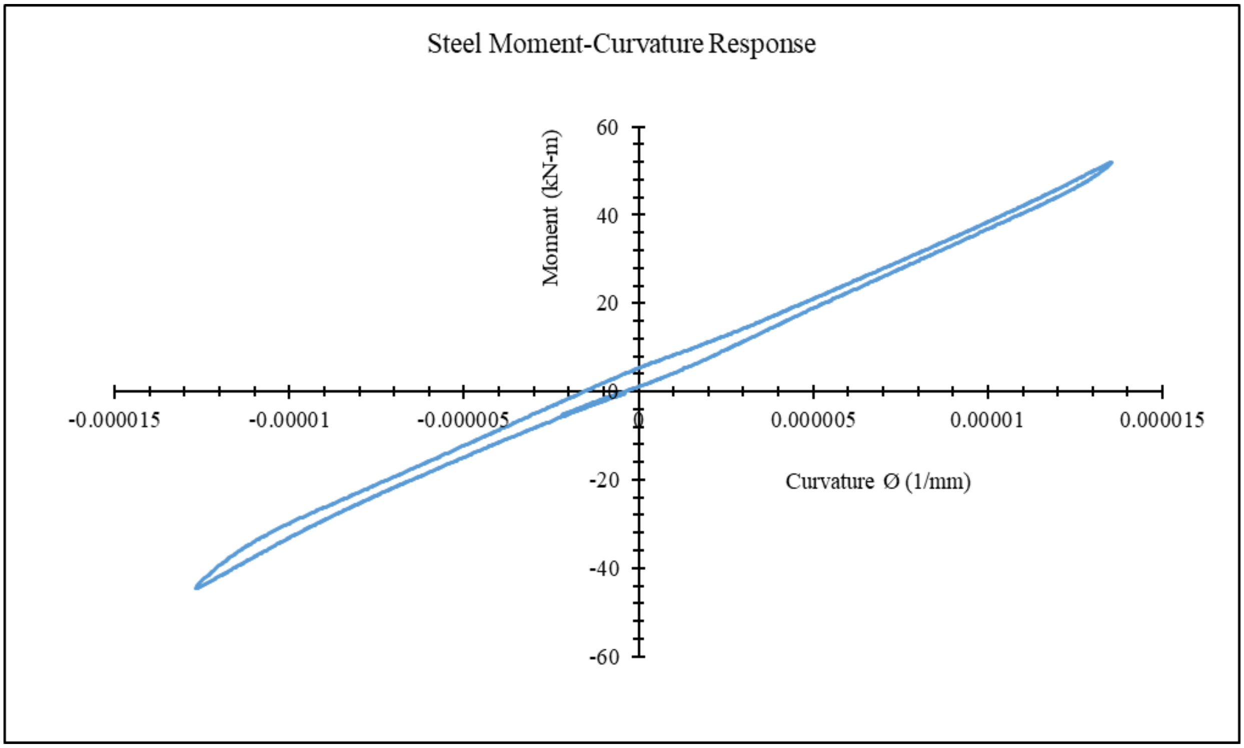

Figure 6.18. Moment-Curvature prior to yielding from steel strain of beam No.3

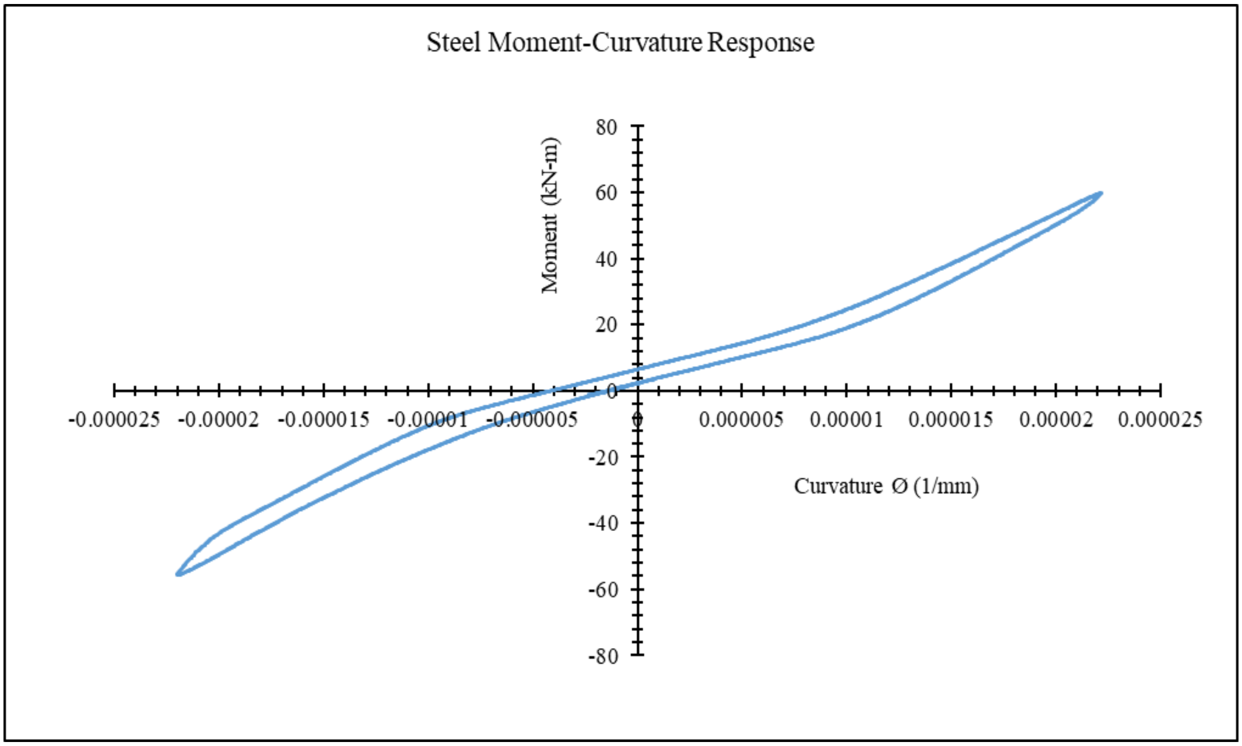

Figure 6.19. Moment-Curvature after yielding from steel strain of beam No.3

6.3.1.2. Thick FRP Sheet (Beam No.4)

The response of Beam No.4, strengthened with thick CFRP sheets, exhibited similar characteristics to that of Beam No.3 reinforced with thin CFRP sheets. For instance, there was not flip or inflection points within the cyclic loops prior to yielding, see Figure 6.20. The hysteretic loops of moment-curvature became narrower and more curvilinear beyond yielding, as shown in Figure 6.21. However, the loops were narrower compared to Beam No.3 due to the application of thicker CFRP sheets. Additionally, the moment-curvature response shifted towards the positive side on the horizontal axis close to failure load, as illustrated in Figure 6.22. It was observed that the use of thick sheets caused the longitudinal steel to experience higher plastic deformation, which could influence the curvature.

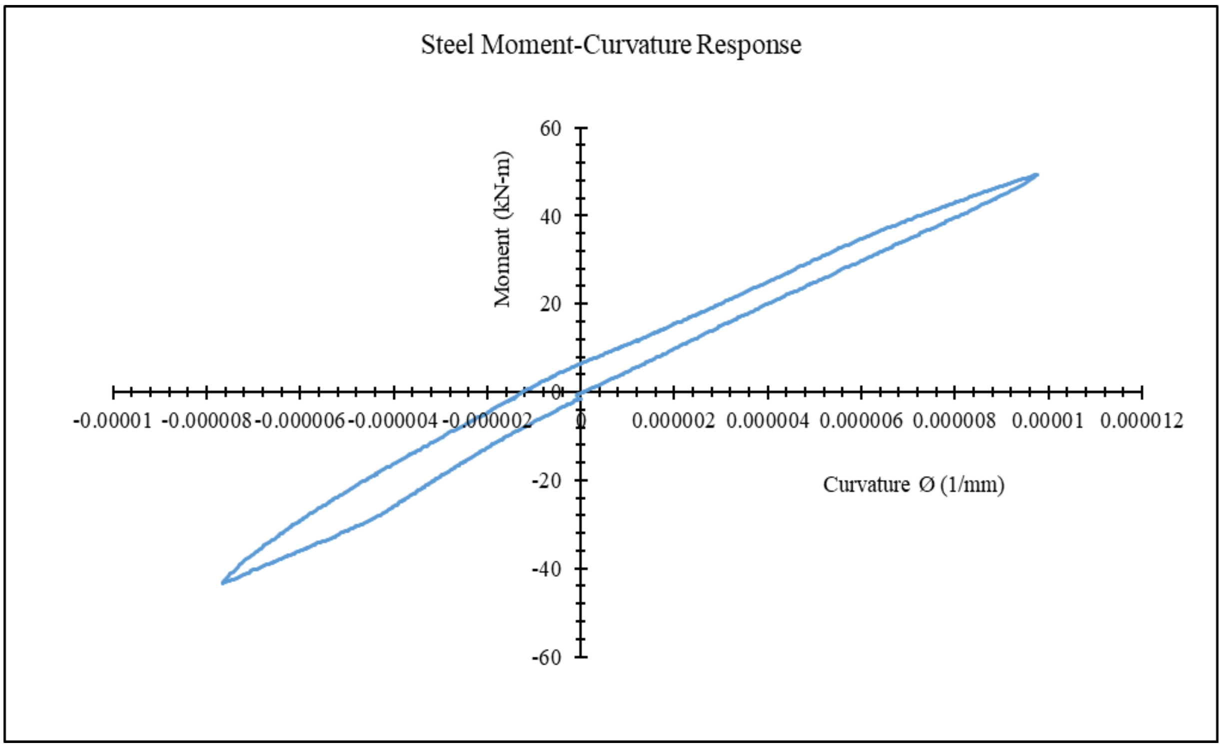

Figure 6.20. Moment-Curvature prior to yielding from steel strain of beam No.4

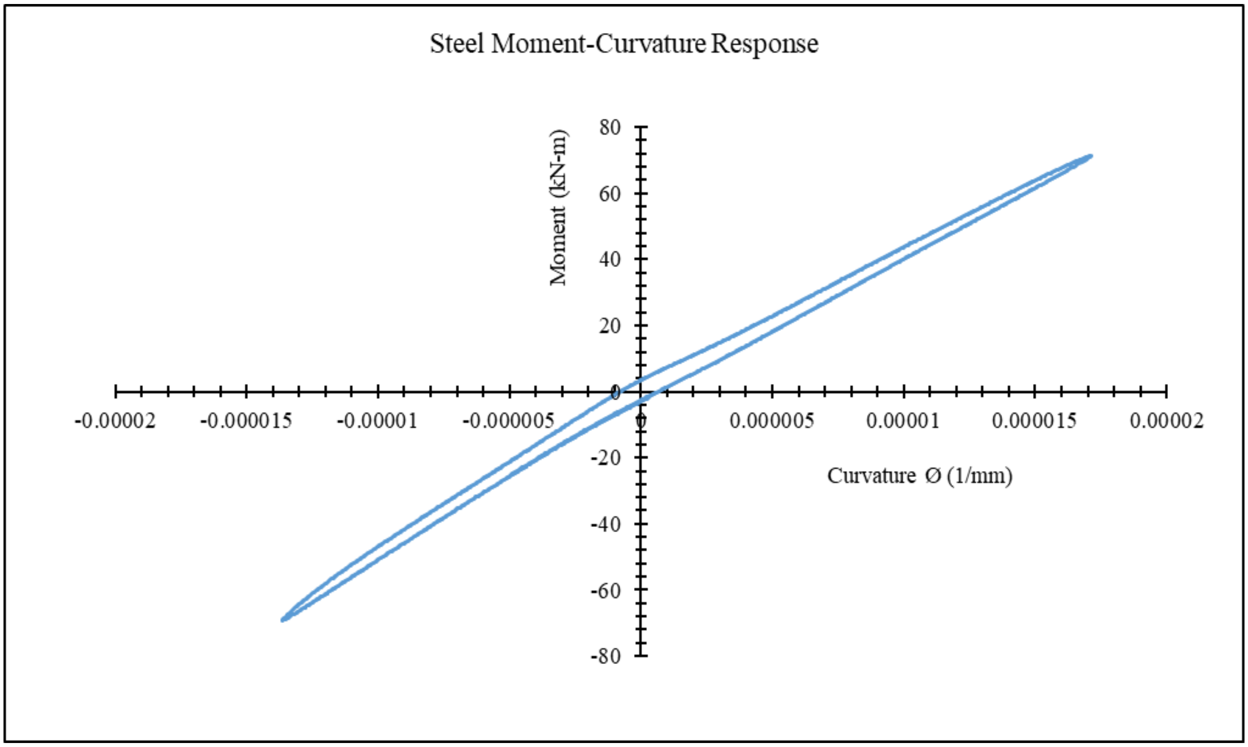

Figure 6.21. Moment-Curvature after yielding from steel strain of beam No.4

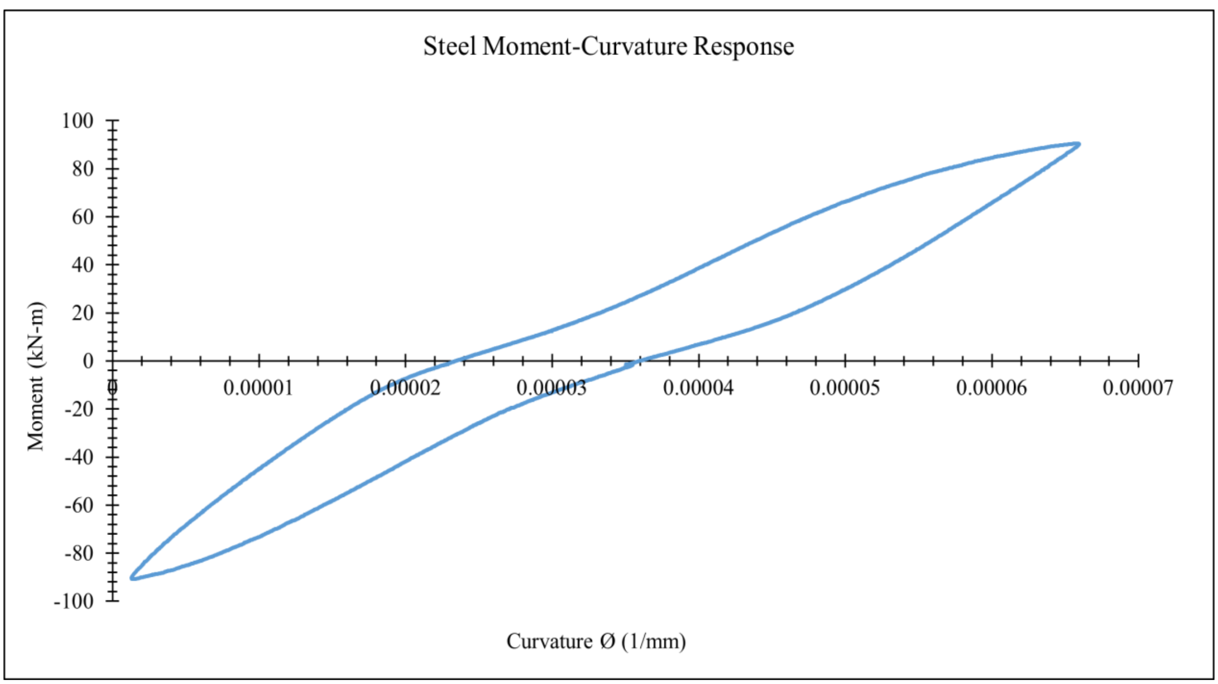

Figure 6.22. Moment-Curvature prior to failure from steel strain of beam No.4

6.3.1.3. Double-Thick FRP Sheet (Beam No.6)

When extracting the moment-curvature curves from the strain experimental data collected from the main reinforcement steel, the behavior observed was similar to that of single thin and thick CFRP sheets, as shown in Figures 6.23 to 6.24. The shape of the loops was initially straight with no inflection or flip points but became curved beyond the yield point. However, the width of the hysteresis loops was narrower compared to the other strengthened configurations, see Figures 6.23 to 6.24. Furthermore, there was an asymmetry in the moment-curvature curves, especially after yielding. This occurred because the bottom layer of the internal steel bars yielded while the top layer remained below the yield point, as seen in Figures 6.6 to 6.7, which show the strain in both the top and bottom steel bar layers, respectively.

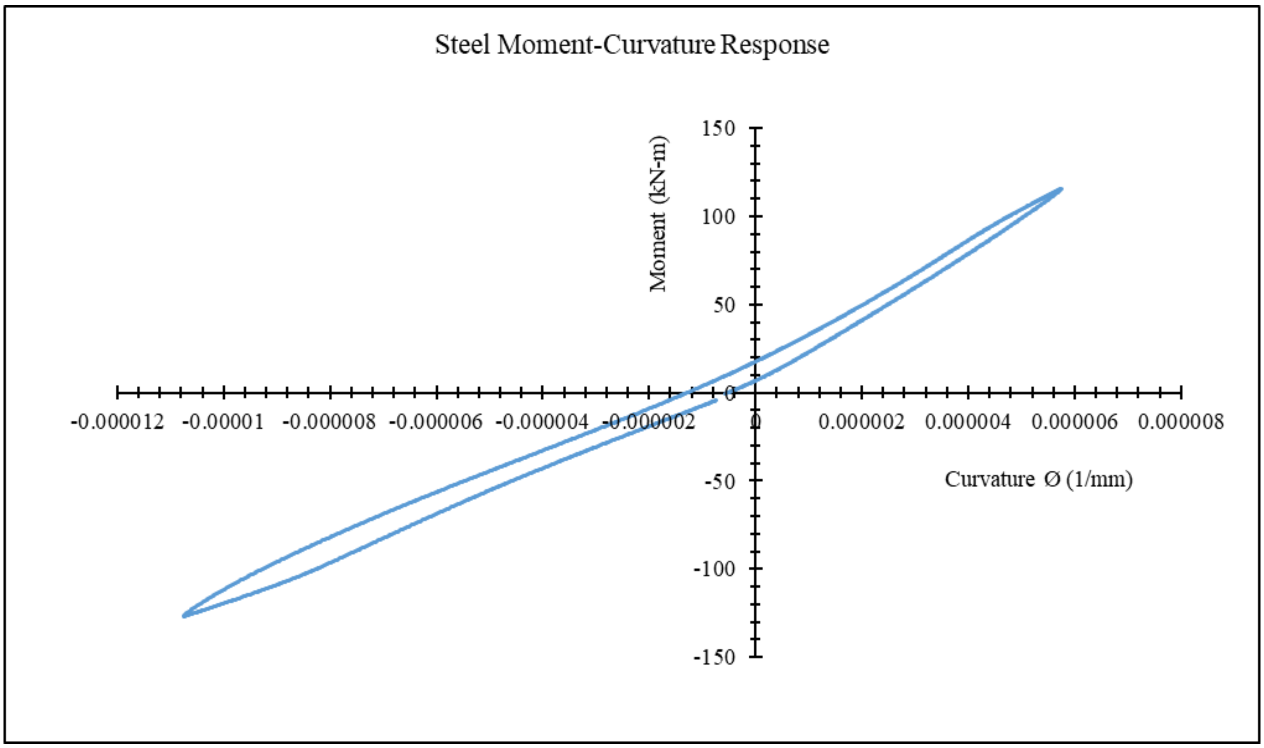

Figure 6.23. Moment-Curvature prior to yielding from steel strain of beam No.6

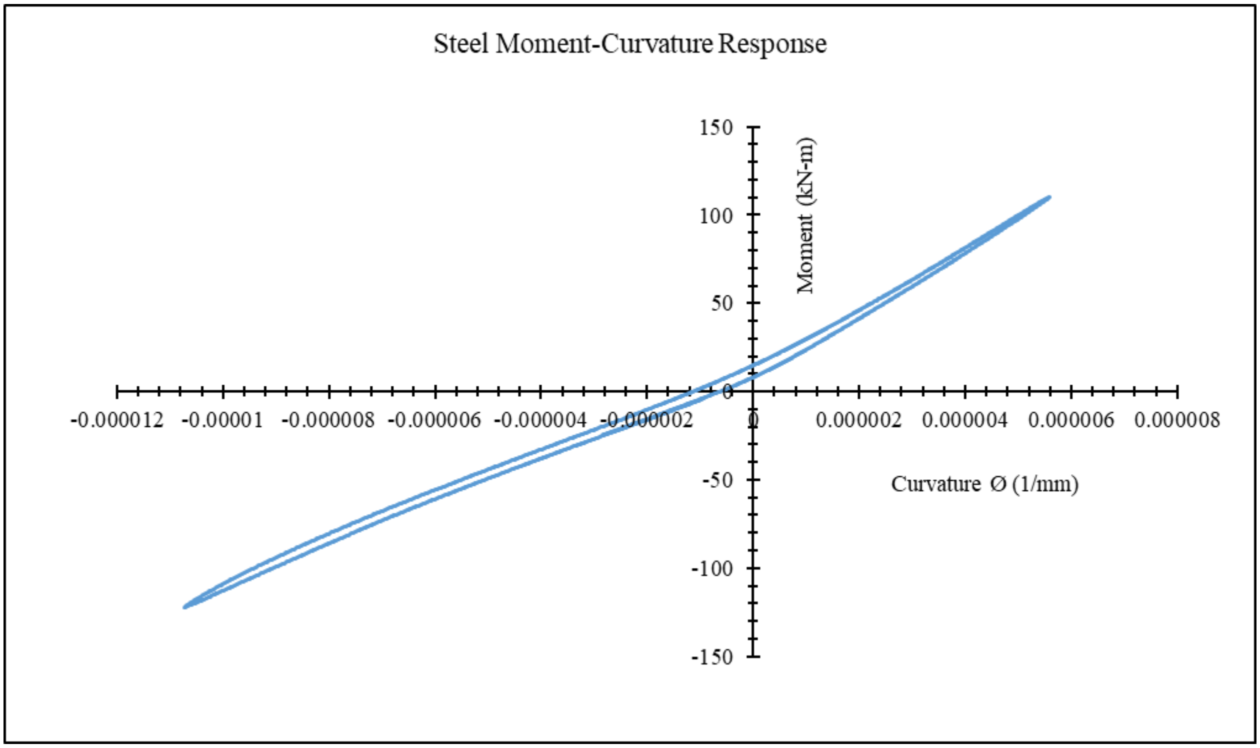

Figure 6.24. Moment-Curvature after yielding from steel strain of beam No.6

6.3.1.4. Double-Thick FRP Sheet with Sandwiched Steel Plate (Beam No.7)

Likewise, the other CFRP strengthening configurations, the shape of the hysteresis loops did not have an inflection and flip points before the longitudinal steel yields, Figure 6.25. However, post yielding response varied such that, the hysteresis loops were less curved than the other strengthening configurations, see Figures 6.26 to 6.27. Moreover, the loops were wider as a result of using a sandwiched steel plate along the constant moment region which will eventually positively impact the total energy dissipation as it is going to be discussed later in load-deflection curves section.

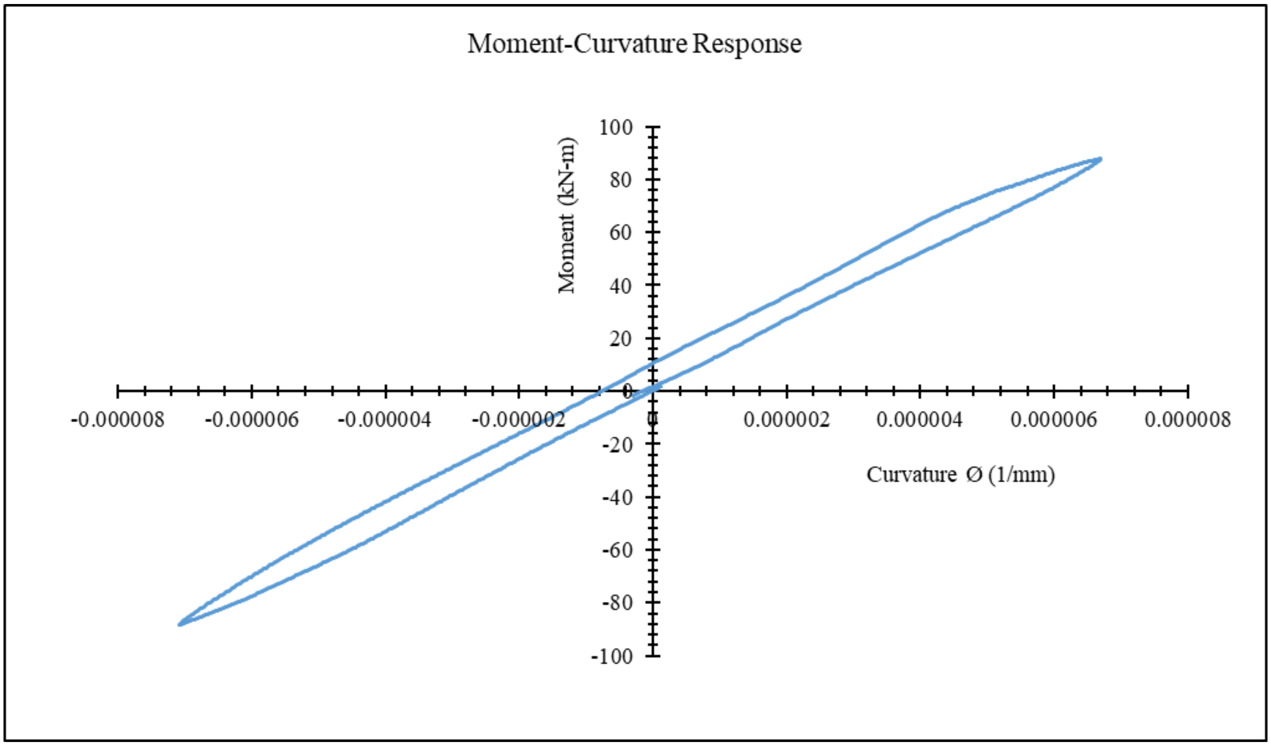

Figure 6.25. Moment-Curvature prior to yielding from steel strain of beam No.7

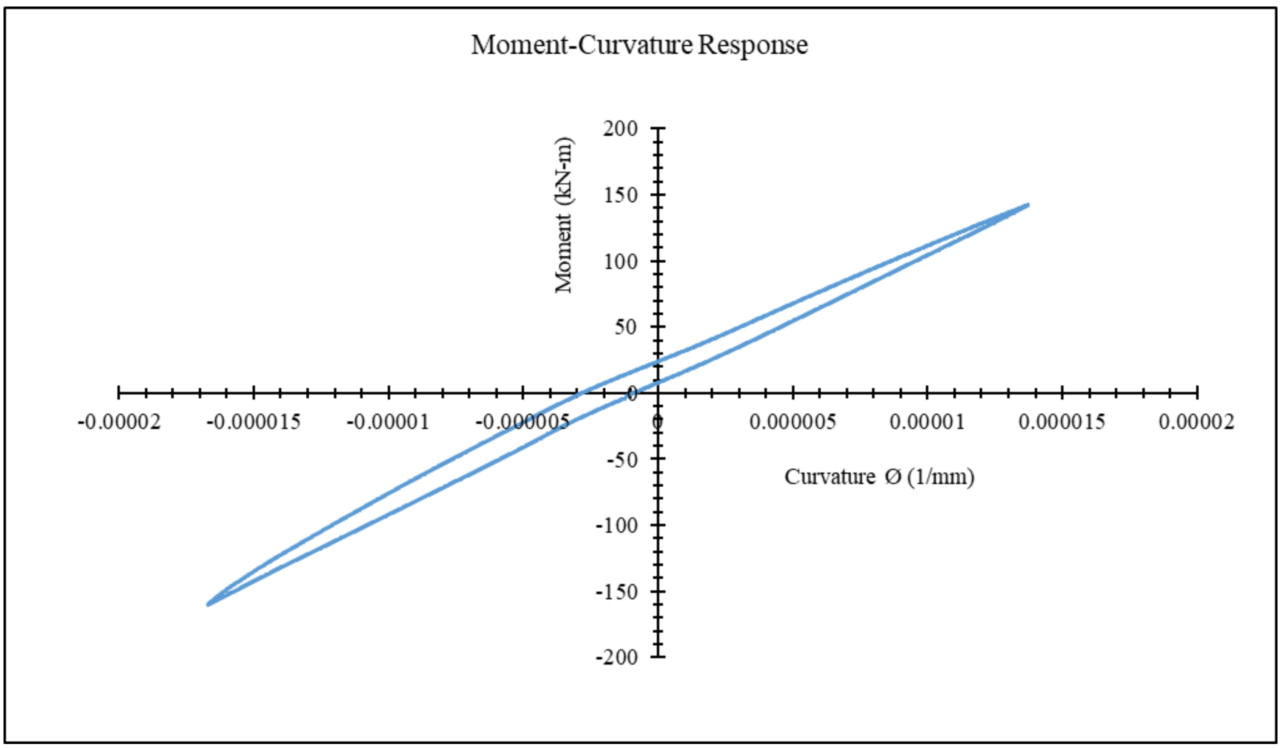

Figure 6.26. Moment-Curvature after yielding from steel strain of beam No.7

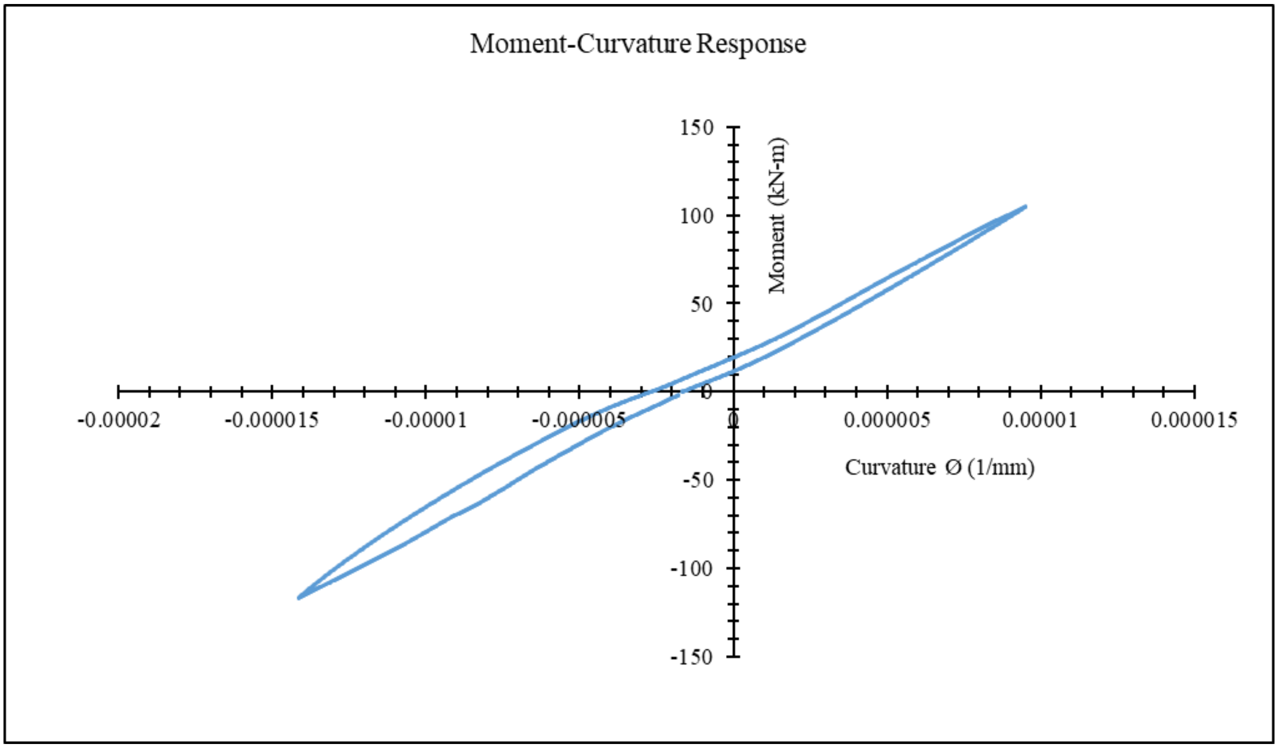

Figure 6.27. Moment-Curvature prior to failure from steel strain of beam No.7

6.3.2. FRP Response

6.3.2.1. Thin FRP Sheet (Beam No.3)

Similar observations were made when examining the moment-curvature response derived from the CFRP data. As shown in Figures 6.28 to 6.29, the hysteresis loops remained straight with no inflection or flip points until the yielding load was exceeded, then, the loops became curved. An important finding emerged when comparing the curvature of CFRP to that of steel. For all cyclic loops, the curvature of the steel was larger than that of the CFRP, as seen in Figures 6.18 to 6.19 versus Figures 6.28 to 6.29, for steel and CFRP curvatures respectively. This could be attributed to the differences in the mechanical behaviors and responses of steel and CFRP to cyclic loading. Steel exhibits significant plastic deformation and ratcheting, resulting in a pronounced curvature in the strain-load curve. In contrast, CFRP primarily exhibits elastic behavior with but follow the steel response if the bond is intact while it exhibits less strains when debonding and slippage of the CFRP takes place, leading to a less pronounced curvature.

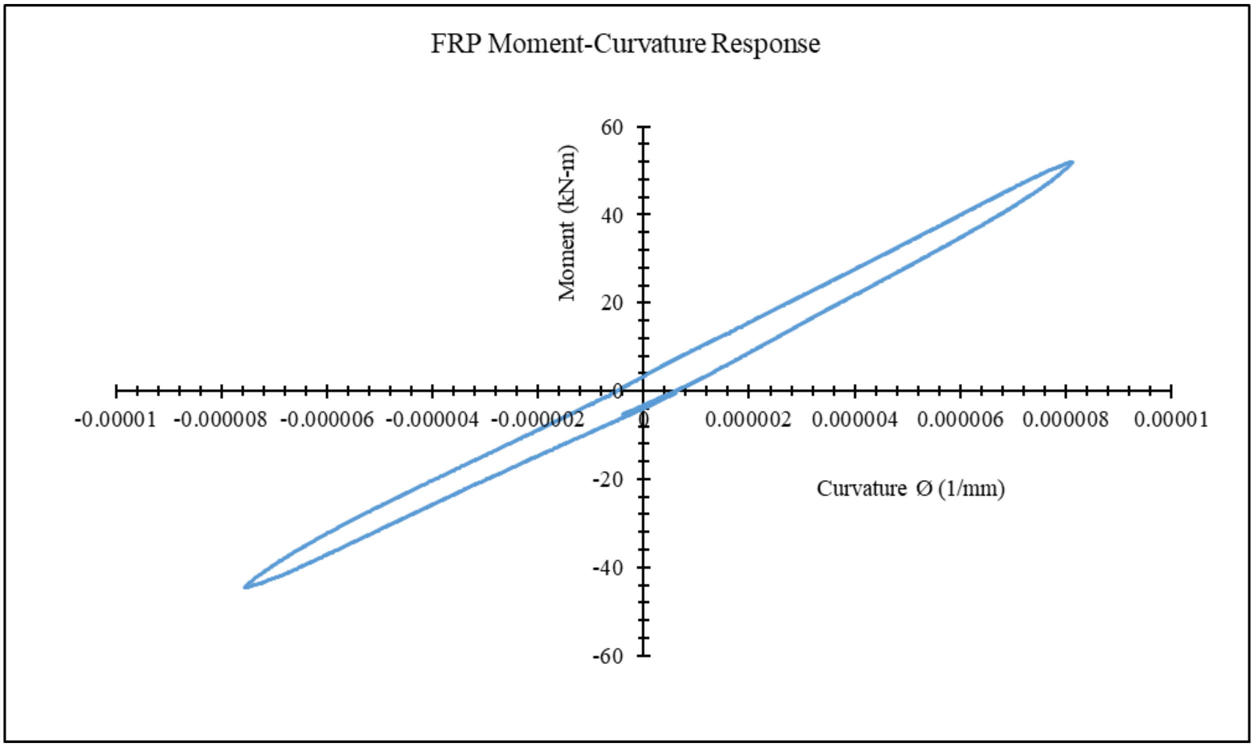

Figure 6.28. Moment-Curvature prior to yielding from CFRP strain of beam No.3

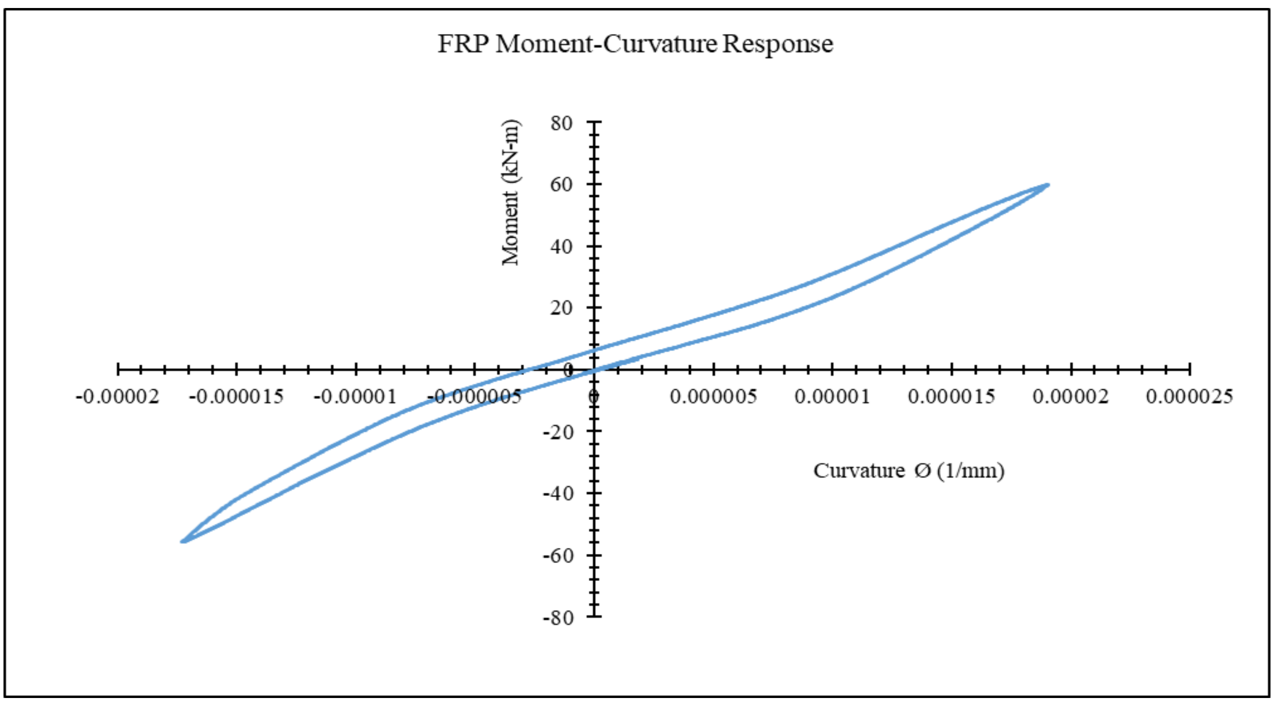

Figure 6.29. Moment-Curvature after yielding from CFRP strain of beam No.3

6.3.2.2. Thick FRP Sheet (Beam No.4)

The moment-curvature hysteresis response of the thick CFRP sheets demonstrated an identical trend to that of thin CFRP sheets. There were no flip or inflection points within the loops before the steel yielded. The shape of the loops started to curve beyond yielding due to the plastic deformation of the steel, as illustrated previously. When comparing the moment-curvature curve obtained from the CFRP data to the steel one, it is clear that, unlike the steel, the curvature remained symmetric even at loads close to failure. This is because the steel experienced significant plastic deformation due to the high constraint provided by the thick CFRP sheet, forcing the steel to behave differently. Figures 6.30 to 6.32 show the moment-curvature curves of beam No. 4 before yielding, after yielding, and close to failure, respectively. Further observations indicated that the hysteresis loops were narrower compared to those of the thin CFRP sheets.

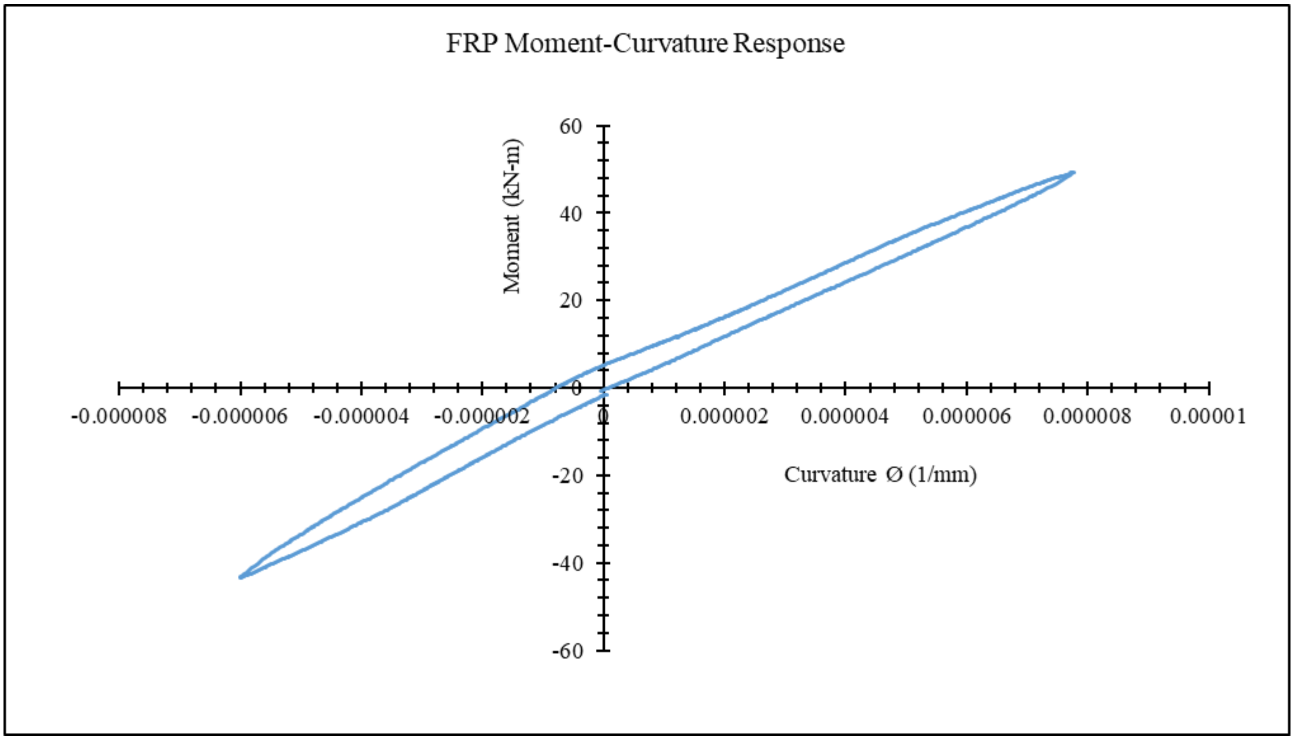

Figure 6.30. Moment-Curvature prior to yielding from CFRP strain of beam No.4

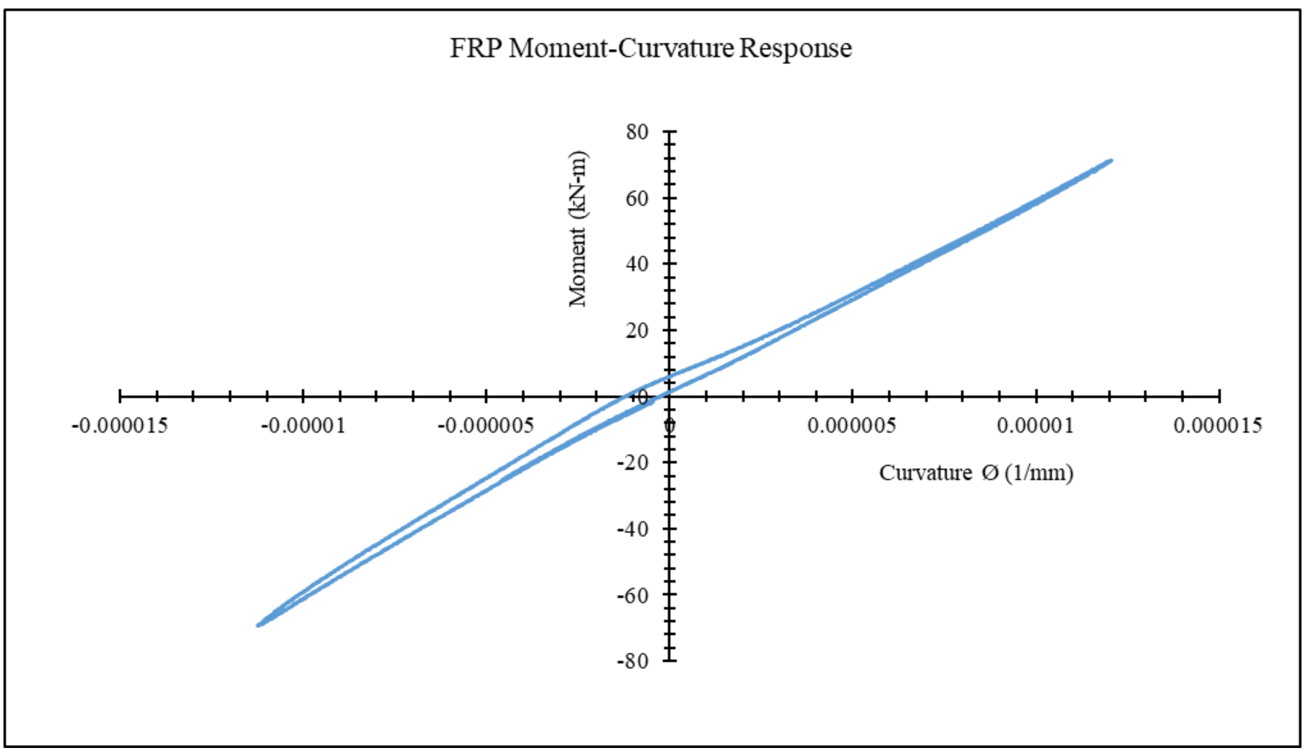

Figure 6.31. Moment-Curvature after yielding from CFRP strain of beam No.4

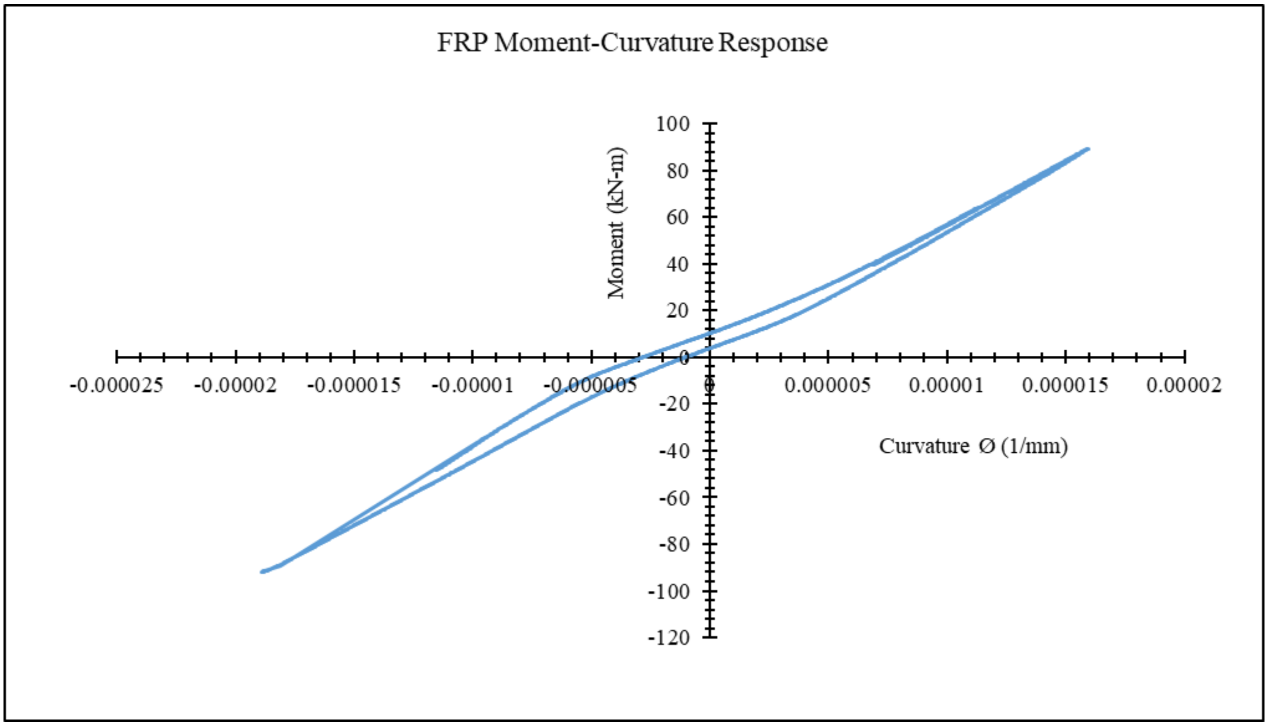

Figure 6.32. Moment-Curvature prior to failure from CFRP strain of beam No.4

6.3.2.3. Double-Thick FRP Sheet (Beam No.6)

By exploring the moment-curvature data of beam No. 6 strengthened with double-thick CFRP sheets, a similar trend was observed to those of single thin and thick sheets. However, the loops were much more compressed, see Figures 6.33 to 6.34. Additionally, the hysteresis loops were less curved beyond yielding because the reinforcement steel did not exhibit high strain and plastic deformation due to the constraint of using the double-thick CFRP sheets. Figures 6.33 to 6.34 below demonstrate the moment-curvature curves of beam No. 6 before and after yielding, respectively.

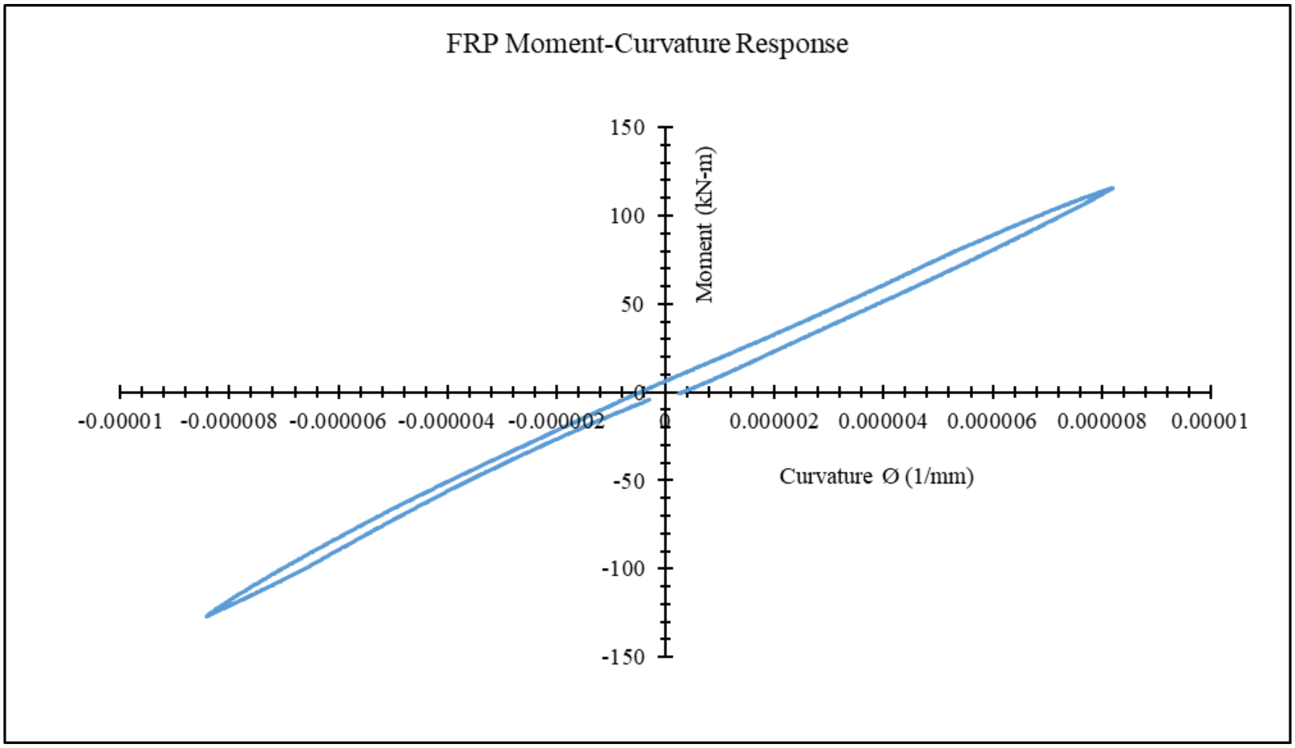

Figure 6.33. Moment-Curvature prior to yielding from CFRP strain of beam No.6

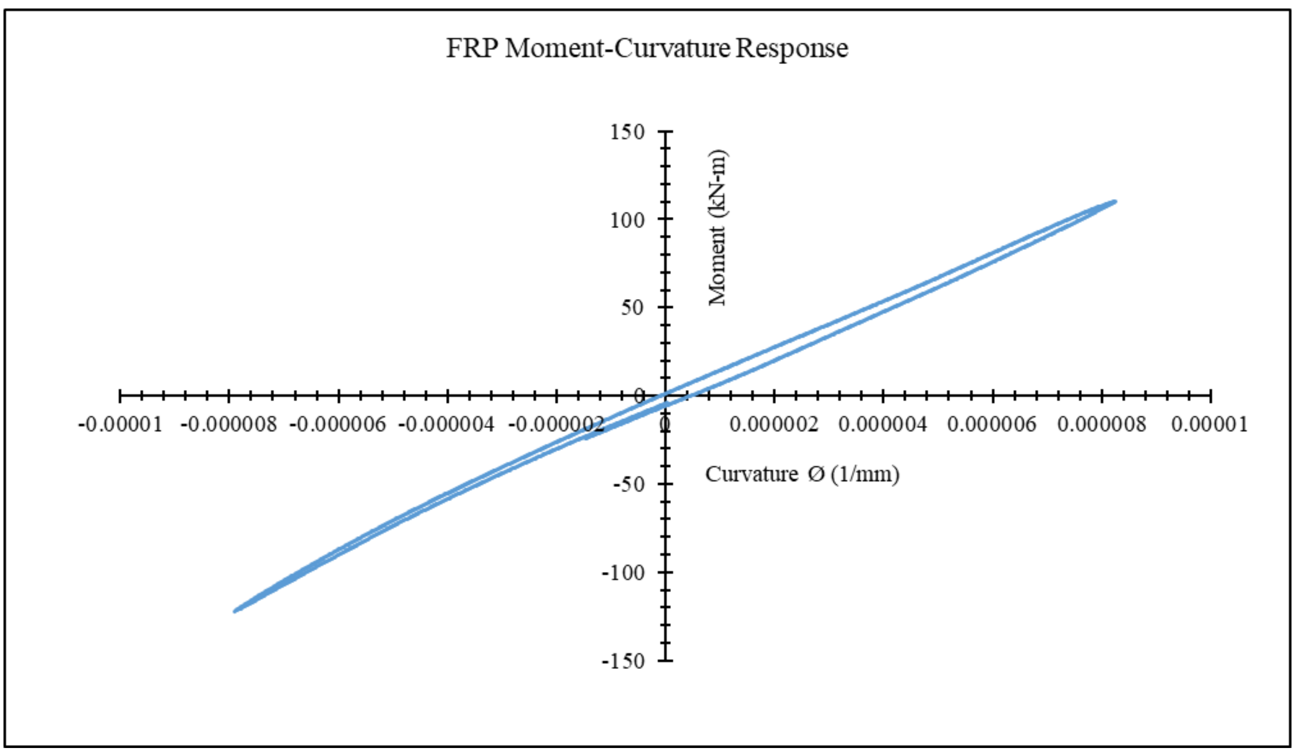

Figure 6.34. Moment-Curvature after yielding from CFRP strain of beam No.6

6.3.2.4. Double-Thick FRP Sheet with Sandwiched Steel Plate (Beam No.7) Plus Shear Strengthening

The response of beam No.7, strengthened with a double-thick CFRP sheet and a sandwiched steel plate, exhibited behaviors similar to other strengthening configurations, as shown in Figure 6.35. There were no flip or inflection points observed prior to the yielding of the steel. Additionally, it displayed a trend similar to its twin, beam No.6, with less pronounced curvature in the loops beyond the yielding point. However, there was a noticeable impact on the width of the loops due to the use of the steel plate fuse, resulting in wider and more substantial moment-curvature loops, see Figure 6.36 to 6.37. Further conclusions highlight that the curvatures of the CFRP sheets were comparable to those obtained from steel data, which can be attributed to the utilization of the steel plate fuse.

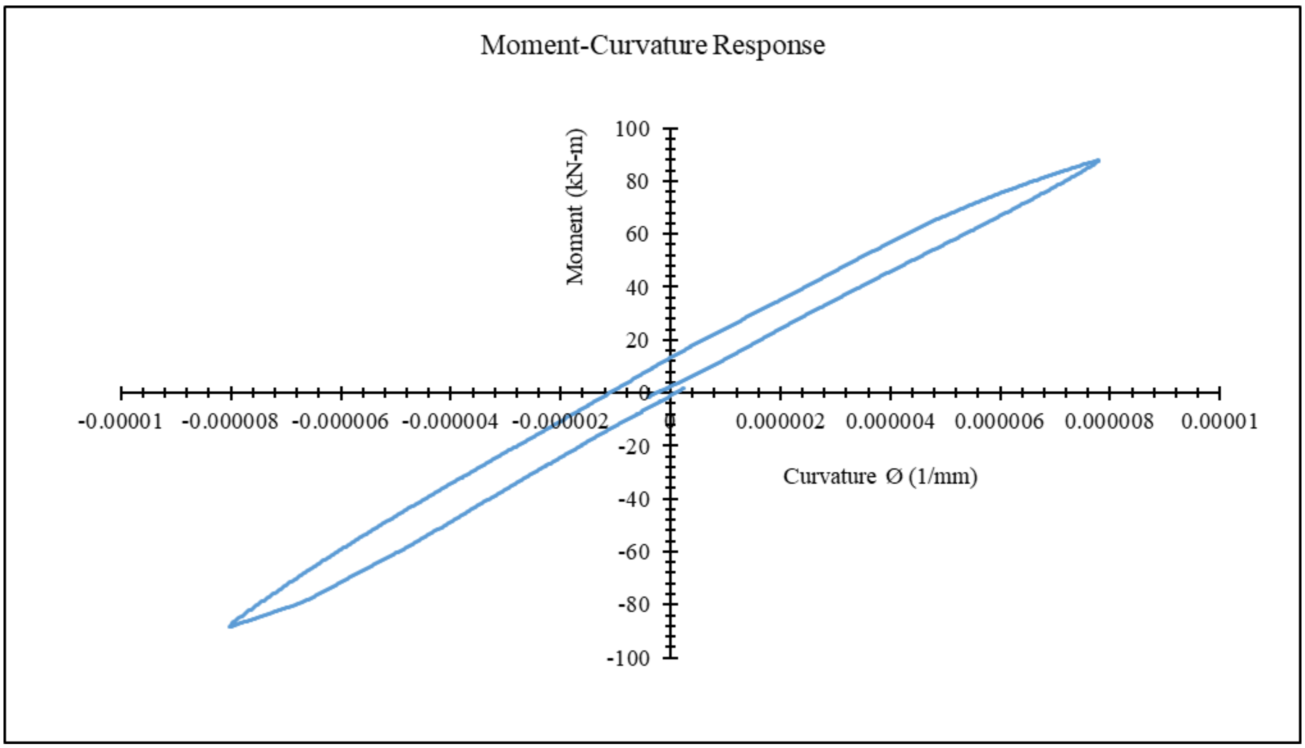

Figure 6.35. Moment-Curvature prior to yielding from CFRP strain of beam No.7

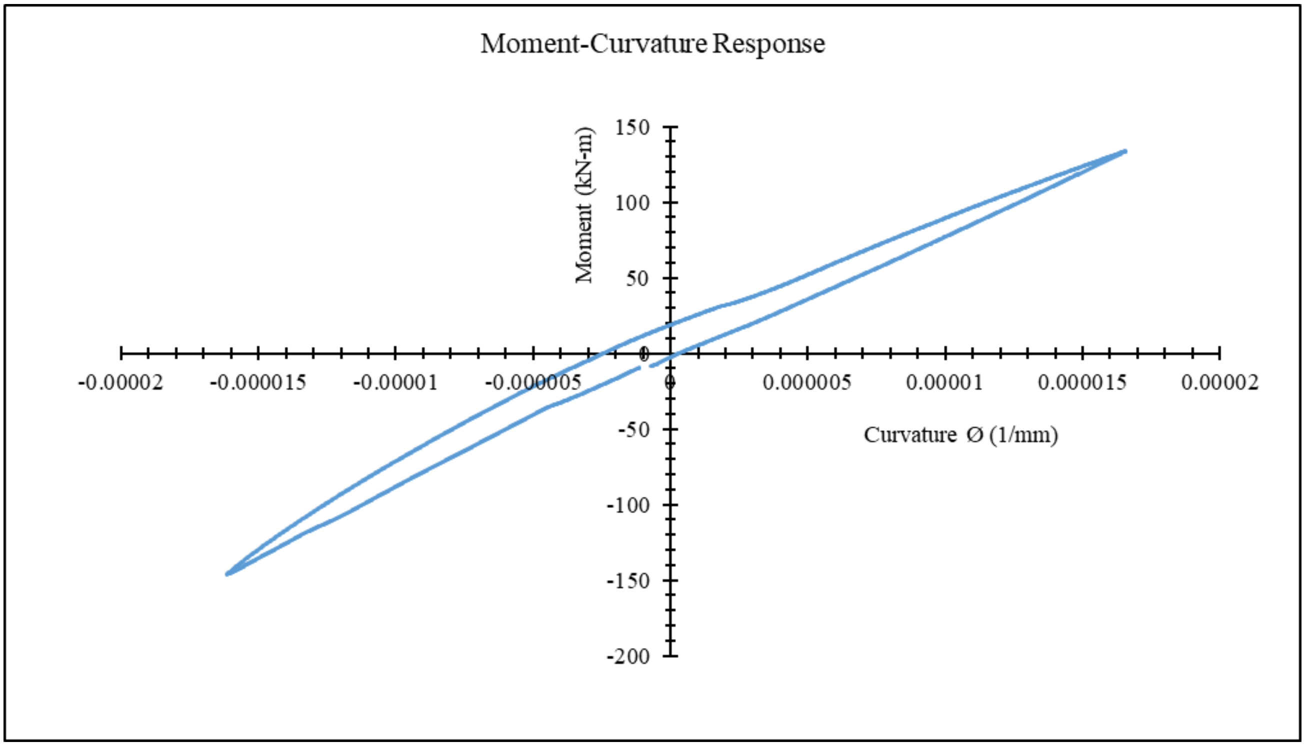

Figure 6.36. Moment-Curvature after yielding from CFRP strain of beam No.7

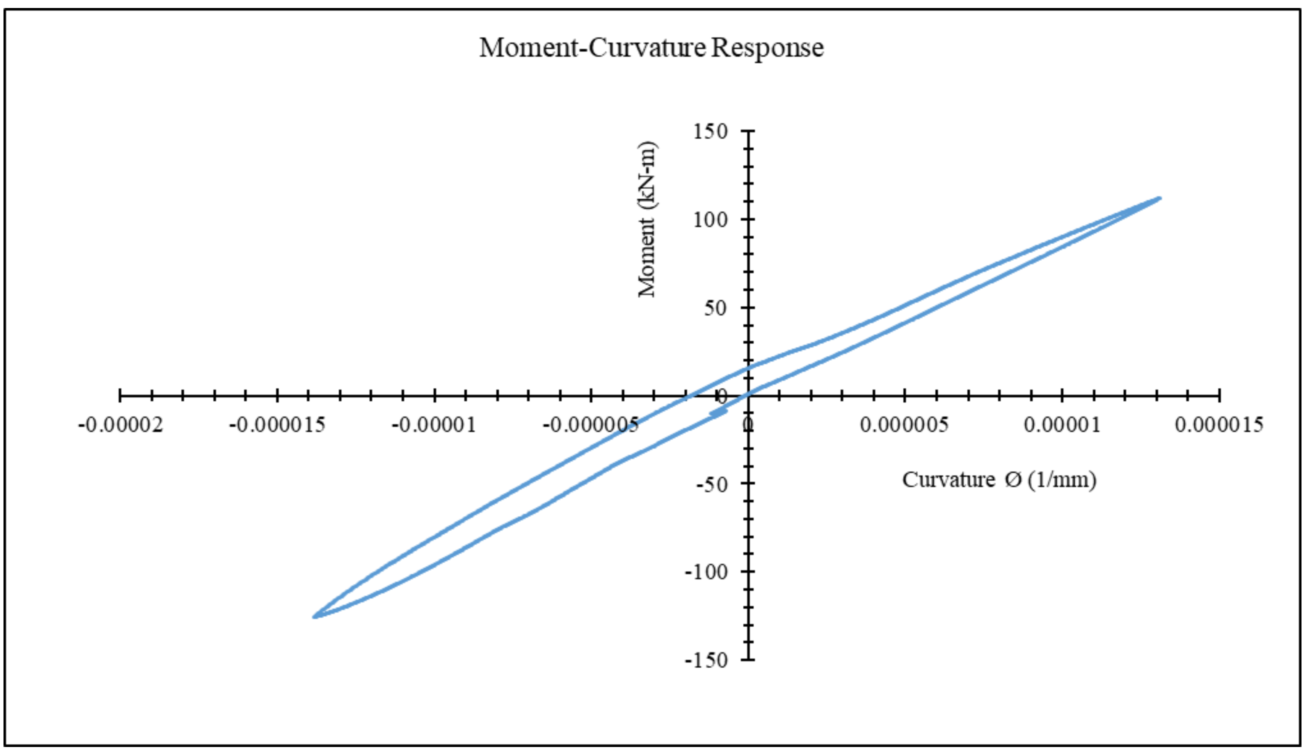

Figure 6.37. Moment-Curvature prior to failure from CFRP strain of beam No.7

6.4. Load-Deflection Curves

To investigate the ductility, stiffness and energy dissipation, the load-deflection curves were developed using collected experimental data.

6.4.1. Thin FRP Sheet (Beam No.3)

The load-deflection curve of beam No.3, strengthened with a thin CFRP sheet, is illustrated in Figure 6.38. It is evident that the use of thin sheets enhanced the ductility, such that beam No.3 sustained a midspan displacement of 38.00 mm (1.50 in). Additionally, the beam exhibited intermediate energy dissipation due to the use of thin sheets, although it had the lowest ultimate capacity. Figures 6.39 to 6.41 compare the four beams (No. 3, 4, 6 and 7) in terms of energy dissipation, ultimate capacity, and ductility, respectively.

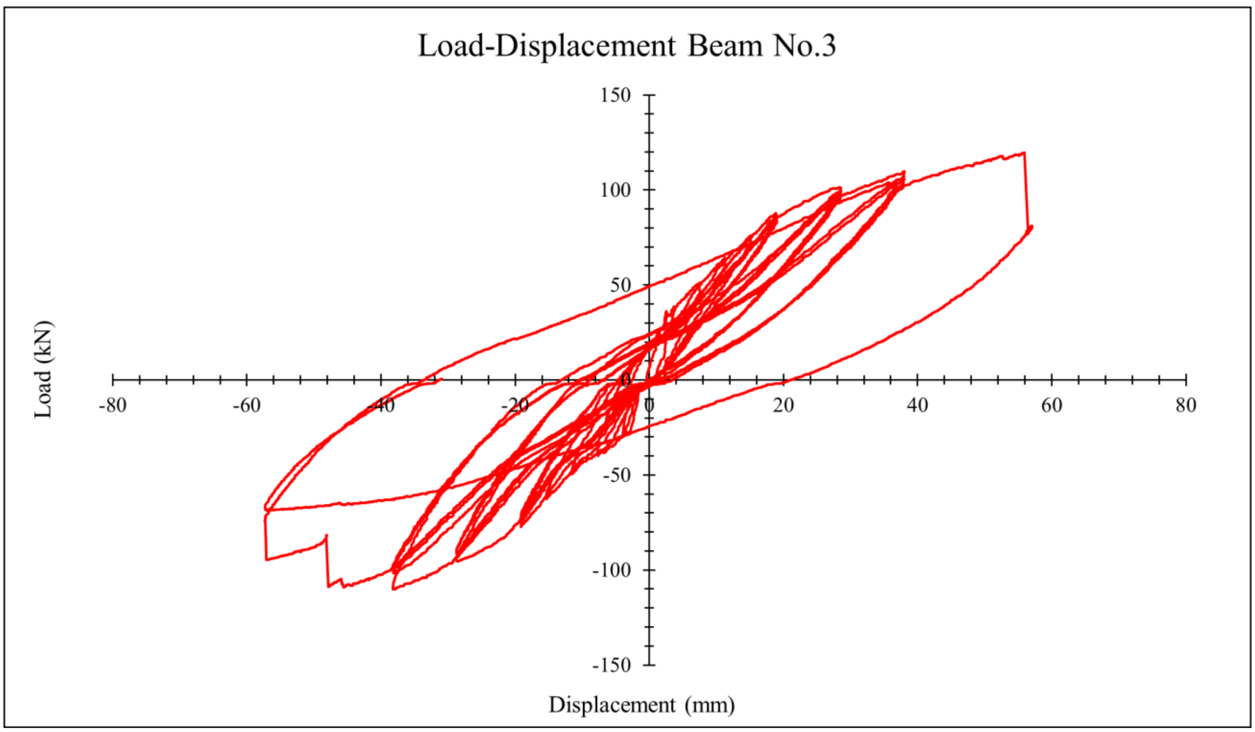

Figure 6.38. Load-Deflection response of beam No.3

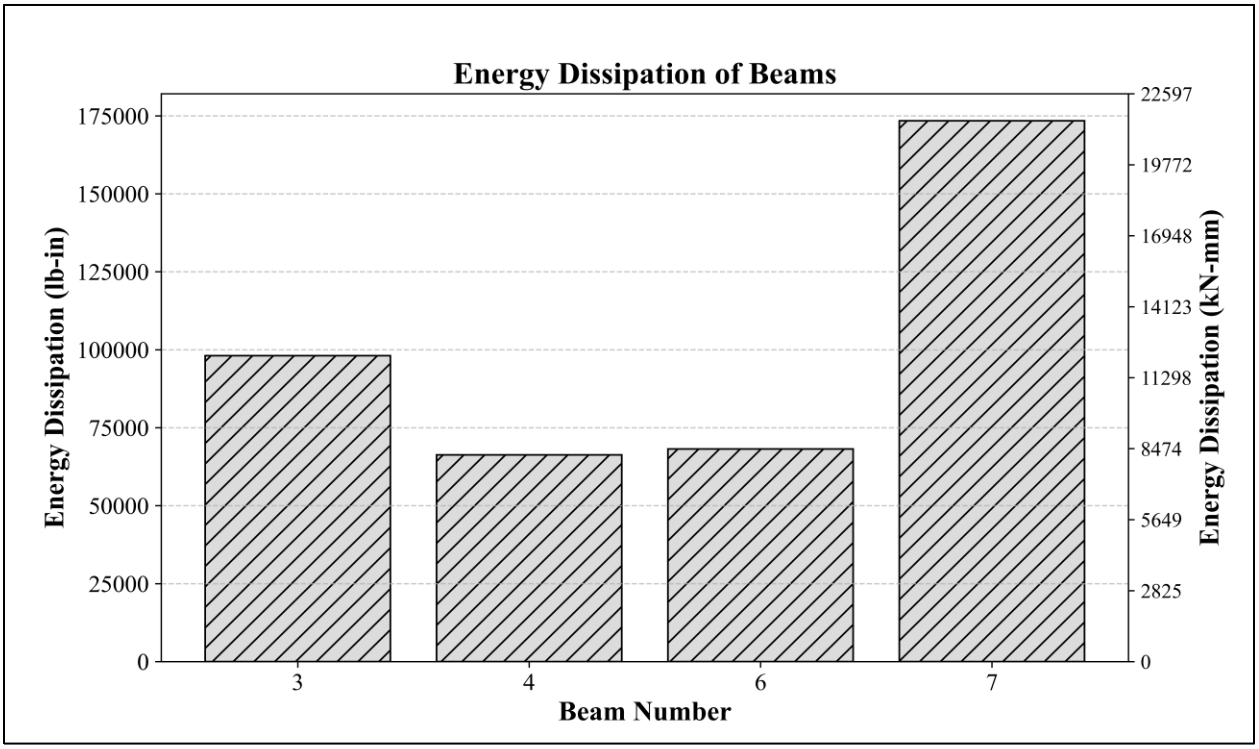

Figure 6.39. Energy dissipation comparison of all specimens investigated herein[7].

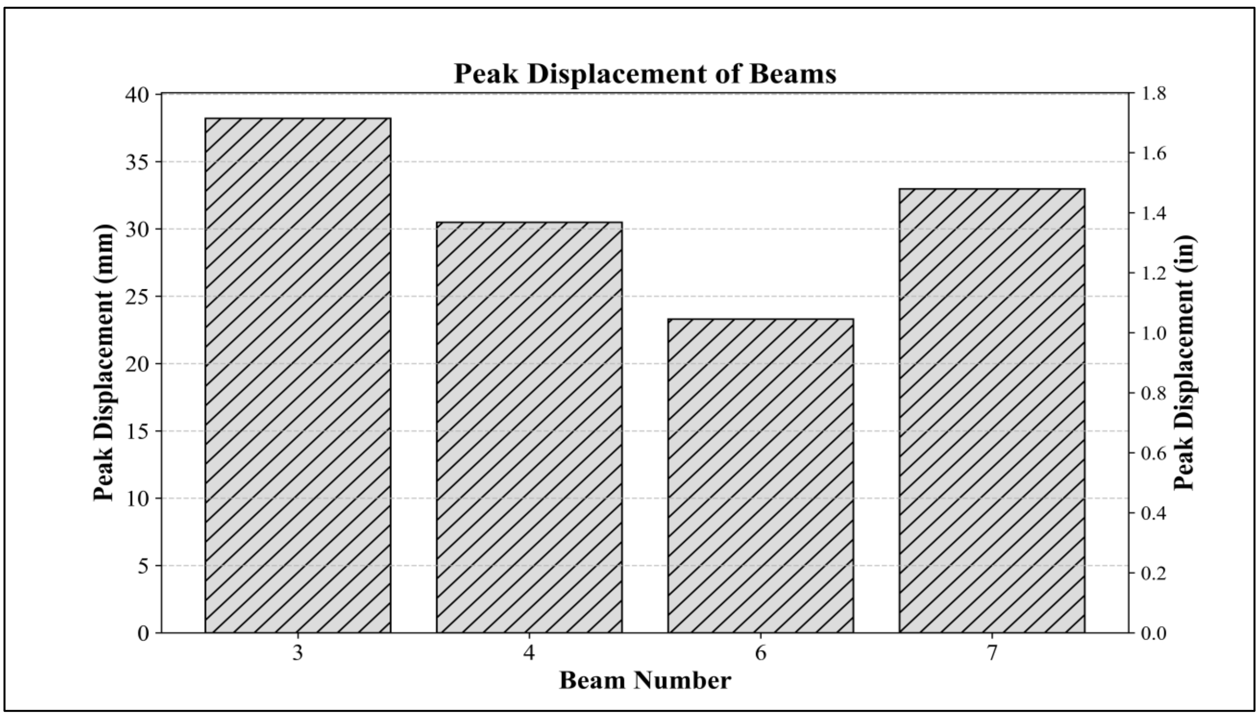

Figure 6.40. Peak displacement comparison of all specimens investigated herein.

[7] Energy dissipation for CFRP strengthened beams is measured up to the failure of the strengthening system and not beyond that.

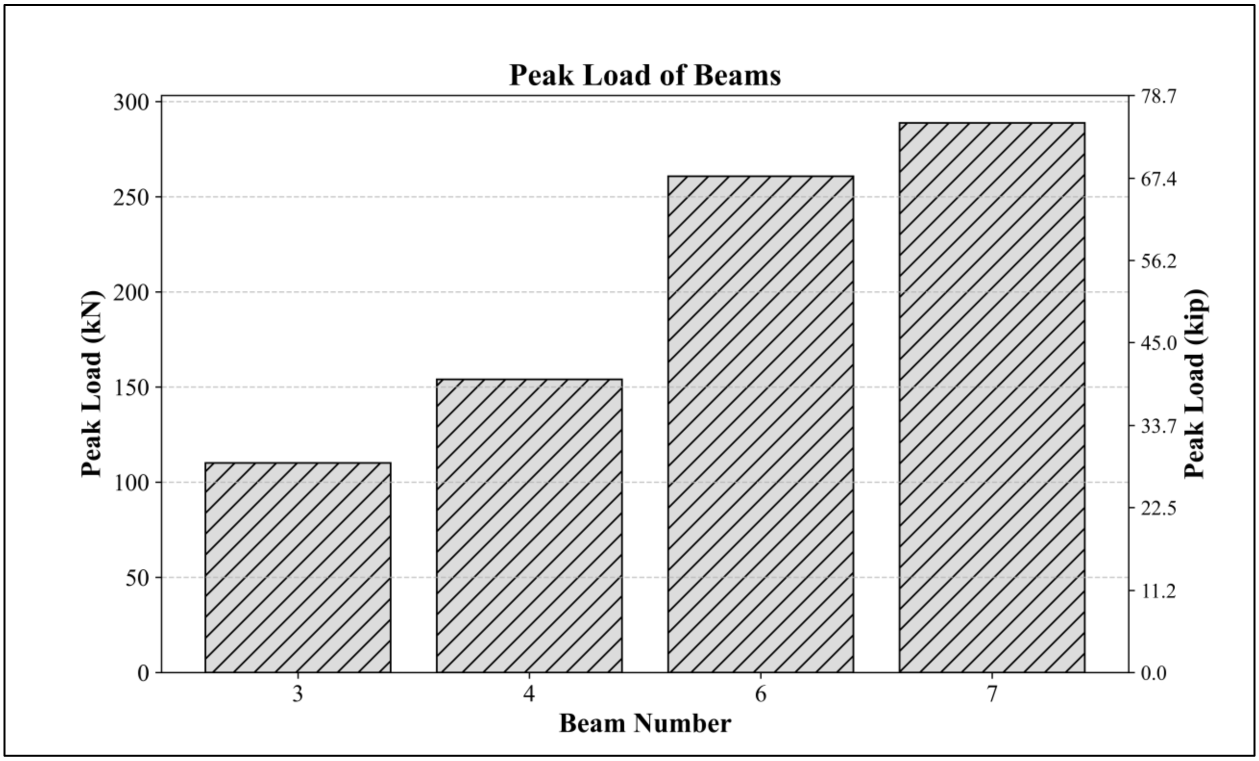

Figure 6.41. Peak load comparison of all specimens investigated herein.

6.4.2. Thick FRP Sheet (Beam No.4)

Applying one layer of thick CFRP sheets instead of thin one increased the ultimate capacity by about 40% compared to beam No.3. However, there was a noticeable impact on the energy dissipation as well as ductility. According to the experimental data, beam No.4 experienced less ductility by about 28% in comparison to beam No.3, Figure 6.40. Moreover, there was a significant reduction in energy dissipation by about 30% in comparison to thin CFRP sheet strengthening, refer to Figure 6.39 for more details. Also, it is important to note that the use of a single thick layer of CFRP sheet caused the beam to have more pinching as it shown in load-deflection response in Figure 6.42. Figure 6.43 demonstrates a comparison between beam No.3 and No.4.

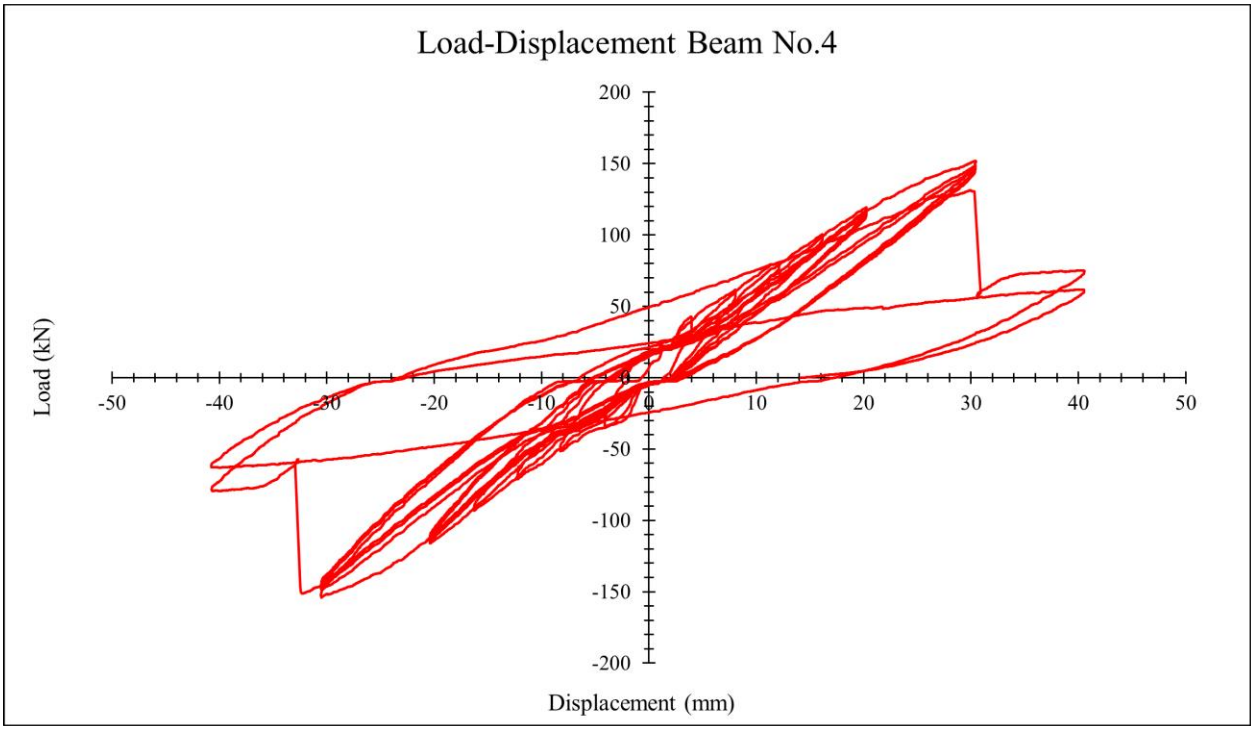

Figure 6.42. Load-Deflection response of beam No.4

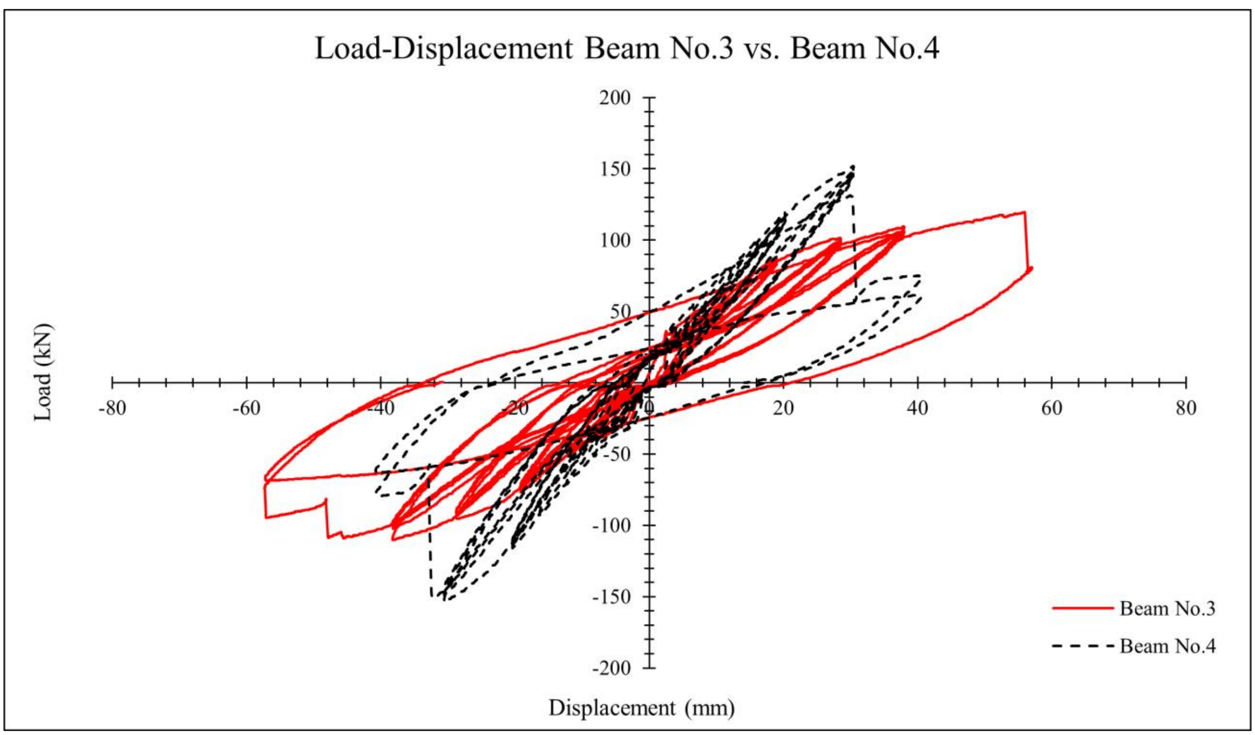

Figure 6.43. Load-Deflection response of beam No.3 vs beam No.4

6.4.3. Double-Thick FRP Sheet (Beam No.6)

The response of beam No.6, strengthened with double-thick CFRP sheets, demonstrated slightly lower ductility than beam No.4 by about 26%, Figure 6.40. The energy dissipation, however, was similar to beam No.4 even the use of more than one layer of CFRP caused the loops to be narrower, see Figure 6.44. Furthermore, the ultimate capacity was increased by about 57% and 117% compared to beams No.3 and No.4, respectively. Figure 6.44 illustrates the load-deflection response of beam No.6. It was also observed that the use of double-thick CFRP sheets led to more pinching compared to beams No.3 and No.4.

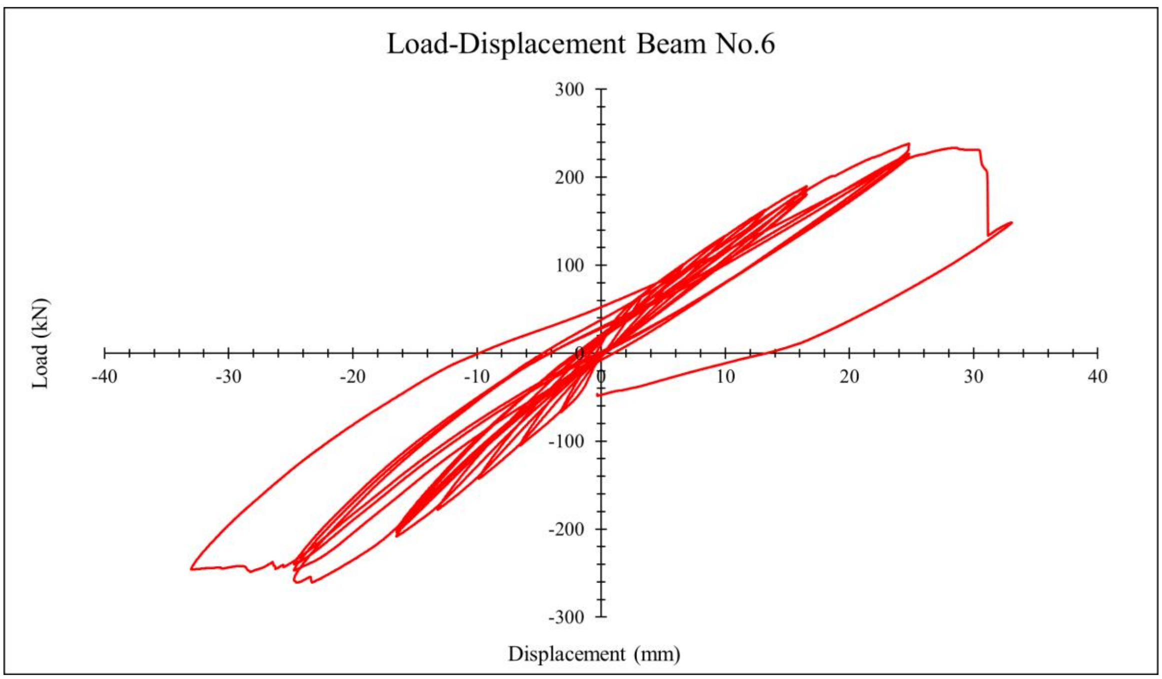

Figure 6.44. Load-Deflection response of beam No.6

6.4.4. Double-Thick FRP Sheet with Sandwiched Steel Plate (Beam No.7) Plus Shear Strengthening

By exploring the load-deflection response, it is obvious that the beam experienced a significant enhancement in terms of ductility, and ultimate load capacity compared to beam No.6 by 45% and

13%, respectively, see Figures 6.45 and 6.46. Further improvement in the performance was observed resulting in that energy dissipation of beam No.7 being higher than beam No.6 by about 135% as shown in Figure 6.39. Also, it is worth noting that the hysteresis loops of beams No.7 were wider as demonstrated in the load-deflection response compared to all other beams. Moreover, unlike beam No.6, beam No.7 did not exhibit a sudden decrease in the loading capacity beyond the failure. Thus, the use of a sandwiched steel plate had significant positive effects on the overall performance of RC beams strengthened with CFRP sheets secured with fiber anchors in the presence of CFRP shear strengthening.

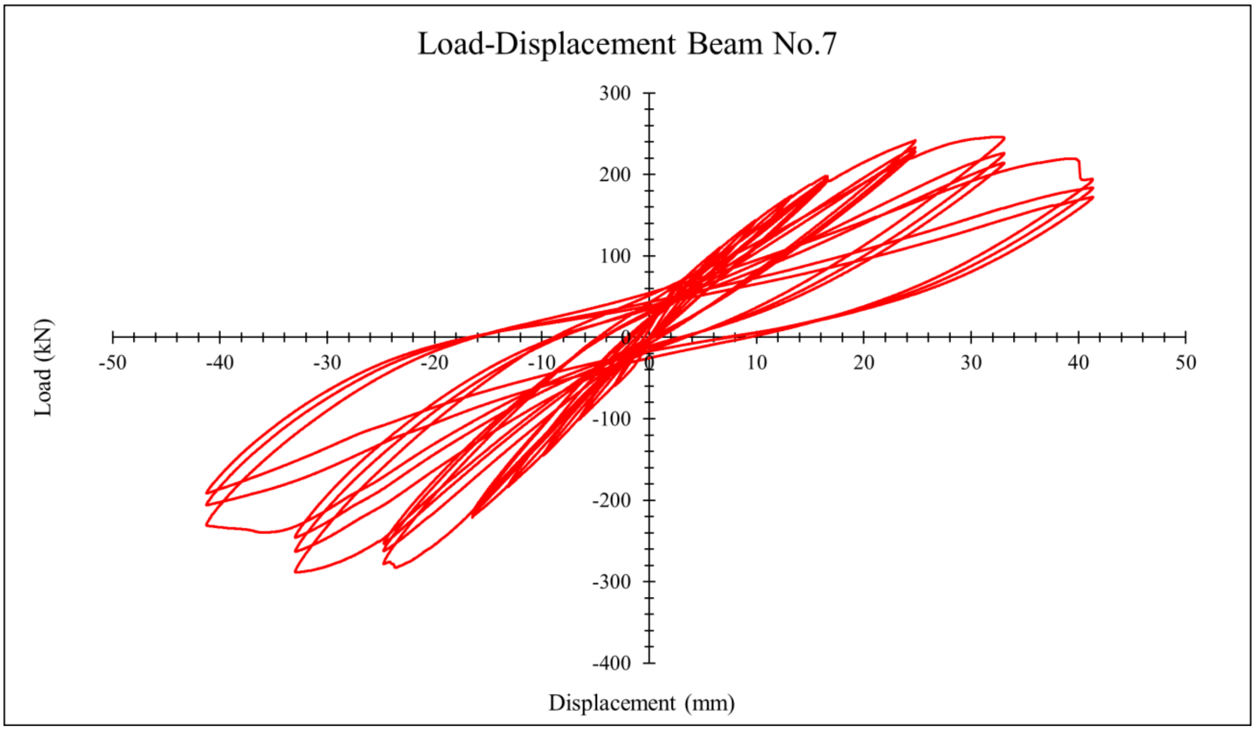

Figure 6.45. Load-Deflection response of beam No.7

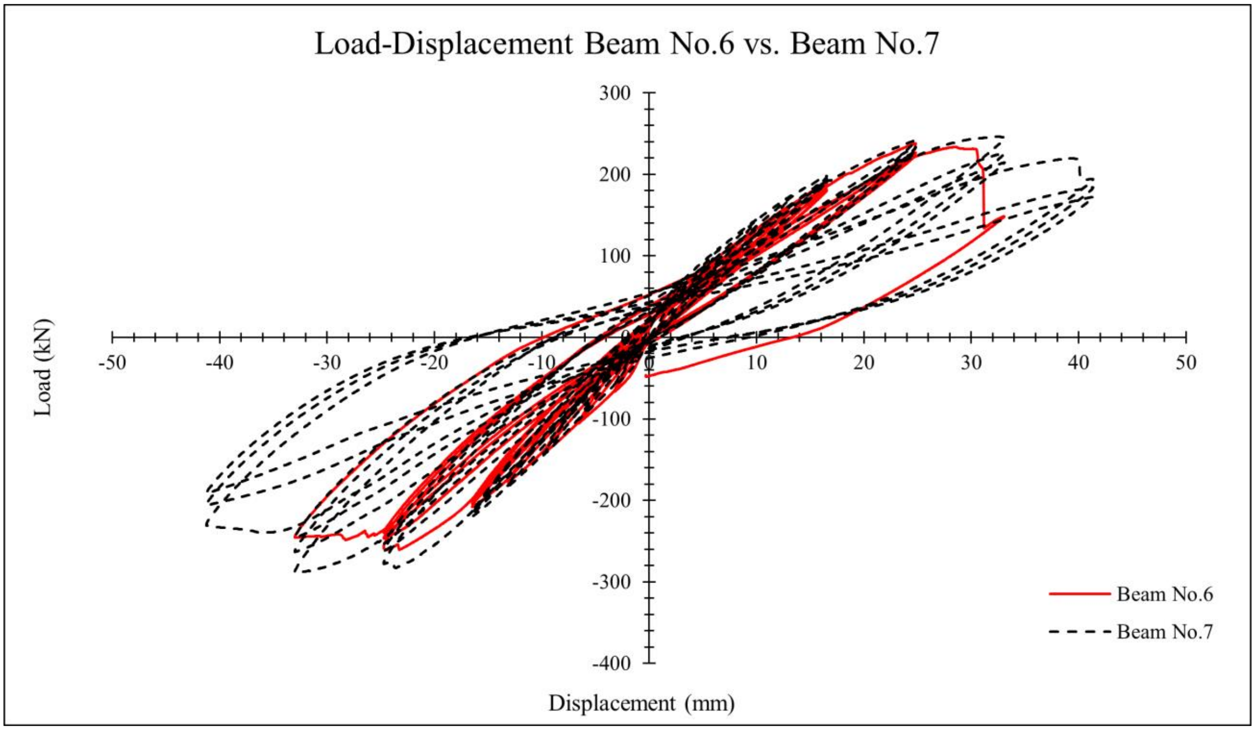

Figure 6.46. Load-Deflection response of beam No.6 vs beam No.7

6.5. Conclusions

Several experimental responses of strengthened RC beam with various CFRP configurations were carefully investigated and the following conclusions were drawn:

1- There is a direct relationship between the thickness of CFRP sheets and the level of the strain in the longitudinal steel as well as the CFRP sheets, such that the thicker the sheets without a sandwiched steel plate the lower the strain.

2- More pinching and less ductility were associated with the use of thicker CFRP sheets without steel plate fuse.

3- The use of a single layer of thick sheets caused the steel to have significant plastic deformation.

4- The curvature obtained from steel data was larger than that constructed using CFRP strain data for all CFRP strengthening configurations expect the one with steel plate which showed the similarities of the CFRP and steel curvatures.

5- The implementation of a steel plate fuse led to enhancements of the strengthened beams in terms of ductility, load capacity, and energy dissipation in the presence of shear strengthening.

Chapter 7 - Conclusions And Recommendations

7.1. Conclusions

An experimental investigation was conducted to evaluate the seismic performance of RC beams strengthened using various CFRP configurations with and without fiber anchors. A toral of fourteen fully scale RC beams, divided into two groups based on concrete compressive strength and reinforcement steel ratios, were subjected to reversed cyclic loading until failure. Twelve beams were strength using different CFRP strengthening schemes varied in terms of sheets thickness, number of sheets, number of fiber anchors, diameter of fiber anchors, depth of fiber anchors, and the use steel plate as well as its thickness. Two of the specimens were tested as control beams to evaluate the advantages of using CFRP strengthening. Each group was subdivided into seven sets based on the CFRP strengthening configuration, including control beam, thin CFRP sheets, thick CFRP sheets, thin CFRP sheet with fiber anchors, thick CFRP sheets with fiber anchors, double thick CFRP with fiber anchors, and double thick CFRP sheets with sandwiched steel plate secured with fiber anchors.

The experimental results of group one, with low concrete compressive strength and low steel ratio, showed that the use of carbon fiber splay anchors along with thin CFRP sheets had limited effect on the load-displacement response prior to yielding of reinforcing steel compared to the response without anchoring. In contrast, the ultimate capacity was noticeably enhanced due to the fact that anchors delayed the CFRP debonding. The use of carbon fiber splay anchors along with thick CFRP sheets had slight effect on the load-displacement response even after yielding of reinforcing steel compared to the one without anchoring even though the anchors shifted the failure mode to complete cover delamination around the anchor depths as opposed to sheet debonding. This is attributed to the use of no more than two anchors per shear span located back-to-back at the sheet ends with a limited fiber anchor embedment depth. On the other hand, the increase in CFRP thickness positively influenced the ultimate strength while negatively impacting the energy dissipation and ductility for thicker CFRP sheets. Furthermore, the implementation of double-thick CFRP sheets with more, deeper, and larger anchors significantly enhanced the ultimate capacity and slightly improved energy dissipation compared to the use of a single thick layer. In contrast, incorporating a sandwiched steel plate within the plastic hinge region, along with double-thick CFRP sheets and shear strengthening, resulted in substantial improvement in beam performance, leading to higher ultimate capacity, energy dissipation, and ductility.

By exploring the experimental investigations of the second group, characterized by normal concrete compressive strength and a typical steel ratio, it was observed that the higher the CFRP thickness applied, the less energy dissipation and the more pinching is observed, leading to the conclusion that heavily strengthened RC beams with externally bonded CFRP will behave less favorably to anticipated seismic response. The higher the CFRP thickness applied, the higher the ultimate loading capacity experienced, especially with the application of CFRP anchors. Conversely, the use of anchors with the thin CFRP layer resulted in no tangible benefit compared to the twin beam with no anchors. Failure modes were controlled by CFRP rupture or debonding on the shear span side of the load point. The control beam had the highest ductility while the beam with double-thick CFRP sheets along with a sandwiched steel plate had the second highest ductility. It is important to note that the use of end anchors in the thin CFRP sheet beam reflected no benefit in behavior, while the use of two end anchors per shear span in the thick CFRP sheet beam illustrated a noticeable improved performance over the beam’s unanchored twin. The used of double-thick CFRP sheets secured with fiber anchors, resulted in a remarkable improvement in the loading capacity, and slightly enhanced the energy dissipation. Regarding the utilization of a fuse steel plate combined with secured double-thick CFRP sheet, there was a major improvement in terms of the ultimate capacity, energy dissipation.

Further analytical investigations were carried out including the use trilinear moment-curvature approach developed by (Charkas et al. 2003) to determine the full nonlinear load-deflection response for CFRP-strengthened reinforced concrete beams. The resulting envelope curves matched the experimental ones closely. A phenomenological hysteretic load-deflection model was proposed, calibrated using experimental hysteresis loops from two beams. The model accurately depicted these loops by using a three-region approach, with master curves for slope degradation as load increases. Additionally, the drift span within each cycle was divided into 25%-50%-25% for unloading, inflection, and reloading regions, respectively. When applied to two others similarly strengthened beams, the model showed excellent agreement in blind comparisons. The model demonstrates promise in capturing envelope curves and hysteresis loops at various loading levels and can potentially be extended to other structural systems with some modifications based on experimental data. It is expected that the calibrated normalized slope degradation curves for region A-C to be applicable to case of similar CFRP flexural ratio ($\rho_f = \frac{A_f}{bd}$). This poses a limitation on the applicability of these degradation graphs to the range of CFRP ratios covered by the present experiments.

Finally, several experimental responses of strengthened RC beam with viruses CFRP configuration were carefully investigated and the following conclusions were drawn. There is a direct relationship between the thickness of CFRP sheets and the level of the strain in the longitudinal steel as well as the CFRP sheets, such that the thicker the sheets without a sandwiched steel plate the lower the strain. More pinching and less ductility were associated with the use of thicker CFRP sheets without steel fuse plate. The use of singular layer of thick sheets caused the steel to have significant plastic deformation.

7.2. Recommendations

The findings and conclusions of this research study suggested several recommendations for future work.

- Extending the experimental work to investigate the effects of using GFRP instead of CFRP sheets.
- Using a sandwiched steel plate within the constant moment region with single thick and thick layer of CFRP sheets.
- Extending the shear strengthening to cover the area underneath the loading points to avoid failure at that point and shifting the mode of failure into flexural.
- Conducting an experiment on RC beams reinforced with GFRP bars instead of typical steel reinforcement.
- Developing an analytical model to predict the flexural response of RC beams strengthened with CFRP sheet and taking into account the effects of fiber anchors.
- Establishing an analytical or numerical model to simulate the cyclic load-disparagement response of RC beams strengthening with CFRP sheets.

References

Abdalla, J. A., Hawileh, R. A., & Rasheed, H. A. (2022). Behavior of Reinforced Concrete Beams Strengthened in Flexure using Externally Bonded Aluminum Alloy Plates. Procedia Structural Integrity, 37, 652-659.

AC125 Acceptance criteria for concrete and reinforced and unreinforced masonry strengthening using externally bonded fiber-reinforced polymer (FRP) composite systems. ICC-ES (2021).

ACI 318-19: Building code requirements for structural concrete: CCOMMENTARY on building code requirements for structural concrete (ACI 318R-19). (2019). American Concrete Institute.

Alabdulhady, M. Y., Ojaimi, M. F., & Chkheiwer, A. H. (2022). The efficiency of CFRP strengthening and repair system on the flexural behavior of RC beams constructed with different concrete compressive strength. Results in Engineering, 16, 100763.

Alhassan, M., Al-Rousan, R., & Ababneh, A. (2021). Anchoring of the main CFRP sheets with transverse CFRP strips for optimum upgrade of RC Beams: Parametric experimental study. Construction and Building Materials, 293, 123525.

Alkhawaldeh, A. A., & Alrousan, R. Z. (2023). Improving cyclic response of heat-damaged non-ductile RC joints using CFRP hybrid systems. Construction and Building Materials, 377, 131150.

Al-Salloum YA, Almusallam TH. Seismic response of interior RC beam-column joints upgraded with FRP sheets. I: Experimental study. Journal of Composites for Construction. 2007 Dec;11(6):575-89.

Alsayed SH, Al-Salloum YA, Almusallam TH, Siddiqui NA. Seismic response of FRP-upgraded exterior RC beam-column joints. Journal of Composites for Construction. 2010 Apr;14(2):195-208.

Alshamrani S, Rasheed HA, Salahat FH, Borwankar A, Divilbiss N. Seismic flexural behavior of CFRP strengthened reinforced concrete beams secured with fiber anchors. Engineering Structures. 2024 Apr 15;305:117728.

Al-Tamimi, A. K., Hawileh, R., Abdalla, J., & Rasheed, H. A. (2011). Effects of ratio of CFRP plate length to shear span and end anchorage on flexural behavior of SCC RC beams. Journal of Composites for Construction, 15(6), 908-919.

Anil, Ö. (2008). Strengthening of RC T-section beams with low strength concrete using CFRP composites subjected to cyclic load. Construction and Building Materials, 22(12), 2355-2368.

Arslan, G. and Polat, Z., 2013. Contribution of concrete to shear strength of RC beams failing in shear. Journal of Civil Engineering and Management, 19(3), pp.400-408.

Barris, C., Baena, M., Jahani, Y., Codina, A., & Torres, L. (2023). Experimental Study on Flexural Cracking and Deformation of Reinforced-Concrete Beams Strengthened with NSM FRP Reinforcement. Journal of Composites for Construction, 27(2), 04023006.

Capani, F., D'Ambrisi, A., De Stefano, M., Focacci, F., Luciano, R., Nudo, R., & Penna, R. (2017). Experimental investigation on cyclic response of RC elements repaired by CFRP external reinforcing systems. Composites Part B: Engineering, 112, 290-299.

Carrillo, J., González, W. & Benjumea, J. Cyclic stress–strain behavior of low-diameter reinforcing bars for thin concrete walls. Bull Earthquake Eng 21, 5505–5523 (2023). https://doi.org/10.1007/s10518-023-01723-w

Ceroni, F. (2010). Experimental performances of RC beams strengthened with FRP materials. Construction and Building materials, 24(9), 1547-1559.

Ceroni, F., Pecce, M., Matthys, S., & Taerwe, L. (2008). Debonding strength and anchorage devices for reinforced concrete elements strengthened with FRP sheets. Composites Part B: Engineering, 39(3), 429-441.

Chalot, A., Roy, N., Michel, L., & Ferrier, E. (2021). Mechanical behavior of a full-scale RC wall-slab connection reinforced with frp under cyclic loading. *Engineering Structures*, *239*, 112146.

Chen, C., Sui, L., Xing, F., Li, D., Zhou, Y., & Li, P. (2018). Predicting bond behavior of HB FRP strengthened concrete structures subjected to different confining effects. Composite Structures, 187, 212-225.

Chen, J. F., Yuan, H., & Teng, J. G. (2007). Debonding failure along a softening FRP-to-concrete interface between two adjacent cracks in concrete members. Engineering Structures, 29(2), 259-270.

Codina, A., Barris, C., Jahani, Y., Baena, M., & Torres, L. (2024). Experimental and theoretical study on the flexural behaviour of RC beams strengthened with externally bonded reinforcement on grooves CFRP laminates. Engineering Structures, 299, 117091.

Coleman, I. (2014). The Development of Modelling Tools for Railway Switches and Crossings.

Desayi, P., Iyengar, K., and Reddy, T. (July 1, 1979). "Stress-Strain Characteristics of Reinforcing Steel Bars Under Cyclic Loading." ASTM International. J. Test. Eval.. July 1979; 7(4): 199–207. https://doi.org/10.1520/JTE11381J

Diab, H. M., & Farghal, O. A. (2014). Bond strength and effective bond length of FRP sheets/plates bonded to concrete considering the type of adhesive layer. Composites Part B: Engineering, 58, 618-624.

Dias, S. J., Barros, J. A., & Janwaen, W. (2018). Behavior of RC beams flexurally strengthened with NSM CFRP laminates. Composite Structures, 201, 363-376.

Dirks, B., Enblom, R., Ekberg, A., & Berg, M. (2015). The development of a crack propagation model for railway wheels and rails. Fatigue & Fracture of Engineering Materials & Structures, 38(12), 1478-1491. doi:10.1111/ffe.12318

Dollevoet, R. P. B. J. (2010). Design of an Anti Head Check Profile Based on Stress Relief. (PhD), University of Twente, Enschede, The Netherlands.

Dong, J. F., Wang, Q. Y., & Guan, Z. W. (2012). Structural behaviour of RC beams externally strengthened with FRP sheets under fatigue and monotonic loading. Engineering Structures, 41, 24-33.

Dowell, O. K., Seible, F., & Wilson, E. L. (1998). Pivot hysteresis model for reinforced concrete members. ACI Structural Journal, V.95, No 5. pp. 607-617. doi: 10.14359/575

Esmaeili, J., Aghdam, O. R., Andalibi, K., Kasaei, J., & Gencel, O. (2022). Experimental and numerical investigations on a novel plate anchorage system to solve FRP debonding problem in the strengthened RC beams. Journal of Building Engineering, 45, 103413.

Fu, B., Teng, J. G., Chen, G. M., Chen, J. F., & Guo, Y. C. (2018). Effect of load distribution on IC debonding in FRP-strengthened RC beams: Full-scale experiments. Composite Structures, 188, 483-496.

Gao, W. Y., Teng, J. G., & Dai, J. G. (2012). Effect of temperature variation on the full-range behavior of FRP-to-concrete bonded joints. Journal of Composites for Construction, 16(6), 671-683.

Garcia, J., Sun, W., Kim, C., Ghannoum, W. M., & Jirsa, J. O. (2014). Procedures for the installation and quality control of anchored CFRP sheets for shear strengthening of concrete bridge girders (No. FHWA/TX-13/5-6306-01-1).

Golias, E.; Zapris, A.G.; Kytinou, V.K.; Osman, M.; Koumtzis, M.; Siapera, D.; Chalioris, C.E.; Karayannis, C.G. Application of X-Shaped CFRP Ropes for Structural Upgrading of Reinforced Concrete Beam–Column Joints under Cyclic Loading–Experimental Study. Fibers 2021, 9, 42. https://doi.org/10.3390/fib9070

Hollaway, L. C., & Leeming, M. (Eds.). (1999). Strengthening of reinforced concrete structures: Using externally-bonded FRP composites in structural and civil engineering. Elsevier.

Jawdhari, A., Peiris, A., & Harik, I. (2018). Experimental study on RC beams strengthened with CFRP rod panels. Engineering structures, 173, 693-705.

Jun-Tao Zhu, Xin-Ling Wang, Zhao-Dong Xu, Chen-Hui Weng, Experimental study on seismic behavior of RC frames strengthened with CFRP sheets, Composite Structures, Volume 93, Issue 6, 2011, Pages 1595-1603, ISSN 0263-8223, https://doi.org/10.1016/j.compstruct.2011.01.007.

Karayannis, C. G., & Golias, E. (2022). Full-scale experimental testing of RC beam-column joints strengthened using CFRP ropes as external reinforcement. Engineering Structures, 250, 113305.

Khalifa, A. M. (2016). Flexural performance of RC beams strengthened with near surface mounted CFRP strips. Alexandria Engineering Journal, 55(2), 1497-1505.

Kim, Yail Jimmy, ed. Advanced composites in bridge construction and repair. No. 50. Elsevier, (2014).

Laseima, S. Y., Mutalib, A. A., Osman, S. A., & Hamid, N. H. (2020). Seismic Behavior of Exterior RC Beam-Column Joints Retrofitted using CFRP Sheets. Latin American Journal of Solids and Structures, 17.

Lee, L. S., & Jain, R. (2009). The role of FRP composites in a sustainable world. Clean Technologies and Environmental Policy, 11, 247-249.

Li, X., Deng, J., Liu, Z., Zhu, M., & Luo, S. (2023). Cracking behavior of prestressed CFRP strengthened RC beams subjected to wetting/drying cycling under flexural load. Construction and Building Materials, 398, 132403.

Liu, D., Qin, F., Di, J., & Zhang, Z. (2023). Flexural behavior of reinforced concrete (RC) beams strengthened with carbon fiber reinforced polymer (CFRP) and ECC. Case Studies in Construction Materials, 19, e02270.

Liu, D., Qin, F., Di, J., & Zhang, Z. (2023). Flexural behavior of reinforced concrete (RC) beams strengthened with carbon fiber reinforced polymer (CFRP) and ECC. Case Studies in Construction Materials, 19, e02270.

Liu, L., Yu, S., & Ma, X. (2023). Flexural capacity of RC beams reinforced with ECC layer and steel plate. Journal of Building Engineering, 65, 105781.

Mohammad Razavi, Davood Mostofinejad, Mohammadreza Eftekhar, Behavior of RC columns and those strengthened with FRP composite under an innovative reversing cyclic eccentric axial loading, Engineering Structures, Volume 241, 2021, 112438, ISSN 0141-0296, https://doi.org/10.1016/j.engstruct.2021.112438.

Nehdi M, Said A. Performance of RC frames with hybrid reinforcement under reversed cyclic loading. Materials and structures. 2005 Jul;38:627-37.

Paimushin, V.N., Kayumov, R.A., Kholmogorov, S.A. (2022). Accumulation of Microdamages During Cyclic Loading of CFRP Structure Elements. In: Badriev, I.B., Banderov, V., Lapin, S.A. (eds) Mesh Methods for Boundary-Value Problems and Applications. Lecture Notes in Computational Science and Engineering, vol 141. Springer, Cham. https://doi.org/10.1007/978-3-030-87809-2_28

Rasheed, H. A., & Pervaiz, S. (2002). Bond slip analysis of fiber-reinforced polymer-strengthened beams. Journal of engineering mechanics, 128(1), 78-86.

Rasheed, H. A., & Pervaiz, S. (2003). Closed form equations for FRP flexural strengthening design of RC beams. Composites Part B: Engineering, 34(6), 539-550.

Rasheed, H. A., Charkas, H., & Melhem, H. (2004). Simplified nonlinear analysis of strengthened concrete beams based on a rigorous approach. Journal of Structural Engineering, 130(7), 1087-1096.

Rasheed, H. A., Decker, B. R., Esmaeily, A., Peterman, R. J., & Melhem, H. G. (2015). The influence of CFRP anchorage on achieving sectional flexural capacity of strengthened concrete beams. Fibers, 3(4), 539-559.

Roberto Realfonzo, Annalisa Napoli, Joaquín Guillermo Ruiz Pinilla, Cyclic behavior of RC beam-column joints strengthened with FRP systems, Construction and Building Materials, Volume 54, 2014, Pages 282-297, ISSN 0950-0618, https://doi.org/10.1016/j.conbuildmat.2013.12.043.

Samiullah Qazi, Laurent Michel, Emmanuel Ferrier, Seismic behaviour of RC short shear wall strengthened with externally bonded CFRP strips, Composite Structures, Volume 211, 2019, Pages 390-400, ISSN 0263-8223, https://doi.org/10.1016/j.compstruct.2018.12.038.

Sandeep G. Sawant, H.S. Jadhav, Flexural behaviour of GFRP strengthened RC beams under cyclic loading, Materials Today: Proceedings, Volume 59, Part 1, 2022, Pages 188-195, ISSN 2214-7853, https://doi.org/10.1016/j.matpr.2021.10.396.

Saqan, E. I., Rasheed, H. A., & Alkhrdaji, T. (2018). Evaluation of the seismic performance of reinforced concrete frames strengthened with CFRP fabric and NSM bars. Composite Structures, 184, 839-847.

Saqan, E. I., Rasheed, H. A., & Alkhrdaji, T. (2020). Seismic Behavior of Carbon Fiber-Reinforced Polymer-Strengthened Reinforced Concrete Members with Various Anchors. ACI Structural Journal, 117(4).

Saqan, E. I., Rasheed, H. A., & Hawileh, R. A. (2013). An efficient design procedure for flexural strengthening of RC beams based on ACI 440.2 R-08. Composites Part B: Engineering, 49, 71-79.

Sbahieh, S., Rabie, M., Ebead, U., & Al-Ghamdi, S. G. (2022). The mechanical and environmental performance of fiber-reinforced polymers in concrete structures: Opportunities, challenges and future directions. Buildings, 12(9), 1417.

Sbahieh, S., Tahir, F., & Al-Ghamdi, S. G. (2022). Environmental and mechanical performance of different fiber reinforced polymers in beams. Materials Today: Proceedings, 62, 3548-3552.

Sharma, A., Eligehausen, R., & Reddy, G. R. (2013). Pivot Hysteresis Model Parameters for Reinforced Concrete Columns, Joints, and Structures. ACI Structural Journal, V.110, No 2. doi: 10.14359/51684402.

Shi-Jie Mei, Yu-Lei Bai, Jian-Guo Dai, Qiang Han, Seismic behaviour of shear critical square RC columns strengthened by large rupture strain FRP, Engineering Structures, Volume 280,2023, 115679, ISSN 0141-0296, https://doi.org/10.1016/j.engstruct.2023.115679.

Siddika, A., Al Mamun, M. A., Ferdous, W., & Alyousef, R. (2020). Performances, challenges and opportunities in strengthening reinforced concrete structures by using FRPs–A state-of-the-art review. Engineering Failure Analysis, 111, 104480.

Singh, V., Bansal, P. P., Kumar, M., & Kaushik, S. K. (2014). Experimental studies on strength and ductility of CFRP jacketed reinforced concrete beam-column joints. Construction and Building Materials, 55, 194-201.

Smith, S. T., Rasheed, H. A., & Kim, S. J. (2017). Full-range load-deflection response of FRP-strengthened RC flexural members anchored with FRP anchors. Composite Structures, 167, 207-218.

Teng, J. G., Chen, J. F., Smith, S. T., & Lam, L. (2002). FRP: strengthened RC structures (p. 266).

Vijayan, D. S., Sivasuriyan, A., Devarajan, P., Stefańska, A., Wodzyński, Ł., & Koda, E. (2023). Carbon Fibre-Reinforced Polymer (CFRP) Composites in Civil Engineering Application—A Comprehensive Review. Buildings, 13(6), 1509.

Vijayan, D.S.; Sivasuriyan, A.; Devarajan, P.; Stefa ´nska, A.; Wodzy ´nski, Ł.; Koda, E. Carbon Fibre-Reinforced Polymer (CFRP) Composites in Civil Engineering Application—A Comprehensive Review. Buildings 2023, 13, 1509. https://doi.org/10.3390/buildings13061509

Wang, Q., Zhu, H., Li, T., Wu, G., & Hu, X. (2019). Bond performance of NSM FRP bars in concrete with an innovative additional ribs anchorage system: an experimental study. Construction and Building Materials, 207, 572-584.

Yasir M. Saeed, Wisam A. Aules, Franz N. Rad, Flexural strengthening of RC columns with EB-CFRP sheets and NSM-CFRP rods and ropes, Composite Structures, Volume 301, 2022, 116236, ISSN 0263-8223, https://doi.org/10.1016/j.compstruct.2022.116236.

Zaki, M. A., Rasheed, H. A., Roukerd, R. R., & Raheem, M. (2020). Performance of reinforced concrete T beams strengthened with flexural CFRP sheets and secured using CFRP splay anchors. Engineering Structures, 210, 110304.